IMPROVEMENTS TO THE ANALYTICAL PERFORMANCE OF ION TRAP MASS SPECTROMETRY

Desmond Allen Kaplan

A dissertation submitted to the faculty of the University of North Carolina at Chapel Hill in partial fulfillment of the requirements for the degree of Doctor of Philosophy in the Department of Chemistry.

Chapel Hill
2006

Approved by
Advisor: Professor Gary L. Glish
Reader: Professor James W. Jorgenson
Reader: Professor Tomas Baer

ABSTRACT

Desmond Allen Kaplan

Improvements to the Analytical Performance of Ion Trap Mass Spectrometry
(Under the direction of Professor Gary L. Glish)

Mass spectrometry is a powerful analytical technique that is capable of a wide range of chemical and biological analyses. The quadrupole ion trap mass spectrometer (QITMS) is known for its ruggedness, sensitivity, and high efficiency for tandem mass spectrometry (MS/MS) experiments. Non-idealities in electrode geometry result in small contributions of higher order fields (HOFs) to the primary quadrupolar electric field of the ion trap. These HOFs have been useful in enhancing the resolution, MS/MS efficiency, and sensitivity in the QITMS. A portion of the work presented in this dissertation is intended to serve as a basis for improved ion trap performance through the judicious use of HOFs.

Development of rf circuitry and characterization of a compensated cylindrical ion trap (CCIT) mass spectrometer, designed for studying the effects of HOFs, are also described herein. An additional set of grounded electrodes was introduced into the CCIT instrument to remove detrimental effects of capacitive coupling and HOFs were successfully introduced. Mass spectra acquired after the introduction of HOFs showed improvements to the injection efficiency over a broad range of rf voltages.

The optimal conditions for resonance ejection in the CCIT occurred at an octapole HOF non-linear resonance, which gave improvements both to mass resolution and sensitivity (i.e., the number of ions detected). Resonance ejection performed at an octapole non-linear

resonance was successful in improving the sensitivity of the CCIT for the analysis of volatile organic compounds in the presence of a heavy buffer gas.

A novel higher order field ion trap, possessing predominantly octapole fields, was developed. This octapole ion trap exhibited higher trapping capacity than a quadrupole ion trap of similar geometry. However, mass analysis in the octapole ion trap was not achievable because ions were resonantly ejected over a broad frequency range. A second generation octapole ion trap, with improved resonance ejection characteristics, also was developed. Resonance ejection experiments in this geometry were in agreement with ion trajectory simulations, but mass analysis using resonance ejection was again not possible due to broad band ejection. A non-destructive Fourier transform detection method was simulated and found to be viable.

For my parents and brother who have always supported me and who have instilled in me a level of dedication and drive that will live in me forever.

To my loving wife, without your love and support none of this would have been possible. It is a great comfort to know you will always be there.

To every teacher who has believed in me along the way.

In memory of my grandparents:

Benjamin and Floris Kaplan

ACKNOWLEDGEMENTS

My success during my graduate career would not have been possible without the support and friendship of many people whom I have met along the way. First I would like to thank my advisor, Gary L. Glish, who has supported me both in my research and my career. I would particularly like to thank him for having the confidence in me to let me teach at his side and on my own, while still successfully completing research. The knowledge and experience I have gained through working in his lab will truly help me in my future endeavors.

I would like to thank the past and present members of the Glish Group for their support, guidance and camaraderie throughout my graduate career. Graduate school would have been much more difficult if it was not for their friendships. I would like to particularly acknowledge Ryan Danell, Collin McKinney and John Peterson for their specific contributions to the research contained in Chapter 2, as well as Karen Wendling and Jared Bushey for their contributions to the project described in Chapter 3. I would also like to thank those have read and helped to edit parts of this dissertation, particularly Phil Remes, Karen Wendling, Jared Bushey, Brittany Butler, and David Burinsky.

During my last year I had the unique opportunity to do research at Thermo Electron Corporation in Austin, Texas under the direction of Scott Quarmby and Brody Guckenberger. I am forever grateful to both of them and I will cherish the professional and personal relationships that I developed with them. The knowledge and experience I gained during that summer will forever change my life.

TABLE OF CONTENTS

Page

LIST OF TABLES

LIST OF FIGURES

LIST OF ABBREVIATIONS AND SYMBOLS

A_n	Weighting term for higher order field component
ac	Alternating current
APC	Automated parameter control
ASGDI	Atmospheric sampling glow discharge ionization
a_r	Mathieu equation parameter related to the dc (radial)
a_u	Mathieu equation parameter related to the dc (axial or radial)
a_z	Mathieu equation parameter related to the dc (axial)
°C	Degrees Celsius
C	Capacitance
CIT	Cylindrical ion trap
CCIT	Compensated cylindrical ion trap
CI	Chemical ionization
CID	Collision-induced dissociation
cm	Centimeters
Da	Daltons
dB	Decibels
dc	Direct current
DDE	Data dynamic exchange
e	Fundamental unit of charge (1.602×10^{-19} Coulombs)
EI	Electron ionization
eV	Electron volt

F	Force
FFT	Fast Fourier Transform
f_r	Radio frequency circuitry resonant frequency
FT	Fourier Transform
GC	Gas chromatography
GC/MS	Gas chromatography/mass spectrometry
GDI	Glow discharge ionization
GHz	Gigahertz
GUI	Graphical user interface
ICR	Ion cyclotron resonance
ID	Inner diameter
K	Kelvin
kJ/mol	Kilojoules per mole
kHz	Kilohertz
L	(1) Liter (2) Inductance
L_n	Inductance per turn
L/min	Liters per minute
LC	Circuit with inductive and capacitive components
LMCO	Low mass cut off
M_g	Angular momentum
m	Mass
mA	MilliAmperes
mg	Milligrams

MHz	Megahertz
mL	Milliliters
mL/min	Milliliters per minute
mm	Millimeters
ms	Milliseconds
MS/MS	Tandem mass spectrometry
MS^n	Multiple stages of mass spectrometry
mV	Millivolts
m/z	Mass-to-charge ratio
ng	Nanograms
nL/min	Nanoliters per minute
nm	Nanometers
n_t	Number of turns to increase or decrease while tuning resonant circuitry
OCIT	Octapole cylindrical ion trap
OEOCIT	Open endcap octapole cylindrical ion trap
OEQCIT	Open endcap quadrupole cylindrical ion trap
OD	Outer diameter
PA	Proton affinity
PCI	Peripheral component interconnect
pF	Picofarads
ppb	Parts per billion
ppm	Parts per million
PTR-MS	Proton-transfer reaction mass spectrometry

PXI	Peripheral extension instrumentation
QITMS	Quadrupole ion trap mass spectrometer
Q	Quality factor for resonant circuitry
q_r	Mathieu equation parameter related to the rf (radial)
q_u	Mathieu equation parameter related to the rf (axial or radial)
q_z	Mathieu equation parameter related to the rf (axial)
q_4	Mathieu equation parameter related to the rf (axial) in octapole ion trap
R	Resolving power
RE	Recombination energy
r_{in}	Radius of intermediate ring electrode
r_0	(1) Radius of the ring electrode (2) Inscribed radius of quadrupole mass filter
rf	Radio frequency
rf_1	Voltage of rf circuitry for center ring electrode
rf_2	Voltage of rf circuitry for left compensating ring electrode
rf_3	Voltage of rf circuitry for right compensating ring electrode
s	Seconds
s	Geometry relationship between electrodes in octapole ion trap
s_0	Dimension of normalization based on the electrode geometry
SICI	Selected ion chemical ionization
SID	Surface-induced dissociation
S/N	Signal-to-noise ratio
SWIFT	Stored waveform inverse Fourier transform
TTL	Transistor Transistor Logic

U	Amplitude of the dc voltage
V	Volt
VOCs	Volatile organic compounds
W	Watt
X_c	Reactance for capacitor
X_L	Reactance for inductors
x_0	Spacing between x-rod of quadrupole mass filer and center of device
y_0	Spacing between y-rod of quadrupole mass filer and center of device
Z_{series}	Series impedance
$Z_{parallel}$	Parallel impedance
z_0	Spacing between the ring and endcap electrodes
z	(1) Charge; (2) Axial direction in cylindrical coordinates
β_u	Beta parameter, axial or radial
ξ	Unit less parameter from Mathieu equation for quadrupole ion trap
ζ	Unit less parameter from Mathieu equation for octapole ion trap
ρ	Distance from the origin of the center of the trap to a point (r, z)
ϕ	Electric potential
Ω	(1) The fundamental rf frequency of an ion trap (2) Ohms
μA	MicroAmperes
μg/L	Micrograms per liter
μg/mL	Micrograms per milliliter
μH	Microhenry
μL	Microliters

μm	Micrometers
μs	Microseconds
ω_z	The secular frequency for an ion (axial)
ω_r	The secular frequency for an ion (radial)
2xOEOCIT	Larger dimension open endcap octapole cylindrical ion trap
2-D	Two-dimensional
3-D	Three-dimensional

Chapter 1

Introduction to Mass Spectrometry, Quadrupole Ion Traps and Higher Order Fields

1.1 Introduction

In today's biotechnology-rich environment there is an increasing demand on the analytical chemist to be an interdisciplinary problem solver. Mass spectrometry is an indispensable tool for applications such as homeland security, forensics, drug discovery, bio macromolecule research, and space exploration.[1] Mass spectrometry is capable of achieving femptomole detection limits on the microsecond time scale. Perhaps one of the most common uses for mass spectrometry is to identify unknown compounds. Although, the technique is being used more and more frequently as a means to study chemical, biological, or physical problems and not solely as a detector attached to a chromatograph. The mass spectrometer analyzes compounds in the gas phase, by ionizing them (adding or subtracting charge to make a neutral molecule into an ion), and then separating them according to their mass-to-charge (*m/z*) ratios. Ions are manipulated in the mass spectrometer by using electric or magnetic fields. The mass of an ion is typically reported in daltons (Da) and the charge is an integer value. Each unit of charge corresponds to the magnitude of the fundamental electronic charge, e. If the charge of a given ion is known then the molecular mass of that ion, and thus the neutral analyte molecule, can be determined. Depending on the ionization technique utilized, a variety of ions at different mass-to-charge ratios can be generated from a

population of analyte molecules and further information about the structure of those molecules can be obtained. If sufficient structural information is not obtained from the mass spectrum then tandem mass spectrometry (MS/MS) is performed. During tandem mass spectrometry, ions of a single mass-to-charge ratio from the mass spectrum are selected, typically referred to as the parent ion, and then purposefully dissociated to form additional ions, called product ions. In this way, tandem mass spectrometry can identify a compound as uniquely as a fingerprint identifies a person.

The quadrupole mass spectrometer was first introduced by Nobel Laureate Wolfgang Paul in 1953 and patented in 1960.[2] The usefulness of the quadrupole mass spectrometer was quickly realized and the instrument was commercialized. Since then, it has become one of the most common mass spectrometers in an analytical chemistry laboratory. The quadrupole ion trap mass spectrometer, described in the same patent, was listed as an alternative electrode arrangement to the quadrupole mass spectrometer. Until the early 1980s, the quadrupole ion trap remained solely a research instrument and was used mainly by physicists as an ion storage device for spectroscopic studies.[3-5] In 1984, following an innovation by researchers at Finnigan MAT corporation, the quadrupole ion trap was commercialized.[6] The quadrupole ion trap has the advantage of being able to store ions for tandem mass spectrometry (MS/MS) and multiple stage mass analysis (MS^n).[7] Additionally, the quadrupole ion trap is known for its high MS/MS efficiency and sensitivity. Technological advances over the past decade have helped the quadrupole ion trap become a highly sensitive, versatile, robust, and inexpensive mass spectrometer.[8]

During the commercialization of the ion trap, researchers realized that the quadrupole ion trap contained electric fields that were not intended from the theoretical design.[9] These

additional electric fields, referred to as higher order fields, originally degraded the performance of the quadrupole ion trap. Since that time, researchers have shown that proper utilization of these higher order fields can in fact improve the overall performance of the ion trap.[10] All commercially available ion traps contain higher order fields; therefore, it is important to understand the full impact of them on ion trap performance.[8] In fact, researchers recently have introduced an ion trap with a different composition of higher order fields that is capable of trapping significantly more ions than previous versions of the device.[11] This advancement suggests that a more in-depth understanding of higher order fields could lead to further improvements in ion trap performance.

The focus of this dissertation discusses methods aimed at improving the analytical performance of ion trap mass spectrometry. More specifically, experiments described in this dissertation utilize or study the effects of higher order fields that are present in all ion traps. This introductory chapter will describe the different components and types of mass spectrometers. Because of the similarity and importance of both analyzers, a detailed description of the theory and operation of quadrupole mass filters and quadrupole ion traps is presented. Finally, the origin, theory and effects of higher order fields are discussed.

1.2 Quadrupole Mass Filters

1.2.1 Electrodes

The quadrupole mass filter electrodes consist of a four rod array oriented such that they form two pairs, one in the x-plane and one in the y-plane as shown in **Figure 1.1**. The conventional quadrupole rods are hyperbolic and the cross section of the surfaces are described by **Equation 1.1** and **Equation 1.2** for the x rods and y rods respectively.[13]

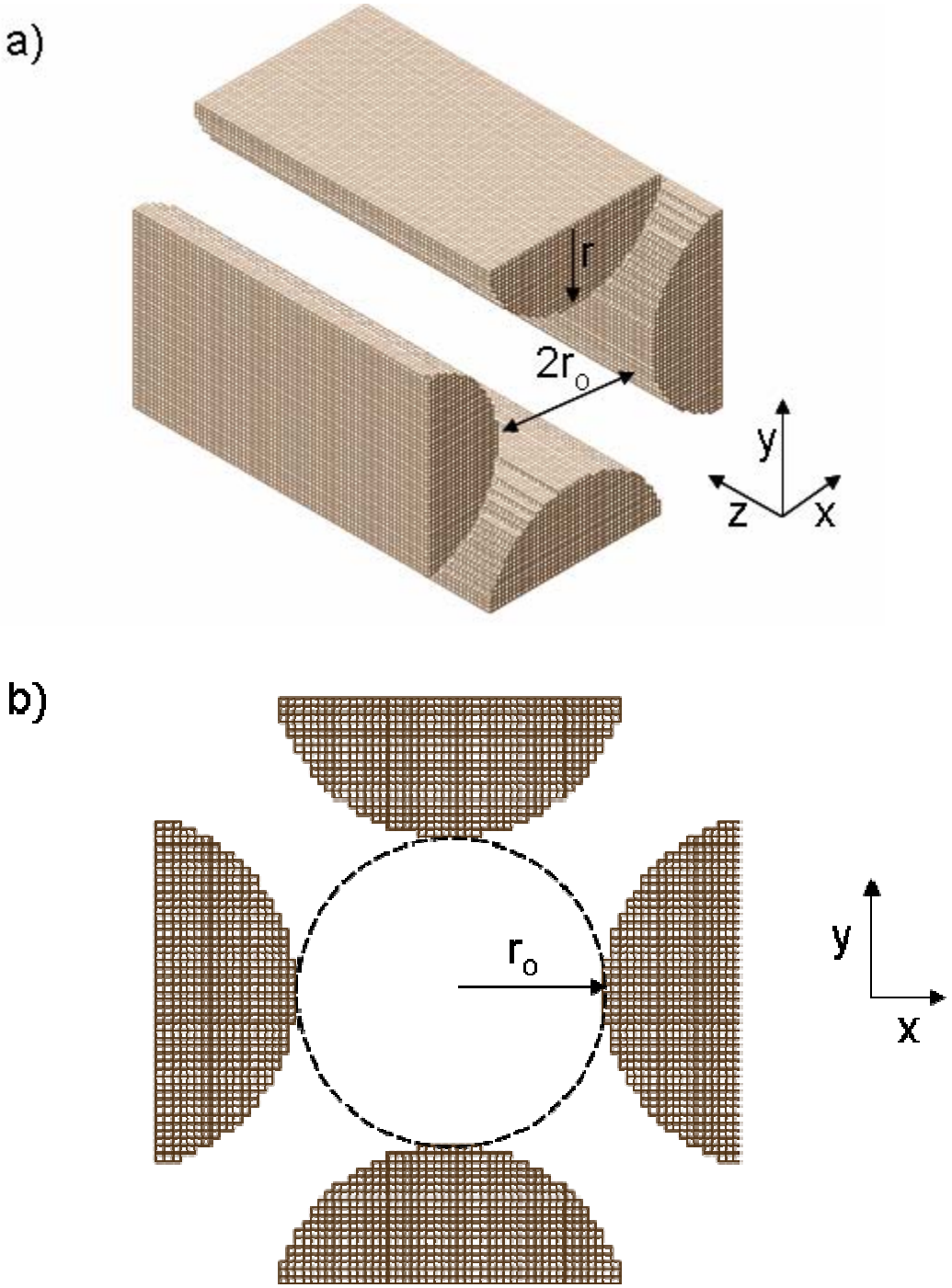

Figure 1.1 – Quadrupole mass analyzer: a) Three dimensional representation of circular rod assembly, b) Two dimensional representation of circular rod assembly showing inscribed radius (r_0) and the potential applied to rods.

$$x^2 - y^2 = r_0^2 \qquad \textbf{EQ 1.1}$$

$$x^2 - y^2 = -r_0^2 \qquad \textbf{EQ1.2}$$

These equations assume that inscribed radius of the circle (r_0), shown in **Figure 1.1,** is equal to the shortest distance between the x rods (x_0) and the shortest distance between the y rods (y_0); **Equation 1.3**.

$$x_0 = y_0 = r_0 \qquad \textbf{EQ 1.3}$$

Practically, the machining required to produce accurate hyperbolic electrodes can be quite difficult and costly; therefore, many commercially available quadrupole mass analyzer electrodes are round rods. The profiles of the rods shown in Figure 1.1 are round rods. To compensate for the effects of round rods, which will be addressed in **Section 1.2.2**, the radius of each rod (r) is traditionally made to be 1.148 times the radius of the inscribed circle.[14] In recent years, research has shown that the value is more variable and can range from $r = 1.12 \times r_0$ to $1.13 \times r_0$.[15] The reason for the decrease in the inscribed radius from the "traditional" value was attributed to further reduction of higher order fields (see **Section 1.4**) present as a result of the round rods.

1.2.2 Quadrupole Fields

The electric potential ($\phi_{x,y}$) at any point in a quadrupole field depends on the square of the distance from the center of the device (or another reference point). The electric potential as a function of the x and y dimensions is described by **Equation 1.4,** where r_0 is the inscribed radius of the rod array.[2, 13, 14] The potential difference, $\phi_{0,}$, between the voltage applied to the quadrupole rods as shown in **Figure 1.1** is described in **Equation 1.5**; where U is the dc potential and V is zero-to-peak amplitude of the voltage oscillating at the frequency Ω (in radians) for time t. The frequency is usually in the radio frequency (rf) range, and

therefore will subsequently be referred to as an rf voltage. (Note: **Equation 1.4** is based on hyperbolic rod geometries) When the rod geometry is not hyperbolic, r_0 is adjusted so that the electric field is equivalent to a hyperbolic rod of radius (r*correction factor).[14]

$$\phi_{x,y} = \frac{\phi_0}{2r_0^2}(x^2 - y^2) \qquad \textbf{EQ 1.4}$$

$$\phi_0 = 2(U + V\cos\Omega t) \qquad \textbf{EQ 1.5}$$

Two important concepts can be taken from **Equation 1.4**. First, the electric potential does not depend on the z dimension. The implication of this will be discussed shortly. Second, the effect of the electric potential on the x dimension and y dimensions are independent, meaning that the electric field can be treated independently for each dimension. Therefore at constant y values, the electric field $\left(\frac{d\phi}{dx}\right)_y$ varies linearly as a function of x, as shown in **Equation 1.6**. As shown in **Equation 1.7,** the force, (F_x), acting on an ion is also linear as a function of x, where e is integer value of the charge times the charge of an electron.

$$\left(\frac{d\phi}{dx}\right)_y = \frac{\phi_0 x}{r_0^2} \qquad \textbf{EQ 1.6}$$

$$F_x = -e\left(\frac{d\phi}{dx}\right)_y = -e\frac{\phi_0 x}{r_0^2} \qquad \textbf{EQ 1.7}$$

Using Newton's second law, **Equation 1.8,** the force acting on an ion of mass m and charge e can be related to the acceleration (a_x) of that ion in the presence of the electric potential.

$$F_x = ma_a = m\left(\frac{d^2x}{dt^2}\right) = -e\frac{\phi_0 x}{r_0^2} \qquad \textbf{EQ 1.8}$$

Substituting **Equation 1.5** into **Equation 1.8** and through minor manipulations the acceleration $\left(\frac{d^2x}{dt^2}\right)$ of an ion in the x dimension is shown in **Equation 1.9**.[13, 14]

$$\left(\frac{d^2x}{dt^2}\right)+\left(\frac{2eU}{mr_0^2}+\frac{2eV\cos\Omega t}{mr_0^2}\right)x=0 \qquad \textbf{EQ 1.9}$$

This second order differential equation does not have a simple solution. However, **Equation 1.9** matches the form of well known modified form of the general equation, **Equation 1.10**, developed by Emile Mathieu in the late 1860s.[16] In this equation ξ is a dimensionless parameter shown in **Equation 1.11**, u is a dimension x or y, and a_u and q_u are the Mathieu parameters.

$$\frac{d^2u}{d\xi^2}+(a_u-2q_u\cdot\cos 2\xi)u=0 \qquad \textbf{EQ 1.10}$$

$$\xi=\frac{\Omega\cdot t}{2} \qquad \textbf{EQ 1.11}$$

Substituting **Equation 1.11** into **Equation 1.10** with modifier **Equation 1.12** yields **Equation 1.13**.[13, 14]

$$\frac{d^2u}{dt^2}=\frac{\Omega^2}{4}\frac{d^2u}{d\xi^2} \qquad \textbf{EQ 1.12}$$

$$\frac{d^2u}{dt^2}+\left(\frac{\Omega^2}{4}a_u-\frac{\Omega^2}{2}q_u\cdot\cos\Omega t\right)u=0 \qquad \textbf{EQ 1.13}$$

The a_x and q_x parameters can be determined by comparing **Equation 1.9** and **Equation 1.13**, which are in **Equation 1.14** and **Equation 1.15** respectively.

$$a_x = -a_y = \frac{8eU}{mr_0^2\Omega^2} \qquad \textbf{EQ 1.14}$$

$$q_x = -q_y = \frac{-4eV}{mr_0^2\Omega^2} \qquad \textbf{EQ 1.15}$$

Because of the relationship shown in parenthesis in **Equation 1.4**, a_y and q_y are opposite in sign to a_x and q_x.

There are two solution sets to the Mathieu equation. In the first solution set, ions have a periodic motion which does not take them through the center of the quadrupole; therefore ions do not have a stable trajectory in these solutions. In the second set of solutions, ions have a periodic motion that does move them through the center of the quadrupole; therefore ions have a stable trajectory in these solutions. Because ion motion is decoupled, ions can have a stable trajectory in the x and not have stable trajectory in the y dimensions and vice versa. Ions will only traverse the quadrupole successfully when their trajectory is both x and y stable. **Figure 1.2** shows these stable solutions plotted in a_u, q_u coordinates. If an ion has a_u and q_u parameters that are between the solid lines, its trajectory is x-stable and when an ion's a_u and q_u parameters are between the dotted lines its trajectory is y-stable. The shaded overlap region is where ions can have both x and y stable trajectories. This region is often called the Mathieu stability diagram. This region is the first stability region, but is not the only region where the x-stable and y-stable curves overlap. If the plots were extended three additional regions of stability can be found. These other regions of stability are not practical for operation of the device because the dc and rf voltage required to reach the a_u and q_u parameters in these regions are too large. Therefore, operation of the quadrupole mass filter is typically performed in the first region of stability.

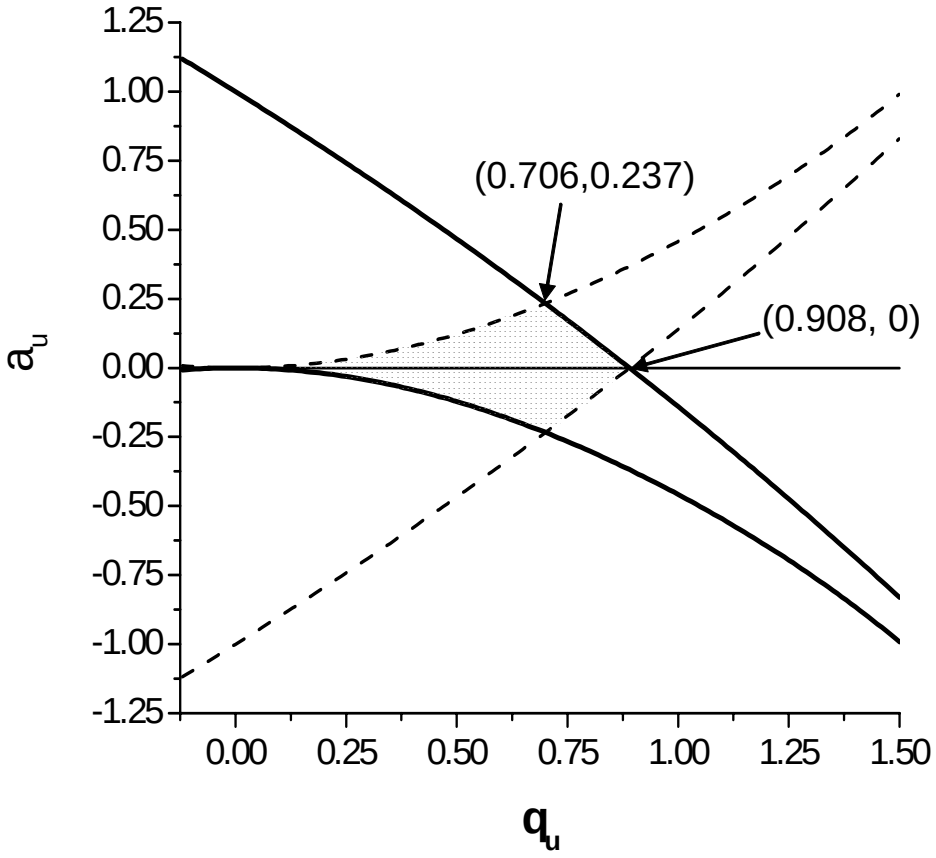

Figure 1.2 – Mathieu stability diagram for quadrupole mass filter. Ions with a_u and q_u parameters in shaded region have both x and y stable trajectories.

1.2.3 Quadrupole Operation

At a given dc and rf voltage applied to the quadrupole rods, ions (represented by gray circles) will have a and q parameters that are on a line as shown in **Figure 1.3a.** The line is often referred to as the "scan line" because ions of different mass-to-charge values are effectively "scanned" through the quadrupole by increasing the rf and dc voltages at a constant ratio. The quadrupole mass analyzer is normally operated by setting the slope of the scan line so that it passes through a point just below the apex of the stability diagram, which is at the (q_u, a_u) point (0.706, 0.237) (note the line must travel through 0, 0). This is done so that only ions of a single mass-to-charge ratio will have a_u and q_u parameters that result in a stable trajectory through the entire length of the device. As shown in **Figure 1.3b,** as the rf and dc voltages are increased linearly or scanned at a constant ratio the ions' a_u and q_u parameters move along the line. In order of increasing mass-to-charge ratio, ions with a_u and q_u parameters in the stability diagram are allowed to traverse through the quadrupole. When the slope of the scan line is decreased, a broader range of mass-to-charge ratio ions attain stable trajectories and are allowed to pass through the quadrupole. In some hybrid instruments, the quadrupole mass analyzer is used with no dc voltage (referred to as "rf only" mode), which allows the largest possible range of mass-to-charge ratios to traverse the quadrupole, as shown in **Figure 1.3c**.

When ions have a stable trajectory, the time it takes an ion to traverse the entire length of the quadrupole is based on the ion's axial velocity. After traversing the length of the quadrupole rods, ions strike a detector, such as an electron multiplier. The mass spectrum is created by correlating the rf voltage and dc voltage used to pass an ion through the quadrupole with the calculated mass-to-charge ratio from **Equation 1.14** and **Equation 1.15.**

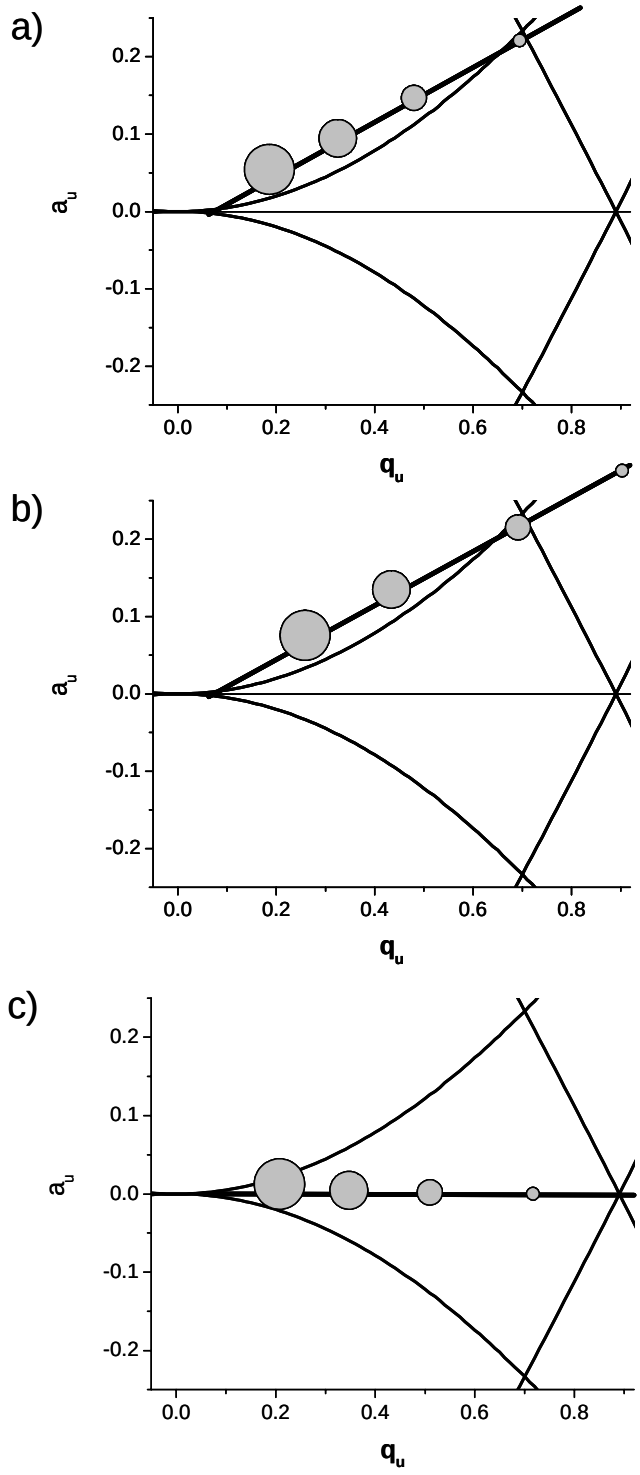

Figure 1.3 – Mathieu stability diagram with a) Ions along scan line, smallest ion passing through quadrupole b) Second ion passing through quadrupole and c) Operated in rf only mode.

A figure of merit for the mass analyzer is the mass resolving power (R), which is mathematically defined in **Equation 1.16;** where m is the mass of the ion and Δm is the full width of the corresponding peak at half of the maximum intensity. The slope of the scan line determines the range of mass-to-charge ratio ions that will traverse the quadrupole. When the scan line passes through the apex of the stability diagram the peak width with be as small as possible and the resolving power will be at its maximum value.

$$R = \frac{m}{\Delta m} \qquad \textbf{EQ1.16}$$

1.3 Quadrupole Ion Trap Mass Spectrometers

1.3.1 Electrode Geometries

Quadrupole ion trap electrode geometries come in a variety of shapes and sizes, ranging from hyperbolic electrodes with radii of a centimeter to cylindrical electrodes with radii on the micrometer scale.[17, 18] The overall electrode geometries can fall in to two classes: three-dimensional (3-D) and two-dimensional (2-D) ion traps. The term "dimension" does not refer to the electrode shape but rather the number of dimensions in which ion motion is affected by the voltages applied to the electrodes. This issue will be discussed in more detail in **Section 1.3.2.**

1.3.1.1 Three-Dimensional Ion Trap Electrode Geometries

The 3-D ion trap electrode geometry consists of three electrodes: one central ring electrode and two end cap electrodes. The conventional forms of these electrodes have hyperbolic surfaces, which are described by **Equation 1.17** and **Equation 1.18** for the ring electrode and end cap electrodes, respectively. These equations are expressed in polar coordinates and are plotted in the r and z dimensions in **Figure 1.4**.

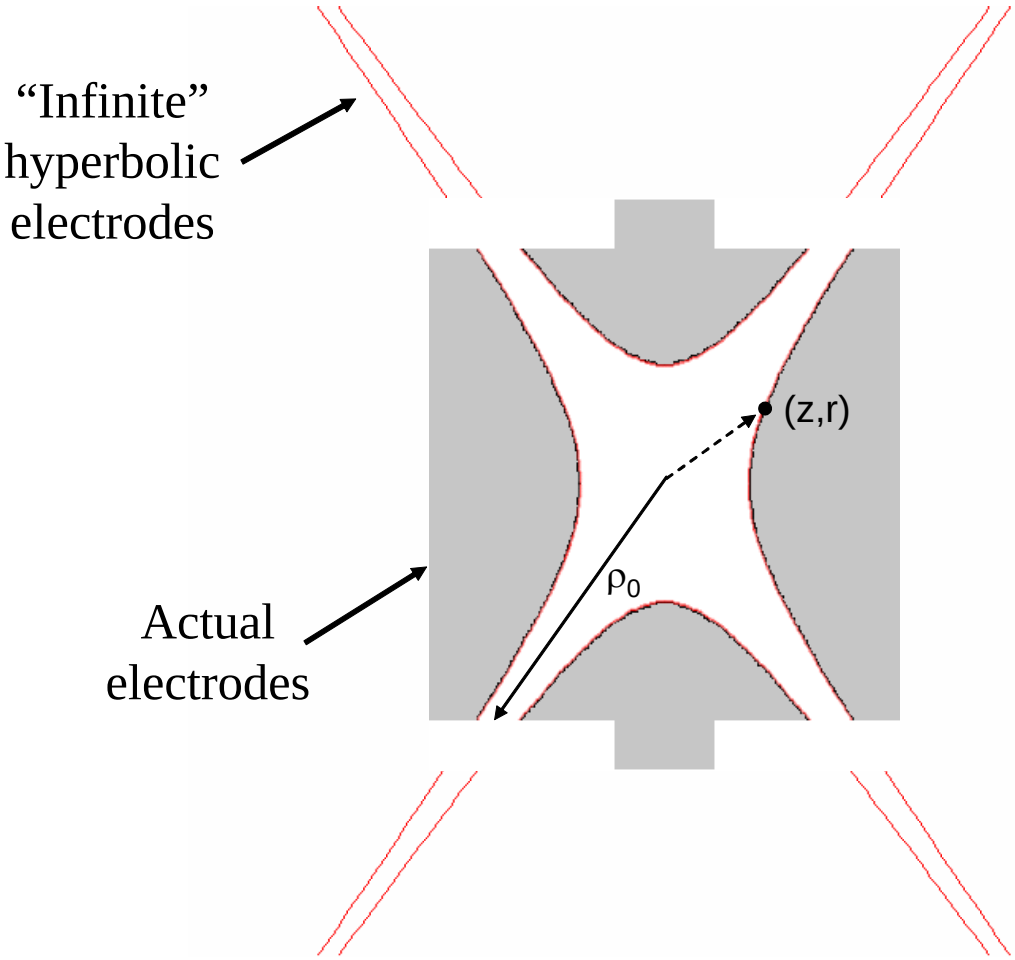

Figure 1.4 – Theoretical infinite hyperbolic quadrupole ion trap electrodes versus actual truncated electrodes.

When z = 0 then r = r_0 which is the inner diameter of the ring electrode. When r = 0 then z = z_0, which is the shortest distance between the surface of the end cap electrodes.[2, 19, 20]

$$\frac{r^2}{r_0^2} - \frac{2z^2}{r_0^2} = 1 \qquad \textbf{EQ 1.17}$$

$$\frac{r^2}{2z_0^2} - \frac{2z^2}{z_0^2} = -1 \qquad \textbf{EQ 1.18}$$

Because these equations have no limits, the surfaces of the electrodes should be infinitely long. However, as shown in **Figure 1.4,** the actual electrodes are truncated. The dimensions of the theoretical 3-D ion trap are r_0 = 1 cm and z_0 = 0.707 cm and the electrodes are truncated at distance ρ_0 from the center of the ion trap. The truncation distance (ρ_0) is usually $2r_0$.[2, 8, 21] The effects of this electrode truncation will be discussed in **Section 1.4**. These dimensions are based on the theoretical relationship expressed in **Equation 1.19.** Not all commercially available 3-D quadrupole ion trap electrode geometries satisfy **Equation 1.19**. In one example, which occurred during the commercialization of the ion trap, the distance between the endcap electrodes was increased 10.8% to 0.783 cm.[21] Mechanical tolerances of the machining techniques used to construct these electrodes make them difficult to fabricate. An additional difficulty in the production of these electrodes is that holes must be drilled in the end caps for ion entry and exit.

$$r_0^2 = 2z_0^2 \qquad \textbf{EQ 1.19}$$

An alternative (and easier to manufacture) electrode geometry is that of the cylindrical ion trap.[22] As shown in **Figure 1.5**, the cylindrical ion trap is a 3-D ion trap with three cylindrical electrodes. The electrode geometry is simple enough that the electrodes can be machined simply by drilling a hole in 3 parallel plates, there is no requirement that the plates be circular.[23] Because of the simplicity in manufacturing the cylindrical ion trap, it has

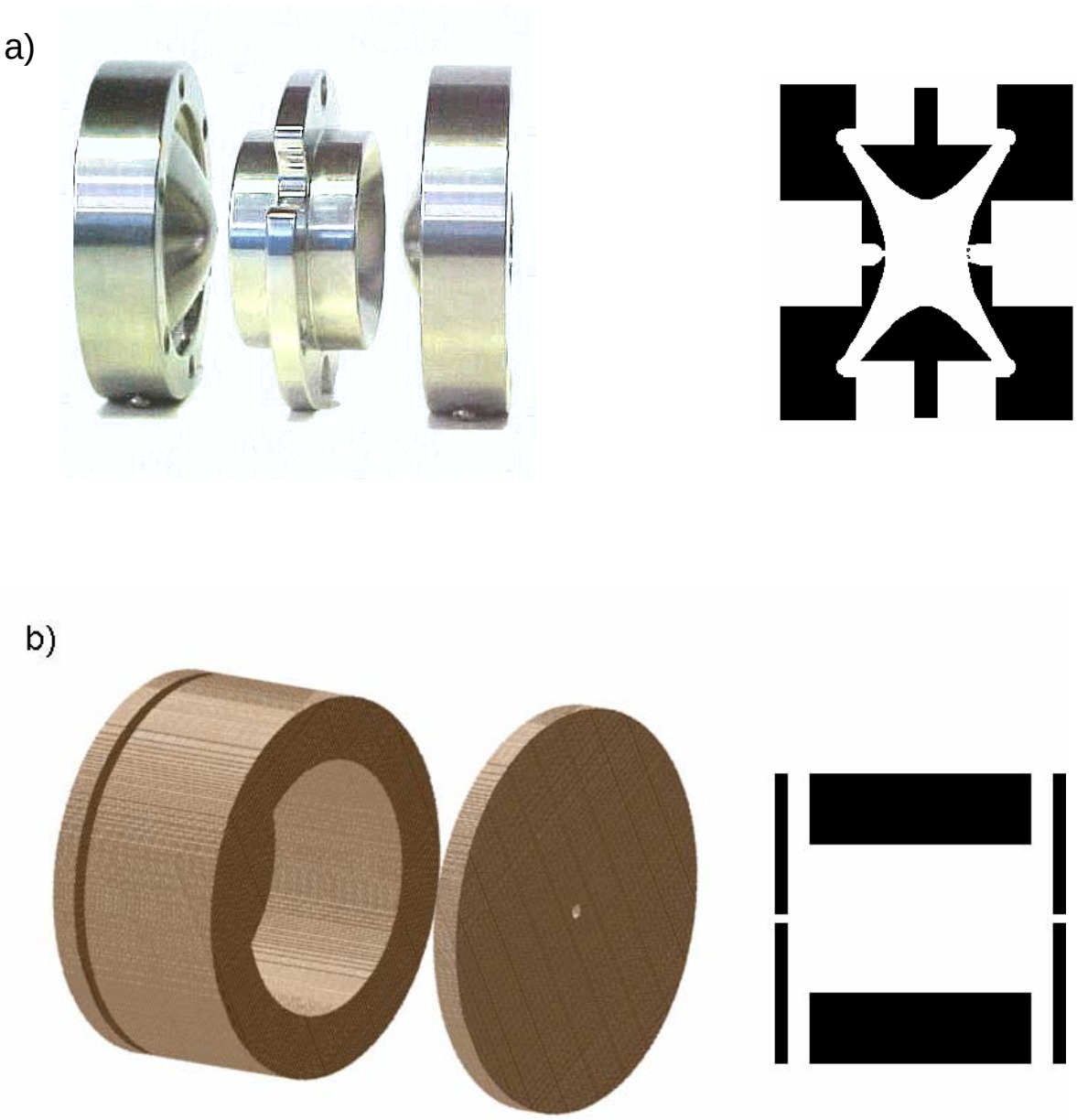

Figure 1.5 – 3-D Quadrupole ion trap electrode geometries
a) Hyperbolic electrodes b) Cylindrical electrodes

been miniaturized down to sub-micron dimensions.[17, 18, 24, 25] This 3-D ion trap geometry shows great promise as a field portable mass spectrometer and consequently has been commercialized in the past 5 years.[17, 26] Operation of the cylindrical ion trap is similar to that of the conventional quadrupole ion trap geometry, which will be discussed in **Section 1.3.3.** However, the change in the shape of the electrodes does affect the electric fields within the ion trap as will be discussed further in **Section 1.4**.[25]

1.3.1.2 Two-Dimensional Ion Trap Electrode Geometries

The concept of the 2-D ion trap was first introduced more than two decades ago.[27, 28] The general operational concept is to trap ions in a quadrupole mass analyzer using a dc potential applied to gate electrodes at either end of the quadrupole. The gate electrodes can take the form of simple cylindrical electrodes. In one recent example of this geometry, a hybrid triple quadrupole mass analyzer was converted into a linear ion trap; where the last quadrupole is the linear ion trap.[29] Another approach is to segment a quadrupole mass analyzer into three sections in which each of the sections can be electrically isolated so that an independent dc offset potential can be applied to each section.[30, 31] This dc potential is separate from the dc that is used in the combination with the rf potential for radial confinement of ions. In one report of this approach, the rods were hyperbolic and r_0 = 4mm.[37] The dc potentials (U_{s1}) applied to the first and last segment (U_{s3}) act as the gate electrodes of the 2-D ion trap. A pictorial representation of this approach is shown in **Figure 1.6**. As shown in **Figure 1.6c,** one embodiment of the segmented 2-D ion trap electrode geometry also has a slot cut into the x-rods through which ions are ejected. [37] These slots do cause imperfections in the electrical fields, thus, to improve performance, the

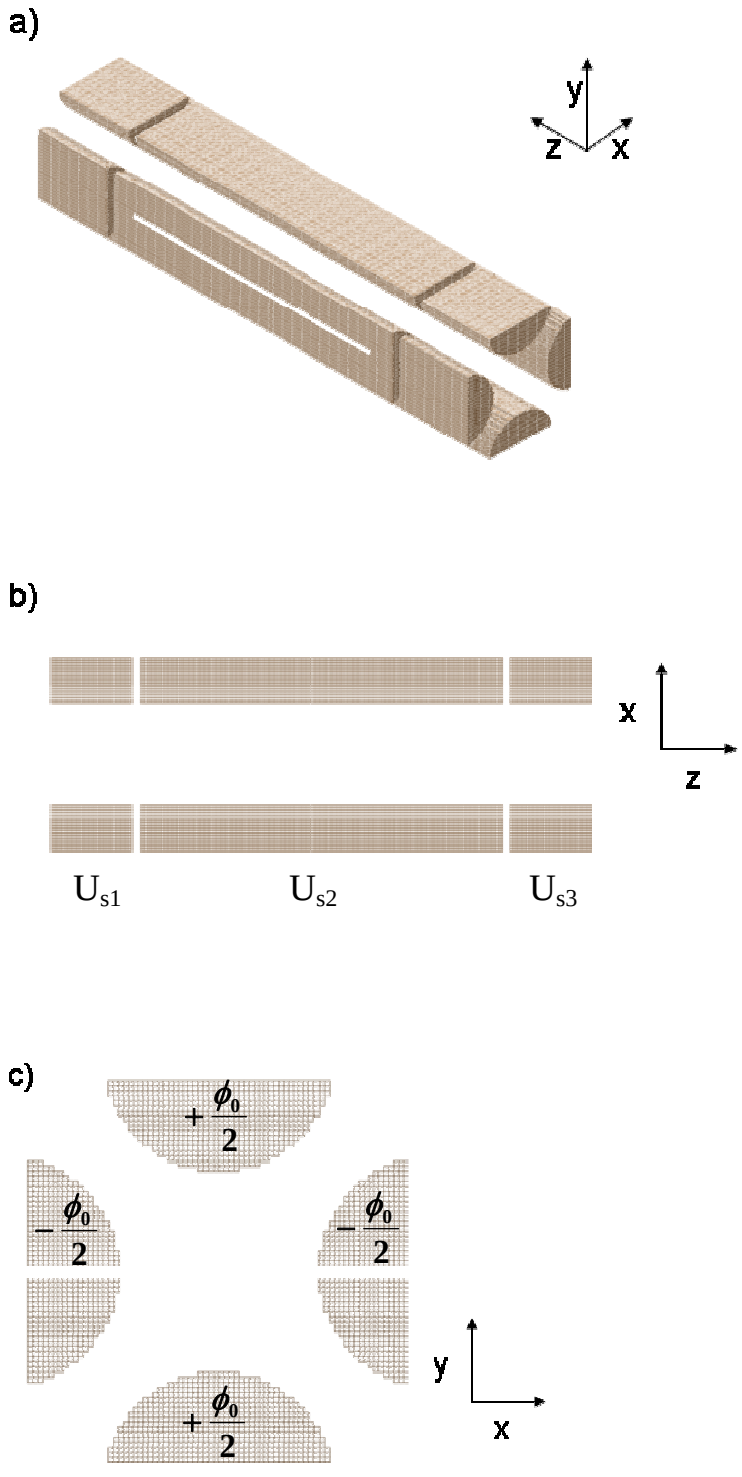

Figure 1.6 – Segmented 2-D ion trap a) Three dimensional view, b) Two dimensional XZ axis view, c) Two dimensional YX axis view.

x-rods have been moved 0.75 mm beyond their normal spacing.[31] Operation of and ion motion within the 2-D ion trap will be further discussed in **Section 1.3.4.**

As with the quadrupole mass filters, the shape of the electrodes can also be changed. One of the most recent alternative 2-D ion trap geometries is the rectilinear ion trap, as shown in **Figure 1.7**.[32] This 2-D ion trap geometry is analogous to the cylindrical ion trap as an alternative to the conventional 3-D ion trap. As shown in **Figure 1.7c**, the rectilinear ion trap has rectangular electrodes, where the x-rectangles have slots in them for ion ejection. The rectilinear ion trap uses two flat electrodes at either end of the ion trap to confine ions, as seen in **Figure 1.7b**.

1.3.2 Quadrupole Fields in Three-Dimensional Ion Traps

The electric potential ($\phi_{x,\,y,\,z}$) in the 3-D ion trap is similar to the electric potential in the quadrupole mass filter discussed in **Section 1.2.2**. The quadrupole field still depends on the square of the distance from a reference point. In the quadrupole ion trap, the rf voltage is typically applied to the ring electrode and the two end cap electrodes are typically held at ground potential. Although not very common, a quadrupole ion trap can also be operated by applying rf voltages of equal amplitude and opposite phase to ring electrode and endcap electrodes. This second operation is not used because injecting ions through the high amplitude rf voltage on the endcaps will not be efficient. In contrast with the electric potentials of the quadrupole mass analyzer, the electric potentials in the 3-D trap vary in the x, y, and z dimensions as a function of electrode geometry, as shown in **Equation 1.20.**

$$\phi_{x,y,z} = \frac{\phi_0}{r_0^2 + 2z_0^2}(x^2 + y^2 - 2z^2) \qquad \textbf{EQ 1.20}$$

The three-dimensional potential of **Equation 20** can be simplified by converting the equation into spherical (r,z) coordinates. Substituting **Equation 1.21** and **Equation 1.22** into

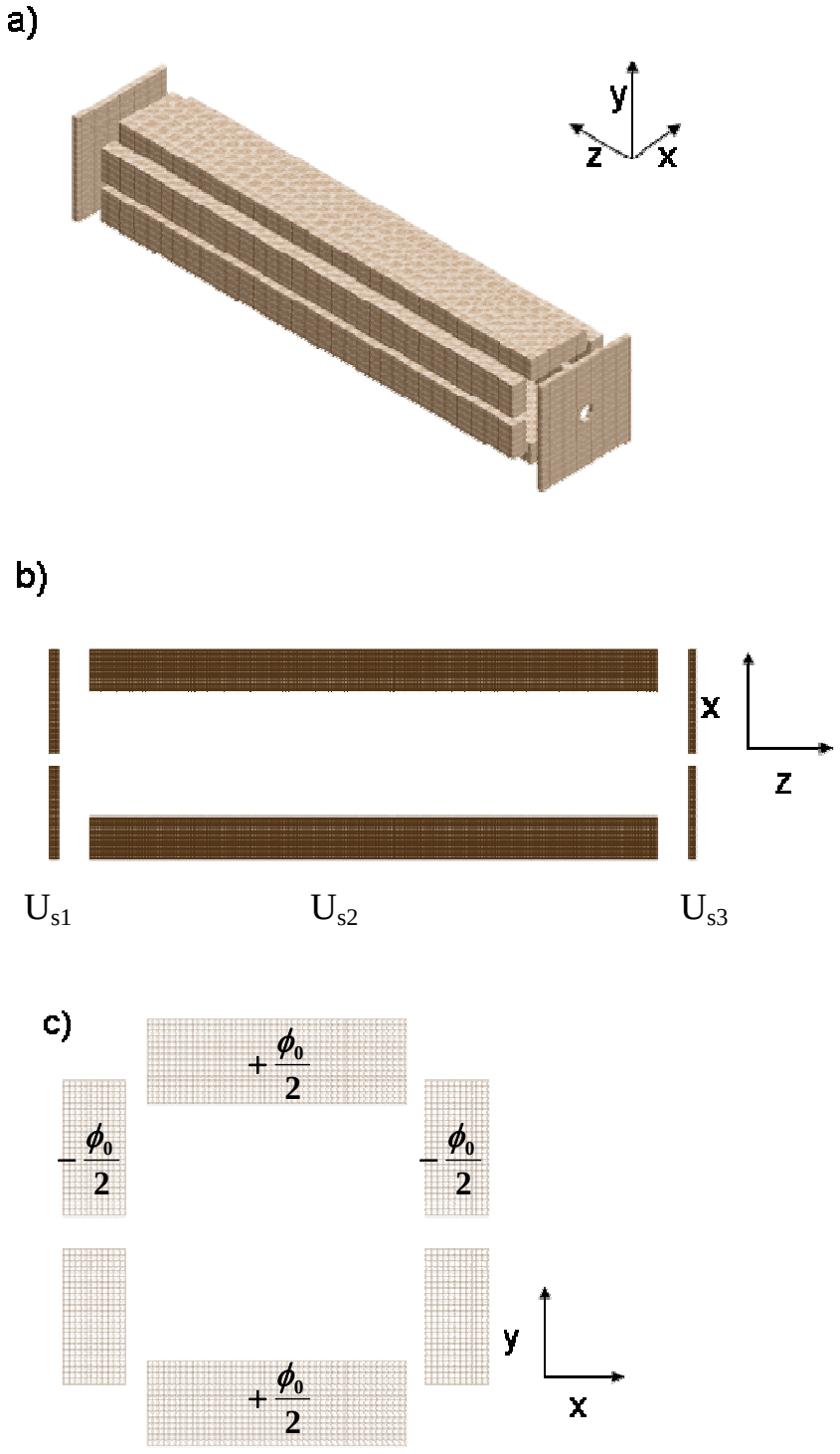

Figure 1.7 – Rectalinear ion trap a) Three dimensional view, b) Two dimensional XZ axis view, c) Two dimensional YX axis view.

Equation 1.20 and factoring using **Equation 1.23** yields the electric potential in spherical coordinates, **Equation 1.24**. Note that the x and y dimensions are transformed into the r dimension, while the z dimension remains unchanged.

$$x = r\cos\theta \qquad \textbf{EQ 1.21}$$

$$y = r\sin\theta \qquad \textbf{EQ 1.22}$$

$$\cos^2\theta + \sin^2\theta = 1 \qquad \textbf{EQ 1.23}$$

$$\phi_{r,z} = \frac{\phi_0}{r_0^2 + 2z_0^2}(r^2 - 2z^2) \qquad \textbf{EQ 1.24}$$

It is interesting to note that geometric relationship of the ring electrode radius to the axial radius in **Equation 1.18** can be found by setting the equation in the parenthesis of **Equation 1.24** equal to zero. With the simplification of the spherical coordinates it can be seen that the electric potentials affect the r and z dimensions independently, meaning that there are no cross terms, such as rz. This means that the force acting on an ion results in the r and z directional components of ion motion being independent of one another. While this behavior may appear similar to that of the quadrupole mass analyzer; the radial dimension is a composite of the x and y such that the motion of ions is independent in all three dimensions.

The voltage difference between the ring and the end cap electrodes, when the endcap electrodes are at ground potential is shown in **Equation 1.25**. The same mathematical treatment to determine the electric field and resulting force acting on an ion that was carried out in **Section 1.2.2** (**Equation 1.6-1.8)**, can be applied to **Equation 1.24** and **Equation 1.25**. The result, which is the acceleration of an ion in the z direction $\left(\frac{d^2z}{dt^2}\right)$ in the presence of the oscillating rf voltage applied to the ring electrode, is shown in **Equation 1.26**

$$\phi_0 = U + V\cos\Omega t \qquad \textbf{EQ 1.25}$$

$$\left(\frac{d^2z}{dt^2}\right)+\left(\frac{4eU}{m\left(r_0^2+z_0^2\right)}+\frac{4eV\cos\Omega t}{m\left(r_0^2+z_0^2\right)}\right)z=0 \qquad \textbf{EQ 1.26}$$

When this equation is compared to the Mathieu equation, **Equation 1.10**, the a_z and q_z parameters can be determined and are shown in **Equations 1.27** and **1.28,** respectively.

$$a_z=-2a_r=\frac{16eU}{m(r_0^2+z_0^2)\Omega^2} \qquad \textbf{EQ 1.27}$$

$$q_z=-2q_r=\frac{8eV}{m(r_0^2+z_0^2)\Omega^2} \qquad \textbf{EQ 1.28}$$

The relationship between a_z and a_r or q_z and q_r is a result of the geometric relationship between the z and r dimensions of the device, as defined in **Equation 1.24**. Because the Mathieu equation is a general second order differential equation, the general concepts about the two solution sets (stable and unstable) as described for the quadrupole mass analyzer remain the same. There are still four regions of stable ion trajectory in terms of r and z trajectories, with the stability region closest to the center axis (0, 0) having the most utility. The shape of the Mathieu stability diagram (**Figure 1.8)** is slightly different than for the quadrupole mass analyzer in **Figure 1.2** because of the differences in the geometrical symmetry between the quadrupole mass analyzer and the quadrupole ion trap. More specifically, the stability diagram is no longer symmetrical about the a_u axis. The cylindrical ion trap geometry will also have a slightly different shape in its stability diagram because of the differences in the electrode geometry; however, it will operate under the same general principles as the conventional 3-D ion trap.

The boundaries and intersecting curves on the stability diagram, shown in **Figure 1.8,** are referred to as iso-beta curves. As shown in **Equation 1.29**, the iso-beta curves are a recursive function of the a_u and q_u parameters. The thickest of the lines represents the edges

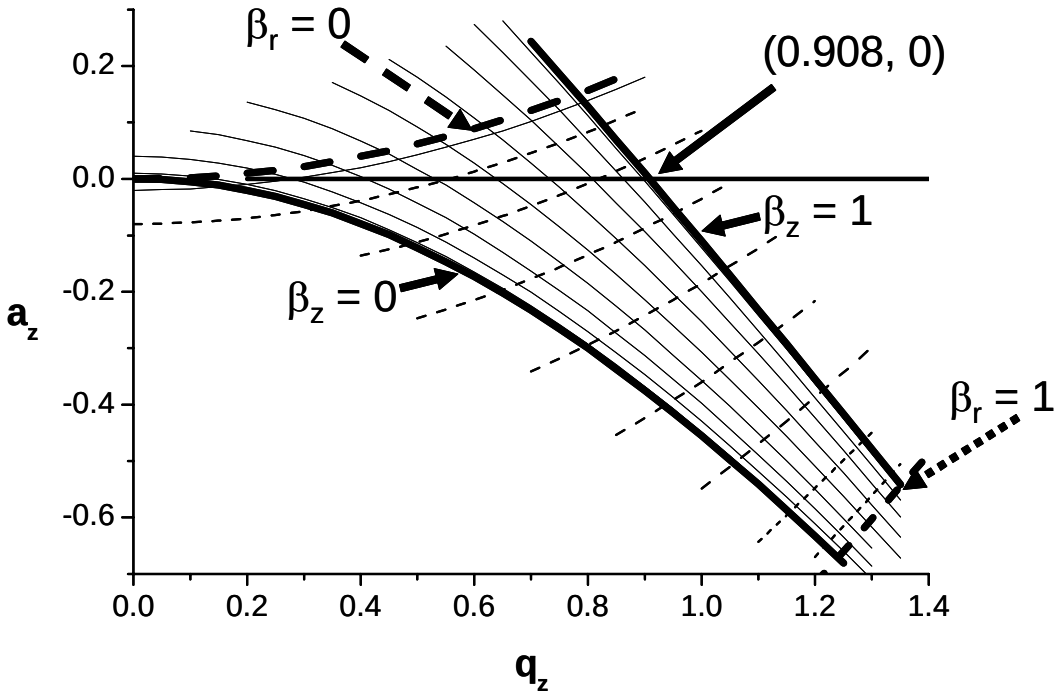

Figure 1.8 – Mathieu stability diagram for 3-D quadrupole ion trap.

of the stability diagram at $\beta_z = 0$, $\beta_z = 1$, $\beta_r = 0$ and $\beta_r = 1$. When an ion's a_z and q_z parameters are between the two thick solid lines, its trajectory is stable in the z-dimension. When an ion's a_z and q_z parameters are between the two thick dotted lines, the ion's trajectory is stable in the r-dimension. An ion that has a_z and q_z parameters that are in between both sets of lines the ion's trajectory is stable in both dimensions and is effectively "trapped" within the ion trap.

$$\beta_u^{\,2} = a_u + \cfrac{q_u^{\,2}}{(\beta_u+2)^2 - a_u - \cfrac{q_u^{\,2}}{(\beta_u+4)^2 - a_u - \cfrac{q_u^{\,2}}{(\beta_u+6)^2 - a_u - \ldots}}} \qquad \textbf{EQ 1.29}$$

$$+ \cfrac{q_u^{\,2}}{(\beta_u-2)^2 - a_u - \cfrac{q_u^{\,2}}{(\beta_u-4)^2 - a_u - \cfrac{q_u^{\,2}}{(\beta_u-6)^2 - a_u - \ldots}}}$$

1.3.3 Three-Dimensional Quadrupole Ion Trap Operation

1.3.3.1 Trapping Ions

As mentioned in **Section 1.1,** it took almost 30 years from the patent release of the quadrupole ion trap until it was introduced as a commercial instrument.[6] This long period of time does not mean that research on the device was stagnant; but rather reflects how it was being operated and the implications of those decisions.[9] As stated previously, in its original publication the ion trap was listed as an alternative geometry to the quadrupole mass filter. For this reason, early researchers operated the ion trap similar to a quadrupole mass filter, in a mass selective stability mode as described in **Section 1.2.3**.[33, 34] In this mode of operation, a dc voltage and an rf voltage are applied to the ring electrode to position ions along a scan line that intersects the stability diagram just below the apex (similar to what is shown in

Figure 1.3a). Ions having a_z and q_z parameters that are in the stability diagram will have stable trajectories and will be trapped. After some period of time, the rf voltage is turned off and the trapped ions are pulsed out of the ion trap using a dc voltage. The inefficiency of mass selective stability is that each ion of different mass-to-charge must be trapped individually and then ejected individually, which is time consuming and can lead to unnecessary sample consumption.

In 1983, a more efficient mode of operation was realized for the quadrupole ion trap. In this mode of operation (termed mass selective instability[6]), all ions are trapped at the same time and then ejected sequentially according to their mass-to-charge ratio. It is implemented by applying an rf voltage to the ring electrode typically with no dc voltage ($a_z = 0$). The scan line described earlier is therefore coincident with the q_z axis (similar to what is shown in **Figure 1.3c**). Ions with a q_z value smaller than 0.908 have stable trajectories and are trapped. At a given rf voltage, the lowest mass-to-charge ion that is trapped is an ion with a q_z value of 0.908; this is referred to as the low mass cut off (LMCO). Ions with mass-to-charge ratios corresponding to a q_z value greater than 0.908 (i.e., lower than the LMCO) do not have stable trajectories and are not trapped. Theoretically, when there is no dc offset voltage on the ion trap, there is no upper mass-to-charge limit for the ion trap. When the mass selective instability mode is employed, ions are ejected out of the ion trap by linearly increasing the amplitude of the rf voltage. As an ion's q_z value approaches 0.908 its axial motion increases and the ion is ejected out of the holes in the end cap electrodes. A mass spectrum is recorded by correlating the rf voltage used to eject an ion with a given mass-to-charge ratio using **Equation 1.28**. Because the rf voltage is directly proportional to mass-to-charge ratio of the ion that is ejected from the ion trap; an upper limit to the mass-to-charge

range of the ion trap is imposed by the magnitude of rf voltage that can be applied to the electrodes. This issue will be discussed further in **Chapter 2**.

1.3.3.2 Ion Manipulation

Ions that are trapped in the quadrupole ion trap have a periodic motion that is characterized by a frequency unique to their mass-to-charge value, termed their "secular frequency", which is a fraction of the frequency of the rf voltage applied to the ring electrode. As described in **Section 1.3.2,** ion motion in the radial and axial dimensions is decoupled, so ions have an axial secular frequency (ω_z) and a radial secular frequency (ω_r). These secular frequencies can be calculated using **Equation 1.30**, where β_u is the iso-beta line defined in **Equation 1.29**, and Ω is the frequency of the rf voltage. The maximum secular frequency for any ion is one half of the frequency of the rf voltage, which occurs just before an ion is ejected ($\beta_u = 1$).

$$\omega_u = \frac{\beta_u \Omega}{2} \qquad \textbf{EQ 1.30}$$

Ions can be resonantly excited when a supplemental ac voltage of the same frequency as the ion's axial secular frequency is applied to the end cap electrodes. When ions are resonantly excited, the amplitude of their axial motion begins to increase. If the amplitude of the supplemental ac voltage is sufficient, ions can be ejected out of the ion trap, which is referred to as resonance ejection. A third mode of ion detection can be employed when resonance ejection is performed in conjunction with mass selective instability.[35] This mode of operation is referred to as resonance ejection and has been used to improve sensitivity and mass resolution (reciprocal of **Equation 1.16**) of the quadrupole ion trap.[35, 36] When resonance ejection is performed, the ions of interest move away from the center of the ion trap before ion ejection takes place.[37] This repositioning of the ions prevents them from

being affected by the space charge of ions of different mass-to-charge that are present in the center of the ion trap. In mass selective instability (no resonance ejection) ions would suffer from these space charge effects, which cause the ions of interest to interact with ions of different mass-to-charge and be delayed during ion ejection. Additionally, the resonance voltage causes the ions motion to be coherent thus they are ejected in a more compact packet. The result of these two effects are the time differential between the first ion of a given mass-to-charge ratio and the last ion of that same mass-to-chare ratio striking the detector is reduced/minimized, which results in improved mass resolution and sensitivity.

Theoretically the mass-to-charge range that can be trapped in an ion trap is unlimited. As mentioned previously, the mass-to-charge range of the ion trap is limited by the maximum rf voltage that can be applied to the electrodes. Larger mass-to-charge ions can be ejected out of the ion trap by performing resonance ejection at $\beta_z < 1$.[38] For example, in an ion trap operated at 1.1 MHz with a maximum zero-to-peak voltage of 7.5 $kV_{0\text{-}p}$ the nominal mass-to-charge range is 5-640, ejecting with $\beta_z = 1$. By resonantly ejecting ions at $\beta_z = 0.253$, ions of a larger mass-to-charge ratio can be ejected and the new mass-to-charge range is 13-1664. If there were any ions between *m/z* 5 and *m/z* 13 they would need to be ejected before resonance ejection, otherwise these ions would eject at $\beta_z = 1$.

Resonance ejection voltages can also be used to isolate an ion of a given mass-to-charge ratio within the trap. For example if an ion of interest is *m/z* 134, ions with smaller mass-to-charge ratios can be ejected by linearly increasing the rf voltage until the LMCO is *m/z* 133. After resetting the LMCO to a lower value (e.g., *m/z* 40), ions of greater mass-to-charge ratio can be ejected by applying a resonance ejection voltage with a frequency corresponding to the secular frequency of *m/z* 135 and then increasing the rf voltage until the

LMCO is *m/z* 133. Another method of ion isolation developed over the past decade is to use a waveform that is composed of multiple frequencies. To isolate a given ion the composite waveform will contain frequencies that are equal to all frequencies except the secular frequency of the ion (mass-to-charge ratio) of interest. The frequency resolution of the waveform (e.g., every 0.5 kHz or every 1 kHz) will affect the ion isolation efficiency. One example of these waveforms is a stored waveform inverse Fourier transform (SWIFT).[39, 40] This waveform is constructed in the frequency domain and then converted into the time domain.

1.3.3.3 Buffer Gas

Buffer gas plays an important role in the trapping, storage, dissociation, and ejection of ions in/from the ion trap. The buffer gas that is most commonly used is helium; research has shown that the optimal operating pressure is ~1 m torr, although this is dependant on the ion trap geometry and other experimental conditions. When ions are injected into the ion trap they can collide with the buffer gas and some of their kinetic energy is transferred to the helium atoms. As the ions continue to under go subsequent collisions their kinetic energy is further reduced and the ion trajectory condenses to the center of the ion trap. The role of the buffer gas in ion dissociation will be discussed in **Section 1.3.3.4.** As a result of the collisions with the buffer gas as previously mentioned, during ion ejection ions are closer together and are better focused. The result is that ions of the same mass-to-charge ratio are ejected in a more compact group thus peak widths are reduced and mass resolution and sensitivities are improved.

1.3.3.4 Tandem Mass Spectrometry

One method of tandem mass spectrometry that can be performed in an ion trap is collisions induced dissociation (CID). This method is accomplished by first isolating ions of a given mass-to-charge ratio using the methods described in **Section 1.3.3.2**. Ions are then resonantly excited with a hundred to several hundred millivolts supplemental ac voltage applied to the endcap electrodes. Collisions between the buffer gas and the kinetically excited ions can convert some of an ion's kinetic energy into internal energy. Ions will dissociate when the total internal energy is greater than the critical energy for that given dissociation process. This method of tandem mass spectrometry is referred to as collision induced dissociation (CID). The isolated ions are called parent ions. Following dissociation, the resulting ions, called product ions, are trapped. Depending on the value of the LMCO during the excitation process some of the resulting product ions may not be trapped because their q_z parameter is greater than 0.908. Typically the product ions that will be lost have a mass-to-charge ratio less than one-third of the parent ions mass-to-charge ratio. Recently methods have been developed to reduce the LMCO immediately after the excitation process so that minimal product ions are lost as a result of the LMCO.[41]

1.3.4 Two-Dimensional Ion Trap Operation

The stability diagram for a 2-D ion trap is the same as that for the quadrupole mass filter, **Figure 1.2.** Unlike the mass analyzing quadrupole mass filter, the 2-D ion trap is operated in the rf only mode so that all ions are transmitted into the 2-D ion trap, as shown in **Figure 1.3c**. The stability diagram defines the stability of an ion's trajectory in the x and y directions, but not the z direction. The axial or z motion of an ion in the 2-D ion trap is determined by the dc offset of the different lenses/sections of the 2-D ion trap. If the ion's

kinetic energy is greater than or equal to the potential on the entrance lens, ions will be injected into the 2-D ion trap. Following the injection process, the dc potential on the entrance lens/section is raised to a value greater than the kinetic energy of the ions, thereby trapping the ions. Ions are dispersed along the axial dimension of the linear ion trap and ion cloud is described as having a cylindrical geometry. In the segmented 2-D ion trap, the ions are trapped in the center section and dispersed in a cylindrical ion cloud over 30 mm of the 72 mm section. Trapped ions have periodic motion in the x and y directions that is similar to the secular frequencies described in **Section 1.3.3.2** and their secular frequency can be calculated in an identical fashion using **Equation 1.30**. Ions can be resonantly ejected from the 2-D ion traps through a slot in the x rods by applying supplemental ac voltages to the x-rods. Detection efficiency can approach ~99% because a detector can be put on either side of the 2-D ion trap to detect ions that are ejected through either x-rod. In 2-D ion traps without slots in the x-rods, ions are axially ejected by resonantly exciting ions and allowing higher order fields, which allow the motion of an ion to be coupled in the x, y, and z direction, to push the ions out of the ion trap. Ion isolation and activation is accomplished in a similar manner to that used in the 3-D ion trap, which is discussed in **Section 1.3.3.2** and **Section 1.3.3.4**. To date, the operating pressure of the buffer gas used in 2-D ion traps (0.1-0.4 mTorr), is lower than in the 3-D ion trap (~1 mTorr). Differences and comparisons between the 3-D and 2-D ion traps will be discussed in **Chapter 4**.

1.4 Higher Order Fields

Non-idealities in the electrode geometry of the quadrupole mass analyzer, the 3-D quadrupole ion trap, and the 2-D quadrupole ion trap result in the presence of higher order fields. These non-idealities result from the necessary truncation of the hyperbolic electrodes in the quadrupole mass filter and the quadrupole ion trap, holes in the end caps for ion injection or ejection, slots in the x-rods of the 2-D ion trap to eject ions, and machining imperfections in the manufacturing of electrodes.[10] **Equation 1.4** and **Equation 1.19** assume that the electric field is purely quadrupole and contains no higher order fields. The actual electric fields are still predominately quadrupolar; however, there is a contribution to the overall field from higher order fields. The description of higher order fields that follows is derived for the case of a 3-D quadrupole ion trap. Despite this fact, the general concepts described below apply for all higher order fields regardless of the mass analyzer. Minor changes in the equations will occur due to geometric differences among the specific devices.

Using the Laplace equation, there is at least one potential, ϕ, within a closed region devoid of charge, which must satisfy **Equation 1.31.**

$$\nabla^2 \phi = 0 \qquad \textbf{EQ 1.31}$$

Multiple solutions to the Laplace equation exist that satisfy the above condition. If each individual solution is considered to be a component (or fraction) of the overall potential, one additional solution is the linear combination of the component potentials. The component potentials may be expressed in terms of a multipole expansion in Legendre polynomials $P_n(\cos\theta)$. The result of the summation with the Legendre polynomials in spherical coordinates takes the form in **Equation 1.32.**[8, 10, 42]

$$\phi_{(\rho,\theta,\varphi)} = \phi_0 \sum_{n=0}^{\infty} A_n \left(\frac{\rho}{s_0} \right)^n P_n(\cos\theta) \qquad \textbf{EQ1.32}$$

where the coefficients A_n represent the relative contribution of each of the component potentials, s_0 is a dimension of normalization based on the electrode geometry as described by **Equation 1.33**, and ρ is the distance from the origin of the coordinate system at the center of the trap to a point (r, z) as described by **Equation 1.34**.

$$s_0 = \sqrt{.5r_0^2 + z_0^2} \qquad \textbf{EQ1.33}$$

$$\rho = \sqrt{r_0^2 + z_0^2} \qquad \textbf{EQ1.34}$$

The nomenclature for the nth order fields is listed in **Table 1.1**.

n	1	2	3	4	5	6
Field name	Dipole	Quadrupole	Hexapole	Octapole	Decapole	Dodecapole

Table 1.1 Higher order field nomenclature.

Even order functions (n=2, 4, 6 …) are symmetrical about the z-axis and the odd order functions (n=1, 3, 5 …) are asymmetrical.

When the Legendre polynomials are put into cylindrical polar coordinates (r,z), the full equation takes the form in **Equation 1.35**. The values of the A_n coefficients can be calculated by electrostatic calculations of the electric fields. The values for the coefficients are determined by fitting the calculated electric fields to the functions in **Equation 1.35** (in the appropriate coordinates). The sum of all of the A_n terms should add to 1. The value of the A_2 term in the stretched 3-D quadrupole ion traps is 0.894 with the A_4 term, the next largest field, having a value of 0.0144.[10]

$$\frac{\phi_{(r,z)}}{\phi_0} = A_0 + A_1 z + A_2\left(\frac{r^2 - 2z^2}{(r_0^{\,2} + 2z_0^2)}\right) + A_3\left(\frac{3r^2 z - 2z^3}{2\left(.5r_0^{\,2} + z_0^2\right)^{3/2}}\right)$$
$$+ A_4\left(\frac{3r^4 - 24r^2 z^2 + 8z^4}{8\left(.5r_0^{\,2} + z_0^2\right)^2}\right) + A_5\left(\frac{15r^4 z - 40r^2 z^3 + 8z^5}{8\left(.5r_0^{\,2} + z_0^2\right)^{5/2}}\right) \qquad \textbf{EQ1.35}$$
$$+ A_6\left(\frac{5r^6 - 90r^4 z^2 + 120r^2 z^4 - 16z^6}{16\left(.5r_0^{\,2} + z_0^2\right)^3}\right) + \ldots$$

The equations following each of the A_n coefficients represents how the electric potential varies as a function of the r and z dimensions. All of the equations above the quadrupole (A_2) term have cross terms, which means that ion motion in the r and z dimensions will be coupled. As shown in **Equation 1.36**, the electric field ($E_{r,z}$) is the derivative of the electric potential ($\phi_{r,z}$) in all dimensions (∇)

$$E_{r,z} = \nabla \phi_{r,z} \qquad \textbf{EQ1.36}$$

Note that the quadrupole potential will still vary linearly as a function of r and z. Electric fields components that are non-linear (see **Table 1.2**) are termed higher order fields. A summary of the electric field orders and the electrical potential orders is given in **Table 1.2.** The force acting on an ion, **Equation 1.7**,

Higher Order Field	**Electric Potential Varies**	**Electric Field Varies**
Dipole (n=1)	Linearly	Constant
Quadrupole (n=2)	Quadratically	Linearly
Hexapole (n=3)	Cubically	Quadratically
Octapole (n=4)	With fourth power	Cubically
Decapole (n=5)	With fifth power	With fourth power
Dodecapole (n=6)	With sixth power	With fifth power

Table 1.2 Summary of how the electric potential and field varies for each higher order field.

in the presence of a higher order field varies as the same function as the electric field. Therefore, the force resulting from higher order fields is non-linear.

The presence of higher order fields in the quadrupole ion trap has both advantages and disadvantages. In the early years of research, ion losses, shifts in the observed mass-to-charge-ratio of ions and some "ghost" peaks (peaks observed at spurious mass-to-charge values) were attributed to the effects of higher order fields.[8] Researchers have also shown methods to minimize all of these phenomena.[8, 10] In more recent years, researchers have recognized that higher order fields can be beneficial to ion trap performance.[43] The advantages and impact of octapole fields will be addressed in **Chapter 5** and **Chapter 6.** Hexapole fields are often used to aid in ion ejection because of their asymmetry, which will allow ions to be preferentially ejected out of the exit endcap.[10] An additional example is the presence of non-linear resonances.[10] As will be discussed in more detail in **Chapter 3**, at certain iso-β values in the stability diagram, excited ion motion is more affected by a given higher order field component than at other iso-β values. Because the force imposed on an ion by higher order fields is non-linear in nature, the resulting resonance is also said to be non-linear. A non-linear resonance can further enhance the resolution and sensitivity improvements achieved previously with resonance ejection alone. [8, 10]

Conventionally, the method for introducing higher order fields into a quadrupole ion trap has been through mechanical alterations of the electrode surfaces. More recently, researchers have added additional electrodes to electrically compensate for the higher order fields.[44-46] The hope in both of these approaches is to gain a better understanding of the effects of higher order fields. With a better understanding of higher order fields, it may be possible to suggest a method of introduction or a certain amount of higher order field content that will produce the next generation of quadrupole ion traps.

1.5 Summary

A description of mass spectrometry instrumentation and the techniques involved have been provided in this chapter. Specifically, the different geometries of ion traps were presented and the theory of operation for an ideal ion trap was discussed. The non-idealities in ion traps lead to the presence of higher order fields. The theory and effects of these higher order fields were discussed. A brief outline of the remaining chapters in this dissertation follows.

Chapter 2 addresses the characterization of a compensated cylindrical ion trap (CCIT), which was designed to electrodynamically study higher order fields in ion traps. Results from this characterization revealed the need for the development of second generation rf circuitry. The theory, development, and characterization of this rf circuitry are discussed. Solutions for more effective control over the voltage applied to the compensated cylindrical ion trap electrodes are also addressed.

The use of resonance ejection at non-linear resonances in the quadrupole ion trap and the CCIT is discussed in Chapter 3. The technique is applied to the analysis of environmentally relevant compounds. Comparisons are made between the effects of non-linear resonance in the quadruple ion trap and the CCIT. Other figures of merit for the technique are also discussed.

Chapter 4 describes the studies of ion fragmentation during ion injection in conventional (3-D) quadrupole ion traps and linear (2-D) ion traps. The effects of the rf voltage amplitude during ion injection, ion kinetic energy, and buffer gas pressure on ion fragmentation are explored. To better understand how the factors influence ion fragmentation manifest themselves, experiments were conducted on stand-alone instruments.

A hybrid quadrupole-quadrupole ion trap and a hybrid quadrupole-linear ion trap were then developed to more accurately understand ion fragmentation. The experiments performed on the stand alone instruments were then repeated on the hybrid instruments. Increasing the kinetic energy, rf amplitude during ion injection, and buffer gas pressure were all shown to affect the amount of fragmentation in both the conventional 3-D quadrupole ion trap and the 2-D ion trap. Additional comparisons between the instruments are also discussed.

Chapter 5 describes the theory, modeling and instrument development for a new octapole ion trap. Several figures of merit are analyzed for the new ion trap, and its operation is compared to a cylindrical ion trap with similar geometry.

Chapter 6 describes the modeling and instrument development for an improved second generation octapole ion trap. Image current detection methods are described with the possibility of creating a Fourier transform octapole ion trap. Several figures of merit are analyzed for the second generation octapole ion trap.

Chapter 7 provides a summary of all of the experiments performed throughout this dissertation, and discusses the future directions for each project.

Appendix I describes experimental design software, instrument control software and data analysis software developed for a quadrupole ion trap mass spectrometer.

Appendix II provides mechanical and electrical schematics for various components described throughout the dissertation.

1.6 References

1. Glish, G. L.; Vachet, R. W., *The basics of mass spectrometry in the twenty-first century*. Nature Reviews Drug Discovery, 2003. 2(2): p. 140-150.

2. Paul, W.; Steinwedel, H. Apperatus for Separating Charges Particles of Different Specific Charges. United States Patent # 2,939,952 1960.

3. Dehmelt, H. G., *Radiofrequency Spectroscopy of Stored Ions. I. Storage*, in *Advances in Atomic and Molecular Physics*; Bates, D. R., Estermann, I., Eds.; Academic Press: New York, 1967; Vol. 3, pp 53-72.

4. Neuhauser, W.; Hohenstatt, M.; Toschek, P. E.; Dehmelt, H. G., *Visual Observation and Optical Cooling of Electrodynamically Contained Ions.* Applied Physics, 1978. 17(2): p. 123-129.

5. Wineland, D. J.; Dehmelt, H. G., *Principles of Stored Ion Calorimeter*. Journal of Applied Physics, 1975. 46(2): p. 919-930.

6. Stafford, G. C. J.; Kelley, P. E.; Syka, J. E. P.; Reynolds, W. E.; Todd, J. F. J., *Recent Improvements in and Analytical Applications of Advanced Ion Trap Technology*. International Journal of Mass Spectrometry and Ion Processes, 1984. 60: p. 85-98.

7. Cooks, R. G.; Glish, G. L.; McLuckey, S. A.; Kaiser, R. E., *Ion Trap Mass Spectrometry*. Chemical and Engineering News, 1991. 69: p. 26-41.

8. March, R. E.; Todd, J. F. J., Eds. *Quadrupole Ion Trap Mass Spectrometry*, 2nd ed.; John Wiley & Sons, Inc.: Hoboken, NJ, 2005.

9. Syka, J. E. P., *Commercialization of the Quadrupole Ion Trap*, in *Practical Aspects of Ion Trap Mass Spectrometry*; March, R. E., Todd, J. F. J., Eds.; CRC Press: Boca Raton, FL, 1995; Vol. I, pp 169-205.

10. Franzen, J.; Gabling, R.-H.; Schubert, M.; Wang, Y., *Nonlinear Ion Traps*, in *Practical Aspects of Ion Trap Mass Spectrometry. Volume I. Fundamentals of Ion Trap Mass Spectrometry*; March, R. E., Todd, J. F. J., Eds.; CRC Press: Boca Raton, 1995; Vol. I, pp 49-167.

11. Mordehai, A.; Miller, B.; Kuhlmann, F. *A New Higher-Capacity 3D Quadrupole Ion Trap*. in *51st ASMS Conference on Mass Spectrometry and Allied Topics*. 2003. Montreal, Quebec, Canada.

12. Dietz, L. A., *Basic Properties of Electron Multiplier Ion Detection and Pulse Counting Methods in Mass Spectrometry*. Review of Scientific Instruments, 1965. 36(12): p. 1763.

13. Leary, J. J.; Schmidt, R. L., *Quadrupole Mass Spectrometers: An Intuitive Look at the Math.* Journal of Chemical Education, 1996. 72(12): p. 1142-1145.

14. Miller, P. E.; Denton, M. B., *The Quadrupole Mass Filter: Basic Operating Principles.* Journal of Chemical Education, 1986. 63(7): p. 617-622.

15. Gibson, J. R.; Taylor, S., *Numerical Investigation of the effect of electrode size on the behavior of quadrupole mass filters.* Rapid Communications in Mass Spectrometry, 2001. 15: p. 1960-1964.

16. Mathieu, E., J. Math Pure Appl., 1868. 13: p. 137.

17. Blain, M. G.; Riter, L. S.; Cruz, D.; Austin, D. E.; Wu, G. X.; Plass, W. R.; Cooks, R. G., *Towards the hand-held mass spectrometer: design considerations, simulation, and fabrication of micrometer-scaled cylindrical ion traps.* International Journal of Mass Spectrometry, 2004. 236(1-3): p. 91-104.

18. Kornienko, O.; Reilly, P. T. A.; Whitten, W. B.; Ramsey, J. M., *Micro Ion Trap Mass Spectrometry.* Rapid Communications in Mass Spectrometry, 1999. 13: p. 50-53.

19. March, R. E., *Quadrupole ion trap mass spectrometry: Theory, simulation, recent developments and applications.* Rapid Communications in Mass Spectrometry, 1998. 12(20): p. 1543-1554.

20. March, R. E., *Quadrupole Ion Trap Mass Spectrometry*, in *Encyclopedia of Analytical Chemistry*; Meyers, R. A., Ed.; John Wiley & Sons Ltd.: Chichester, 2000; Vol. 13, pp 11848-11872.

21. Louris, J. N.; Schwartz, J.; George C. Stafford, J.; Syka, J. E. P.; Taylor, D. *The Paul Ion Trap Mass Selective Instability Scan: Trap Geometry and Resolution*. in *The 40th ASMS Conference on Mass Spectrometry and Allied Topics*. 1992. Washington, DC.

22. Bonner, R. F.; Fulford, J. E.; March, R. E.; Hamilton, G. F., *The Cylindrical Ion Trap. Part I. General Introduction.* International Journal of Mass Spectrometry and Ion Physics, 1977. 24: p. 255-269.

23. Wells, J. M.; Badman, E. R.; Cooks, R. G., *A Quadrupole Ion Trap with Cylindrical Geometry Operated in the Mass-Selective Instability Mode.* Analytical Chemistry, 1998. 70: p. 438-444.

24. Badman, E. R.; Cooks, R. G., *A Parallel Miniature Cylindrical Ion Trap Array.* Analytical Chemistry, 2000. 72: p. 3291-3297.

25. Badman, E. R.; Johnson, W. R.; Plass, W. R.; Cooks, R. G., *A Miniature Cylindrical Quadrupole Ion Trap: Simulation and Experiment.* Analytical Chemistry, 1998. 70: p. 4896-4901.

26. Patterson, G. E.; Guymon, A. J.; Riter, L. S.; Everly, M.; Griep-Raming, J.; Laughlin, B. C.; Ouyang, Z.; Cooks, R. G., *Miniature Cylindrical Ion Trap Mass Spectrometer.* Analytical Chemistry, 2002. 74: p. 6145-6153.

27. Church, D. A., *Storage-Ring Ion Trap Derived from Linear Quadrupole Radio-Frequency Mass Filter.* Journal of Applied Physics, 1969. 40(8): p. 3127.

28. Beaugrand, C.; Jaouen, D.; Mestdagh, H.; Rolando, C., *Ion Confinement in the Collision Cell of a Multiquadrupole Mass-Spectrometer - Access to Chemical-Equilibrium and Determination of Kinetic and Thermodynamic Parameters of an Ion-Molecule Reaction.* Analytical Chemistry, 1989. 61(13): p. 1447-1453.

29. Hager, J. W., *A new linear ion trap mass spectrometer.* Rapid Communications in Mass Spectrometry, 2002. 16(6): p. 512-526.

30. Bier, M. E.; Park, M.; Syka, J. E. P.; Senko, M. W. Ion Trap Mass Spectrometer System and Method. US Patent 54205425, 1995.

31. Schwartz, J. C.; Senko, M. W.; Syka, J. E. P., *A two-dimensional quadrupole ion trap mass spectrometer.* Journal of the American Society for Mass Spectrometry, 2002. 13(6): p. 659-669.

32. Ouyang, Z.; Wu, G.; Song, Y.; Li, H.; Plass, W. R.; Cooks, R. G., *Rectilinear Ion Trap: Concepts, Calculations, and Analytical Performance of a New Mass Analyzer.* Analytical Chemistry, 2004. 76: p. 4595-4605.

33. Todd, J. F. J.; Waldren, R. M.; Mather, R. E., *The Quadrupole Ion Store (QUISTOR) Part IX. Space-Charge and Ion Stability. A Theoretical Background and Experimental Results.* International Journal of Mass Spectrometry and Ion Processes, 1980. 34: p. 325-349.

34. Todd, J. F. J.; Penman, A. D.; Smith, R. D., *Some Alternative Scanning Methods for the Ion Trap Mass Spectrometer.* International Journal of Mass Spectrometry and Ion Processes, 1991. 106: p. 117-135.

35. Schwartz, J. C.; Syka, J. E. P.; Jardine, I., *High Resolution on a Quadrupole Ion Trap Mass Spectrometer.* Journal of the American Society for Mass Spectrometry, 1991. 2: p. 198-204.

36. Goeringer, D. E.; Whitten, W. B.; Ramsey, J. M.; McLuckey, S. A.; Glish, G. L., *Theory of High-Resolution Mass Spectrometry Achieved via Resonance Ejection in the Quadrupole Ion Trap.* Analytical Chemistry, 1992. 64: p. 1434-1439.

37. Williams, J. D.; Cooks, R. G.; Syka, J. E. P.; Hemberger, P. H.; Nogar, N. S., *Determination of Positions, Velocities, and Kinetic Energies of Resonantly Excited Ions in the Quadrupole Ion Trap Mass Spectrometer by Laser Photodissociation.* Journal of the American Society for Mass Spectrometry, 1993. 4: p. 792-797.

38. Kaiser, R. E. J.; Louris, J. N.; Amy, J. W.; Cooks, R. G., *Extending the Mass Range of the Quadrupole Ion Trap Using Axial Modulation.* Rapid Communications in Mass Spectrometry, 1989. 3: p. 225-229.

39. Guan, S.; Marshall, A. G., *Stored Waveform Inverse Fourier Transform Axial Excitation/Ejection for Quadrupole Ion Trap Mass Spectrometry.* Analytical Chemistry, 1993. 65(9): p. 1288-1294.

40. Marshall, A. G.; Wang, T.-C. L.; Ricca, T. L., *Tailored Excitation for Fourier Transform Ion Cyclotron Resonance Mass Spectrometry.* Journal of the American Chemical Society, 1985. 107(26): p. 7893-7897.

41. Cunningham, C., Jr.; Glish, G. L.; Burinsky, D. J., *High Amplitude Short Time Excitation: A Method to Form and Detect Low Mass Product Ions in a Quadrupole Ion Trap Mass Spectrometer.* J Am Soc Mass Spectrom, 2006. 17(1): p. 81 - 84.

42. Griffiths, D. J., *Chapter 3: Special Techniques,* in *Introduction to Electrodynamics,* 3rd ed.; Prentice Hall: Upper Saddle River, NJ, 1999, pp 110-159.

43. Hager, J. W., *Recent trends in mass spectrometer development.* Analytical and Bioanalytical Chemistry, 2004. 378(4): p. 845-850.

44. Ding, L.; Sudakov, M.; Brancia, F. L.; Giles, R.; Kumashiro, S., *A digital ion trap mass spectrometer coupled with atmospheric pressure ion sources.* Journal of Mass Spectrometry, 2004. 39(5): p. 471-484.

45. Hager, J. W., *Performance optimization and fringing field modifications of a 24-mm long RF-only quadrupole mass spectrometer*. Rapid Communications in Mass Spectrometry, 1999. 13(8): p. 740-748.

46. Franzen, J.; Wang, Y. Quadrupole Iontrap with switchable mutlipole fractions. US Patent Re. 36906, 2000.

Chapter 2

Radio Frequency Circuitry Development and Characterization of a Compensated Cylindrical Ion Trap Mass Spectrometer

2.1 Introduction

One of the most important circuitry elements for the operation of the Paul ion trap is the radio frequency (rf) tank circuit. The rf voltage generated by the tank circuit in connection with electrode geometry, entry and exit holes, and any other machining defects determine the overall electric field responsible for the trapping of ions. A novel compensated cylindrical ion trap (CCIT) has been modeled and developed in our lab to study the effects of different types of electric fields on ions in ion traps. The work described in this chapter will cover the characterization of the CCIT following its development.[1, 2] First generation rf circuitry was found to be untuneable, unable to generate sufficient rf voltage. Furthermore, the control of the rf amplitude was also questionable. To address these issues, the development of second generation rf circuitry for the CCIT was undertaken and will be discussed in this chapter. Additionally some of the rf development methods employed for the CCIT will be explored on rf circuitry for conventional 3-D ion traps.

2.2 Compensated Cylindrical Ion Trap

2.2.1 Background

As described in **Section 1.4**, the presence of higher order fields (HOFs), also termed non linear fields, in trapping instruments has existed since the commercialization of the quadrupole ion trap.[3-10] Although originally unintentional, modern implementations of HOFs has lead to an improvement in overall ion trap performance.[3, 11] With the advantages discussed in **Chapter 1**, such as improved MS/MS efficiency, trapping efficiency and ejection efficiency, it is important to note that there are still some disadvantages to the presence of HOFs. As described in **Chapter 1**, further elaborated on in **Chapter 4**, the two main disadvantages of HOFs include chemical mass shifts resulting from ion fragmentation and ion losses during tandem mass spectrometry experiments.[5, 6, 9, 12] There is some research that suggests that if a pure quadrupole field was obtainable, ion trap performance would be optimal; however, other researchers believe that the presence of HOFs are necessary for the successful injection and subsequent trapping of ions.[13-15] Thus there is a need to truly understand the effects of HOFs.

The primary causes of HOFs are due to holes in the electrodes for ion entry, ion exit, truncation of the electrodes (as described in **Section 1.4)**, and machining tolerances.[11] In 3-D ion traps it is believed that HOFs are strongest directly at the holes in the end caps.[11, 14] To date the primary methodology for altering the HOF content is through mechanical means, which is limited because the fields are static over the course of an experiment.[16] One mechanical method that has been studied to alter the HOF content is to change the axial spacing of the end cap electrodes.[3, 7, 17] A second mechanical method that was explored in the early 1990s involved altering the angle of the hyperbolic electrodes, as well as the

location where the endcap truncation occurs.[18] In recent years researchers have also explored replacing the holes in the end caps with mesh to create a more uniform electric field.[19]

An alternative methodology for the introduction of HOFs is through electrical means. In this method additional electrodes are placed in a given system and a voltage is applied to them to alter the shape of the electric fields, thus introducing HOFs. The advantage of electrically altering the HOF content is that the field can be varied dynamically during the experiment. For example, hexapole fields are optimal for ion ejection; therefore, it is advantageous to have this field be at a higher percentage during ion ejection but not present during ion injection.[20] Electrical implementation of HOFs has been growing in popularity and can be found in the literature.[21,22] The majority of the research published on this method with 3-D ion traps has been aimed at altering the electrical environment directly around the end cap electrodes.

Techniques primarily aimed at electrical implementation of HOF are either static or dynamic during the course of an experiment; referred to as electro-static or electro-dynamic introduction of higher order fields. In one interesting application of electro-dynamically introducing higher order fields researchers suggested placing electrodes inside of the ion trap that follow the hyperbolic contour of the end cap electrodes.[21] These electrodes are approximately 2 mm above the endcap electrode surface and are isolated from the electrically grounded endcaps with ceramic insulators. An rf voltage applied to these extra electrodes, at one or both endcaps, can then be switched on or off to allow the higher order field to be created during different parts of an experiment. Because of the complexity of the circuitry involved in the switching of the rf voltage, the device never took any form other than in the patent.[21] A similar but more robust approach is to put electrodes, that are always on, that are

within the trapping volume. The amplitude of the rf voltage on these electrodes can be changed so as to electro-dynamically alter the electric field environment in the ion trap. A cylindrical ion trap with added compensating electrodes, referred to as a compensated cylindrical ion trap mass spectrometer (CCIT), was developed with the goal of electro-dynamically studying the effects of HOF in a 3-D ion trap.

2.2.2 Operation and Previous work

The conventional cylindrical ion trap (CIT) electrode geometry consists of a ring electrode and two end caps. CIT electrodes are significantly easier to machine than conventional hyperbolic 3-D electrodes; therefore, the electrode geometry chosen for this work was a cylindrical geometry, as shown in **Figure 1**. The rf voltage for the CIT is applied to the ring electrode and the endcaps are either held at ground potential or supplemental waveforms can be applied to the endcaps. The operation of a CIT is identical to that of traditional hyperbolic 3-D quadrupole ion traps, with only slight differences occurring in the Mathieu Stability diagram.[23-25] The trapping potential of the CIT and the 3-D ion trap are similar, but there are some differences. The equipotential curves of a CIT and a 3-D trap both with $r_0 = 1$ cm and $z_0 = 0.707$ cm are illustrated in **Figure 2.1**. Equipotential curves are a plot of the voltage as a function of distance, with each curve representing a separate but constant voltage. Voltages of the equipotential curves are greatest closest to the surface of an electrode and decrease as they approach the center of the ion trap. As observed in **Figure 2.1**, differences in the electric fields between these two geometries are most notable near the end caps. HOFs are at higher percentages in the CIT over the 3-D trap; however, significant research has been done on mechanical optimization of the HOF content in CIT to

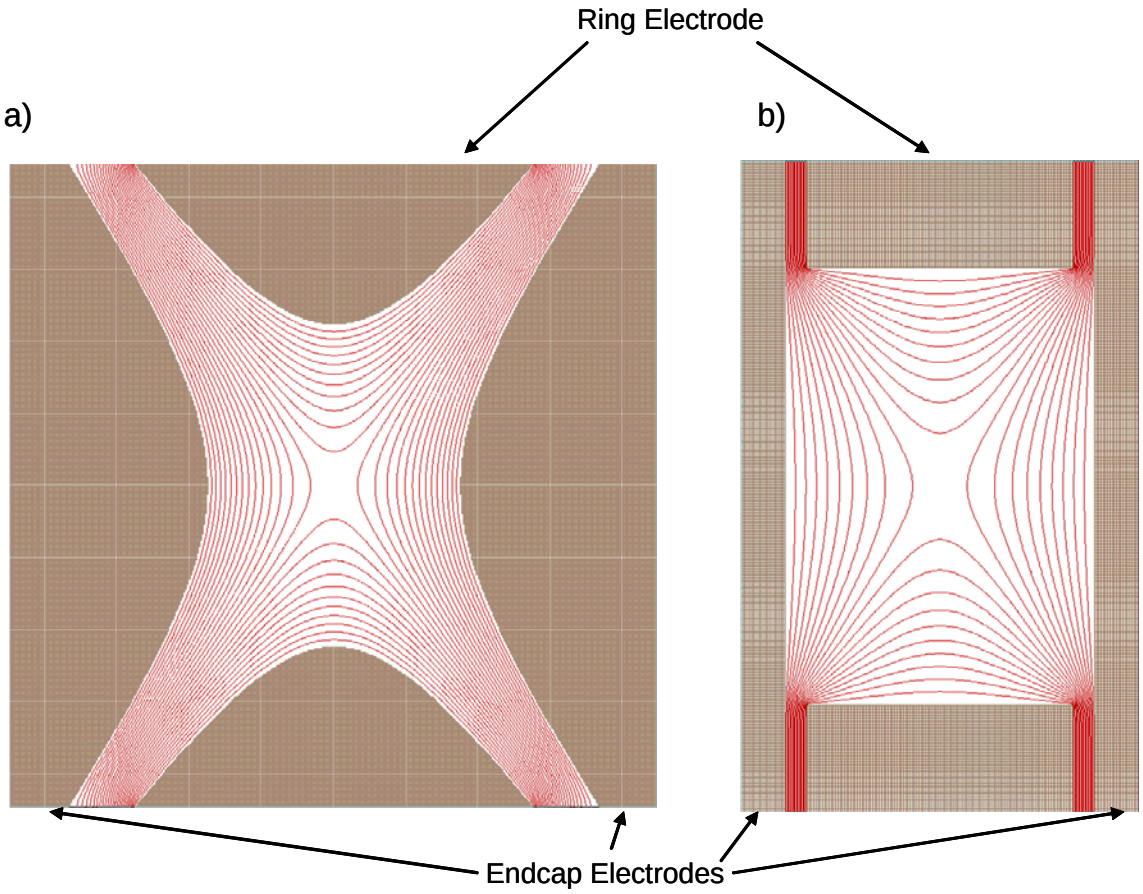

Figure 2.1 – 2-D cross section of equipotential curves in 3-D on traps with a) Hyperbolic electrodes and b) Cylindrical electrodes. The dimensions of each ion trap are r_0=1.0 cm and z_0 = 0.707 cm.

improve performance.[26] Geometrical optimization of the electrode geometry and spacing has lead to a better understanding of the HOF content necessary to yield analytically useful CITs, and within the past 5 years CITs have become commercially available.[27] Recently a 3-D ion trap with significantly higher ion capacity has become commercially available. Researchers reported that this ion trap is geometrically different from previous generations of this company's 3-D ion traps.[28] With such improvements, a need still exists for a systematic study of the effects of HOFs on the analytical performance of ion traps.

To electrodynamically study HOFs in a CIT, one electrode must be added on both sides of the ring electrode; these two electrodes will be called compensating ring electrodes. The geometry of the five electrodes, for the CCIT shown in **Figure 2.2**, consist of two compensating ring electrodes, a larger center ring electrode and two mesh covered end caps.[1, 2] The specific dimensions used for the CCIT mass spectrometer discussed here are as follows:

$$r_0 = 2 \text{ cm}$$

$$z_0 = 1.7 \text{ cm}$$

$$\Delta z_c = 0.35 \text{ cm}$$

$$z_g = 0.1 \text{ cm}$$

A separate rf voltage is applied to each of the three ring electrodes.[29] The HOF content is altered by varying the relative amplitude of the voltage on the compensating ring electrodes to the voltage on the center ring electrode. Symmetrical, even order, HOFs are introduced when the voltage on the compensating ring electrodes are equal to each other. Asymmetrical, odd order, HOFs are introduced when the amplitudes of the compensating ring electrodes are different from one another. The exact ratio of the voltages relative to the

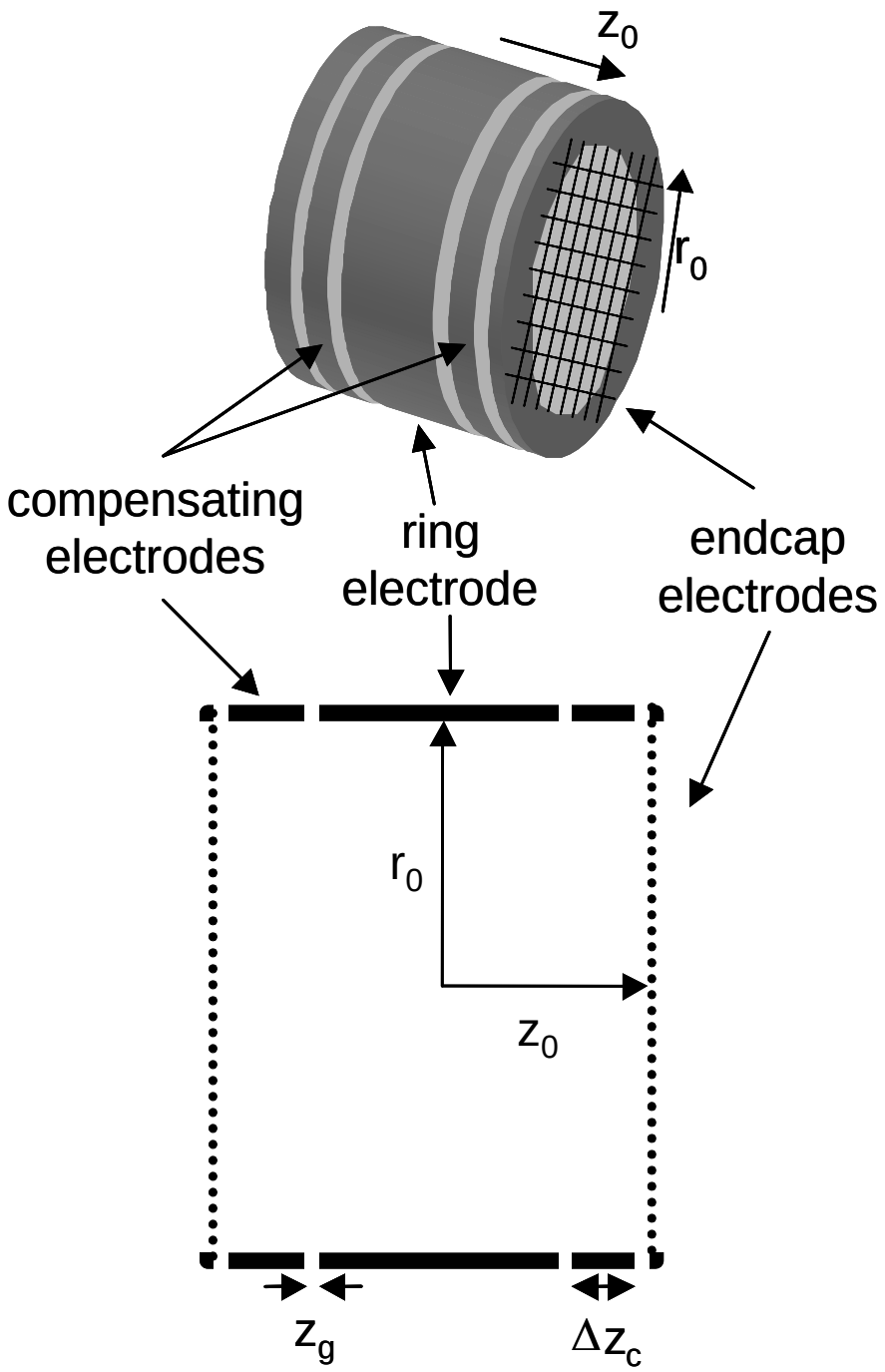

Figure 2.2 – 3-D image of compensated cylindrical ion trap electrodes and a 2-D cross section of the CCIT electrodes.

center ring electrode voltage determines the percentage of each HOF that is present in the ion trap.[2] As described in **Section 1.4** the overall electrical potential is described as an algebraic sum of the individual field components times a weighting coefficient. Electrostatic modeling methods have previously been developed to determine the rf voltages which are required to produce certain higher order field contributions, and thus will not be discussed here.[2]

A general diagram of the vital mass spectrometer components is shown in **Figure 2.3**. The EI source used is from a Finnigan (San Jose, CA) 4000 mass spectrometer system. The detector is an electron multiplier (model 4716 Burle Electro-Optics Inc., Sturbridge MA) equipped with a guard ring and conversion dynode. The design, construction, initial operation, and other details of the CCIT system have been previously described.[1] In this initial work, the CCIT system was used to control conventional hyperbolic quadrupole ion trap electrodes (these electrodes are not depicted in **Figure 2.3**). The control software, rf circuitry, and other hardware were shown to successfully function by obtaining electron impact ionization MS and MS/MS spectra of n-butylbenzene on a conventional 3-D ion trap.[1] No mass spectra were previously taken with the CCIT electrodes. Following the characterization with the quadrupole ion trap mass spectrometer (QITMS) electrodes, the CCIT electrode stack were installed into the system. The design of the electrodes and the construction of the electrode stack have been previously described.[1] The rf system with the CCIT electrodes was found to optimally operate at 856 kHz. The exact procedure for determining this operating frequency will be described in **Section 2.3.4.5**.

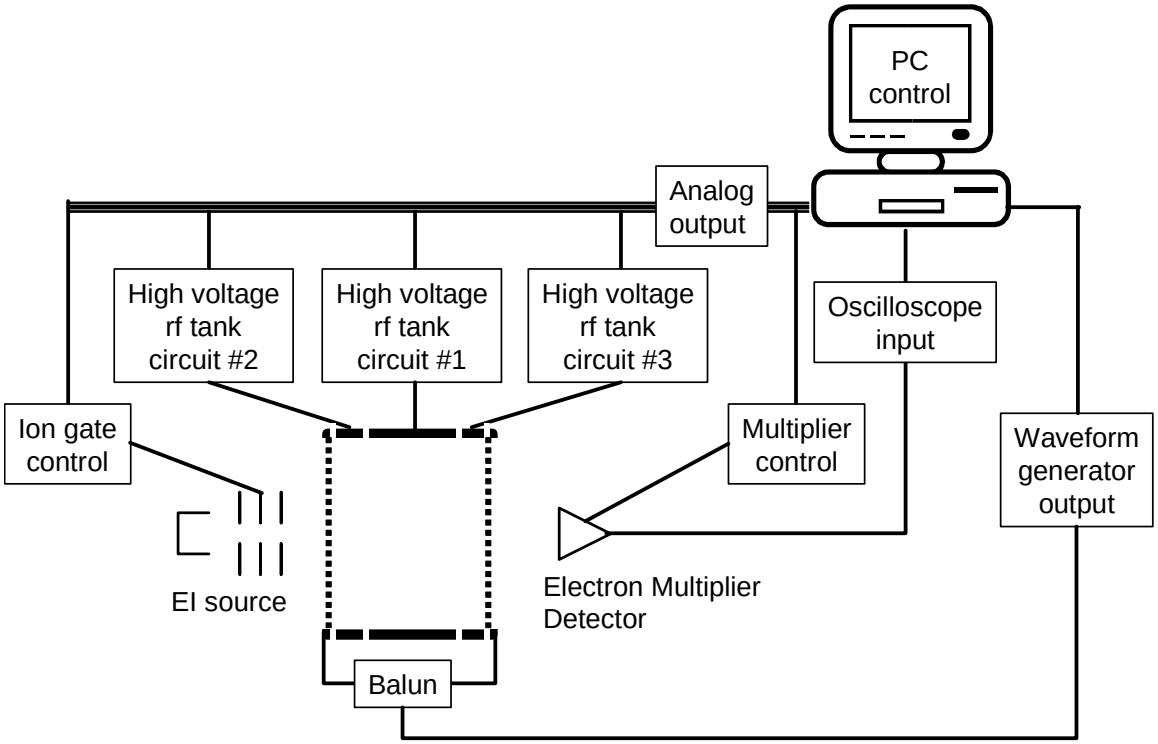

Figure 2.3 – General schematic of CCIT mass spectrometer.

2.2.3 Continued CCIT Characterization

2.2.3.1 Methods

EI mass spectra acquired in the work described below were obtained with the electron energy at 70 eV, the current at 4 mA, the ion source block at -31 V, and the einzel lenses were at -33, -200, and -35 V. Ions were blocked when the middle einzel lens was changed to 100 V. The guard ring was held at -400 V and the dynode was at -7 kV. The electron multiplier potential was at -1800 V during the analytical scan and 0 V during all other portions of the experiment. Analyte vapors of n-butylbenzene were introduced into the EI source through a needle valve with 1/8 inch tubing and swagelock^{TM} connections.

2.2.3.2 Mass Range

Figure 2.4a shows the mass spectrum acquired with resonance ejection at β=2/3 when n-butylbenzene was leaked in to the EI source. During the experiment the rf amplitude was equal on all 3 electrodes, a configuration which should be the electrical equivalent of a cylindrical quadrupole ion trap. The mass spectrum of n-butylbenzene was only acquired up to *m/z* 112 because the rf system could not reach a sufficient rf amplitude to eject higher mass-to-charge ratio ions. To observe higher mass-to-charge ratio ions, resonance ejection was performed at lower β_{eject} values; however, no molecular ion was observed. Originally the inability to generate sufficient rf voltages was thought to be the problem; however, mass spectra taken of xenon (*m/z 128-136)*, see **Chapter 5**, proved that this was not the case. Another possibility is that the molecular ion is fragmenting upon entering the ion trap, a topic which will be addressed in **Chapter 4**. The mass range obtained with no resonance ejection is about 90 Da, which is shown in **Figure 2.4b**. Because the detectable mass-to-charge range is directly proportional to the amplitude of the rf voltage the rf development for the CCIT,

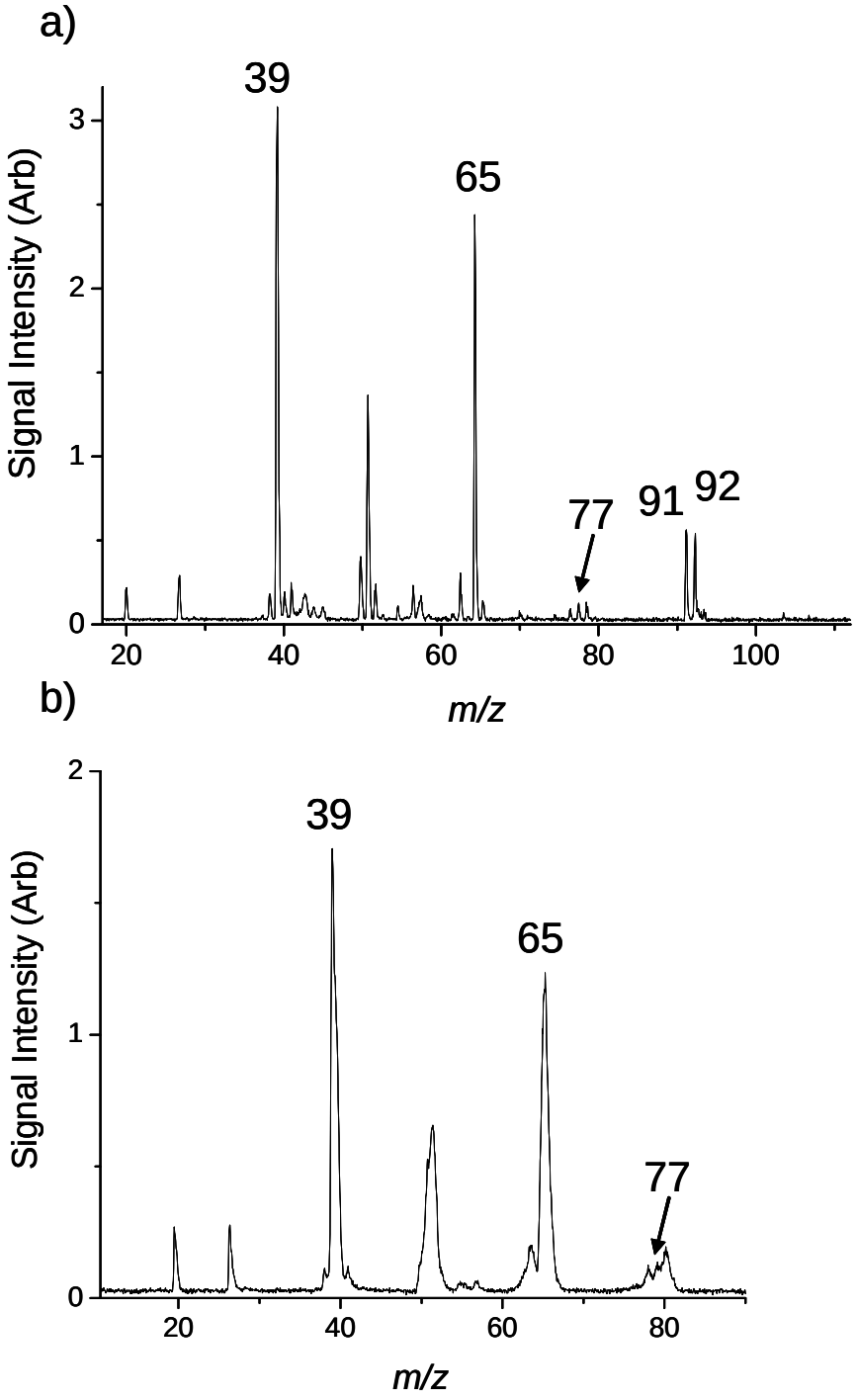

Figure 2.4 – EI mass spectrum of n-butylbenzene (*m/z* = 134) acquired with CCIT electrodes a) Resonance ejection at $\beta_z = ⅔$, b) No resonance ejection.

discussed in this chapter, was partially done with the motivation of generating greater amplitude rf voltages.

2.2.3.3 Resolving Power

Resolving power, **Equation 2.1**, is defined as the ability of a mass analyzer to yield distinct ion signals for two ions of slightly different *m/z*. For the purposes of this work, peak width (Δm) is determined at the full width at half height for the mass (m) of the peak of interest.

$$\frac{m}{\Delta m} \qquad \textbf{EQ 2.1}$$

The resolving power of an ion trap can be enhanced by resonance ejection, which will excite ions of the same mass-to-charge ratio allowing their motion to become coherent and be ejected over a smaller period of time than without resonance ejection. The benefit of using resonance ejection is an improvement in mass resolving power as is clear when comparing the mass spectra in **Figure 2.4**. As ions are about to be ejected from the ion trap, both with and without resonance ejection, there is a rapid increase in the kinetic energy of the ions. If the ions are allowed to approach the excitation process at a slower rate the energy uptake will be more uniform, regardless of whether the kinetic energy during ion ejection is being increased solely due to the rf voltage or through resonance excitation. Therefore decreasing the rate at which the rf amplitude is increased during ion ejection will enhance the resolving power of the instrument. The resolving power was calculated for the fragment ions of *m/z* 91 and 92 at several scan rates. The result of which are shown in **Figure 2.5**. The resolving power increases from 30 to 110 when decreasing the scan rate from 175 μsec/Da to 1000 μsec/Da. Previous studies suggests that mass resolution is linked to both time dependent and time independent factors.[30] Therefore, as the scan rate of an ion trap is decreased, the

resolution increases until the resolution is no longer dependant on scan rate. At slower scan rates the resolution is dependant on factors such as pressure and space charge. Because the time dependent factors are constant in these experiments the resolution will level off. As illustrated in Figure 2.5, in these experiments the resolution leveled off at scan rates slower than 1000 μsec/Da in the experiments presented here in, as predicted.

2.2.3.4 Rf Circuitry Issues

The rf circuitry previously designed for the CCIT was successful in operating the instrument as a mass spectrometer; however, several electrical design and engineering flaws may limit the mass range, stability, and tunablity of the rf system. A schematic of the rf resonant circuitry is in **Figure 2.6.** The overall circuit is enclosed in one single container with three sections, each with a transformer coil supported on an acrylic cylinder. The wire used for the coils was 28 American wire gauge (AWG) magnet wire, which has a resistance of about 0.2507 Ω/meter and can result in voltage losses. The wire gauge should ideally be reduced to 12-16 AWG wire, which is 0.00614-0.01552 Ω/meter. The coil consists of primary coil wrapped over top of the secondary coil. The two coils are separated by the covering of the magnet wire and vinyl electrical tape (3M, St. Paul MN). Electrical tape is used for its mechanical binding properties but does not effectively insulate rf voltages. The varnish covering of the magnet wire is used to keep turns from shorting to each other; however, the varnish does not prevent leakage of the voltage. There will be distributed capacitance between the windings and thus AC leakage currents. Another issue is that rf voltage is only generated on all three parallel coils when the coil sitting to the left of the center coil is driven out of phase from the other two coils. This is believed to be because one coil was wrapped in the opposite direction when compared to the other two coils. Another

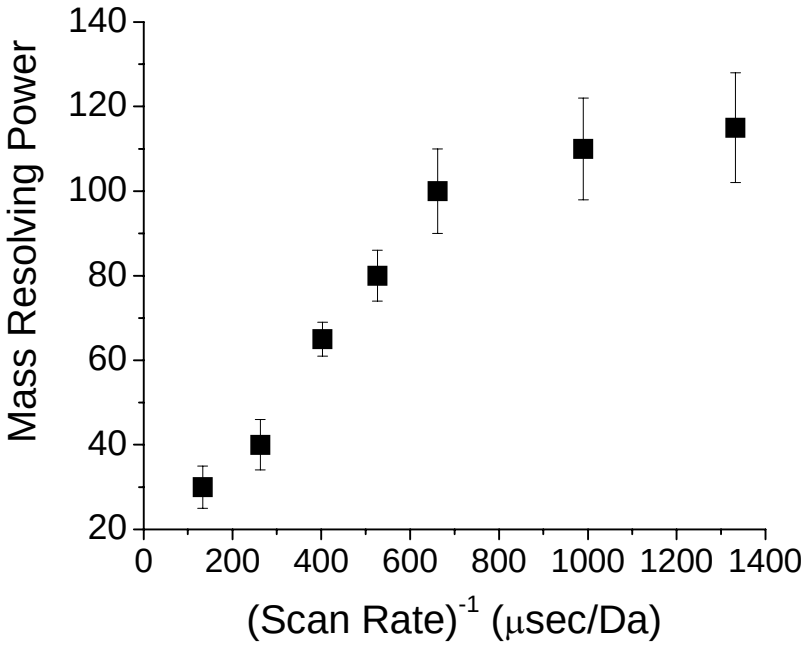

Figure 2.5 – Improvement of mass resolving power with decreased scan rate.

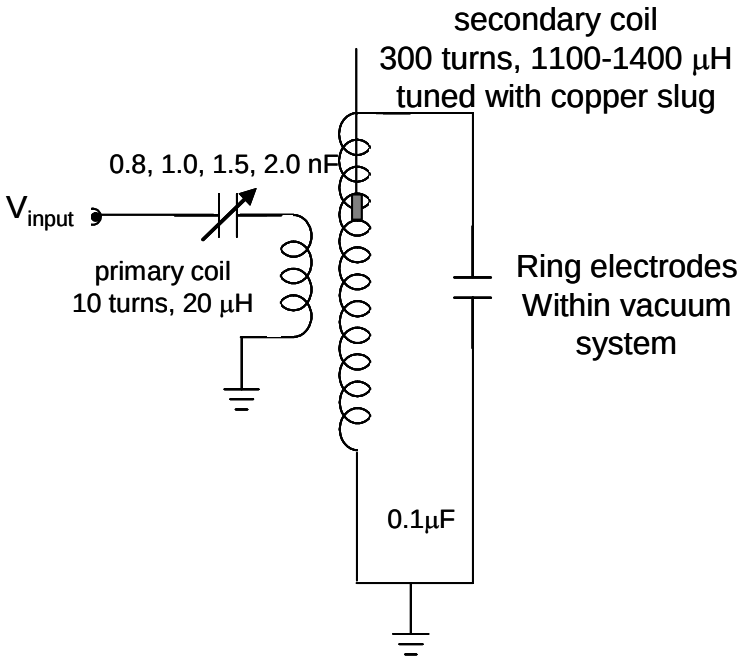

Figure 2.6 – Circuit schematic for rf resonant circuit previously designed for CCIT.

alternative explanation is that because the three coils sit in close proximity in the same plane there is some magnetic coupling between the devices. Consequently the phase mismatch helps to reduce this phenomenon. All of the previously described issues affect rf stability and the maximum obtainable rf voltage. The last two issues affect the tunablity of the rf circuitry. As previously published, a series capacitor is used to match the input impedance of the rf circuitry with the input voltage device.[1] The series capacitors appear to accomplish this because an optimal capacitance value, from the values available, can be found. This series LC resonant circuit will operate most efficiently when the resonant frequency of the primary coil matches the resonant frequency of the secondary coil. It is not clear that the variable capacitor makes the primary coil resonant frequency match the secondary coil resonant circuit. Lastly, the copper slug used to tune the secondary coil had very little effect on the resonant frequency of the system. One reason for the lack of response from the copper slug is that it is connected to a stainless steel threaded rod which travels through both the primary and secondary coils. Given that no design is ever perfect in its first draft, this design was quite functional; however, after a closer examination of the system it was time for the developments of a second generation rf system.

2.2.3.5 Goals for Second Generation rf System

The goals for this second generation rf system are that it is capable of generating a stable rf voltage with a maximum output of at least 10 $kV_{pp,}$ that the device should be tunable over a frequency range of 700 kHz – 1.2 MHz, and that the voltages on each electrode should be independent of the voltage on adjacent electrodes.

2.3 Creating Radio Frequency Voltage

2.3.1 Circuit Design

A general block diagram of the circuitry for creating the rf voltage necessary to operate a quadrupole ion trap is illustrated in **Figure 2.7**. The circuitry can be broken up in to three main sections: generation and modulation of the low voltage rf signal, power amplification, and resonant amplification. Generation and modulation of the low voltage rf signal is responsible for setting the level of the rf voltage that determines the lowest *m/z* ion that can be trapped. Typically, analog modulation is accomplished by using an analog dc signal (0-10V) to vary the amplitude of the rf voltage coming from a rf source, such as a quartz crystal oscillator. The power amplification step is necessary to increase both the current and voltage of the rf signal. This amplification step is a significant power increase and can be in the range of a 50,000 – 150,000 times increase in power, depending on the power amplifier for the given system. During the course of this work a commercial Kalmus (AR worldwide; Bothell, WA) model rf 150, 50W power amplifier was used, as well as a home built power amplifier that was developed and will be described in **Section 2.3.3**. The last stage, resonant amplification, is a voltage amplification and current reduction stage. The amount of amplification in this stage is determined by the amount of electrical losses in the resonant system and can vary based on tuning factors that will be described in **Section 2.3.3**. Reproducibility of the generated rf voltage can be greatly improved through the use of rf detection and feed back circuitry, which is used to control the output of the multiplier circuit to ensure the amplitude requested by the computer is produced.

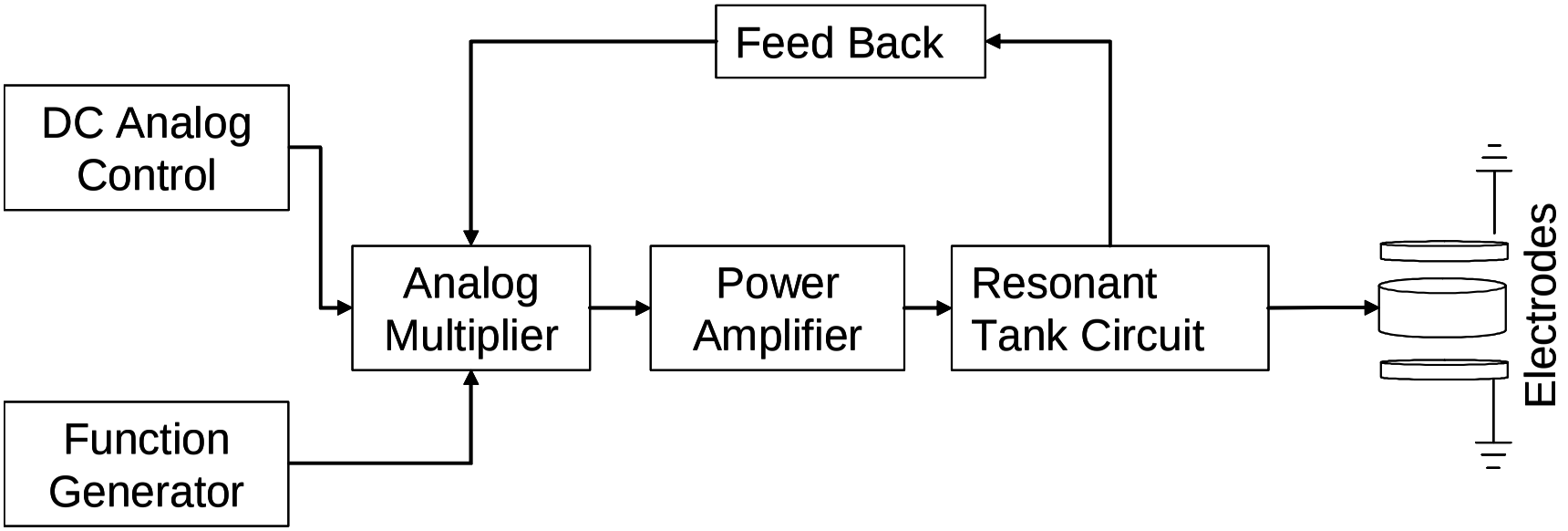

Figure 2.7 – Schematic flow for the generation of rf voltage for an ion trap

There is a separate rf circuit for of the three electrodes; however only one rf voltage is used to generate the rf voltage for the three ring electrodes. The single rf voltage is split into three signals that each drives a separate analog multiplier. There is a separate dc voltage to control the amplitude of the output voltage from the analog multiplier. Each of the analog multiplier then drives a separate circuit as shown in the block diagram in **Figure 2.7.** The complexity of the overall system is increased by the fact that each component in the three circuits needs to be tuned to operate as close as it can to the other two replicates. Small differences may be calibrated for; however, if the circuits are not closely matched the rf voltages can be out of phase and amplitude control can be come more complicated.

2.3.2 Amplitude Modulation

Amplitude modulation is a key step in the generation of rf voltage for the operation of an ion trap. Generally a variable dc voltage is multiplied with a constant low amplitude rf voltage. The amplitude modulation for the CCIT is accomplished using a BurrBrown MPY634KPU analog multiplexing chip (Texas Instruments; Dallas, Texas). This chip allows the amplitude of the rf voltage (1.5 $V_{0\text{-}p}$) to be controlled based on **Equation 2.2**. In this expression V_{DC} is a 0-10V control signal produced by a National Instruments (Austin, TX) PCI-6713 analog output board and V_{rf} is an rf sine wave produced by a Stanford Research Systems (Sunnyvale, CA) model DS340 function generator.

$$V_{out} = \frac{V_{DC} \times V_{rf}}{10} \qquad \textbf{EQ 2.2}$$

The maximum output current of the chip is 30 mA, which means that if this chip is connected to a 50 Ω load the maximum voltage out is 1.5 $V_{0\text{-}p}$. Operating this multiplier at its current limits can lead to distortion that can be harmful to the chip, the power amplifiers, and detrimental to the overall amplification. Noise can be a significant problem as fluctuations

before amplification in the mV range can translate to several volts following the full amplification. Instability in the rf voltage results in broadening of peaks in an averaged mass spectrum. The output voltage of the MPY634KPU is limited by a maximum 30 mA output, which into a 50 Ω load like the power amplifier limits the output voltage to 1.5 $V_{0\text{-}p}$. The output voltage can be improved by increasing the load (> 1 kΩ), by the use of a buffer like a voltage follower. An alternative multiplier was developed with an AD835 multiplier chip (Analog Devices; Norwood, MA) for a conventional 3-D ion trap. This multiplier has a slightly different operation from that described in **Equation 2.2**. Instead of a division by 10 the AD835 divides by 1.05. As shown in the circuit diagram illustrated in **Figure 2.8,** a division of 10 is accomplished by putting a simple voltage divider on the input for the dc voltage. The AD835 is a very fast device and is therefore quite susceptible to rf oscillations. To minimize oscillations ferrite beads were used at the legs of the opamp. Additionally, all grounds were connected to a single ground plane with the shortest leads possible and then the ground plane was subsequently connected to the aluminum enclosure. Improvements in resolution observed in mass spectra acquired when using the AD835 compared to the MPY634KPU are illustrated in **Figure 2.9**. The mass spectra shown in **Figure 2.9** are the average of 10 replicates, which has caused the peaks to be broadened. The observed broadening is due to the lack of feed back control, which will be described in **Section 2.3.6**. The improved peak widths show that small deviations at the analog multiplier can lead to large deviations in the final rf voltage. Therefore it is important to have a stable output voltage from the analog multiplier.

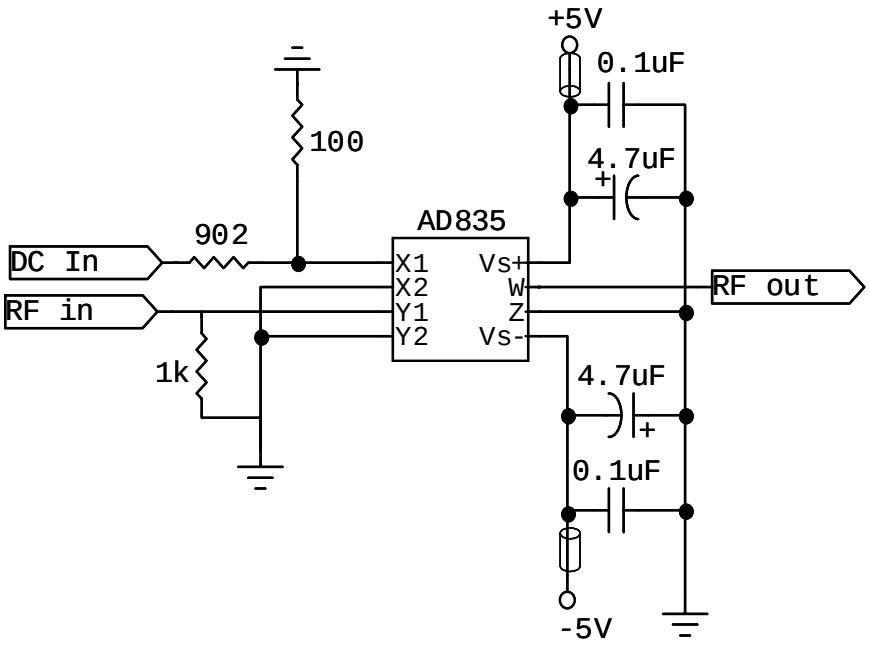

Figure 2.8 – Analog Multiplier circuit which uses the dc input to control the amplitude of the rf voltage output.

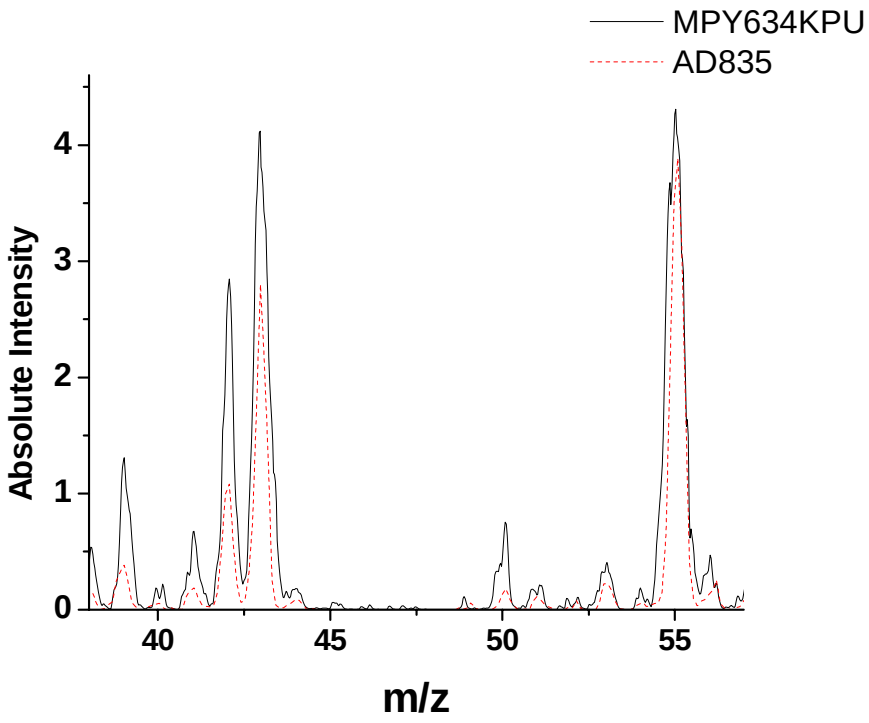

Figure 2.9 – Improved resolution in EI mass spectra of methyl vinyl ketone from MPY634KPU (——) to AD835 (-------).

2.3.3 Power Amplifier

Commercially available power amplifiers can range in price from a few thousand dollars to several hundred thousand dollars. Some important factors in determining this cost are the maximum power (e.g. 50 W, 150 W, 300 W…etc.), the bandwidth or frequency range, and the level of input and output protection of the amplifier. For generating rf for quadrupole ion traps the power requirement is typically between 50 – 100 W, the frequency range is 500 kHz – 2 MHz, and good input and output protection is needed. One major issue in deciding what power amplifier to use is that most commercially available power amplifiers are intended for the GHz frequency range. Some amplifiers are available with sub MHz operation and they can typically operate from 0.3 MHz to a few GHz. Therefore much of the electronics inside the amplifier is wasted to allow the amplifier to operate over such a broad range. Several published studies have reported where research groups have developed there own amplifiers optimized for the desirable frequency range of an ion trap.[27, 31, 32] The power amplifiers used to operate the CCIT are 50 W power amplifiers with a frequency range of 0.2 – 50 MHz This amplifier has no output or input protections; therefore, a 5 W 20 dB attenuator was put on the input to prevent too large of a voltage from going to the input of the amplifier. A 25 W 3 dB attenuator was used to attenuate the output of the amplifier. The voltage gain in a system is defined by **Equation 2.3**, where V_{out} is the output voltage and V_{in} is the input voltage. The input 20 dB attenuator results in a division of 10 on the input voltage. The maximum input voltage of the Kalmus amplifier (specified by the data sheets) is 0.634 V_{pp}. Using the 20 dB attenuator the maximum input voltage is theoretically 6.34 V_{pp}; however, experimentally the maximum was experimentally found to be about 5 V_{pp} and the output voltage increased linearly up to 3 V_{pp}. The 3 dB attenuator divides the output

voltage by √2 or the output power by 1/2, which may not appear to be beneficial to the over all circuit design. However voltage that is reflected from the coil, which can harm the amplifier, will also be divided by the attenuator. In this case the direction of the attenuators used does not matter.

$$gain(dB) = 20\log\left(\frac{V_{out}}{V_{in}}\right) \qquad \textbf{EQ 2.3}$$

Although the Kalmus amplifier functions, a power amplifier needed to be designed that was capable of generating at least 100 W and which provided more protection than the Kalmus amplifier. In connection with the Electronics Design Facility at the University of North Carolina at Chapel Hill a power amplifier was designed for use on quadrupole ion traps. The circuit diagram, a description and characterization of the amplifier, is located in **Appendix II** of this dissertation**.**

2.3.4 Transformers

The nominal mass-to-charge range of the ion trap can be calculated from **Equation 2.4,** where m is the mass of the ion, z is the number of charges, e is the fundamental unit of charge, Ω is the operating frequency of the ion trap, r_o is the distance to the radial center of the ring electrode, and z_0 is half the distance between the end caps.

$$\frac{m}{z} = \frac{8eV}{0.908(r_0^2 + 2z_0^2)\Omega^2} \qquad \textbf{EQ 2.4}$$

For a given operating frequency and ion trap geometry, the maximum *m/z* that can be ejected is determined by the maximum obtainable rf voltage. This is often the voltage at which electrical breakdown occurs. The lower *m/z* range is limited by trapping phenomenon, which will be discussed in **Chapter 4**. The output voltages (0.1 -100 $V_{0\text{-}p}$) from the power amplifiers are capable of a mass range of 2-8 *m/z*. Clearly the voltage needs to be amplified.

In an ion trap operated at a frequency of 1.1 MHz, $r_0 = 1$ cm, and $z_0 = 0.707$ the voltage required to eject a 650 *m/z* ion at q_z=0.908 is 7500 $V_{0\text{-}p}$. Meaning that at least 75 fold amplification is required. The voltage is amplified with a transformer.

2.3.4.1 General Transformer Theory

A transformer is a device that contains at least two inductors that transfer energy through mutual inductance. As an ac source current flows through the first inductor (primary coil) the resulting expanding and contracting magnetic fields can travel through the turns of the second inductor (secondary coil) and cause a current to flow. This process is called mutual inductance. The size and shape, permeability of the "core" material, and the spacing and orientation between the two inductors can determine how efficiently power is transferred between the two devices. The "core" material or the material between the two inductors can be made from a variety of materials. Some of the most common are ferrite and air core. The mutual inductance between the two devices can be calculated using **Equation 2.5**, where M is the voltage and L_1 and L_2 are the individual inductances (units of Henry). It is important to note that the value of the inductors must be measured in the condition that they will be operated. The ratio of the magnetic flux created by the secondary coil to the flux of the primary coil is termed the coefficient of coupling (k), a value that is usually less than 1. The maximum mutual inductance will occur when the coupling factor is 1.

$$M = k\sqrt{L_1 L_2} \qquad \textbf{EQ 2.5}$$

The voltage induced by a magnetic field in a coil is proportional to the number of turns of the inductor. The voltage that will be induced with two coils in the same magnetic field will therefore be proportional to the number of turns in the coils, as shown in **Equation 2.6.** The

output voltage of the secondary coil (V_s) is equal to the input voltage (V_p) times the ratio of the number of turns in the secondary coil (N_s) to the number of turns in the primary coil (N_p).

$$V_s = V_p\left(\frac{N_s}{N_p}\right) \qquad \textbf{EQ 2.6}$$

If there is perfect coupling between the devices, and no other electrical losses, the power into the system must equal the power out of the system. For example, the ion trap described previously, required 7500 $V_{0\text{-}p}$ to eject a 650 *m/z* ion. Given that the power amplifier outputs 100 $V_{0\text{-}p}$, this ion trap would need a transformer with primary coil of 1 turn and a secondary with 75 turns to increase the voltage by a factor of 75. Utilizing ohms law and that power (P) is equal to the current (I) times the voltage (V), **Equations 2.7** and **Equation 2.8**, the input current decreases by a factor of 75 and the power can be related to just the impedance and voltage, **Equation 2.9**. Assuming a perfect power transfer the power in (P_p) will equal the power out (P_s), **Equation 2.10**. Furthermore, using the voltage transformation based on the turns ratio in **Equation 2.6**, the impedance (R) will increase by the square of the turns ratio or a factor of 5625 in this case, **Equation 2.11**.

$$V = IR \qquad \textbf{EQ 2.7}$$

$$P = IV \qquad \textbf{EQ 2.8}$$

$$P = \frac{V^2}{R} \qquad \textbf{EQ 2.9}$$

$$P_p = P_s \qquad \textbf{EQ 2.10}$$

$$R_s = R_p\left(\frac{N_s}{N_p}\right)^2 \qquad \textbf{EQ 2.11}$$

The power transfer from coil to coil is rarely perfect because electrical losses are inherent in any transformer. The wire of a transformer has resistance, which is dependant on

the gauge, or thickness, and the length of the wire. Additional losses can also occur because of the capacitance that exists from turn to turn of the coil, which are essentially small voltage dividers from turn to turn. Enclosures for the transformer can also create series capacitance and result in power loss. Stray capacitance can cause a reduction in the amplification because it can act as a load on the transformer, which removes some of the stored power. Losses can be minimized by using large diameter wire (12-14 gauge), and maximizing the distance between the enclosure walls and the coil. If losses cannot be avoided, more power or more turns on the secondary coil may be necessary. Increasing the turn ratio can be geometrically difficult because as the number of turns increase the length of the coil needs to increase or the coil has to wrap over top of itself. Unfortunately, wrapping the coil on itself can lead to increased capacitive losses.

2.3.4.2 Transformer Geometry

The transformer geometry described up to this point is for a system where the primary and secondary coils are two separate coils. The layout of these coils relative to each other is crucial to the performance of the transformer. The coupling of the two coils must be maximized, while attempting to minimize resistive and capacitive losses. Ideally the primary coil is placed at the center of the secondary coil for maximum overlap; however, at the center of the secondary coil the voltage is too high and the primary coil begins to float at higher potentials. A compromise is met by putting the primary coils closer to the low voltage side of the secondary coil but not all the way at the end. The actual distance of the primary coil along the secondary coil is determined empirically and depends on the gauge of the wire, the number of turns in the primary, the turn to turn spacing of both coils, and the core of the transformer. An example layout illustrating the geometry is depicted in **Figure 2.10a.** In this

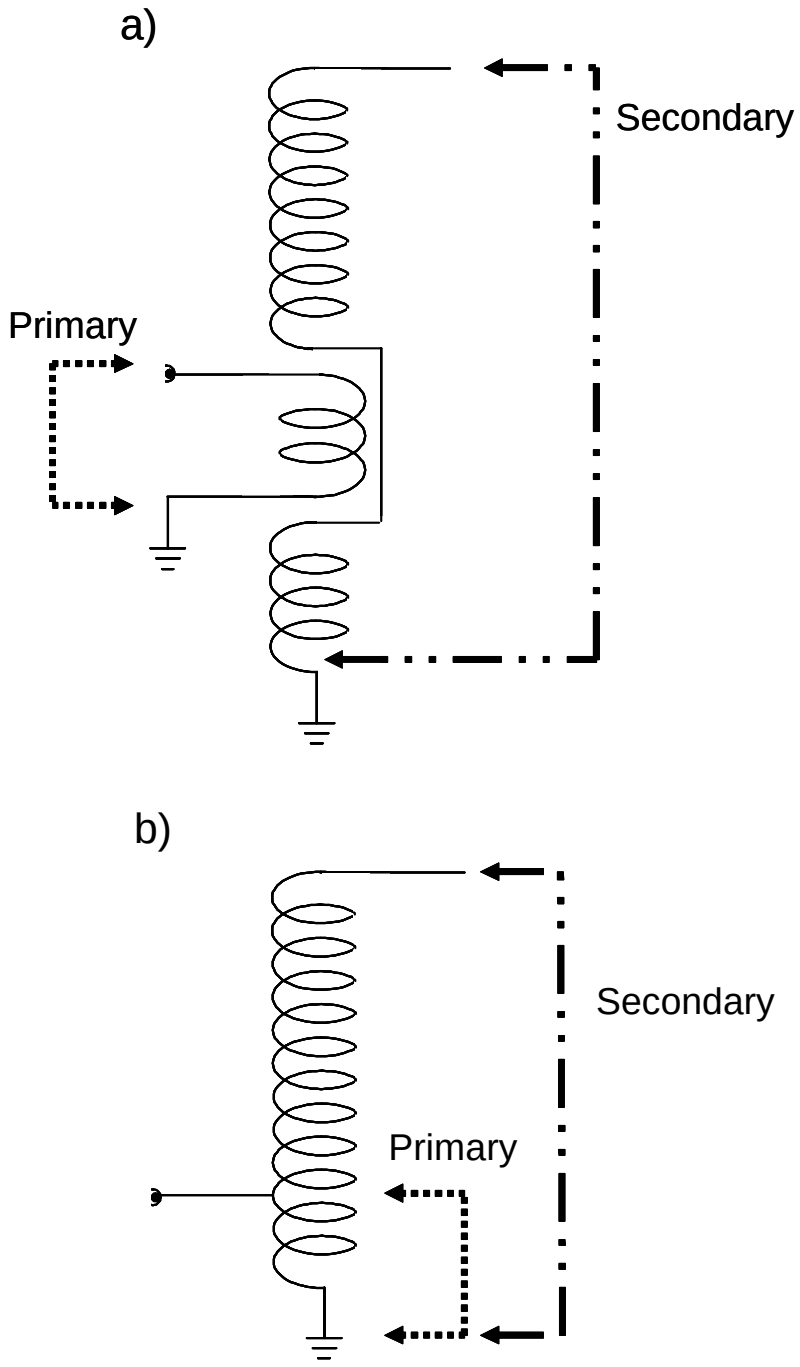

Figure 2.10 – Two possible configurations for transformers a) 2-coil transformer 12:2 turn ratio b) auto transformer 12: turn ratio. Primary coil (**…..**) and secondary coil (**— · · —**).

figure the primary coil begins inside of the secondary after three turns. The secondary coil is subsequently connected from the third turn to the fourth turn, with the connection traveling over the face of the wire of the primary coil. An alternative geometry to the 2-coil geometry is a single coil or auto transformer, which has a coupling factor of 1 and thus resulting in the maximum possible mutual inductance. As outlined in **Figure 2.10b**, the auto transformer's secondary coil is the entire coil and the primary coil shares the first few turns of the secondary coil. There are advantages and disadvantages to both geometries. The 2-coil system is more complex than the autotransformer and requires some experimentation to find the optimal location for the primary coil. In the previously developed first generation rf system, creating 3 identical 2-coil rf systems proved quite difficult. In comparison the autotransformer is quite simple and generating identical coils is much more reasonable. Because the mutual inductance is at its maximum value the autotransformer may be the more efficient transformer; however, this perfect coupling creates problems because slight changes to the primary affect the secondary and vice versa. The autotransformer was chosen for the design of the CCIT rf system because at the time of the design of this circuit the focus was on the creation of 3 identical rf circuits. The design of the rf tank circuitry, enclosure and mounting scheme will be described in **Section 2.4** of this chapter.

2.3.4.3 Resonant Circuit Theory

Quite often one turn on the primary coil is not always optimal, in fact up to 4-5 turns may be necessary to approach a 50 Ω impedance of the primary coil. This many turns on the primary coil means at least 375 turns on the secondary coil, in order to approach the 75 fold amplification. Increasing the number of turns can be an inefficient method of increasing the amplification factor of the transformer. A more attractive method to increase the

amplification factor of a coil, without increasing the number of turns of coil, can be achieved through what is termed resonant circuitry. The advantage of this type of circuitry is that it more efficiently stores energy in the coil, having the same effect as increasing the number of turns in the same magnetic field. As described in **Equation 2.12**, the efficiency at which a component like an inductor stores energy can be described as the ability to store energy or the reactance of a component (X_L for an inductor and X_C for a capacitor) relative to the sum of all energy losses in the system (R).

$$Q = \frac{X}{R} \qquad \textbf{EQ 2.12}$$

The output of the transformer connects directly to the ion trap. Because the ion trap electrodes will have capacitance the transformer-ion trap circuit can be described as a parallel LC circuit, which is shown in **Figure 2.6** and **Figure 2.7**. This circuit can also be called the tank circuit. The resistance or reactance of a capacitor (X_C) and transformer (inductor; X_L) as a function of frequency (f) are described in **Equations 2.13** and **Equation 2.14** respectively. When the reactance of the transformer and the capacitor equal each other the system is said to be in resonance. The resonant frequency (f_r) can calculated using **Equation 2.15**.

$$X_C = \frac{1}{2\pi f C} \qquad \textbf{EQ 2.13}$$

$$X_L = 2\pi f L \qquad \textbf{EQ 2.14}$$

$$f_r = \frac{1}{2\pi\sqrt{LC}} \qquad \textbf{EQ 2.15}$$

$$Q = \frac{f_r}{\Delta f} \qquad \textbf{EQ 2.16}$$

Instead of the turn ratio determining the output voltage of the transformer, roughly the Q of the LC network times the input voltage determines the output voltage. Because the impedance of both the inductor and capacitor are equal at the resonant frequency, the Q of the LC network is described in a similar manner as the individual components using **Equation 2.12**. More practically, the Q of a resonant circuit can be determined by measuring the frequency response of the circuit and calculating the width (Δf) of the resonant peak at -3dB points and then dividing as in **Equation 2.16**. The width of the resonant peak is a measure of the resistive losses of the LC system. Autotransformers are known for having Q values less than 100, whereas 2-coil systems are capable of having Q values as high as 200.

.The current through a capacitor lags the voltage whereas the current through an inductor leads the voltage. The result of the phase of the current through the two devices is that in a series LC circuit the impedance (Z_{series}) is zero at the resonant frequency, **Equation 2.17**, and in a parallel LC circuit the impedance ($Z_{parallel}$) is infinite at the resonant frequency, **Equation 2.18**. Because of the higher impedance at non-resonant frequencies and the low impedance on resonance a series LC circuits act as pseudo notch filters which remove non resonant frequencies with minimal power loss. In some older commercial systems the rf voltage is a square wave and a series LC created at the input of the rf coil is used to turn the signal into a sine wave. The high impedance at the resonant frequency in a parallel LC results in the greatest voltage drop across the LC circuit at the resonant frequency.

$$Z_{series} = X_L - X_C \qquad \textbf{EQ 2.17}$$

$$Z_{parallel} = \frac{X_L X_C}{X_L - X_C} \qquad \textbf{EQ 2.18}$$

Putting filter circuits on autotransformers or 2-coil systems can have both advantages and disadvantages. A series LC filter circuit clearly can act as a filter in both cases and can be used to match impedances of the primary with the output of the power amplifier. In an autotransformer, the series LC circuit on the primary may affect the secondary coil, because of the optimal coupling. However, if the circuit were attached to a 2-coil system, the series LC circuit would create a resonant frequency for the primary circuit that could be different than that of the resonant frequency of the secondary parallel LC circuit. This is due to the fact that the resonant frequency of the primary and secondary coils must match for optimal power transfer between the two coils.

2.3.5 Tuning rf Circuits

Methodology for tuning rf circuitry can be separated in to 5 basic steps:

1) Measure the physical values of inductive and capacitive components.
2) Measure the resonant frequency of all resonant circuits.
3) Adjust resonant frequency by altering the number of turns on the secondary coil, by adding parallel capacitance, or by tuning with copper slug.
4) Match the input impedance with number of turns on primary coil or use of external circuitry.
5) Re-measure the resonant frequency.

Each of these steps will be discussed in more detail in the following sections.

2.3.5.1 Measurement of Physical Components

With the construction of any complex circuitry the initial conditions must be well characterized and understood before the system can be tuned. The inductances of the coils, used in the 3 coil system for the CCIT, were measured with an LCR meter (BK Precision,

875B, Yorba Linda, CA) while the coils were both in and out of the enclosures. The capacitances of the electrodes were measured using the LCR meter with 3 inch leads terminated with alligator clips. The capacitance of the leads was zeroed out of the LCR meter. Because the capacitance of the leads is quite variable, positioning and separation of the leads is critical to this measurement, zeroing was accomplished with one alligator clip hooked onto the feed-through and the other taped to the next connection but not contacted. The location of the feed-through and other portions of the rf system can be observed in **Figure 2.11** (The high voltage feed-throughs are labeled with an arrow.) The capacitance of each CCIT electrode was measured from atmospheric side of the high voltage feed-through relative to ground and from electrode to electrode. Because the capacitance values of the electrodes are quite small and the measurement imprecise, 10 replicate measurements were made for each electrode. For conventional ion traps the capacitance of the electrodes is only one value; however, for the CCIT a total of six capacitances exist. As shown in **Figure 2.12**, three are from the actual electrode capacitance to ground and three are due to inter-electrode capacitance. With the measured capacitance values and inductance value known, **Equation 2.5** can be used to calculate the resonant frequency range to monitor.

2.3.5.2 Measuring the Resonant Frequency

The resonant frequency of a circuit can be measured by monitoring how the amplitude of the voltage across the circuit changes as a function of frequency. The two circuits are a series LC circuit and a parallel LC circuit. Because the series LC circuit is a low voltage circuit, the amplitude can be monitored using a 10x oscilloscope probe. The scope probe in parallel with the primary coil does not significantly alter the resonance frequency. Monitoring the parallel LC circuit during the course of an experiment is more

a)

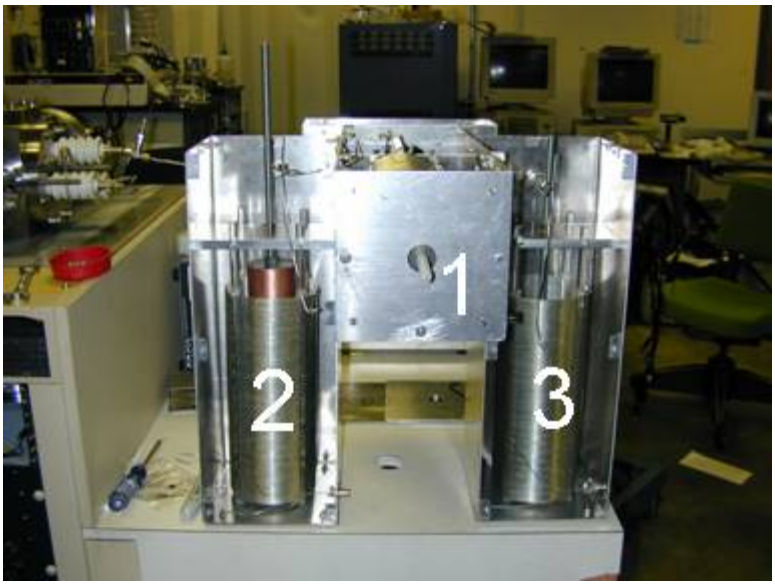

b)

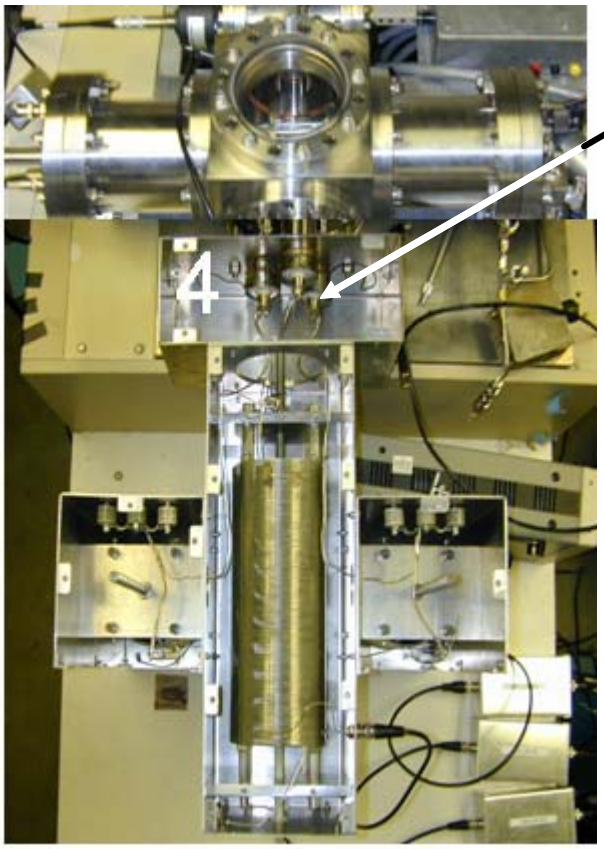

Figure 2.11 – Layout of rf coil boxes numbered 1-4 a) Front view and b) Top view.

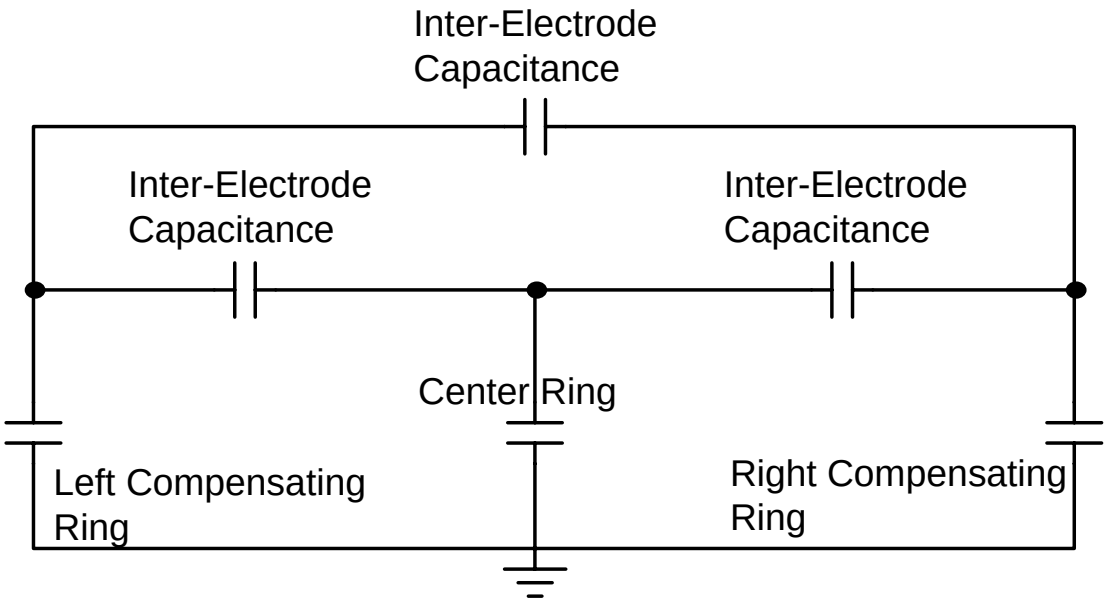

Figure 2.12 – Circuit equivalent for three electrode capacitances to ground and three inter-electrode capacitances.

complicated because it is a high voltage circuit. To avoid perturbing the circuit a capacitive pick-up, positioned 1 inch radially from the high voltage feed-through, was used to measure the voltage on the secondary coils. Using the amplitude modulation chip MPY634KPU, a dc level of 1 V, input rf voltage of 3 V_{pp}, and the three 50 W power amplifiers, the frequency was varied from 600 kHz to 2 MHz at various intervals. Pick-up voltages were monitored on a digital oscilloscope (TDS420, Tektroniks,) at each frequency step and the waveforms were downloaded from the oscilloscope utilizing the general purpose interface bus (GPIB) and a software program, written in Lab VIEW™ (National Instruments, Austin, TX), to communicate with the oscilloscope. The amplitudes were then extracted from the files and plotted as a function of frequency in Excel™ (Microsoft). The original waveforms were kept for comparison purposes.

2.3.5.3 Tuning the Resonant Frequency

From **Equation 2.15** altering the inductance and the capacitance values will change the resonant frequency. The parallel circuit which sets the resonant frequency is the circuit created by the secondary coil and electrodes of the ion trap. In a two coil transformer the value of the inductance can be changed by simply decreasing or increasing the number of turns on the secondary coil. In an auto transformer, a wire connecting high voltage feed-through to the coil is soldered or clipped on to the coil. This connection is often termed a tap. The position of the tap determines the inductance of the secondary coil, which is a fine adjustment to the resonant frequency because the inductance typically only changes by ~1-2% per turn for the coils used in these experiments. Once the resonant frequency is measured, the resonant frequency can be increased by increasing the number of turns on the secondary coil (increasing the inductance) and vice versa to decrease the resonant frequency.

An estimation of the number of turns can be determined using a simple equality, **Equation 2.19**, where f_{r1} and L_1 are the resonant frequency and inductance of the coil under the present conditions and f_{r2} and L_2 are the desired resonant frequency and the final inductance of the coil.

$$f_{r1}\sqrt{L_1} = f_{r2}\sqrt{L_2} \qquad \textbf{EQ 2.19}$$

$$n_t = \frac{L_2 - L_1}{L_n} \qquad \textbf{EQ 2.20}$$

This equality is derived from **Equation 2.15** and assumes that the capacitance of the system will not change, which means that the number of turns can not change significantly. Using the measured $f_{r1,}$ L_1, and the desired f_{r2} the final inductance can be calculated. If L_1 is not known a number can be used which is reasonable for the coil dimensions. The number of turns can then be calculated using **Equation 2.20**, where L_n is the inductance per turn and n_t is the number of turns to increase or decrease. If the result is positive increase the number of turns and if the result is negative decrease the number of turns. The L_n factor is a measured factor, which is not linear over the entire coil but can be linear over a 25% of the coil.

Parallel capacitance can be added to the circuit to reduce the resonant frequency. Because large value capacitances can be used, capacitors can act as a more coarse adjustment to the resonant frequency than changing the slug or the tap position. To withstand the high voltage rf, the capacitors added are high voltage ceramic capacitors from High Energy Corp (Parkesburg, PA) rated to 10 $kV_{0\text{-}p}$. These capacitors are only available in certain intervals; therefore, tuning was first accomplished with low voltage ceramic capacitors rated at 50 $V_{0\text{-}p}$. Once the system was tuned ceramic capacitors were ordered at the appropriate values to achieve the desired resonant frequency range. The maximum resonant frequency will be

limited by the capacitance of the ion trap electrodes, which can be on the order of 20-30 pF. In addition to varying the inductance and capacitance to alter the resonant frequency, the Q of the circuit can be reduced by inserting a device that disturbs the mutual inductance. This was accomplished by inserting a hollow copper slug into the secondary coil, which results in a fine adjustment to the resonant frequency.

2.3.5.4 Impedance Matching

The number of turns used on the primary coils depends on the desired impedance of the transformer. To minimize power loss and reflected power, the input impedance of the transformer should match that of the output impedance of the power amplifier. In the autotransformers used, the number of the turns on the primary coils or primary tap was kept to less than 5 turns so as to reduce losses in the coils. Impedance transducer circuits can be put in between the power amplifier and the coil to match the impedance. Two circuits that have been used are balun circuits and simple series capacitors. The baluns used are simply transformers wrapped around a magnetic core. Using **Equation 2.11**, if a balun with 2 turns on the primary and 1 turn on the secondary is used the impedance will increase 4 fold. This balun would therefore be termed a "4:1" balun. Both "16:1" and "9:1" baluns were used to match the impedance of the CCIT transformers. Baluns can be used to either step up or step down the impedance. There should be no impact on the resonant frequency as a result of the balun circuit. The second type of circuit is mica capacitors (Cornell-Dublier; Liberty, SC) in series with the primary coil. The capacitor type is important because the inductance inherent in some capacitor designs must be minimized.

Measuring the impedance of an LC circuit can be complicated. A measuring device, called an impedance analyzer, is the ideal tool for measuring the input impedance of an LC

circuit. These devices are costly (> $25k) and would only be used during the initial setup of an rf system; therefore, it was not practical to purchase this device for these studies. In the absence of a sophisticated device, such as the impedance analyzer, more "low tech" measurement techniques are appropriate to get an estimate of the input impedance of the primary coil. Three methods were employed. First a low value resistor was put in series with the input of the coil. The voltages before and after the resistor were monitored as a function of frequency. The voltage after the resistor is the voltage that is dropped across the primary coil. When the voltage across the primary is half the voltage across the resistor, then the impedance of the resistor and the primary coil are equal. Several resistors ranging from 1.8 – 20 Ω were used. Because the power amplifier output impedance is 50 Ω, the input impedance of the coil should be tuned to 50 Ω. Therefore the second method attempted was to compare the output voltage of the power amplifier when connected the coil versus when the power amplifier is terminating into a 50 Ω dummy load. The voltages being input into the three coils were monitored in parallel using three 10x oscilloscope probes. All three coils were driven at the same potential to avoid cross talk between the devices. By comparing the output voltage of the power amplifier driving the two different loads over the full operating range a calibration can be obtained to give rough idea of input impedance of the coil. The last method employed used an impedance analyzer device called a vector voltmeter, which actually measures the input impedance, on a single auto transformer. This device could not be used on the CCIT unless 2 identical devices were available to drive all three circuits with the same voltage. However, to illustrate the applicability of the vector voltmeter to rf circuitry for ion traps, it was used on a single coil system driving a conventional 3-D ion trap. The vector voltmeter, which applies a low voltage sine wave to a LC circuit, monitors the

current drawn to determine the phase and impedance of the connected device. A HP model 4193A vector voltmeter (Pal Alto, CA), which is an older analog version of the modern digital impedance analyzer, was used to measure the input impedance on an autotransformer being used on a conventional 3-D ion trap. The Vector voltmeter frequency generator has an analog frequency dial for the drive voltage. The frequency of this waveform was determined by monitoring the output of the voltmeter on a digital oscilloscope.

2.3.6 Calibrating the rf Voltage

Although Q times the input voltage theoretically predicts the output voltage, a measurement of the rf voltage is more desirable. The capacitive pick-up is used to get a low voltage reading of the high voltage just before it enters the vacuum housing. To determine how the voltage on the capacitive pick-up correlates to the actual rf voltage, the pick-ups need to be calibrated. A low amplitude rf voltage 1-10$V_{0\text{-}p}$ was put into all three of the rf coils. A 10x probe was hooked directly to the wire of the secondary coil. This probe adds capacitance to the circuit and does change the resonant frequency; however, what is of concern is how the voltage at the wire corresponds to the voltage at the capacitive pick-up. After determining the new resonant frequency, a calibration is created by monitoring both the 10x oscilloscope probes and the capacitive pick-ups with a digital scope. The resulting linear calibration can then be used to correlate the pick-up voltage to what the actual high voltage rf that is on the electrodes. Correlating the dc voltage used to generate the given rf voltage (determined from the pick-up calibration) will give an initial instrument calibration. In a conventional ion trap the rf voltage can be converted to *m/z* using **Equation 2.4**.

2.3.7 Feedback Control

Feed back control in theory is fairly simple. The high amplitude rf voltage is capacitively detected on the secondary side of the rf coil. This low voltage rf is then converted into a dc signal, which is compared to the dc control out of the computer. Depending on whether the dc equivalent of the rf voltage was too high or too low, the output of the multiplier circuit would then be increased or decreased. In practice the circuitry necessary for stable feed back control is somewhat complicated. The circuitry to convert the rf voltage into a dc signal needs to be capable of sampling 1 MHz signals, as well as be calibrated with the dc control from the computer. As is typical with rf circuitry this feed back control is quite prone to oscillations and great care must be taken in the design of the feed back control. Capacitive pick-ups for the detection of the high voltage rf circuitry were developed and will be described in the next section. Because of the complexity already present in the rf circuitry feed back control was not attempted in these experiments; however, it must be stated that performance of all commercial systems would suffer greatly without feed back control.

2.4 Enclosure and LC tank circuit design

The autotransformer coils were Barker and Williamson 4098T (Cocoa, FL) 360 μH , 4x10 inch coils with 10 turns per inch made of 12 AWG wire supported and embedded in 4 acrylic rods. Four enclosures were designed and constructed for the CCIT rf system. Pictures of the boxes are shown in **Figure 2.11**. The mechanical drawings are located in **Appendix II**. Box 1 contains the coil for the center ring electrode and it sits 90° relative to the other two coils. The reason for the perpendicular orientation is to attempt to remove

magnetic coupling from coil to coil. Box 2 is for the left compensating ring electrode and Box 3 is for the right compensating ring electrode. Box 4 contains the capacitive pick-ups which slide over tube shields covering the high voltage feed-throughs, which are attached to a 6 inch conflat flange. The capacitive pick-ups have wires spot welded to them which connect to female BNC bulk heads at the top of Box 4. Wires from each of the 3 coils connect to the high voltage feed-throughs in Box 4. Connection wires from the coils in Box 2 and Box 3 travel through Box 1 before entering Box 4. Two 9/16 inch threaded rods screw into the vacuum housing and are bolted to Box 4. These rods add mechanical stability and electrical ground. The boxes are constructed from 16 gauge (0.065 inch) aluminum sheet metal. The top, bottom, and front face of each box are removable. Inside the boxes are L shaped brackets for the faces to screw into. Electrical ground in each box is connected to the bottom face, which is grounded through Box 4. The high voltage capacitors are screwed onto the back wall of each of the coil boxes. If more than one high voltage capacitor was used, they were joined together with two 12 gauge solder terminals that were connected with a 12 gauge wire.

Each of the coils is mounted in a 3/8 inch thick aluminum block with 4 holes for the acrylic rods and a threaded hole through the center. The center coil is suspended from two aluminum blocks. The coils as purchased did not have acrylic rods long enough to go through the blocks; therefore, 1.5 inch extensions were chemically melted on the existing rods. The hollow copper slug is constructed from a 2 inch diameter copper tube. A solid ½ inch thick, 2.05 inch diameter aluminum slug was press fit into the copper tube. The aluminum slug has a center tapped hole. The copper slug is then bolted onto a threaded rod, which is then screwed into the aluminum coil holder block. The slug is held in place with a

nut with a star lock washer that allows the slug to be screwed in and out of the coil without allowing the nut to move up and down the rod. A slot was cut into the end of the threaded rod to allow a screw driver to be used to move the threaded rod up and down in the coil. Mechanical drawings for the copper slug and coil holder block can be found in **Appendix II**. The slug for the center coil required a different set up because the user would only have access to the primary side of the coil, where as for the two outside coils the user has access to the top or secondary side of the coils. The approach taken was to drill and tap a hole through the second mounting block for the center coil. A Teflon rod would be sent through the low voltage primary side of the coil. The Teflon rod and the stainless steel rod were joined and lock together by screwing the rods together with two nuts. The slug is still supported by the stainless steel rod so that minimal bowing occurs. The user adjusts the Teflon rod to adjust the positioning of the slug.

2.5 Tuning the LC Circuits

2.5.1 Tuning Single rf coil

For an example circuit the tuning methods described above were explored on a rf system for a conventional 3-D ion trap. The circuit has a series capacitor on the primary, which will be characterized in addition to the secondary coil. Additional differences between this circuit and the CCIT rf circuits are the slightly larger diameter (0.127 m) coil and thus larger inductance (500 μH) than the CCIT coils, the 5 μH/turn L_n, the 22 pF electrode capacitance, and an additional 25 pF capacitor in parallel with the inductor. The primary coil is tapped at four turns from the bottom of the coil and the secondary coil is tapped one turn from the top. The rf tune of the circuit is illustrated in **Figure 2.13a**. As the impedance

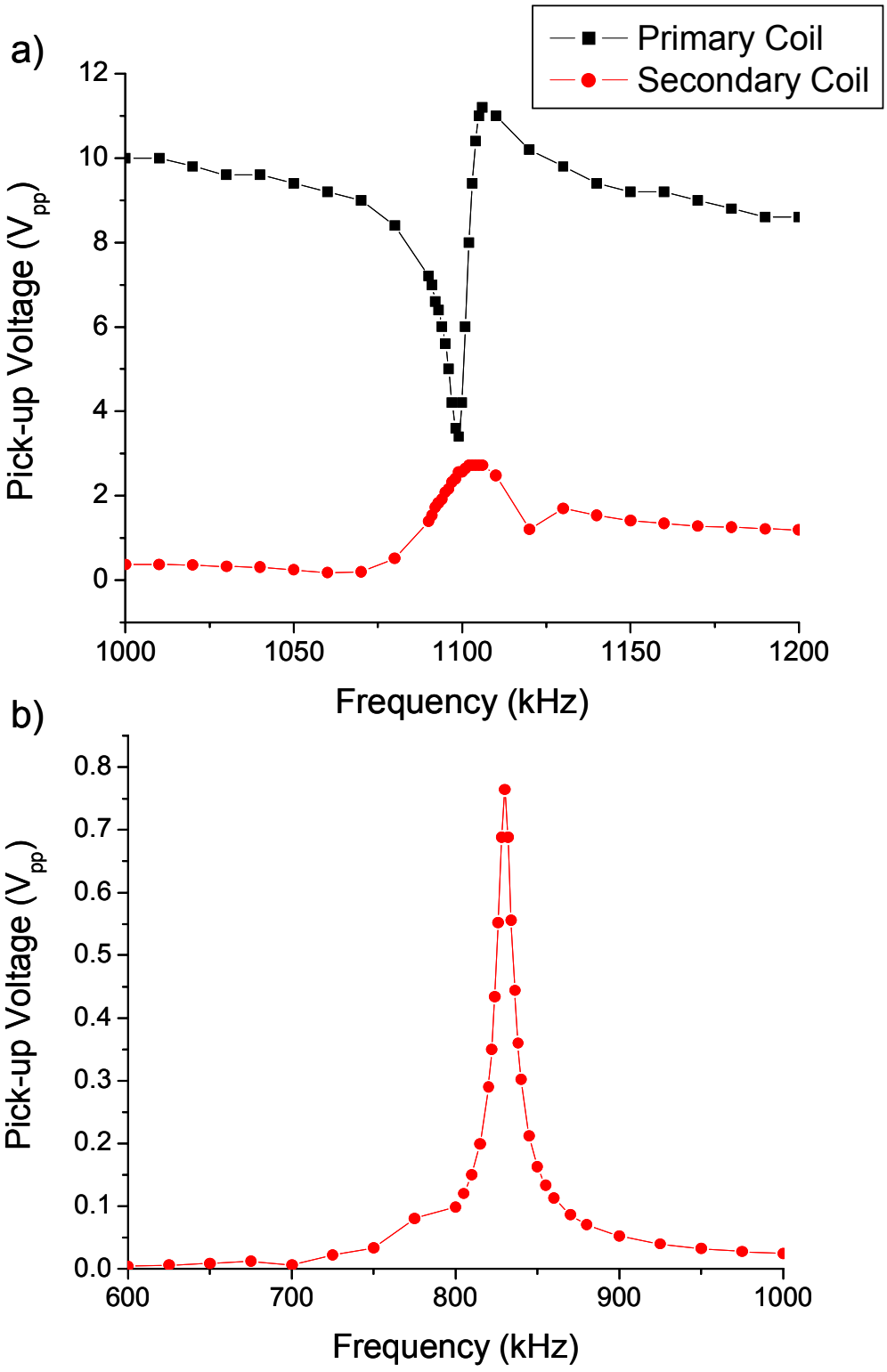

Figure 2.13 – Resonant frequencies of 3-D ion trap rf circuit with a) 25 pF of parallel capacitance and b) 60 pF of parallel capacitance.

Equation 2.17 and **Equation 2.18** suggest, because voltage is directly proportional to the impedance, the primary coil voltage is at a minimum value at resonance and the secondary coil voltage is maximum at resonance. The resonant frequency of this system was 1.104 MHz and the Q of this circuit was about 45. In an identical circuit, on a slightly different instrument, when ~35 pF of additional capacitance was added to the circuit the resonant frequency decreased to 838 kHz with a Q value of nearly 120 **(Figure 2.13b).**

2.5.2 Tuning the CCIT rf Circuits

The capacitance values of the LC circuits are summarized in **Table 2.1**. The overall capacitance of the system is complex because of the intra-electrode capacitance. The capacitance that will hold the most value in determining the resonant frequency is the electrode capacitance to ground.

Electrode Capacitance (pF)	
Center ring to ground	25.5
Left Compensating to ground	30.6
Right Compensating to ground	30.7
Center to Left	15.3
Center to Right	16.1
Left to Right	11.7

Table 2.1: Capacitance of CCIT electrodes, all values are $\pm$ 3%.

The inductances of the coils were 350 μH. Additional parallel capacitance of 65 pF was chosen so that the resonant frequency of the system would be approximately 850 kHz. The resonant frequency of each coil was independently determined with the other two coils disconnected. Each coil had a resonant frequency of 1 MHz with Q values of 27, 42, and 28 for the center coil (rf_1), left compensating electrode coil (rf_2) and right compensating coil (rf_3) respectively (**Figure 2.14a**). In general for the top most 20 turns, adjusting the tap affected the inductance by 3.9 μH and f_r by 4-6 kHz per turn. Adjusting the slug position affected the inductance of the coil 1-20 μH and the resonant frequency 1-20 kHz

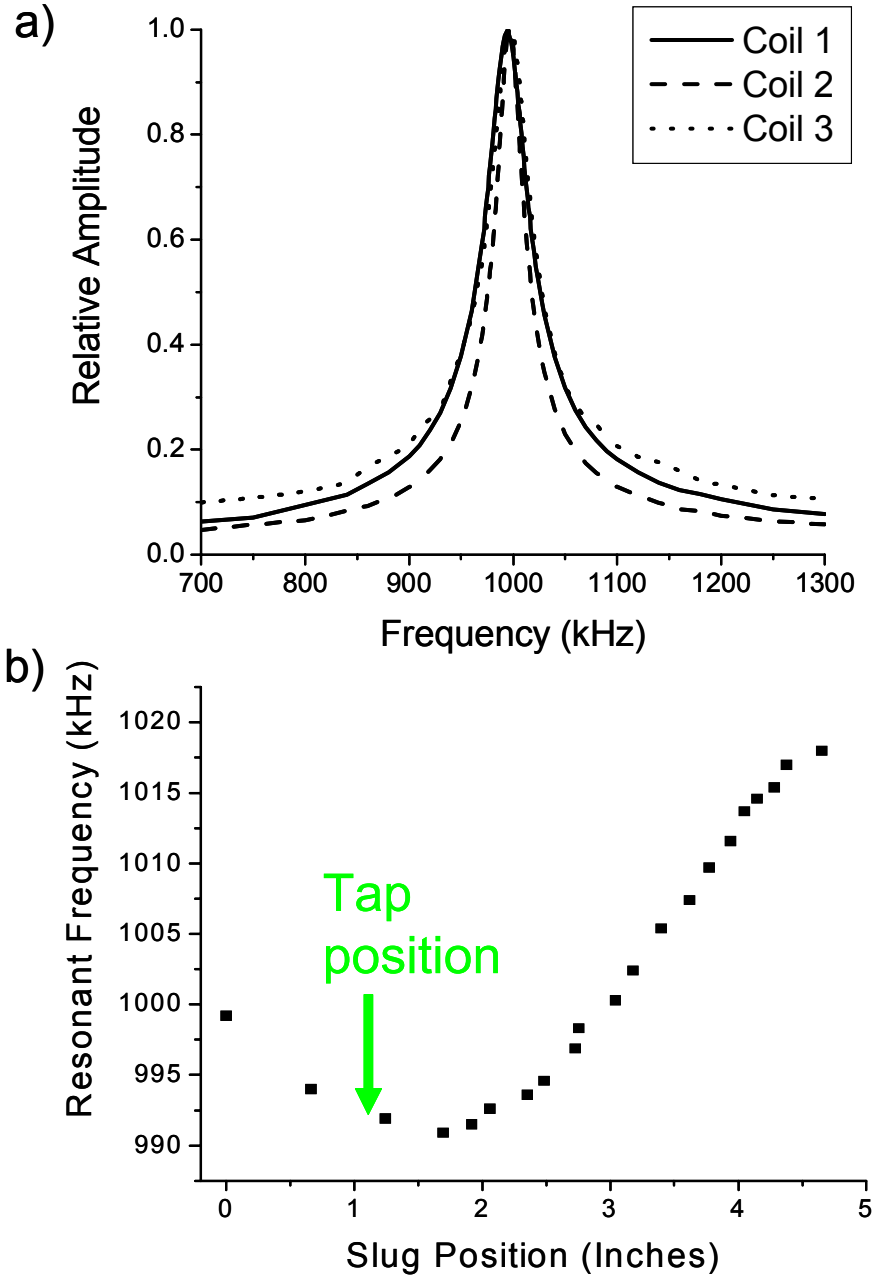

Figure 2.14 – Characterization of stand alone coils a) Resonant frequencies of individual coils and b) Effect of copper slug on resonant frequency.

(Figure 2.14b). The slug position is measured as a distance from the slug fully extracted from the top of the secondary coil (0") to the set position. When the complete system (all primary and secondary coils connected and driven) was assembled, resonant frequencies (f_r) of the system observed were at 940, 990, and 1040 kHz (**Figure 2.15b**). The f_r were greater than expected because the coils had to be trimmed, thus decreasing the inductance. The original measurements were conducted on the coils unaltered from the manufacturer, which came with more than 0.1 meters excess wire. In addition, the overall capacitance was decreased because the aluminum boxes caused coupling from the primary tap to the secondary tap, resulting in an increase in the f_r. All three of the rf voltages were in phase at 1040 kHz (also the largest amplitude for all three rf voltages) and the voltages for rf_2 and rf_3 were out phase with rf_1 at 940 and 990 kHz. Results from the characterization of the original rf system are shown in **Figure 2.15a.** The peaks observed were at 680 kHz, 760 kHz, and 905 kHz. The largest peak where all three rf voltage were in phase at 905 kHz is broader ($Q \approx 10$) than the new rf system. Clearly the new rf system is much more efficient resonant circuit.

Various low voltage capacitors were used to determine, by substitution, the appropriate high voltage capacitor values needed to obtain tuning of the resonant frequency across a range of 700 kHz -1.1 MHz. High voltage capacitors obtained were 5, 10, 35, 55, and 65 pF. The high voltage capacitors have 10% error in the value of their capacitance as reported by the vendor; however, in some cases errors were found to be as large as 25%. Because of the range in errors, capacitors with the closest values were used on rf_2 and rf_3, whenever possibl. Adding 55 pf of parallel capacitance reduced the resonant frequencies of the system to 800, 850 and 881 kHz (**Figure 2.16a**). The capacitance did not have an effect

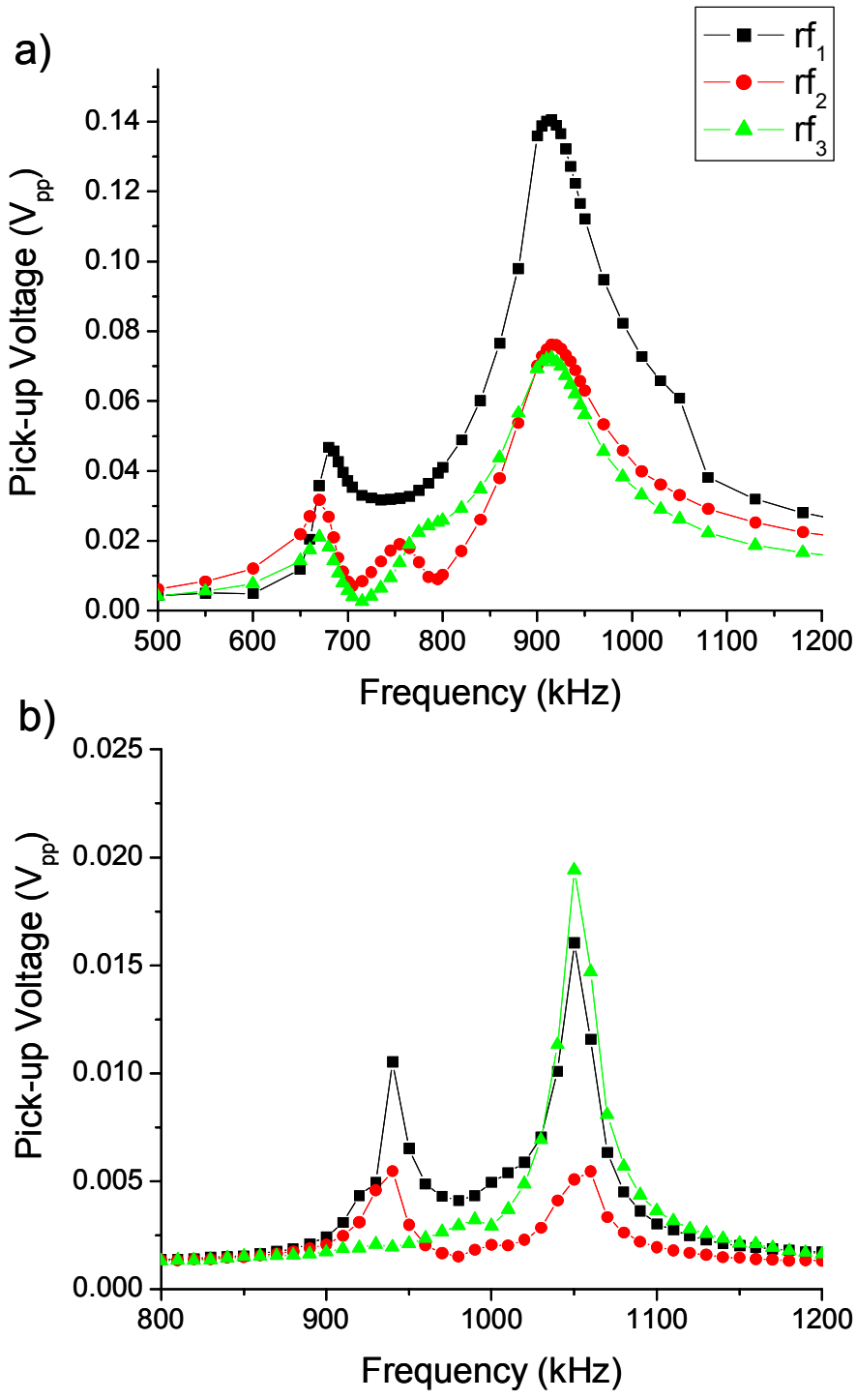

Figure 2.15 - Characterization of a) Old rf system and b) New rf system pre-tuning.

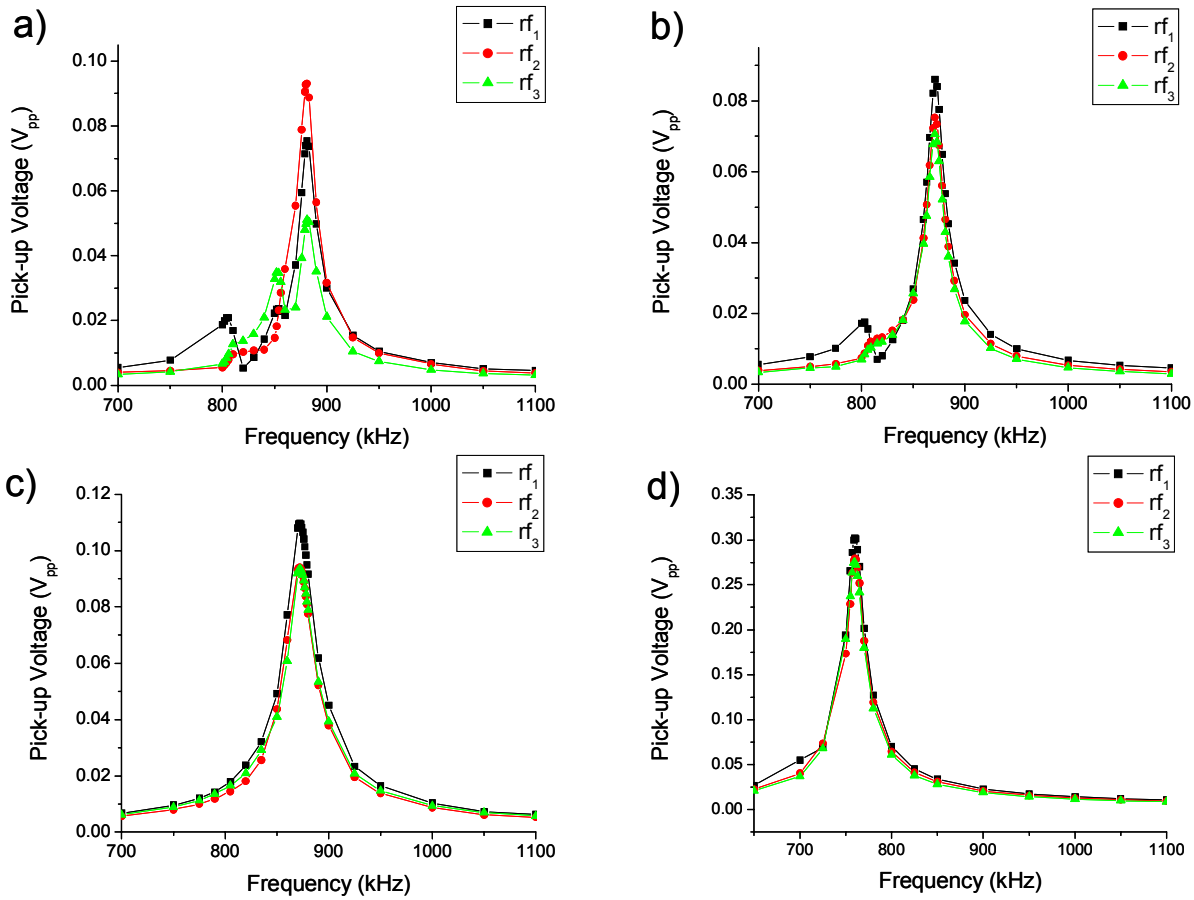

Figure 2.16 – Characterization of rf tune with a) Addition of 55 pF parallel capacitance to all circuits, b) Matching capacitance and secondary taps of rf_2 and rf_3, c) Optimizing primary tap positions, d) Addition of another 55 pF parallel capacitance.

on the relative phases of the rf voltages. By altering the position of the tap on the secondary coil of rf_2 to match rf_3, only two resonant frequencies were observed (**Figure 2.16b**). One at 800 kHz with rf_1 out of phase with rf_2 and rf_3 and the other at 871 kHz with all three rf voltages in phase. After adjusting the slug in each of the autotransformers and increasing the turns on the primary coil of the rf_1 tank circuit, only one resonant frequency at 871 kHz remained (**Figure 2.16c**). The three separate resonant frequencies may have been due to mismatches between the circuits, meaning that each resonance was for each separate circuit. Matching the circuits through adding capacitance, adjusting secondary taps, adjusting slug positions, and adjusting primary taps removed the separate resonance until only one remained. For comparison purposes an additional 15 pF of parallel capacitance was added to achieve the single resonant frequency of 851 kHz, which is close to the original circuitry. Mass spectra were taken under these conditions and results are reported in **Section 2.7.1**. Following the comparison experiments the input impedances were better matched by increasing the turn on the primary coils of rf_2 and rf_3, more parallel capacitance (40 pF) was added to further decrease the resonant frequency, and the number of turns on the secondary coil of rf_1 was decreased. The final resonant frequency of the system was 759 kHz (**Figure 2.16d**). The final tap positions, capacitances, and slug positions are summarized in **Table 2.2.**

Final Tuning Summary			
	rf_1	rf_2	rf_3
Total Parallel Capacitance (pF)	175	182	183
Slug Position (From top)	0.91”	2.99”	2.96”
Secondary Tap (# of turns from top)	8	18	18
Primary Tap (# of turns from bottom)	4	5	5

Table 2.2 - Summary of final tuning parameters for each of the three rf coils.

The Q of the original rf circuitry is < 15 (at 910 kHz) where as the Q of the untuned new rf circuitry is ~ 50 (at 1050 kHz). The final tune at 760 kHz has a Q of almost 60. New rf circuitry can be tuned over a wide frequency range and the quality factor or Q of the circuit is much higher, which should lead to a much greater voltage.

2.6 Maximizing Output Voltage

2.6.1 Calibrating rf Pick-ups

The rf pick-ups are used to get a low voltage reading proportional to the actual rf voltage. Great care must be taken with the pick-ups so as to not bump or move them in anyway, otherwise or the calibration is prone to change. Because the rf pick-ups are not mechanically stable the rf pick-ups were calibrated whenever Box 4 was opened or disturbed. The calibrations for the three pick-up circuits are V_{rf} =173.0x, 156.1x, and 170.1x for rf_1, rf_2 and rf_3 respectively (x is the zero-to-peak pick-up voltage.) Using this calibration the maximum peak-to-peak output of the rf coils at 850 kHz was ~2000 V_{pp}, which is approximately the maximum output of the old rf circuit. The reason why the new circuitry did not produce a greater voltage than the old circuitry is because the Q of the new circuitry was only 35 when operated at 850 kHz. The new system was not optimized at 850 kHz because the goal was to get the system running at a lower frequency. It is quite possible that a Q of 50 is obtainable at 850 kHz with enough tuning, which will result in the new circuitry generating a larger amplitude voltage than the older circuitry. It is not as clear with a Q of 10, how the old circuitry was capable of generating ~2000 V_{pp}; however, if the circuitry is treated using the classical turn ratio (300 to 10) the output of the old circuitry should be about

2500 V_{pp}. One explanation for the lack of amplification is that as the Q approaches extremely low values, the traditional theory for transformers determines the output voltage.[33]

2.6.2 Limiting Factors

Several factors could be limiting the maximum amplitude of the rf voltage. An obvious explanation is that the Q values of the coils are not very high, resulting in resistive and capacitive losses in the system. Perhaps the largest capacitive loss is due to the close proximity of the enclosure to the rf wire. The rf wire has to travel through a long distance through two boxes following the end of the secondary coil and the more wire there is the more resistance. Power limitations may also hinder the maximum output voltage. Adding capacitance to decrease the resonant frequency increases the load of the system and thus more power may be necessary to achieve greater amplitude. Another possible explanation is that power is being lost due to impedance mismatch between the input impedance of the coil and the output of the rf amplifier.

2.6.2.1 More Power

Unfortunately, redesigning the coil box system to reduce power losses does not seem to a practical solution. A 100 W Amplifier Research (Bothell, WA) power amplifier was borrowed from the UNC Chemistry Department Electronics Design Facility. The center coil was driven with the 100 W amplifier while the left and right compensating ring electrodes were driven with the 50 W power amplifiers. The result of driving the circuits with unmatched components resulted in a slight 12° phase shift in rf_2 and rf_3 relative to rf_1. With the four fold increase in power (including effects of 3dB attenuators) the maximum voltage of the center coil reached 4 $kV_{0\text{-}p}$; above this voltage arcing was occurring in the enclosures.

Because more power seems to be helping generate more voltage, development of a custom power amplifier was undertaken.

2.6.2.2 Impedance Matching of a Simple LC Circuit

Using the vector voltmeter into a simple series LC of the conventional 3-D ion trap rf circuitry, the impedance and phase as a function of the rf frequency was measured, **Figure 2.17**. This un-tuned circuit has an impedance of nearly 400 Ω at the resonant frequency. Several capacitors were tried in series with the circuit to match the input impedance and the optimal capacitance was found to be 1325 pF. The impedance with each capacitor was monitored at the resonant frequency, plotted in **Figure 2.18**. With the circuit properly matched an additional 1000 V_{pp} was obtained from the rf system, which was already capable of generating 12,000 V_{pp}. The vector voltmeter greatly simplifies matching impedance.

2.6.2.3 Impedance Matching in Practice

Poor impedance matching can result in more than 90% of the power being lost. But as previously shown in a simple case proper matching can result in an improvement to the overall output of the circuit. The input impedance of the primary coil must be determined before it can be matched. Various resistors were put in series with the primary coil and the voltage drop across the resistors suggested that the input impedance of the coil was ~5 Ω. **Figure 2.19** illustrates how the voltage across a 4.6 Ω resistor changes as a function of frequency. At the resonant frequency (858 kHz) the voltage before the resistor is almost two times the voltage after the resistor. Three "9:1" balun circuits were designed to transform the impedance of the coil from 5 to 45 Ω. The results of the tune with and without the balun are illustrated in **Figure 2.20** The "9:1" balun results in a decrease in the Q value, almost

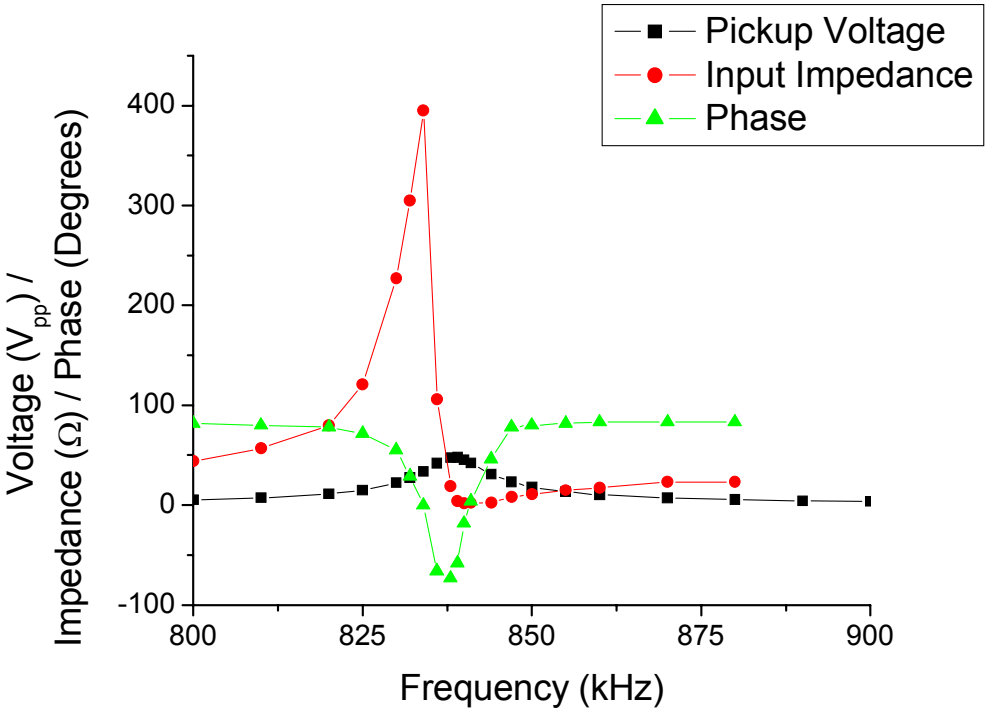

Figure 2.17 – Impedance measurements of series LC circuit. Resonant frequency is 838 kHz.

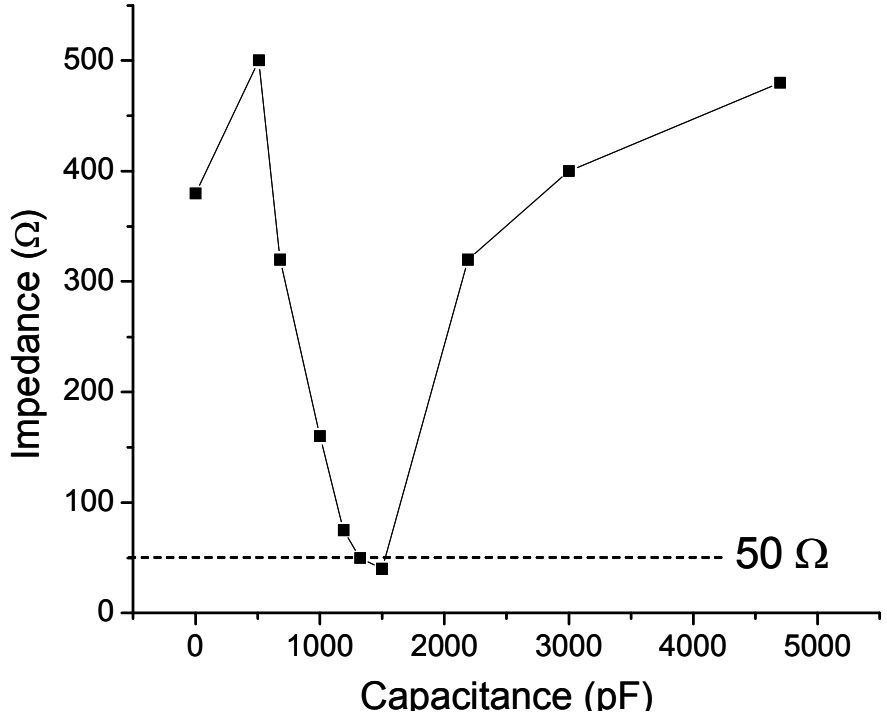

Figure 2.18 – Capacitance tuning to match input impedance to 50 Ω.

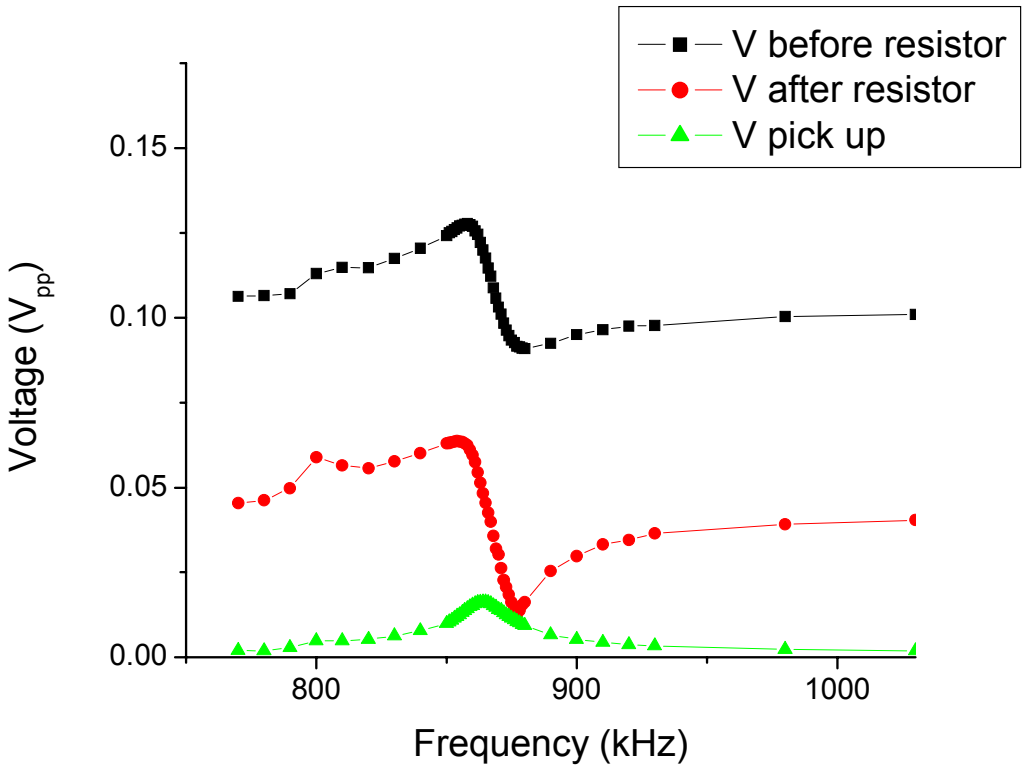

Figure 2.19 - Voltage across a 4.6 Ω resistor in series with rf_1 to determine input impedance.

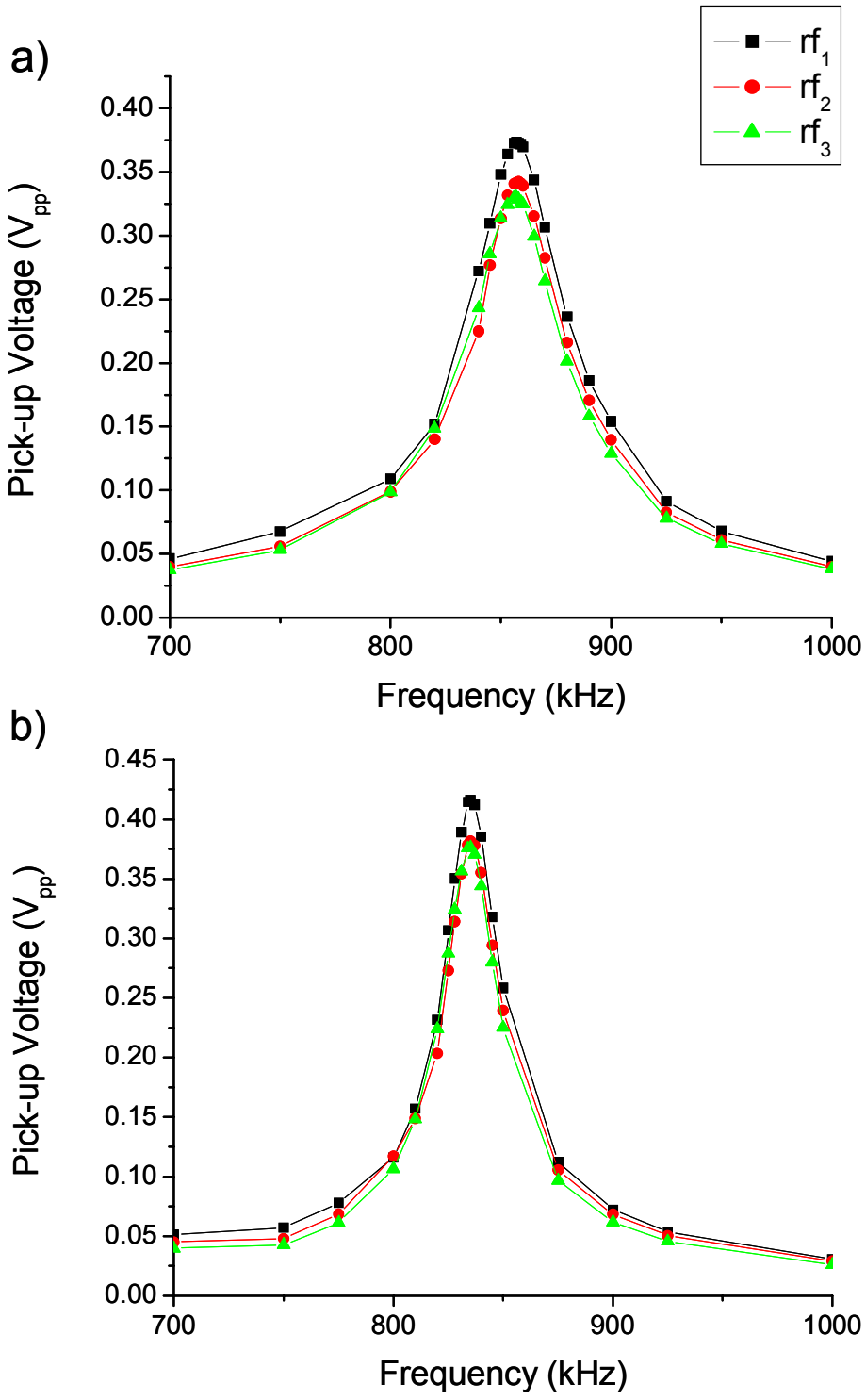

Figure 2.20 – Effect of balun impedance matching circuit on rf tune a) With balun b) Without balun.

10 kHz shift in the resonant frequency, and a decrease in the max amplitude. Both of these effects are non ideal responses of the balun, which should not occur. Some of the poor response is possibly the cause of non ideal circuit construction. Another explanation for the observed response is that the determination of the input impedance was incorrect thus the factor of 9 impedance transformation negatively impacts the operation. Three "4:1" baluns were also constructed, with slightly different results. The baluns did not affect the Q value of the circuits and no frequency shift was observed. The amplitude was noted to increase 20% with the use of the "4:1" balun. These results suggest that impedance is greater than 5 Ω, possibly closer to 12 Ω. Because of these conflicting results an alternative method needed to be explored to determine the input impedance of the coils. Since the desired impedance is a 50 Ω load, the simplest method was to compare the voltage output of the power amplifier when driving a pure 50 Ω load versus driving a coil. The voltage across a 100 W 50 Ω dummy load was monitored over the full amplitude range. The experiment was subsequently repeated with the coil operated at 761 kHz. Results are illustrated in **Figure 2.21**. Note that the voltage across the coil is almost 75% of the voltage across the 50 Ω dummy load. When this system was characterized with only one coil being driven there are two resonant frequencies, one at 712 kHz and another at 761 kHz (the other two coils were hooked up to their power amplifiers, but not driven). When the experiment was repeated at 712 kHz, still with only one coil being driven, the voltages between the 50 Ω load and the coil are within 5%. In fact both the "4:1" balun and the initial resistance measurements were performed with only 1 coil being driven. Two important results can be taken from these experiments. First, all three of the coils must be operated otherwise the performance is drastically changed,

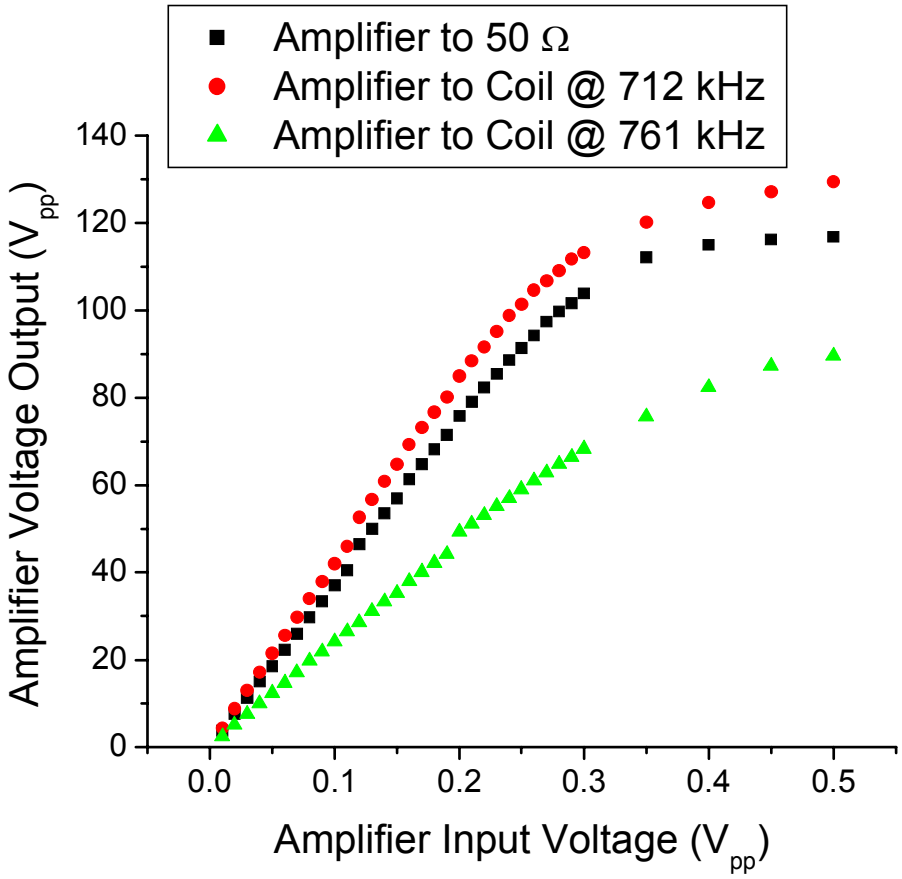

Figure 2.21 – Comparison of power amplifier output voltage while operating a 50 Ω dummy load and rf_1 coil.

a result that may have further implications in the overall desired experiments of HOF. Secondly, when driven on resonance the coil impedance is close to 50 Ω.

2.7 Mass spectrometry Results

An EI mass spectrum of n-butylbenzene taken with the new rf system operated at 761 kHz (resonance ejection 200 kHz 3 V_{pp}) is shown in **Figure 2.22**. No molecular ion was observed and the resolving power obtained was approximately 300. When the new rf system was operated under the same conditions as the old rf system (mass spectrum illustrated in **Figure 2.4a**), was obtained with a resolving power of approximately 100 (data not shown).

With a fully functioning rf system initial HOF experiments were undertaken. Octapole fields were introduced by symmetrically altering the "requested" amplitude of the compensated ring electrodes. The octapole fields were only introduced while injecting ions into the ion trap. Following the injection portion of the experiment the rf voltages were raised or decreased to equal the center ring electrode voltage. The percent of octapole field becomes more positive as the ratio of the voltage on the compensating ring electrodes to the voltage on the center ring electrode increases. Utilizing the electrostatic calculation previously performed the relative octapole to quadrupole field percentages for the voltage ratios used are summarized in **Table 2.3**.

Ratio	Octapole %
0.56	-1.77
0.78	-0.65
1.00	0.46
1.22	1.58
1.89	4.92
2.78	9.38
3.33	12.17

Table 2.3- Percent Octapole field resulting from ratio of compensating ring voltage to center ring voltage.

The intensity of all ions from the EI mass spectrum of n-butylbenzene were monitored and summed at each percent octapole field experiment. The summed intensities were then normalized to data from the lowest percent octapole field introduced. The results of these experiments are illustrated in **Figure 2.23**. As the octapole percentage is increased it appears as though more ions are being trapped. The differences in the restoring force, as described in **Section 1.4,** between octapole field and quadrupole fields helps to explain this result. Because of the larger region over which there is minimal restoring force in the presence of octapole fields more ions may be trapped. Outside of this region the restoring force increases much faster than in a quadrupole field, which has a linear restoring force as a function of axial distance. As individual mass spectra were more closely examined it became clear that all of the ions were not increasing in abundance together with increasing octapole fields. At smaller and more negative percent octapole fields lower mass-to-charge ions, such as *m/z* 39, are greater in abundance than higher mass-to-charge ratio ions such as *m/z* 91 and *m/z* 92 and at greater percent octapole fields the higher mass-to-charge ratio ions are more abundant than the lower mass-to-charge ratio ions. This "mass" bias has been well characterized in conventional ion traps and results from a range of ions with the ideal momentum penetrating the rf potential barrier more efficiently than other ions. Increasing the rf potential allows higher mass-to-charge ratio ions to be more efficiently trapped. A mass bias may account for the results; however, if the octapole field is in fact being increased all ions should increase in abundance. In an attempt to decouple the mass bias from the increased octapole fields the experiments were repeated with the voltage equal on all three ring electrodes. The data is plotted in **Figure 2.23** along with the octapole data. Each data point matches up with the voltage on the compensating ring electrodes. The data points that

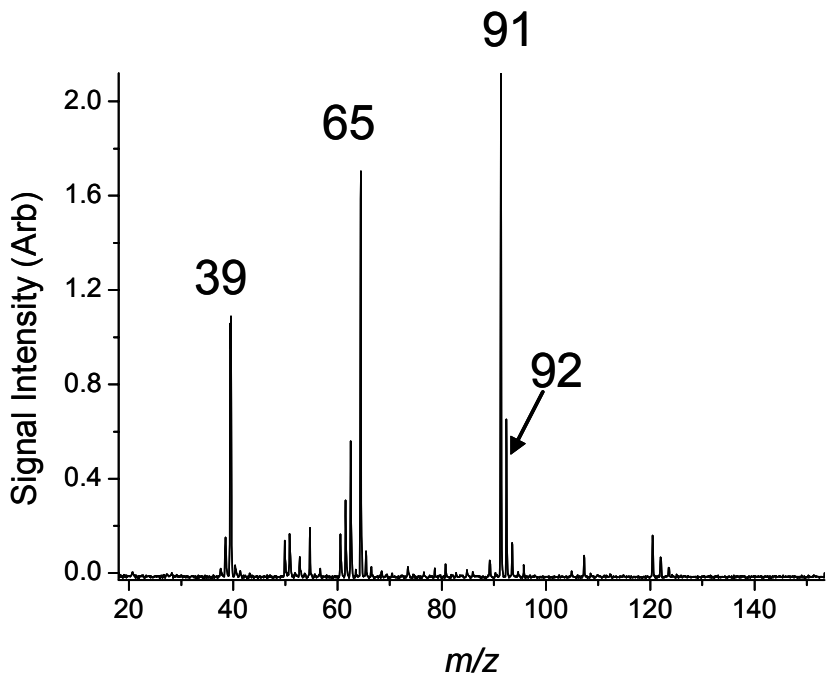

Figure 2.22 – EI mass spectrum of n-butylbenzene (*m/z* = 134) acquired with new rf system.

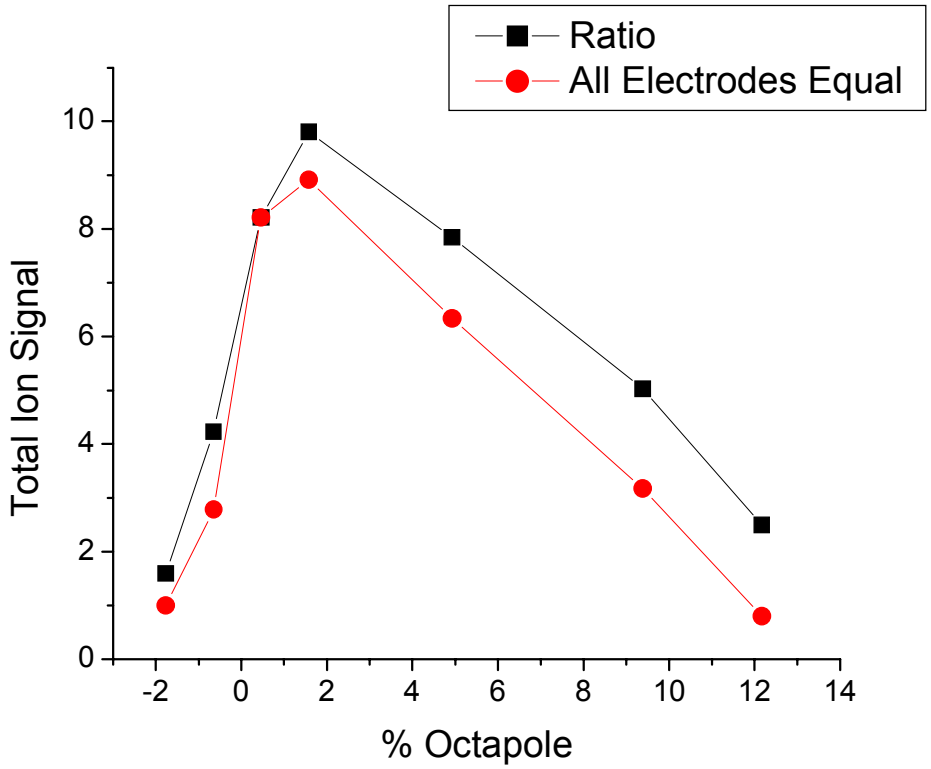

Figure 2.23 – Improvements in total ion signal with increased "% octapole". Plotted along is all voltages equal to what the compensating voltages are equal to in the ratio data point.

match up are when the voltage on all three electrodes was equal in both experiments. The mass spectra acquiring during the octapole experiments have higher signal intensities than the mass spectra with all voltages equal; thus implying that there is an improvement due to octapole fields.

2.8 Amplitude Control

2.8.1 Resonant Amplitude Control

To gain a better understanding of the accuracy of the amplitude control and to verify the voltage ratios during the octapole experiments pick-up voltages were monitored at static rf potentials. Results are summarized in **Table 2.4**. When requesting equal voltages on all three electrodes equal voltages were obtained. When the center ring electrode was not driven and equal voltages were requested on the compensating ring electrodes all voltages on the electrodes were equal again. If the center ring electrode was not driven and the two compensating ring electrodes were driven out of phase, minimal voltage was observed on the center ring electrode.

Requested Voltages‡	rf_1*	rf_2*	rf_3*
550:550:550 @ 759kHz	570	562	573
0:550:550 @ 759kHz	410	400	410
0:-550:550 @ 759kHz	30	300	320
275:810:810 @ 759kHz	502	495	508
275:0:0 @ 439kHz	10	0.8	0.8
275:187:0 @ 439kHz	11	5.5	0.8
275:187:98 @ 439kHz	11	5.5	1.8

Table 2.4 – Requested voltage on rf_1:rf_2:rf_3. ‡Requested voltages are only accurate for 759 kHz.* The measured rf voltages (V_{p-p}) are calculated from the measured pick-up voltage using the calibrations listed in **Section 2.6.1** and are all $\pm$ 5%.

This conclusively shows that the electrodes are coupled and that the improved results in the presence of "octapole" fields are likely not due to higher order field, because the voltages on

the electrodes are equal. Improved performance is because the voltages on the electrodes are approaching a voltage that is more efficient for trapping. The center electrode "feels" and affects both compensating ring electrodes, such that when the voltage of the center ring is set greater than the compensating ring electrodes the observed voltage of the compensating ring electrodes become greater than their set voltage and the center ring is slightly decreased. Oppositely when the requested voltage of the compensating ring electrodes is greater than the center ring the observed voltage on the center ring is higher than the set voltage and the compensating ring voltages are each lower than the requested voltage. Because the voltage on the center ring was chosen to be 450 V the effect in both cases was a shift in voltage that was more effective at trapping ions.

While tuning the input impedance, it was found that the coils operated significantly different when no voltage was applied to them. To ensure that the observations were not solely a result of no voltage being applied to the coils, voltages were applied with ratio of 3:1 (compensating: center ring electrodes). The voltages on all three electrodes were still equal. As described in the impedance matching section, the rf tune is altered when the coils are not driven equally. **Figure 2.24a** is the tune when all rf circuits are driven at the maximum amplitude. Differences between the rf voltages are due to differences in the capacitive pick-up tunes, which are slightly different than the calibration previously reported. When the voltage on the center ring electrode is dropped to 20% of the voltage on the compensating ring electrodes the rf tune drastically changes. The rf tune with these voltage settings, illustrated in **Figure 2.24b**, has two resonant points. The rf tune is changing because of the voltage on each of the three secondary coils is equal due to capacitive coupling; however, the

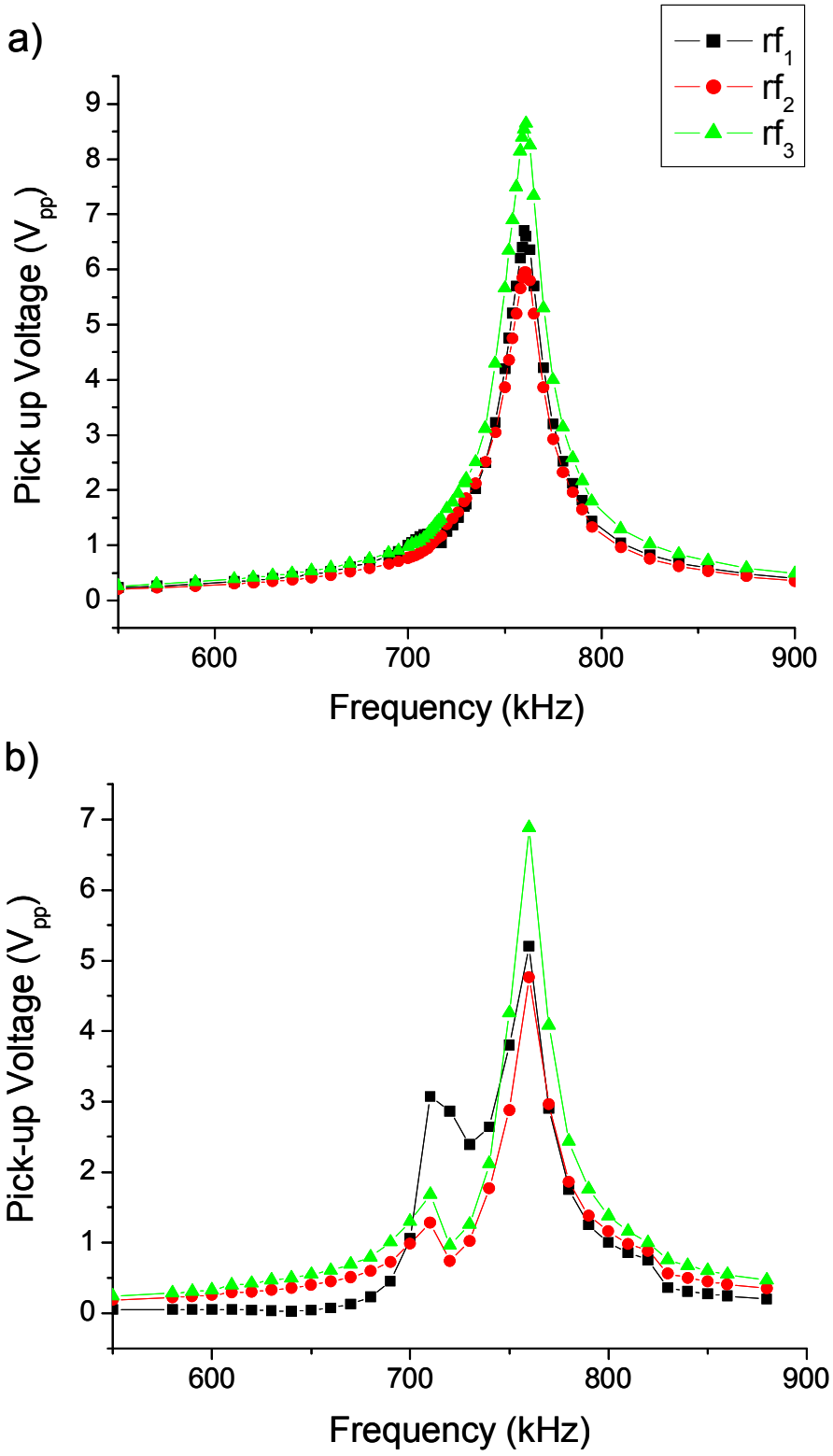

Figure 2.24 – Effect on rf tune when a) All 3 electrodes driven at full potential b) Rf_1 driven at 1/5 voltage of rf_2 and rf_3.

voltage on the primary coils is different thus causing mismatches in the circuitry and the tune. Because of the capacitive coupling other methods need to be explored.

2.8.2 Off Resonant Amplitude Control

Using **Equation 2.13**, the inter-electrode capacitance listed in **Table 2.1** results in impedances of about 14 kΩ. The theoretical output impedance of a parallel LC circuit is infinite. If the output impedance transformer were on the order of 20 kΩ, which is what it would be if the system were treated like a balun with a 20:1 turn ratio, the system would behave like a set of series power supplies connected with resistors. An example circuit diagram of this is illustrated in **Figure 2.25,** where $T_{0\text{-}3}$ represents the transformers and each of the X_c values is for an electrode capacitance taken from **Table 2.1**. The output impedance of the transformer should drastically be reduced off resonance. When the frequency of the rf was changed to 439 kHz, the rf amplitude was able to be controlled as shown in **Table 2.4**. The amplitude of the rf voltages is significantly reduced and because the system is not tuned at 439 kHz there is significant reflected power. The maximum amplitude obtained was about 70 $V_{p\text{-}p}$. This is not enough voltage for mass analysis. In an attempt to get closer to the resonant frequency and take advantage of resonant amplification the frequency was increased to 630 kHz. Operating at this frequency the maximum achievable voltage was 166 $V_{p\text{-}p}$. Ions were able to be trapped at these potentials but not mass analyzed. More power is required to operate the system as a mass spectrometer at this frequency. Although it is not clear if the amplitude control will decline as voltages increase in amplitude.

Another concern when trying to control the amplitudes of resonance is how the phase of the rf voltages changes. The phase of rf_2 and rf_3, with respect to rf_1, was monitored as a function of frequency. As illustrated in **Figure 2.26**, from 640-750 rf_2 and rf_3 are going

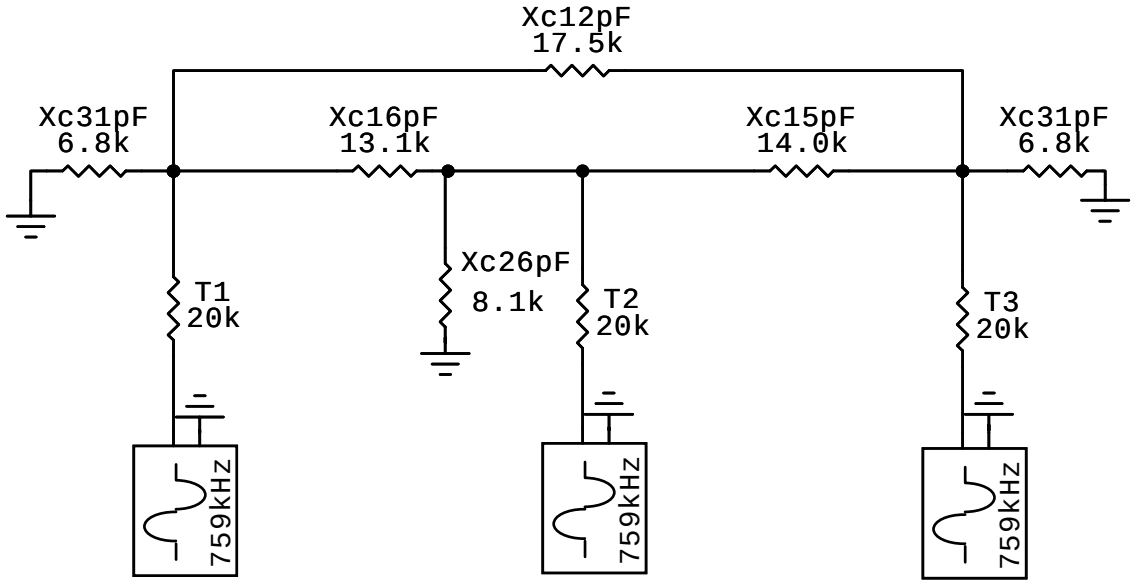

Figure 2.25 – Equivalent circuit showing output impedance of transformers and reactance of electrodes capacitances at 759 kHz.

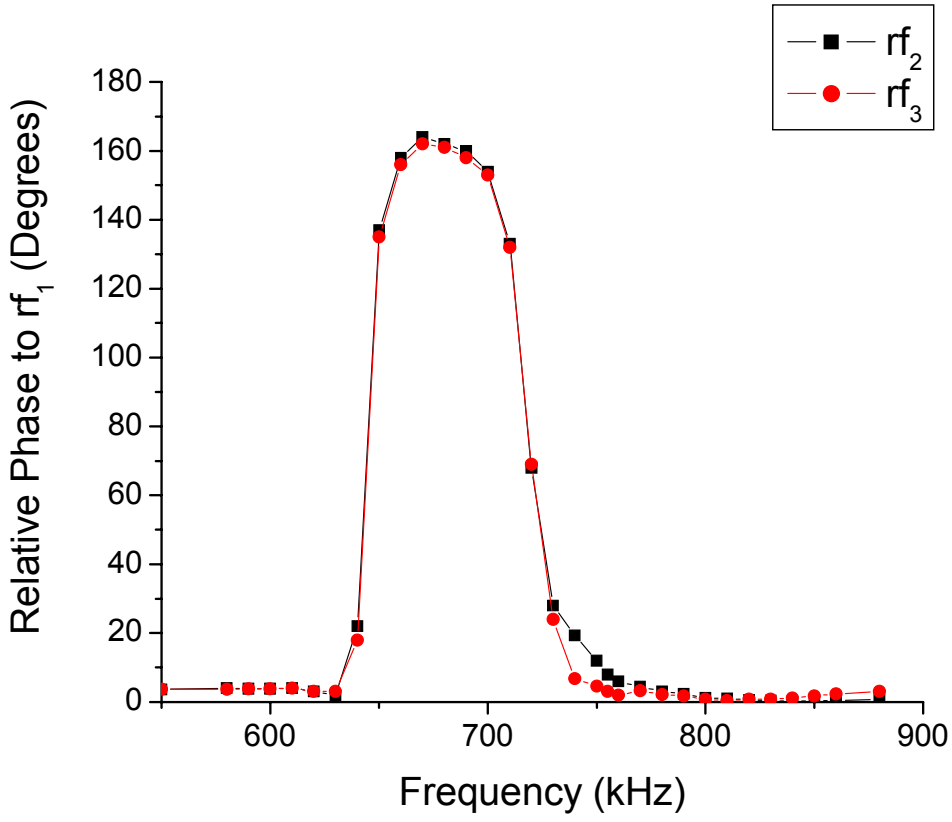

Figure 2.26 – Phase change in rf_2 and rf_3 as the operating frequency is altered.

through rapid phase transformations, therefore operating at the second resonant frequency observed at 712 kHz is not ideal because of the rapidly changing phase of rf_2 and rf_3. While attempting to operate the instrument at 712 kHz, it was noticed that if all 3 electrodes were increased during the analytical scan destructive interferences occurred and the amplitude of the rf voltage began to decrease. This was an effect of the phase differences between rf_2 and rf_3 relative to rf_1.

2.8.3 Shielding Electrodes

If the electrodes are communicating because they are coactively coupled, it seems that the logical solution is to try to decouple them. Inserting thin electrically grounded electrodes, which have the same diameter as the other electrodes, between the compensating and ring electrodes may electrically isolate the electrodes without significantly impacting the trapping fields. Electrodes were designed and constructed with a thickness of 0.020" and a diameter of 1.575". Schematics for these shielding electrodes can be found in **Appendix II**. Electrical connections for the electrodes were accomplished by spot welding a milled 316 stainless steel 1/8" outer diameter rod on the electrode. The end of the rod is threaded for a 4/40 screw. Ceramics, 2 mm thick, were placed in between the compensating ring electrode and the shielding electrode. The existing ceramics that were in between the compensating ring and the center ring were moved to isolate the shielding electrode from the center ring. Including the thickness of the shielding electrodes the trap was elongated axially by 5mm. The electrode stack with shielding electrodes is illustrated in **Figure 2.27**. Because the ledges that are milled into both the center ring electrode and the compensating ring electrodes are different depths the shielding electrodes were located 0.156 inches closer to the compensating ring electrodes. At the electrodes faces without the ledges the shielding

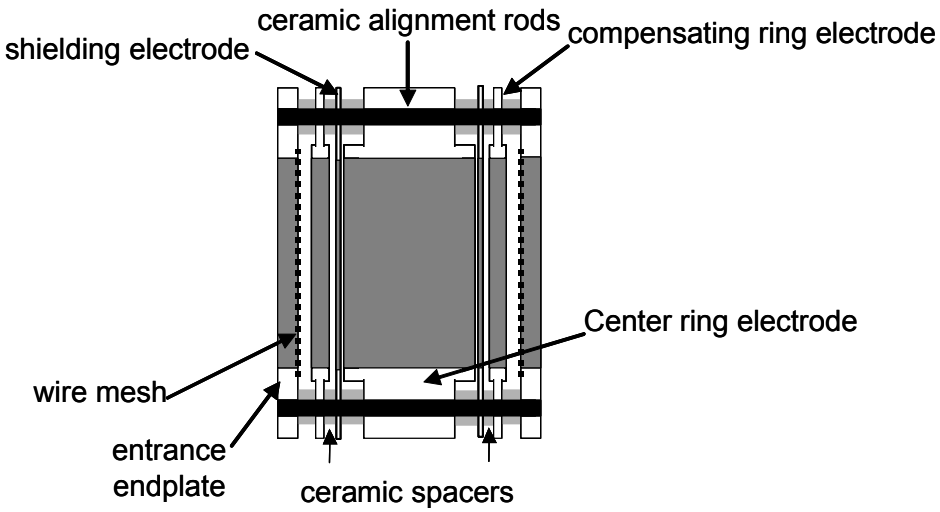

Figure 2.27 – Electrode stack of CCIT electrodes with added shielding electrodes between compensating ring and center ring electrodes.

electrode is located 0.039 inches closer to the compensating ring electrodes. Despite the asymmetry, the characterization of the rf voltage has only one resonant frequency at 736.5 kHz with virtually no change in the Q value of the circuit (66). The capacitances of the electrodes were measured and are summarized in Table 2.5.

Electrode Capacitance (pF)	
Center ring to ground	25.2
Left Compensating to ground	37.5
Right Compensating to ground	37.2
Center to Left Compensating	10.5
Center to Right Compensating	10.2
Left to Right	<5

Table 2.5: Capacitance of CCIT electrodes with shielding electrodes, all values are $\pm$ 3%.

The capacitance of the center ring did not change and the capacitances of both the compensating ring electrodes increased. Increased capacitance on the compensating ring electrodes is understandable because of the grounded shielding electrodes that were introduced and the proximity of these electrodes. The inter electrode capacitance has decreased which should effectively decrease the capacitive coupling. To test if the capacitive coupling has been reduced the center ring electrode (rf_1) was requested to be at a constant amplitude rf voltage with a constant dc control voltage (2 V) and the compensating ring electrodes (rf_2 and rf_3) dc control voltages were varied from 0-10 V. This experiment was repeated on the instrument with and without the shielding electrodes. Results are depicted in **Figure 2.28**. As rf_2 and rf_3 are varied on the instrument without the shielding electrodes, all three rf voltages increase together. The rf_1 voltage is actually a little greater than rf_2 and rf_3, which is probably due the center ring electrode picking up voltage from the two compensating ring electrodes. Results from the same experiment repeated with the shielding electrodes, **Figure 2.28b**, shows an improvement or a decrease in the capacitive coupling. All three rf voltages still increase; however, rf_2 and rf_3 increase with a greater slope than rf_1.

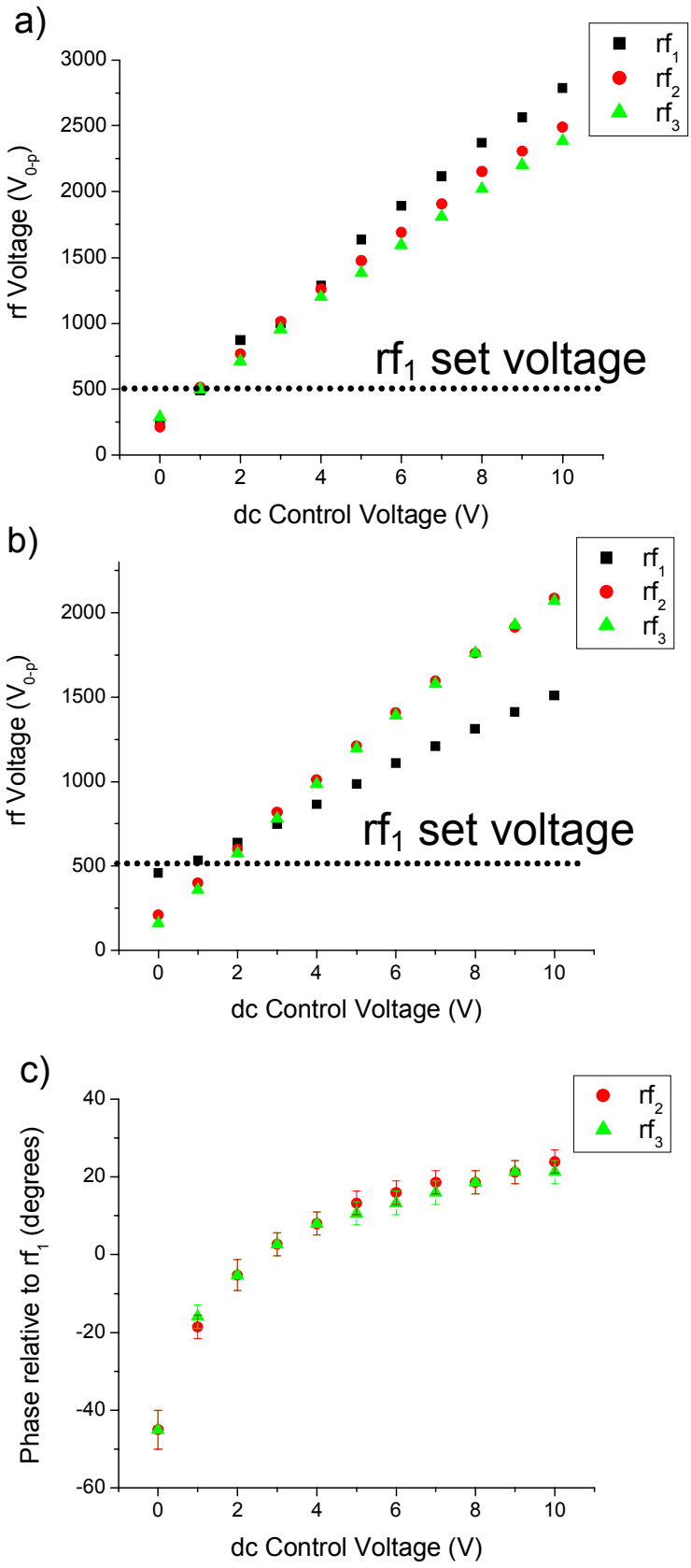

Figure 2.28 Measured rf voltage on electrodes as center ring (rf_1) is held constant and the dc control of the compensating ring electrodes (rf_2 and rf_3) is varied from 1-10V. a) Without shielding electrodes, b) With shielding electrodes and c) Phase of voltages with shielding electrodes.

The shielding electrodes offer a significant improvement to the control of the amplitude of the rf voltages because rf_2 and rf_3 are greater when they are set greater than rf_1 and they are smaller than rf_1 when the voltages are set smaller. A side effect of the shielding electrodes is that the relative phase of rf_2 and rf_3 to rf_1 changes as the voltage ratio is increased. As shown in **Figure 2.28c,** the effect is not linear and seems to begin to level off at higher amplitudes. This phase effect was verified on the rf wires at low voltage with oscilloscope probes. Because the phase of rf_2 and rf_3 are equal as the voltages are symmetrically increased, the imposed higher order fields due to the phase change would also be a symmetrical or even order field. When the voltages of rf_2 and rf_3 are not equal and differ from rf_1 the phase of all three rf voltages is different. Other than the asymmetry of the phases, no clear trend was observed during similar experiments when the voltage of rf_2 and rf_3 were varied with different amplitudes relative to rf_1. The true reason for the phase of the rf voltages changing with amplitude is not yet understood.

The reciprocal experiment, to the one described above, was performed by varying the rf voltage on the center ring electrode and keeping the rf voltage on the compensating ring electrodes constant. According to **Table 2.3**, operating the CCIT in this fashion introduces negative (< 0) percentage of octapole fields. As shown in **Figure 2.29a**, without the shielding electrodes the rf voltage on all three electrodes increase together at the same amplitude similar to what is depicted in **Figure 2.28a**. When rf_1 was increased with rf_2 and rf_3 held constant with the shielding electrodes, **Figure 2.29b**, rf_2 and rf_3 had a smaller slope as rf_1 was increased than rf_1 did when rf_2 and rf_3 were increased in the experiment described previously by **Figure 2.28b**. The observed phase difference of rf_2 and rf_3 relative to rf_1 shown in **Figure 2.29c** is the reciprocal of **Figure 2.28c**. This result is expected because the

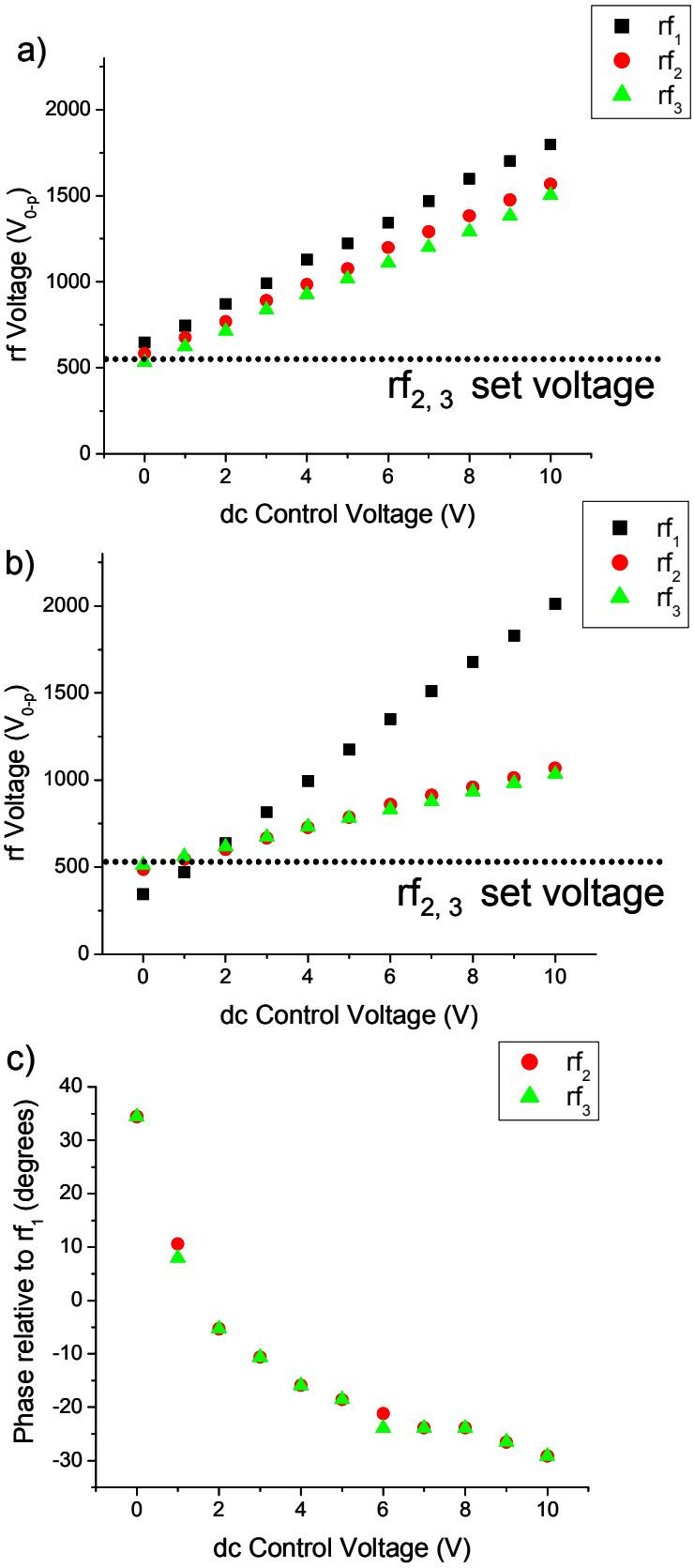

Figure 2.29 – Measured rf voltage on electrodes as compensating ring electrodes (rf_2 and rf_3) are held constant and the center ring (rf_1) dc control of the is varied from 1-10 V. a) Without shielding electrodes, b) With shielding electrodes and c) Phase of voltages with shielding electrodes.

phase is measured relative to rf_1 and now rf_1 is greater than rf_2 and rf_3, whereas in the previous experiments the opposite was true. The differences in the observations between the two experiments is thought to be due to the fact that when rf_1 is held constant both compensating ring electrode voltages can contribute to the pick-up on the center ring electrode. In the reciprocal experiment when rf_2 and rf_3 are held constant each of them pick up an equal amount of voltage and the pick-up can thought to be divided between the two electrodes, hence the smaller overall pick-up voltage. The improved amplitude control may even be further enhanced with the introduction of a feed back loop to actively control the voltages; e.g. to keep rf_1 constant by lowering the dc control as rf_2 and rf_3 are increased.

EI mass spectra of n-butylbenzene were taken with the shielding electrodes in place, and a representative mass spectrum is shown in **Figure 2.30**. Mass spectra were acquired and the TIC of the ion signal was monitored while varying rf_2 and rf_3 and keeping rf_1 constant during ion injection. This experiment with the shielding electrodes produced the same results as the experimental observations as without the shielding electrodes described in **Section 2.7**. As shown in **Figure 2.31a**, the maximum TIC is not the same as when all of the voltages are equal; however, there is now a broader range of voltage over which the ion signal is improved. The "all voltages equal" data that is plotted along with this data is from mass spectra where the voltages on all the center ring and compensating ring electrodes are equal to the voltage on compensating ring electrodes that was used at each corresponding ratio data point. Comparing this data shows how the mass bias that occurs in trapping ions in a 3-D ion trap impacts the data. In this case, now that the voltage on the compensating ring electrodes is better controlled the mass bias is not observed in the data. In the reciprocal experiment where rf_1 is varied and rf_2 and rf_3 are held constant the mass bias is more

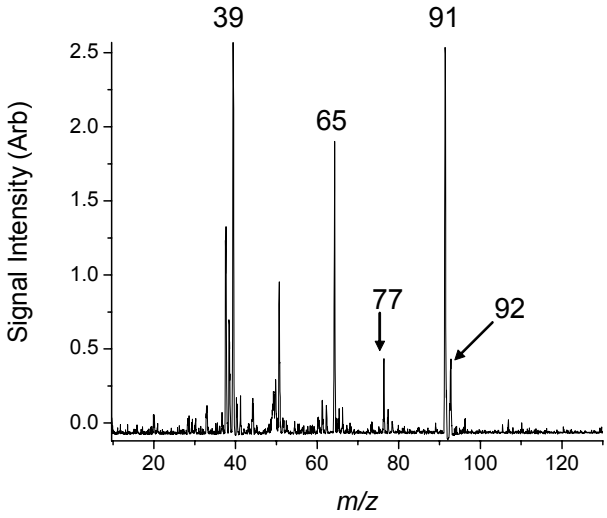

Figure 2.30 – EI mass spectrum of n-butylbenzene acquired with CCIT including shielding electrodes.

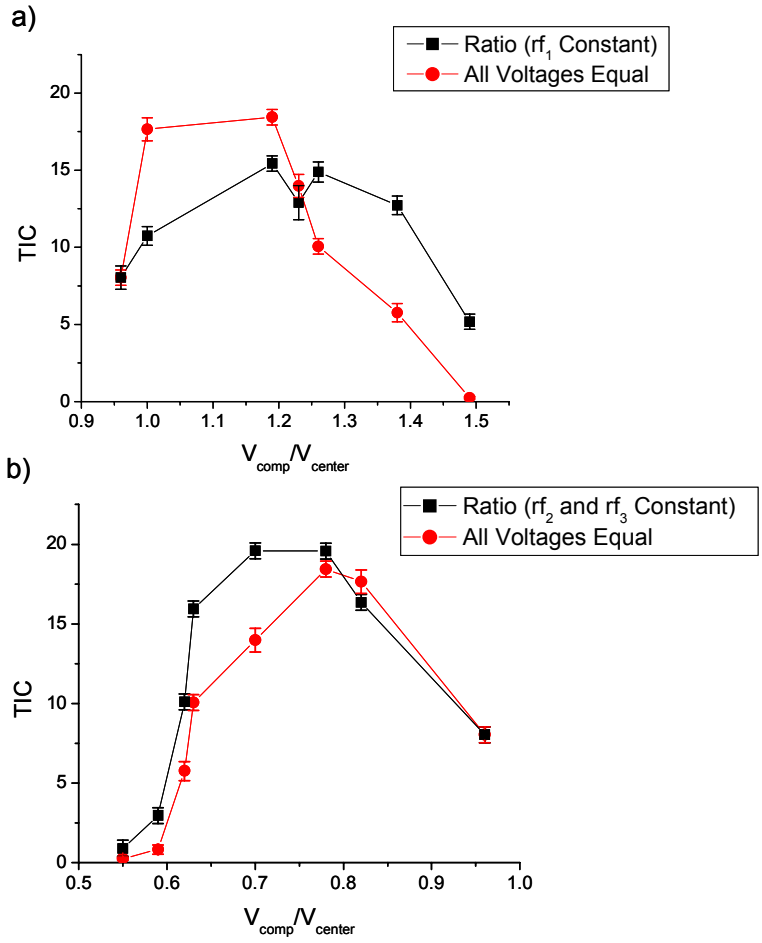

Figure 2.31 – Improvements in ion signal with a) varying voltage of rf_2 and rf_3 while keeping rf_1 constant and b) varying voltage of rf_1 while keeping rf_2 and rf_3 constant. Points with all voltage equal plotted along with data.

prevalent, as can be seen in **Figure 2.31b**. As in the previous experimental results, more ions are detected over a broader range compared to the signal when all of the voltages are equal. The differences in the data may be due to the relative sizes of the electrodes. More specifically the voltage on the center ring electrode has a large role in ion injection because the electric field from that electrode has more of an impact on the overall electric field. It is difficult to quantify the amount of higher order fields in these experiments because of the axial stretch of 5 mm introduced by the ceramics for the shielding electrodes and the phase change of the rf voltages with different amplitudes. Both of these factors will change the field geometry enough that electrostatic modeling must be undertaken to calculate the HOF content with different amplitudes and phase contributions.

2.9 Conclusions

The compensated cylindrical ion trap has now been shown to be a mass spectrometer capable of producing mass spectra with a resolving power of 110. Experimental flaws found in the first generation rf circuitry led to the development of a new resonant rf system consisting of three resonant LC circuits. The new rf system was optimized to have one resonant frequency, which was tunable between 730 – 1050 kHz. Impedance matching circuits were found to be ineffective with the rf circuits as the input impedance was found to be around 50 Ω; however, impedance matching using series capacitors and a vector voltmeter was found to be quite effective on a different rf system for a conventional 3-D ion trap. The new rf system generated voltages of 100 – 2500 $V_{0\text{-}p}$ depending on the operating frequency and the power amplifier used. Experiments attempted to introduce octapole HOFs during ion injection were not successful using the existing CCIT electrodes, because the amplitudes of the three rf voltages were not able to be varied independently as the circuits were found to be

capacitively coupled. Efforts such as off resonant operation and using secondary minor resonant frequencies were found to be ineffective at amplitude control. Inserting shielding electrodes between the compensating and center ring electrodes was found to be effective at improving the ability to independently control the amplitude. Amplitude control was shown to be successful and mass spectra acquired suggest that there were improvements when the voltages on the compensating ring electrodes were varied relative to the voltage on the ring electrode and vice versa. A drawback of the amplitude control was observed in that the phase of the rf voltages of the compensating ring electrodes relative to the phase of the center ring electrode varied as the ratio of the compensating ring voltages to the center ring voltage was increased or decreased. Because of the introduced phase shift and an axial stretch of the ion trap resulting from the ceramics needed when introducing the shielding electrodes, experiments introducing HOF are difficult to interpret because the amount of HOF is not known. Electrostatic modeling of the rf voltages with the elongated electrode geometry and the phase changes will need to be under-taken to gain a new understanding of what voltage ratios are required to introduce different HOF content. The fact that amplitude control is possible with the shielding electrodes does however make electro-dynamically introducing HOF to study the effect of HOF content in ion traps a possibility in the future.

2.10 References

1. Danell, R. M., *Advances In Ion Source And Quadrupole Ion Trap Design And Performance.* Ph.D. Thesis, University of North Carolina, 2001.

2. Ray, K. L. *New Approaches to Tandem Mass Spectrometry on a Quadrupole Ion Trap* Ph.D. Thesis, The University of North Carolina, Chapel Hill, 2000.

3. Syka, J. E. P., *Commercialization of the Quadrupole Ion Trap*, in *Practical Aspects of Ion Trap Mass Spectrometry*; March, R. E., Todd, J. F. J., Eds.; CRC Press: Boca Raton, FL, 1995; Vol. I, pp 169-205.

4. Stafford, G. C. J.; Kelley, P. E.; Syka, J. E. P.; Reynolds, W. E.; Todd, J. F. J., *Recent Improvements in and Analytical Applications of Advanced Ion Trap Technology.* International Journal of Mass Spectrometry and Ion Processes, 1984. 60: p. 85-98.

5. Morand, K. L.; Lammert, S. A.; Cooks, R. G., *Concerning 'Black Holes' in Ion-trap Mass Spectrometry.* Rapid Communications in Mass Spectrometry, 1991. 5: p. 491.

6. Guidugli, F.; Traldi, P.; Franklin, A. M.; Langford, M. L.; Murrell, J.; Todd, J. F. J., *Further Thoughts on the Occurrence of 'Black Holes' in Ion-trap Mass Spectrometry.* Rapid Communications in Mass Spectrometry, 1992. 6: p. 229-231.

7. Johnson, J. V.; Pedder, R. E.; Yost, R. A., *The Stretched Quadrupole Ion Trap: Implications for the Mathieu au and qu Parameters and Experimental Mapping of the Stability Diagram.* Rapid Communications in Mass Spectrometry, 1992. 6: p. 760-764.

8. Eades, D. M.; Johnson, J. V.; Yost, R. A., *Nonlinear Resonance Effects During Ion Storage in a Quadrupole Ion Trap.* Journal of the American Society for Mass Spectrometry, 1993. 4: p. 919-929.

9. Wells, J. M.; Plass, W. R.; Patterson, G. E.; Ouyang, Z.; Badman, E. R.; Cooks, R. G., *Chemical Mass Shifts in Ion Trap Mass Spectrometry: Experiments and Simulations.* Analytical Chemistry, 1999. 71(16): p. 3405-3415.

10. Wells, J. M.; Plass, W. R.; Cooks, R. G., *Control of Chemical Mass Shifts in the Quadrupole Ion Trap Through Selection of Resonance Ejection Working Point and rf Scan Direction.* Analytical Chemistry, 2000. 72: p. 2677-2683.

11. Franzen, J.; Gabling, R.-H.; Schubert, M.; Wang, Y., *Nonlinear Ion Traps*, in *Practical Aspects of Ion Trap Mass Spectrometry. Volume I. Fundamentals of Ion Trap Mass Spectrometry*; March, R. E., Todd, J. F. J., Eds.; CRC Press: Boca Raton, 1995; Vol. I, pp 49-167.

12. McClellan, J. E.; Murphy, J. P.; Mulholland, J. J.; Yost, R. A., *Effects of Fragile Ions on Mass Resolution and on Isolation for Tandem Mass Spectrometry in the Quadrupole Ion Trap Mass Spectrometer.* Analytical Chemistry, 2002. 74: p. 401-412.

13. Ding, L.; Sudakov, M.; Brancia, F. L.; Giles, R.; Kumashiro, S. *Digital Ion Trap Mass Spectrometer developed for MSn Application*. in *Proceedings of the 52nd ASMS Conference on Mass Spectrometry and Allied Topics,*. 2004. Nashville, TN.

14. Doroshenko, V. M.; Cotter, R. J., *Injection of Externally Generated Ions into an Increasing Trapping Field of a Quadrupole Ion Trap Mass Spectrometer.* Journal of Mass Spectrometry, 1997. 31: p. 602-615.

15. Quarmby, S. T.; Yost, R. A., *Fundamental Studies of Ion Injection and trapping of Electrosprayed Ions on a Quadrupole Ion Trap.* International Journal of Mass Spectrometry, 1999. 190/191: p. 81-102.

16. Franzen, J., *The Non-Linear Ion Trap. Part 4. Mass Selective Instability Scan with Multipole Superposition.* International Journal of Mass Spectrometry and Ion Processes, 1993. 125: p. 165-170.

17. Gill, L. A.; Amy, J. W.; Vaughn, W. E.; Cooks, R. G., *In Situ Optimization of the Electrode Geometry of the Quadrupole Ion Trap.* International Journal of Mass Spectrometry and Ion Processes, 1999. 188: p. 87-93.

18. Wang, Y.; Franzen, J., *The Non-Linear Ion Trap. Part 3. Multipole Components in Three Types of Practical Ion Trap.* International Journal of Mass Spectrometry and Ion Processes, 1994. 132: p. 155-172.

19. Baluya, D. L.; Hilton, C. K.; Shortt, B. J.; Darrach, M. R.; Chutjian, A.; Yost, R. A. *Strategies to reduce the effects of field imperfections in quadrupole ion traps*. in *The Proceedings of the 53rd ASMS Conference on Mass Spectrometry and Allied Topics*. 2005. San Antonio, TX.

20. Franzen, J., *Simulation Study of an Ion Cage with Superimposed Multipole Fields.* International Journal of Mass Spectrometry and Ion Processes, 1991. 106: p. 63-78.

21. Franzen, J.; Wang, Y. Quadrupole Iontrap with switchable mutlipole fractions. US Patent Re. 36906, 2000.

22. Wilcox, B.; Hendrickson, C. L.; Marshall, A. G., *Improved Ion Extraction from a linear Octopole Ion Trap: SIMION analysis and Experimental Demonstration.* Journal of the American Society for Mass Spectrometry, 2002. 13(11): p. 1304-1312.

23. Bonner, R. F.; Fulford, J. E.; March, R. E.; Hamilton, G. F., *The Cylindrical Ion Trap. Part I. General Introduction.* International Journal of Mass Spectrometry and Ion Physics, 1977. 24: p. 255-269.

24. Kornienko, O.; Reilly, P. T. A.; Whitten, W. B.; Ramsey, J. M., *Micro Ion Trap Mass Spectrometry.* Rapid Communications in Mass Spectrometry, 1999. 13: p. 50-53.

25. Badman, E. R.; Johnson, W. R.; Plass, W. R.; Cooks, R. G., *A Miniature Cylindrical Quadrupole Ion Trap: Simulation and Experiment.* Analytical Chemistry, 1998. 70: p. 4896-4901.

26. Wu, G.; Cooks, R. G.; Ouyang., Z., *Geometry optimization for the cylindrical ion trap: field calculations, simulations and experiments.* Int. J. Mass Spec. Ion Processes, 2005. 241: p. 119-132.

27. Patterson, G. E.; Guymon, A. J.; Riter, L. S.; Everly, M.; Griep-Raming, J.; Laughlin, B. C.; Ouyang, Z.; Cooks, R. G., *Miniature Cylindrical Ion Trap Mass Spectrometer.* Analytical Chemistry, 2002. 74: p. 6145-6153.

28. Mordehai, A.; Miller, B.; Kuhlmann, F. *A New Higher-Capacity 3-D Quadrupole Ion Trap*. in *51st ASMS Conference on Mass Spectrometry and Allied Topics*. 2003. Montreal, Quebec, Canada.

29. Kaplan, D. A.; Glish, G. L. *Development and performance of radio frequency circuitry for an electrically tunable compensated cylindrical ion trap mass spectrometer*. in *Proceedings of the 51st ASMS Conference on Mass Spectrometry and Allied Topics*. 2003. Montreal, Canada.

30. Goeringer, D. E.; Whitten, W. B.; Ramsey, J. M.; McLuckey, S. A.; Glish, G. L., *Theory of High-Resolution Mass Spectrometry Achieved via Resonance Ejection in the Quadrupole Ion Trap.* Analytical Chemistry, 1992. 64: p. 1434-1439.

31. Hopkins, D.; Alexander, M.; Swanson, K.; Buschbach, M., *Control System for an Ion Trap Mass Spectrometer.* Scientific Computing, 2004. 2(4).

32. Laughlin, B. C.; Mulligan, C. C.; Cooks, R. G., *Atmospheric Pressure Ionization in a Miniature Mass Spectrometer.* Analytical Chemistry, 2005. 77: p. 2928-2939.

33. Reed, D. G., Ed. *The ARRL Handbook for Radio Amateurs*, 79 ed.; ARRL-the national association for Amateur Radio: Newington, CT USA, 2002.

Chapter 3

Impact of Non-linear Resonances on Environmental Applications

3.1 Introduction

Volatile organic compounds (VOCs) are released into the environment through the burning of fossil fuels and directly by plant life.[1] The development of a more sensitive detection method for many of these VOCs is necessary because of the harmful effects that they have on the environment as well as human health.[1, 2] Isoprene (3-methyl-1,3 butadiene) is a highly reactive biogenic volatile organic compound (VOC) emitted mainly from deciduous trees.[2] Other sources of isoprene include emissions from rubber and plastics industries, cigarette smoke, and the human body as isoprene is produced and exhaled. Because isoprene reacts rapidly with $OH^{\bullet}$, it plays an important role in tropospheric chemistry.[1] In the presence of nitrogen oxides (NO_x), isoprene and its major photooxidation products methyl vinyl ketone and methacrolein lead to ozone (O_3) formation. The high concentrations of NO_x and isoprene (in addition to other biogenic hydrocarbons) present in major cities can lead to O_3 smog pollution. Gas chromatographic flame ionization detector techniques are available to detect VOCs in static or slowly changing mixtures (Changes in concentration of greater than 1 hour).[3, 4] However under some conditions the concentration of VOCs can change rapidly (less than 15 min), for example at dusk or at peak automobile travel times. Therefore there is a need for accurate fast online detection methods of VOCs.

Mass spectrometry is well suited for the online detection of VOCs because it is a capable of part-per-trillion detection limits on the millisecond to second timescale without the need for chromatographic techniques.[3, 4]

Over the past forty years, different forms of chemical ionization coupled with a variety of mass spectrometers have been used for the detection of VOCs. In recent years, proton transfer reaction mass spectrometry (PTR-MS) has gained popularity because of the technique's sensitivity to VOCs with minimal fragmentation of the compounds of interest. With most online analysis techniques, no initial separation technique is used before mass analysis. Therefore, minimizing fragmentation is necessary because VOC samples are often composed of a complex mixture of gases. Minimizing fragmentation simplifies the analysis because only one ion is generated from a given analyte. However, a negative effect of this simplification is that mass spectra do not contain sufficient structurally-relevant ions to identify unknowns. Additionally, isomeric and isobaric analytes (compounds which have the same nominal mass but different exact mass) can not be differentiated. Both of these problems can be addressed with the use of tandem mass spectrometry.

The mass analyzer used in most proton transfer reaction mass spectrometers is a quadrupole mass filter. A quadrupole mass filter is a beam instrument that requires additional analyzers to perform tandem mass spectrometry. A quadrupole ion trap mass spectrometer (QITMS) can perform tandem mass spectrometry without the need for additional mass analyzers. In one example in the literature, researchers used tandem mass spectrometry in a PTR-QITMS to identify the isomers methyl vinyl ketone and methacrolein.[5] The reaction chamber in most PTR mass spectrometers is a drift tube, which is not necessary with the QITMS. The QITMS offers the advantage of being both the mass

analyzer and the reaction cell for proton transfer or other ion/molecule reactions. Recently another versatile ionization technique used in a QITMS, called selected ion chemical ionization (SICI), has proved useful for the analysis of VOCs.[6-8] This technique takes advantage of ion/molecule reactions in the quadrupole ion trap to ionize analyte ions without the need for a drift tube. SICI has the same capability for proton transfer reaction mass spectrometry as traditional PTR-MS with a drift tube. Quadrupole ion traps are quite rugged, have good sensitivities, and are capable of being operated at higher pressures (1-5 mTorr). Therefore a quadrupole ion trap is a good analyzer for the analysis of VOCs.

One important aspect for the analysis of VOCs is the capability for online sampling methods. Some online methods can be harmful to QITMS performance because the buffer gas is likely to be a mixture of air and helium. Heavy gases are problematic for small molecules, particularly during ion ejection, because of scattering effects.[9, 10] The effects due to scattering can be reduced by increasing the amount of helium present in the QITMS. However, there is a limited range over which these improvements can be made because when the helium pressure is too high, helium can begin to delay ion ejection and cause effects similar to those of the heavy bath gas. As described in **Chapter 1**, the quadrupole ion trap has non-linear resonances due to higher order field components, which can be utilized to improve performance. The analytical performance of an ion trap operating with some portion of a static heavy gas can be improved by resonantly exciting ions at non-linear resonances during ion ejection.[9] Analysis of isoprene and its photooxidation products methyl vinyl ketone and methacrolein were performed on a compensated cylindrical ion trap (CCIT) and a conventional 3-D quadrupole ion trap mass spectrometer. The CCIT is a different quadrupole ion trap electrode geometry, which still has a predominantly quadrupole trapping

field. Therefore the CCIT has the same advantages as the conventional 3-D quadrupole ion trap for the analysis of VOCs as described earlier. For the rest of this discussion the conventional 3-D quadrupole ion trap mass spectrometer will simply be referred to as the QITMS. As described in Chapter 1, the QITMS has higher order field contributions and therefore should benefit from using resonance ejection at non-linear field resonances. The CCIT has a larger percentage of higher order field contributions, as described in **Chapter 2**, therefore it should have significant improvements when using resonance ejection at non-linear field resonances compared to the QITMS.

3.2 Chemical Ionization

3.2.1 Background

Two common ionization techniques for organic compounds are electron ionization and chemical ionization. Electron ionization was discovered in the 1920s by A. J. Dempster and is one of the most common ionization techniques used in mass spectrometry.[11] Electron ionization occurs via the reaction shown in **Reaction 3.1** and often results in the molecular ion ($M^{+\bullet}$) fragmenting during the ionization process.

$$M + e^- \rightarrow M^{+\cdot} + 2e^- \qquad \textbf{Reaction 3.1}$$

Fragmentation can be useful for the identification of unknowns. However, as mentioned in **Section 3.1**, only one peak per analyte is desired in the analysis of a complex mixture of VOCs. In electron ionization the only way to minimize fragmentation is to minimize the kinetic energy of the electrons, which is usually 70 eV. Low kinetic energy electron ionization (20eV) is effective at reducing the amount of observed fragmentation; however, sensitivity is diminished because the number of molecules that get ionized is reduced. In

contrast to electron ionization, chemical ionization offers the ability to control the amount of observed fragmentation. In chemical ionization analyte ions are generated from ion/molecule reactions in the gas phase. Chemical ionization was first introduced in 1966 and quickly became a complimentary technique to electron ionization.[12] Two of the more powerful and common forms of chemical ionization are proton transfer and charge exchange. Each of these forms of chemical ionization will be discussed more specifically below. In either type of chemical ionization the amount of observed fragmentation depends on the reagent ion that reacts with the analyte molecule.

3.2.2 Proton Transfer

The proton affinity (PA) of a molecule (B) is defined as the negative enthalpy of the reaction provided in reaction 3.2.

$$B + H^+ \rightarrow BH^+ \qquad \textbf{Reaction 3.2}$$

Proton transfer reactions are described by reaction 3.3 and reaction 3.4.[13] Proton transfer reactions for this work will be used to ionize neutral analytes with protonated reagents as described by reaction 3.4. As shown in **Equation 3.1**, the negative enthalpy ($-\Delta H_{rxn}$) of reaction 3.4 is defined as the difference in proton affinities of the reagent gas (B) and of the analyte molecule (M). The proton transfer reaction will only occur if the proton affinity of the analyte is greater than the proton affinity of the reagent gas. In most cases, if the difference between the proton affinities exceeds the critical energy for dissociation, then fragmentation can occur. The critical energy is the minimal energy from the ground state of a molecule to exceed the energy required to start the fragmentation or breaking of a covalent bond. This fragmentation can be minimized by selecting a reagent that has a proton affinity close to the analyte's proton affinity.

$$[M\text{-}nH]^{n-} + BH^{+} \rightarrow [M\text{-}(n\text{-}1)H]^{(n-1)-} + B \qquad \textbf{Reaction 3.3}$$

$$M + BH^{+} \rightarrow MH^{+} + B \qquad \textbf{Reaction 3.4}$$

$$-\Delta H_{rxn} = PA(M) - PA(B) \qquad \textbf{EQ 3.1}$$

A table of some common components of air and other volatile organic compounds with their proton affinities is listed in **Table 3.1**. The proton affinities of the analytes studied (isoprene, methyl vinyl ketone, and methacrolein) are listed in **Table 3.2**. For reference, structures of the analytes are in **Figure 3.1**

Reagent	Proton Affinities (kJ/mole)
He	177.8
Ne	198.8
Ar	369.2
O_2	421.0
N_2	493.8
CH_4	543.5
N_2O	571.1
H_2O	691.0
HCOOH	742.0
C_6H_6	750.4
CH_3OH	754.3
CH_3COH	768.5
CH_3CN	779.2
C_2H_5OH	776.4
CH_3COCH_3	812.0
NH_3	853.5

Table 3.1 – Summary of proton affinities of common components in air, various volatile organic compounds, and other reagents

Analyte	Proton Affinities (kJ/mole)
Isoprene	826.4
Methyl vinyl ketone	834.7
Methacrolein	808.7

Table 3.2 – Summary of analyte proton affinities

Generating reagent ions for proton transfer has been accomplished in a variety of ionization sources ranging from electron ionization sources to cathode discharge sources. The more traditional chemical ionization source uses methane as a reagent gas. In this source, EI is used to generate a molecular ion ($CH_4^{+\bullet}$) from the reagent gas. Additionally the

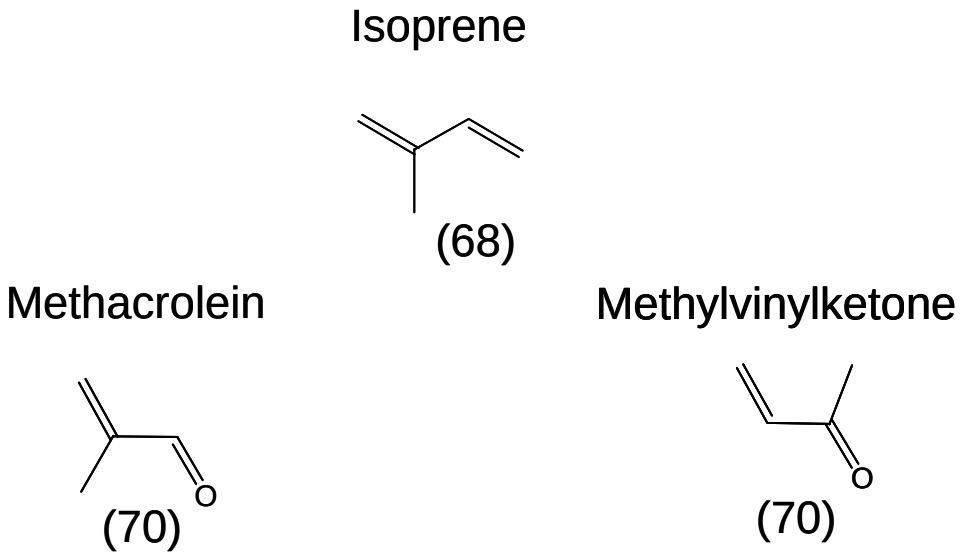

Figure 3.1 – Structures for Isoprene, methyl vinyl ketone, and methacrolein.

fragment ions, CH_3^+ and $CH_2^{+\bullet}$, are generated in the ion source. Because the pressure of methane in the source can be up to 1 Torr, the generated ions then undergo ion/molecule reactions as shown in the reactions schemes 3.5-3.7.

$$CH_4^{+\bullet} + CH_4 \rightarrow CH_5^+ + CH_3^{\bullet} \qquad \textbf{Reaction 3.5}$$

$$CH_3^+ + CH_4 \rightarrow C_2H_5^+ + H_2 \qquad \textbf{Reaction 3.6}$$

$$CH_2^{+\bullet} + CH_4 \rightarrow C_2H_3^+ + H_2 + H^{\bullet} \qquad \textbf{Reaction 3.7}$$

The first generation ions that are most abundant are CH_3^+ and $CH_4^{+\bullet}$. Therefore, the predominant reagent ions produced are CH_5^+ and $C_2H_5^+$. These reagent ions can then undergo proton transfer with the analyte molecule as outlined in reaction 3.4. In this ionization technique, the analyte ions do not typically get ionized via electron ionization because the reagent ions are in excess concentration (10^4 times greater) compared to the analyte molecules. This set of reactions (3.4 – 3.6) is only an example of the variety of reagents that can be used in proton transfer. For the experiments presented in this work, reagent ions were generated in a glow discharge ionization source (GDI) that will be described in **Section 3.3**

3.2.3 Charge Exchange

Another versatile chemical ionization technique is charge exchange, which is sometimes called charge transfer. The general reaction for charge exchange is shown in Reaction 3.8. The process requires that an electron be added to the radical cation of the reagent ion as shown Reaction 3.9. The energy required for this process is called the recombination energy. Because the recombination reaction is the reverse reaction of the electron ionization process (Reaction 3.1), the recombination energy is approximately equal

to the negative of the ionization energy. The amount of observed fragmentation is a function of the

$$R^{+\bullet} + M \rightarrow M^{+\bullet} + R \qquad \textbf{Reaction 3.8}$$

$$R^{+\bullet} + e^{-} \rightarrow R \qquad \textbf{Reaction 3.9}$$

recombination energy (RE) of the analyte M and the reagent R, **Equation 3.2**. As most reference tables contain ionization energies (IE) and not recombination energies, REs are often replaced with ionization energies and **Equation 3.2** takes the form shown in **Equation 3.3**.

$$-\Delta H_{rxn} = RE(M) - RE(R) \qquad \textbf{EQ 3.2}$$

$$-\Delta H_{rxn} \approx IE(R) - IE(M) \qquad \textbf{EQ 3.3}$$

More fragmentation is observed with a greater difference between the analyte molecule IE and the reagent gas IE. A summary of the ionization energies of some common components in air and several other reagent ions is shown in **Table 3.3**. A summary of the ionization energies of the analytes is included in **Table 3.4**.

Reagent	IE(eV)
$NO^{\bullet}$	9.26
NO_2	11
Xe	12.2
O_2	12.5
Kr	14
CO	14.1
CO_2	14.4
Ar	15.6
N_2	15.8
Ne	21.6
He	24.6

Table 3.3 Ionization energies of some common components in air and other potential reagents

Analyte	Ionization Energy (eV)
Isoprene	8.86
Methyl vinyl ketone	9.65
Methacrolein	9.92

Table 3.4 – Summary of analyte proton affinities and ionization energies.

3.3 Glow Discharge Ionization

Glow discharge ionization has been used for a variety of analytical applications including studies of atomic structure, elemental analysis of metal surfaces, and most recently, in the analysis of volatile organic compounds.[14-18] The ionization source has been successfully coupled with emission spectroscopy and mass spectrometry.[16, 17, 19] A glow discharge ionization source, capable of external vapor introduction and atmospheric sampling, was designed and constructed for these experiments and pertinent details are described in **Section 3.6.3**. As shown in **Figure 3.2,** the glow discharge ionization source is essentially two parallel electrodes. A negative direct current (dc) voltage (V_1) is applied to the front electrodes on the atmospheric side of the source while the second back electrode is held at ground. The electrode with the more negative potential is the cathode and the electrode with the more positive potential is the anode. Glow discharge occurs at sub atmospheric pressures between the two parallel electrodes. As a result of cosmic rays and natural radioactivity from outer space, a small amount of electron-ion pairs exist in air. These electrons are accelerated by the applied potential between the electrodes. With this increased kinetic energy, the electrons can collide with molecules and ionize them to create more ion pairs. The electron-ion pairs also strike the surface of the anode and create a current flow between the anode and cathode. If too many ion electron pairs are created, i.e. if the voltage between the electrodes is too high, electrical breakdown or electrical arcing can occur preventing the glow discharge from occurring.

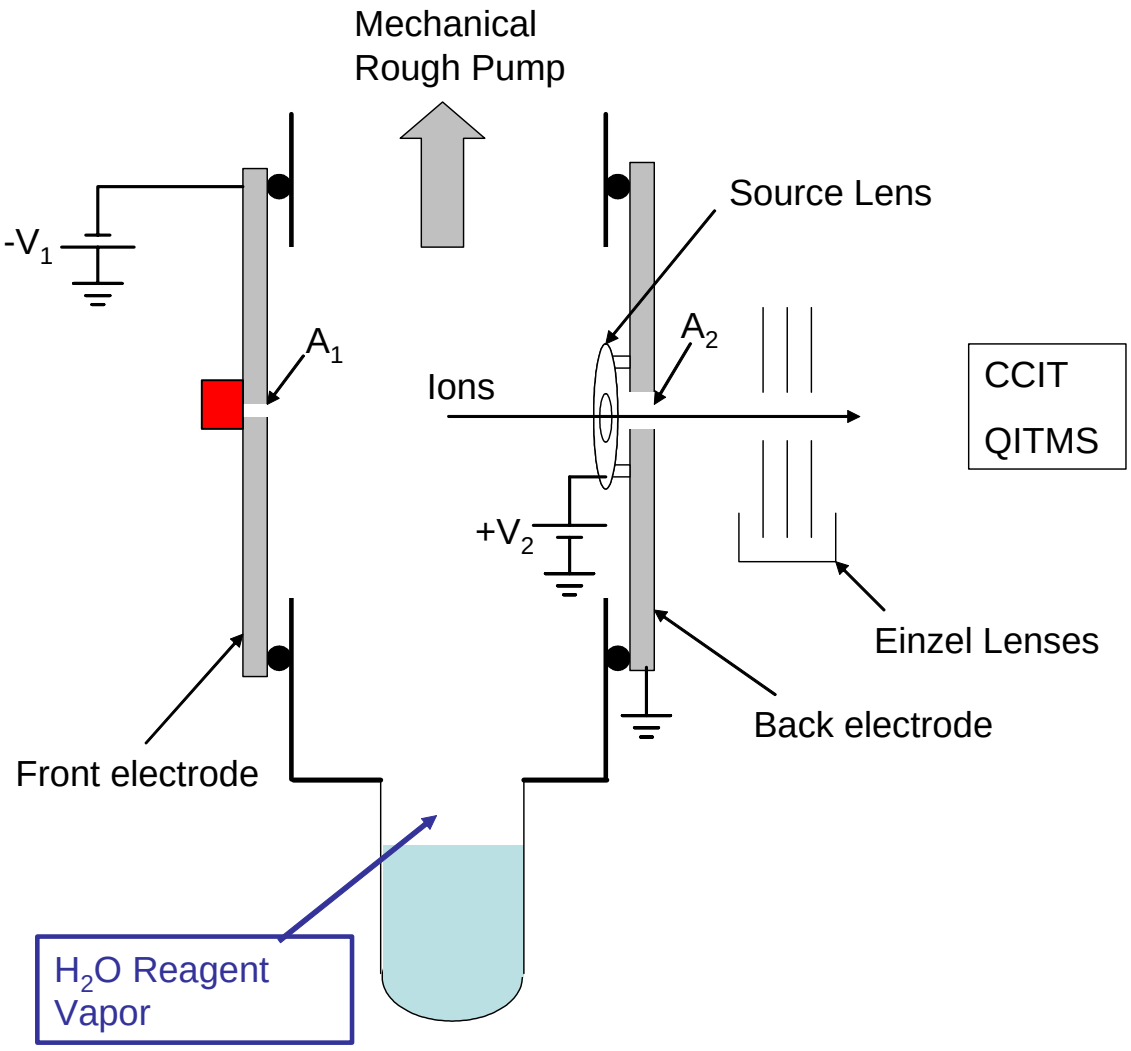

Figure 3.2 – Glow discharge ionization source for the CCIT. Ion source is a representation not drawn to scale, for accurate drawings see Appendix II. Ion source for QITMS contains an additional source lens (Not shown).

Ion current in a glow discharge ionization source is in the milliampere range and is dependant on the gas pressure, the gas composition, the distance between the electrodes, and the voltage applied between the two electrodes. Not all accelerated electrons have sufficient kinetic energy to ionize a molecule. Electrons below an analyte's ionization energy can therefore excite a molecule, which will then relax from an excited electronic state by emitting photons. In the glow discharge ionization of air, nitrogen is the most abundant species. Nitrogen molecules emit a photon during relaxation of wavelength 410 nm, resulting in a purple glow.

Many types of ionization processes can occur in a glow discharge ionization source, including electron ionization, charge transfer, and electron capture. When air is the gas in the glow discharge region, several reagent ions are generated as shown from the reactions listed in reaction schemes 3.10 – 3.18.

$O_2 + e^- \rightarrow O_2^{+\bullet} + 2e^-$ **Reaction 3.10**

$N_2 + e^- \rightarrow N_2^{+\bullet} + 2e^-$ **Reaction 3.11**

$N_2^{+\bullet} + O_2 \rightarrow O_2^{+\bullet} + N_2$ **Reaction 3.12**

$N_2^{+\bullet} + O_2^{+\bullet} \rightarrow N_2O_2^{+\bullet} \rightarrow NO^+ + NO^\bullet$ **Reaction 3.13**

$N_2^{+\bullet} + NO^\bullet \rightarrow NO^+ + N_2$ **Reaction 3.14**

$O_2^{+\bullet} + H_2O \rightarrow O_2 + H_2O^{+\bullet}$ **Reaction 3.15**

$H_2O^{+\bullet} + H_2O \rightarrow H_3O^+ + OH^\bullet$ **Reaction 3.16**

$NO^+ + O_2 \rightarrow NO_2 + O^\bullet$ **Reaction 3.17**

$NO_2 + O_2^{+\bullet} \rightarrow NO_2^{+\bullet} + O_2$ **Reaction 3.18**

As with traditional chemical ionization, several reagent ions are generated from neutrals reacting with molecular ions. It is interesting to note that even though nitrogen is present in

air at a four times greater concentration than oxygen, the predominant ion observed in the glow discharge mass spectrum of air is not that of nitrogen (*m/z* 28) but rather that of oxygen (*m/z* 32). This is simply because the ionization energy of oxygen is 3 eV lower than the ionization energy of nitrogen, thus allowing for charge exchange reaction described in reaction 3.12 to occur. The relative amount of nitrogen ions compared to oxygen ions depends on the amount of time that ions spend in the source or in the ion trap. Specifically in the ion trap this period is the amount of time after ion injection and before mass analysis. If this time is sufficient all of the nitrogen ions can charge exchanged to for oxygen ions.

Atmospheric sampling glow discharge ionization (ASGDI) is implemented using a glow discharge source as described above using air as the discharge gas. The two parallel electrodes in the glow discharge ionization source have apertures for gas introduction and ion extraction. Typical pressures in an ASGDI source are 0.1- 1 Torr depending on the aperture sizes and pumping speeds used. During the majority of the experiments described in this chapter, the front aperture on the glow discharge ionization source on both the compensated cylindrical ion trap and quadrupole ion trap were sealed and an outside reagent gas was orthogonally introduced into the source.

3.4 Selected Ion Chemical Ionization

3.4.1 Theory

Researchers have introduced analyte vapors directly into an ASGDI source along with the reagent gas.[7, 15, 20] The reagent ions of air ($N_2^{+\bullet}$, H_3O^+, NO^+, and $NO_2^{+\bullet}$) ionize the analyte via proton transfer and charge exchange. Thus, the protonated molecule ($[M+H]^+$) and the molecular ion ($M^{+\bullet}$) are generated, which is problematic because ions of different

mass-to-charge are generated from an analyte. Additionally researchers have shown that when analytes are ionized directly in the ASGDI source, extensive fragmentation similar to that observed in EI can occur.[21] An alternative ionization technique is to select a single type of reagent ion from the source and separately ionize the analyte in the volume of the ion trap. This technique is called selected ion chemical ionization (SICI).[6, 22-24] Unlike direct ionization using ASGDI, in SICI the type of chemical ionization can be chosen by the user. Because chemical ionization is still occurring, the energetics discussed previously for proton transfer and charge exchange still apply. Additional selectivity can be achieved by carefully choosing a reagent ion that will only ionize a given analyte molecule. For example, when acetone is used as a reagent ion, methyl vinyl ketone is ionized whereas methacrolein is not ionized because methacrolein's proton affinity is lower than acetone's proton affinity (**Table 3.1**).[8] Additionally, the extent of fragmentation can also be controlled by the careful selection of reagent ions. In general, proton transfer of VOCs with H_3O^+ has been previously shown to produce less fragmentation than charge transfer with $O_2^{+\bullet}$ reagent ions.[8] Because of this, H_3O^+ was used as the reagent ion for the experiments described in this chapter.

3.4.2 Experimental Factors Affecting SICI

Two experimental factors that may affect SICI are space charge effects and bath gas composition. The sensitivity of an ion trap mass spectrometer can be enhanced by increasing the number of trapped ions. However, if too many ions are trapped then the large number of charges can effectively create a dc potential; this effect is called space charge.[25] The three primary effects of space charging on ion trap operation are: (1) ion accumulation becomes non-linear as a function of time, (2) peak widths increase in the mass spectrum, and (3) the observed mass-to-charge ratio of ions shifts to higher values.[26, 27] Space charging affects

trapping efficiency because the extra charge causes ions to be repelled out of the trap. Some theories propose the effective dc potential as a change in the working point in the Mathieu stability diagram (an effective a_z term).[27] As described previously, ions generated with SICI should be immediately trapped because the ionization occurs within the ion trap. Even though analyte ions are generated in the ion trap they can still be affected by space charge. If there are a sufficient number of reagent ions present as analyte ions are generated, the analyte ions may be consequently ejected out of the ion trap due to the space charge effect of the smaller mass-to-charge reagent ions. The increase in peak width and the observed shift in the mass-to-charge ratio of ions are the result of ion/ion interactions, which cause delayed ejection. This result can be effectively described as a horizontal shift in the Mathieu stability diagram because a greater amplitude rf voltage is required to eject ions at $\beta_{z\,\mathrm{eject}} = 1$ (no resonance ejection).[27] The presence of mass shifts can be reduced with internal calibration.[27] Mass shifts will be further addressed in **Chapter 4.**

The composition of the buffer gas is the second instrumental factor that may affect SICI. The buffer gas is vital to the optimal performance of the ion trap. One of its most important roles is to collisionally cool ions to the center of the ion trap, which minimizes the amount of time ions spend near the endcaps where the higher order field components are the greatest. The end result of collisional cooling is an increase in the number of trapped ions. Helium is typically used as the buffer gas in the ion trap. Researchers have explored heavier buffer gasses in the ion trap, such as air and argon.[10, 28, 29] Results have shown that heavier buffer gases lead to a reduction in sensitivity and mass resolving power. Heavier buffer gases can collisionally cool the ions closer to the center of the ion trap, resulting in a higher charge density than with helium buffer gas. This greater charge density leads to space charge

effects as described before. Additionally, resolution and sensitivity can further suffer because as ions are being ejected from the ion trap they can be scattered by the heavier buffer gas. When the use of heavy buffer gasses is unavoidable, such as when air is directly sampled, researchers have shown that the effects of heavy buffer gasses can be reduced by creating a mixture of heavy buffer gas and helium.[28-31] In these examples, the heavy buffer gas is added in addition to the normal operating pressure of helium.

3.5 Non-Linear Resonances

3.5.1 Theory

The second order differential equation describing an ion's motion in the quadrupole ion trap, **Equation 1.10** assumes a pure quadrupole field. When higher order field components are taken into account the equation takes the form shown in **Equation 3.3,**[32] where $\frac{\partial \phi'}{\partial z}$ represents the electric field due to the higher order field components, ξ is the time dependant variable described by **Equation 3.4**, and a_z and q_z are the Mathieu parameters described in **Chapter 1.** The operating frequency of the ion trap in radians is Ω while z is the axial dimension of the ion trap. A corresponding equation for the radial dimension also exists. The radial form of this equation includes a component responsible for the conservation of angular momentum, which is zero for the z dimension. This term in the r dimension is assumed to be negligible; therefore with the appropriate geometric substitutions **Equation 3.3** is also valid for the r dimension.[25, 32]

$$\frac{\partial^2 z}{\partial \xi^2} + [a_z - 2q_z \cos(2\xi)]x = \frac{1}{4}[a_z - 2q_z \cos(2\xi)]\left(\frac{\partial \phi'(r,z)}{\partial z}\right) \qquad \textbf{EQ 3.3}$$

$$\xi = \frac{\Omega t}{2} \qquad \textbf{EQ 3.4}$$

Using the solutions to equation 3.3, ion motion in the presence of higher order fields can be calculated. A nonlinear resonance occurs when the right-hand side of **Equation 3.3** goes to infinity. Through several mathematical manipulations these nonlinear resonances were shown to occur when **Equation 3.5** is satisfied, where n_r, n_z, and ν are integer values and β_z and β_r correspond to iso-beta curves described in **Chapter 1, Equation 1.29**.[32] Note, as will be described shortly, that not all of the theoretically possible non-linear resonances occur.

$$n_r\beta_r + n_z\beta_z = 2\nu \qquad \textbf{EQ 3.5}$$

Substituting **Equation 3.6** and **Equation 3.7** into **Equation 3.5** yields **Equation 3.5** in terms of the axial and radial secular frequencies (in radians) of the ions (**Equation 3.8**), which are ω_z and ω_r respectively.

$$\omega_z = \frac{\beta_z\Omega}{2} \qquad \textbf{EQ 3.6}$$

$$\omega_r = \frac{\beta_r\Omega}{2} \qquad \textbf{EQ 3.7}$$

$$n_r\omega_r + n_z\omega_z = \Omega\nu \qquad \textbf{EQ 3.8}$$

From **Equation 3.8,** nonlinear resonances generally occur when the integral sum of the secular frequencies is a multiple of the drive frequency. This means that nonlinear resonances are in essence an effect of harmonic overlap between the secular frequency of an ion and the drive frequency or side bands of the drive frequency. [25, 32] Nonlinear resonance associated with a given higher order field component occurs when the sum of n_r and n_z is equal to the order (N) of that given higher order field component as in **Equation 3.9**. A full list of components is given in **Table 1.2**; however, for quick reference the hexapole order is

N=3 and the octapole order is N=4. For a given higher order field component a maximum of 2N resonances can exist.[32, 33] The strongest of these resonances occurs when N = n.

$$N = |n_r| + |n_z| \qquad \textbf{EQ 3.9}$$

As noted previously, not all of the resonances that satisfy **Equation 3.5** and **Equation 3.8** are nonlinear resonances. Assuming an ideal ion trap, which is rotationally symmetrical, when n_r is an odd number some of the mathematical operations used to derive the equations fail and those nonlinear resonances should not be observed.[32] When the ion trap geometry is not rotationally symmetrical, some of these "forbidden" resonances have been observed.[34] The non-linear resonances for the octapole and hexapole field components are summarized in **Table 3.5**.[25, 33] The allowed non-linear resonances are also shown colored in a plot of the Mathieu stability diagram in **Figure 3.3** (Color of non-linear resonance in figure description)

Higher order Field Component	n_r	n_z	Non-linear Resonance
Hexapole (N=3)	0	3	$3\beta_z=2$
	3	0	$3\beta_r=2^{\dagger}$
	1	2	$\beta_r+2\beta_z=2^{\dagger}$
	2	1	$2\beta_r+\beta_z=2$
Octapole (N=4)	0	4	$4\beta_z=2$
	4	0	$4\beta_r=2$
	2	2	$2\beta_r+2\beta_z=2$
	3	1	$3\beta_r+\beta_z=2^{\dagger}$
	1	3	$\beta_r+3\beta_z=2^{\dagger}$

Table 3.5 – Summary of possible non-linear resonances for octapole and hexapole fields
† - Denotes non-linear resonance lines that are mathematically forbidden

The strength (or presence) of the non-linear resonances can vary between instruments and is dependant on the relative amount of higher order field components present, which is ultimately dependant upon the geometry of the ion trap.[34, 35]

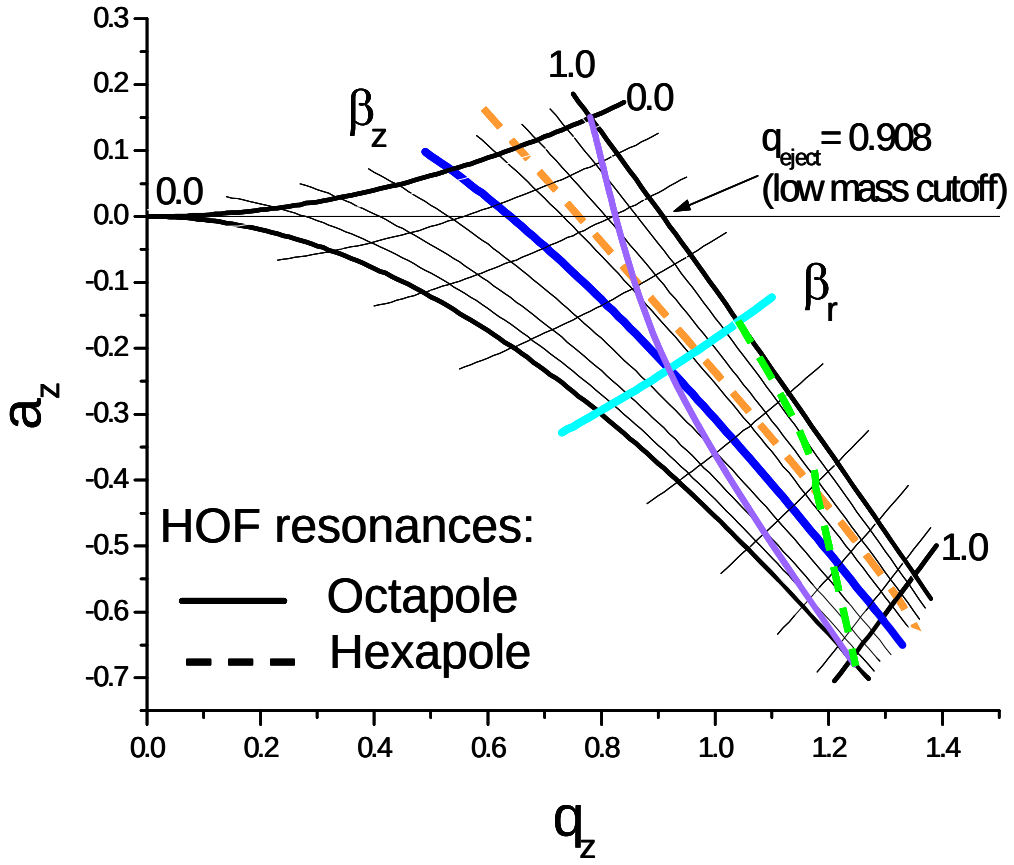

Figure 3.3 – Mathieu stability diagram with vertical iso-β_z curves and horizontal iso-β_r curves. β_z and β_r equal to zero and one are bold for clarity. Octapole non-linear resonances at $\beta_z = 0.5$, $\beta_r = 0.5$, $2\,\beta_r + \beta_z = 2$ are solid lines. Hexapole non-linear resonances at $\beta_z = ⅔$, $2\,\beta_r + 2\,\beta_z = 2$ are dotted lines.

3.5.2 Implications of Non-Linear Resonances

Before non-linear resonances were fully understood researchers noticed that product ions with a $q_z \approx 0.78$ ($a_z=0$) were observed with reduced abundance during tandem mass spectrometry (MS/MS) experiments.[36] These phenomena were originally termed "black holes". Using **Equation 1.30**, which relates β_z to the a_z and q_z parameters, this q_z of 0.78 corresponds to $\beta_z = ⅔$. The proposed "black holes" were nothing more than the effects of non-linear resonances, which in this example is a hexapole resonance. Further exploration of these effects showed that ion losses were also observed at $\beta_z = ½$ and occurred along the entire β_z curve.[37, 38] The phenomenon's name was then updated to "black canyons"; which again are simply non-linear resonances.[38] Other researchers showed that spurious ion ejections occurred as an ion's q_z was increased to a value greater than the non-linear resonance at $q_z \approx 0.78$ and then subsequently decreased to a q_z below the non-linear resonance (termed a reverse scan).[39] This experiment was not performed during an MS/MS experiment so no resonance excitation was introduced; however, reverse scans are common in many MS and MS/MS experiments. One important observation was that no ion losses were observed while scanning in the forward direction. A possible common factor between the observed ion losses in the MS/MS experiments and the reverse scan ion losses is that ions are spending more time near the endcaps because their axial motion was increased. As described in Chapter 1 and Chapter 2, higher order fields are strongest at the endcaps because of the holes in the endcaps for ion entry and exit. Researchers have since shown that the ion losses during a reverse scan are due to a rapid absorption of power from the non-linear resonance points, which is heavily dependant on the initial kinetic energy and position of the ions.[35, 40] The same loss is not observed in the forward direction because the power

absorption from the non-linear resonances in a stretched 3-D quadrupole ion trap is asymmetrical and is not as sharp when the secular frequency of an ion approaches the non-linear resonance from lower frequencies.[35, 40] Losses during reverse scans can be minimized by increasing the rate at which an ion's q_z is decreased.[35] Losses due to non-linear resonances during an MS/MS experiment can only be avoided by choosing the q_z for the dissociation experiment such that no ions have q_z values near the non –linear resonance.

3.5.3 Resonance Ejection at Non-Linear Resonances

All commercially available ion traps contain higher order fields and consequently contain non-linear resonances. The most advantageous way to exploit non-linear resonances to date is to perform resonance ejection at a non-linear resonance.[41] The advantages of resonance ejection on mass resolving power were illustrated in **Section 2.2.3.3** of **Chapter 2**. Resonance ejection is a dipolar excitation process that is performed by applying a supplemental ac signal to each end cap. Each ac waveform is 180º out of phase. Non-linear resonances allow the kinetic energy gained to be coupled into the ion's motion at higher powers ($n \geq 2$) than is possible in dipolar excitation. Therefore, performing resonance ejection at a non-linear resonance is a more efficient process of kinetically exciting ions which results in ion ejection over a smaller range of mass-to-charge as compared to conventional resonance ejection. The result of this smaller range is a further improvement in mass resolving power over conventional resonance ejection. Additionally, because the process is more efficient than conventional resonance ejection, faster scan rates can be used for mass analysis, which will allow for experiments over shorter time scales. Resonances ejection at non-linear resonances has been reported in the literature.[41] Additionally, the Bruker Esquire

Ion Trap (Bruker Daltonics, Bremen Germany) uses resonance ejection at the hexapole non-linear resonance $\beta_z = ⅔$ to eject ions.

3.6 Experimental Methods

3.6.1 Sample Preparation

Methyl vinyl ketone, methacrolein, and isoprene were obtained from Sigma Chemical Company. Analytes were prepared using a simple freeze pump thaw procedure. Using a disposable syringe, 2-4 mL of the liquid analyte was put into a 25 mL, two neck round bottom flask. The sample was frozen by immersing the flask in liquid nitrogen and the flask was evacuated with a rough pump. The sample was allowed to slowly thaw, so as not to splash on the sides of the flask, and then the procedure was repeated two more times. Analyte vapor pressures were measured with an MKS Instruments model 122A 1000 Torr capacitance manometer that was connected to the flask using Tygon™ tubing. An MKS digital readout was used to monitor the measured pressure. A separate piece of Tygon™ tubing was used for each analyte to avoid contamination. 100-L Tedlar™ bags (SKC, Eighty Four, PA) were filled with house air to ~80% of their total capacity (~80-L). Air flow rates were monitored with an analog flow meter and were on the order of 2-3 mL/min. Analyte vapors were extracted from the round bottom flask through a standard 22-4 rubber septum with a Hamilton 5 mL gas tight syringe. The analyte vapors were then injected into the prefilled Tedlar™ bag. The analyte and the air were then allowed to equilibrate for 10 min. The Tedlar™ bag was then connected to the mass spectrometer for analysis. Following each experiment, the analyte/air mixture in the Tedlar bag was purged with a mechanical rough pump, refilled with house air, and purged again to prevent contamination.

3.6.2 Instrumentation

Experiments were conducted with a compensated cylindrical ion trap (CCIT) mass spectrometer and a modified Finnigan ITMS™. The latter of the two instruments is a conventional quadrupole ion trap mass spectrometer (QITMS). A general layout of the instrumentation is depicted in **Figure 3.4**. Although the mass analyzer shown in the figure is the CCIT, all other portions of the instrumentation for the QITMS were very similar. Operation and other instrumental details regarding the CCIT and the QITMS are described in **Chapter 2** and **Chapter 1** respectively. In both instruments analytes were introduced from a Tedlar™ air sampling bag which was connected to a Granville Phillips metering valve (Helix Technology, CO) with ¼" plastic and stainless steel tubing. The gas coming from the metering valve was then directly introduced into the vacuum housing through stainless steel tubing. Air was evacuated from all of the tubing with a mechanical rough pump (not shown in figure) before introducing the analyte.

3.6.3 Reagent Ion Generation

Reagent ions are generated in a Glow Discharge Ionization (GDI) source. The GDI source for the CCIT was designed for this work from a 6" conflat flange (MDC Vacuum, Hayward, CA). A mechanical drawing of the ASGDI source is illustrated in **Appendix II**. Five 0.5" Cajon™ adaptors and one mini conflat flange were welded onto the 6" conflate flange. Three ports were used for pumping, one for reagent vapor introduction, one for electrical connections in the high vacuum chamber, and one for electrical connection in the source. A simplified representation of the source, sans pumping and electrical ports, is shown in **Figure 3.2**. Holes were drilled and tapped in the atmospheric side of the conflat flange for a pre-existing front electrode with a 100 μm aperture (A_1). The front electrode has

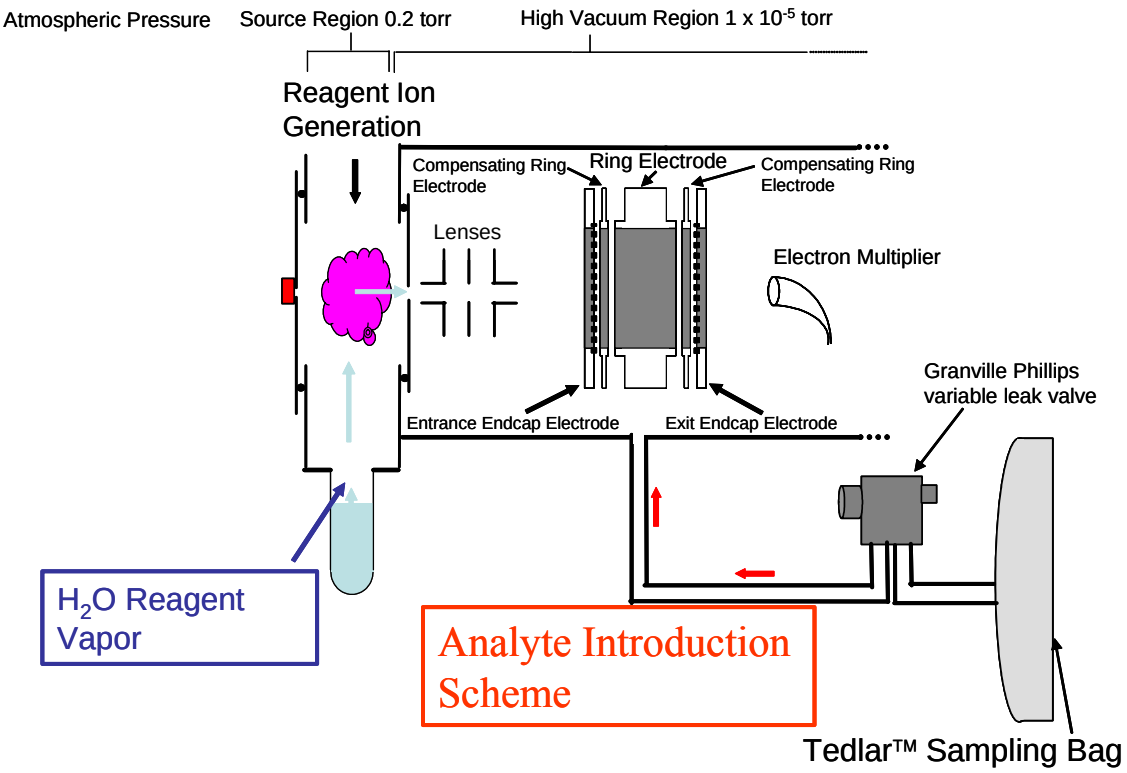

Figure 3.4 – Instrument design for selected ion chemical ionization in a CCIT. Design for QITMS is identical except with QITMS electrodes.

a groove for an o-ring, which creates the vacuum seal. A 3.25" diameter electrode for the high vacuum side of the flange was machined with a centered 1.25" diameter inset. The inset has screw holes and a groove for an o-ring. Pre-existing electrodes with conductance limiting apertures (A_2) ranging from 250-650 μm were screwed into the inset. Additionally, on the high vacuum side of the 3.25" back electrode, holes were drilled and tapped for threaded rods which support ceramics holding focusing einzel lenses. On the source side of the back electrode, holes were drilled for additional source lenses. A small source lens was installed on the source side of the back electrode. Water reagent vapors were introduced from a vial connected to one of the cajon ports. Source pressure was monitored with a 2 Torr capacitance manometer. Pressure in both the CCIT and QITMS ion sources was maintained between 0.2-0.3 Torr. Voltage was applied to the front electrode to cause electrical breakdown and glow discharge. The voltage for sustaining glow discharge of air and water was 370-400 V and 550-600 V respectively. The electrical current for both reagents was maintained at about 2 mA in both ion sources. The source lens in the CCIT was held at 25V and the first and second source lenses in the QITMS were held at 26 and 28 V, respectively. Note, **Figure 3.2** does not show the extra lens for the QITMS. The back aperture (A_2) in both instruments was at electrical ground. The first and third einzel lenses in the QITMS were held at -460 V and the middle einzel lenses is split in half with one at -160 V, and the other half pulsed between 180 V to stop ions and -160 V to transmit ions. In the CCIT the first and third lens were held -380 and -550V respectively. Ions were stopped with +180 V and transmitted with -160 V.

3.6.4 Ion Trap Experimental

Reagent ions were gated into the ion trap for 200 msec with the low mass cut off (LMCO) at 10 Da. Unless otherwise stated, the reagent ions were then allowed to react with neutral analyte for an additional 400msec. Ions coming from the source that were not the desired reagent ions for SICI were resonantly ejected using stored waveform inverse Fourier transform (SWIFT) waveforms during the entire reaction. The ion/molecule reactions were then stopped by ejecting reagent ions with a 1 msec linear increase in the LMCO to a value above the mass-to-charge of the reagent ion, e.g. for the hydronium reagent ion (*m/z 19*) the ramp would be from 10 Da to 22 Da. Analyte ions were then resonantly ejected while linearly increasing the LMCO from 10-150 Da at a rate of 180 μsec/Da in the QITMS and 800 μsec/Da in the CCIT. The frequency of the resonance ejection voltage was varied from experiment to experiment over β_z eject values ranging from 0.35 – 0.96. Unless otherwise stated resonance ejection voltage amplitudes were 3 $V_{0\text{-}p}$. Additionally, experiments were conducted with no resonance ejection at a β_z eject of 1. Resonance ejection waveforms were created using in-house software written in the programming language Lab VIEW and applied using a PCI-5411 arbitrary waveform generator (National Instruments, Austin, TX).

Air/analyte pressures from the Tedlar™ bag were typically about $3x10^{-5}$ Torr. Helium was used as a buffer gas in both ion traps. After the introduction of the analyte, helium was introduced to a final pressure of 1.4 mTorr.

3.7 Results and Discussion

3.7.1 Ionization and Ion Storage

SICI of methyl vinyl ketone (7 ppm in air) with H_3O^+ reagent ions was conducted in the QITMS and CCIT. The abundance of the protonated molecule was monitored while varying the reaction time from 0.5 – 7 sec. As shown in **Figure 3.5**, the protonated molecule abundance in the QITMS increases as a function of time. In the CCIT, however, the protonated molecule abundance increases until the 2.5 sec reaction time, and then begins to decrease. The reaction should proceed under pseudo first order kinetics; therefore the amount of analyte ions should be linearly related to the reaction time. The kinetics scheme agrees with the data from the QITMS but not with the data from the CCIT. The observed reduction in ion abundance in the CCIT can be partially attributed to space charge effects as described in **Section 3.4.2.** However, space charge effects can not be the only reason for the reduction in ion abundance: if the ions do not experience space charge effects before the reaction began, then the ions should not undergo space charging after the set reaction time because the amount of charge present must be conserved over the timeframe of the experiment. This is assuming, however, that ions are not leaking into the ion trap from the ASGDI source. Another explanation for the CCIT's ion losses is due to non-linear resonances. Researchers have shown that ion losses occur when ions are stored for long periods of time (>100 msec) near octapole non-linear resonances.[35] In this study when ion storage time was increased from 100 msec to 400 msec, ion losses increased by 20%. They also stated that these effects increase drastically in the presence of a resonance excitation. Resonance ejection experiments with the CCIT have shown that significant ion losses (~90%) are observed when resonance ejection was performed below 75 kHz.[42] These results

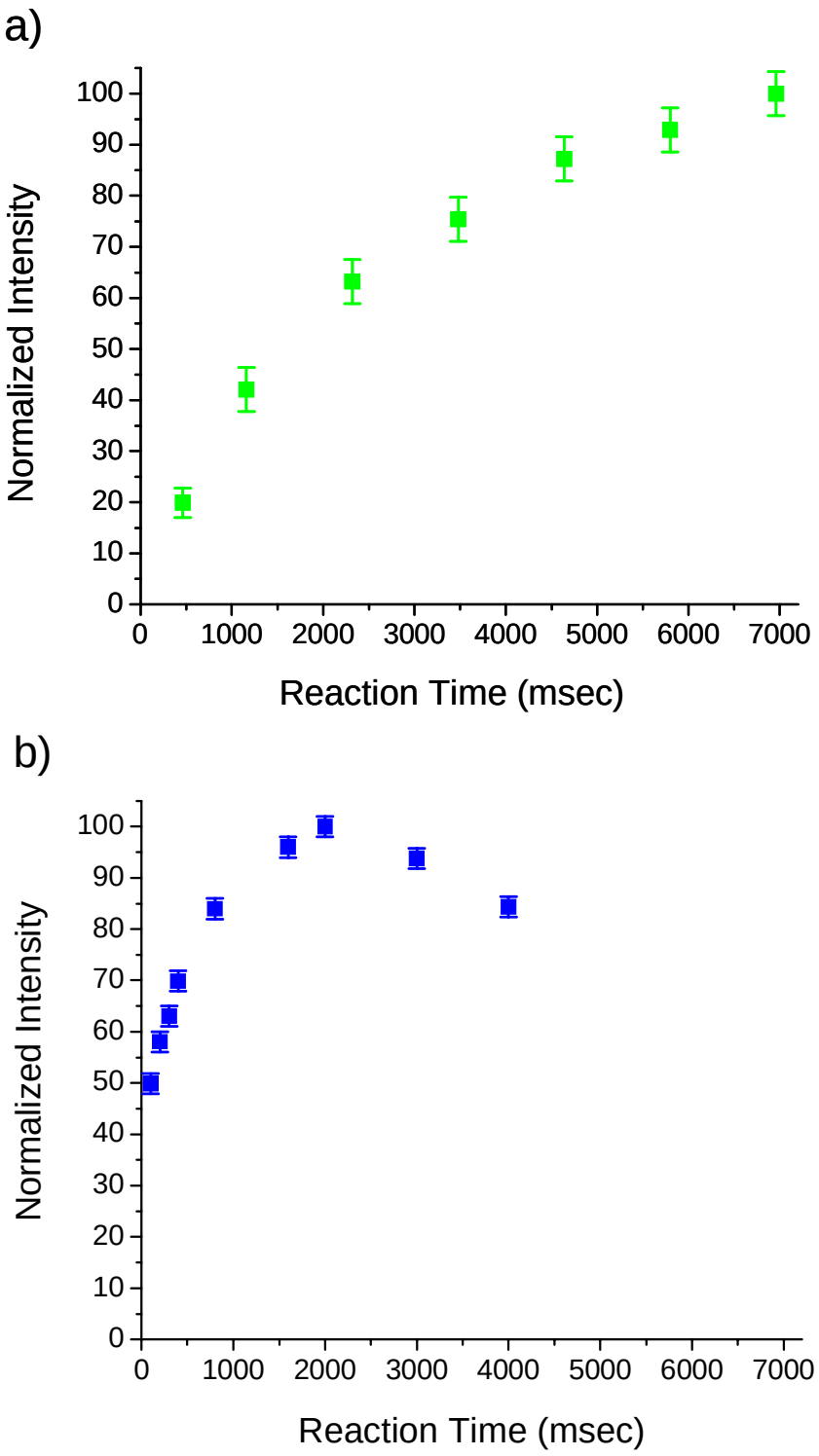

Figure 3.5 – SICI of 7.3 ppm MVK in air with H_3O^+ reagent. Monitoring $[M+H]^+$ intensity as a function of reaction time in a) QITMS and b) CCIT.

were attributed to a non resonance excitation process because of the higher order fields caused by geometry of the CCIT. Ions in the CCIT are possibly under space charge conditions; these conditions expand the ion cloud, putting the ions closer to the end caps. This is the same effect that occurs in resonance excitation. Therefore it is quite possible that ion losses at long reaction times in the CCIT are due to non resonance ejection.

3.7.2 Resonance ejection amplitude

The amplitude of the resonance ejection voltage is often scaled with increasing mass-to-charge ratio to improve ion ejection efficiencies. To find the optimal amplitude for resonance ejection, the amplitude of the supplemental AC voltage was varied and the intensity of protonated methyl vinyl ketone (*m/z* 71) was monitored. As shown in **Figure 3.6**, the ion signal in the ITMS was optimal when no resonance ejection was used, while in the CCIT 4 $V_{0\text{-}p}$ was optimal. In the CCIT from 1.5$V_{0\text{-}p}$ to 4 $V_{0\text{-}p}$ there is minimal change in ion signal; however, above 4 $V_{0\text{-}p}$, peak widths begin to increase due to off-resonance excitation. In resonance ejection, regardless of the amplitude of the applied resonance ejection voltage, the analyte signal intensity should theoretically remain constant because the number of ions ejected should remain constant. Typically this means that with resonance ejection, the intensity of the ion signal should increase while the width of the peaks should decrease. If ions are being lost during ion ejection, for example by striking an electrode, then the peak area will not remain constant. In the QITMS ions are likely being lost during ion ejection. Ion losses are likely the result of multiple factors. For instance, ions could be scattered due to the presence of the heavy buffer gas, which will be further explored in **Section 3.7.4**. This scattering is enhanced due to the kinetic excitation of the resonance ejection process. Another possible reason for ion loss is that ions are being ejected

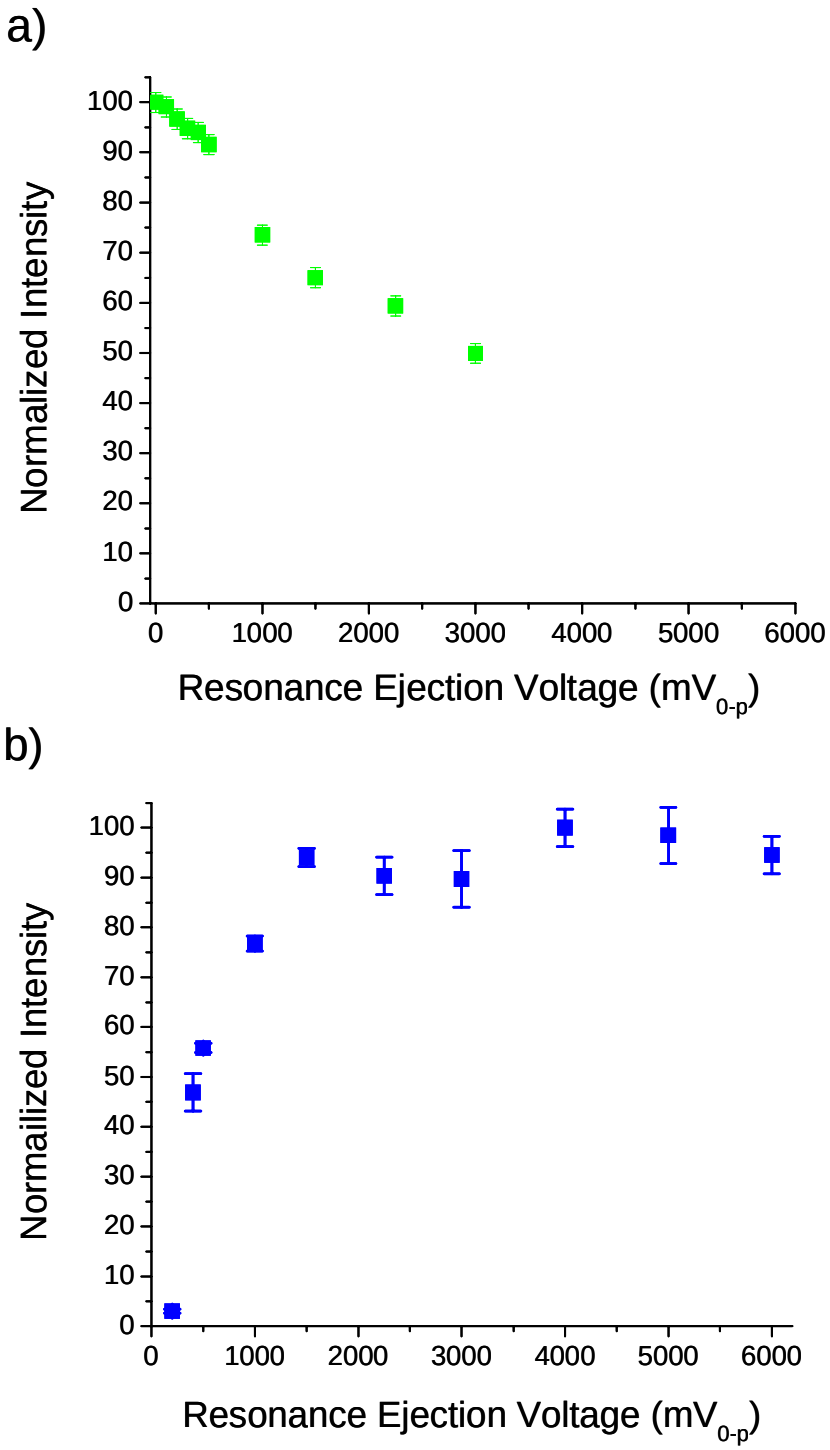

Figure 3.6 – Effects of resonance ejection amplitude on $[M+H]^+$ signal in a) QITMS ejected at $\beta_z = 0.96$ and b) CCIT ejected at β_z=0.5.

preferentially through the entrance endcap because of an asymmetry. This asymmetry might be present if the voltage applied to the exit endcap is slightly greater than the voltage applied to the entrance endcap. While the voltages applied were determined to be identical at the power supply/transformer balun, the voltages were not measured directly at the endcap electrodes, allowing for slight differences in the voltage actually applied to the endcap electrodes. The slight differences may be present due to electrical losses in the electrical connections of the supplemental ac voltage. Another asymmetry could be present because the entrance endcap in the QITMS has more holes present than the exit endcap, creating a geometric asymmetry that is enhanced when performing resonance ejection.

3.7.3 SICI and Resonance Ejection at Non-Linear Resonances

SICI of isoprene (10 ppm), methyl vinyl ketone (7 ppm), and methacrolein (7 ppm) was performed with water as the reagent gas in the QITMS and the CCIT. Ions were resonantly ejected at various β_z eject values and the signal intensity of the protonated molecule was monitored. Results for isoprene, methyl vinyl ketone, and methacrolein are shown in **Figure 3.7, Figure 3.8,** and **Figure 3.9** respectively. The data for all analytes in both instruments shows a drop in analyte signal intensities at the hexapole non-linear resonance (β_z = ⅔). In the QITMS, methacrolein (**Figure 3.8a**) and methyl vinyl ketone (**Figure 3.9a**) both show a decrease in signal intensity at the octapole non-linear resonance (β_z = ½). However isoprene (**Figure 3.7a)** appears to have a slight increase in ion signal in the QITMS at the octapole non-linear resonance (β_z = ½). In the CCIT, an increase was observed in the protonated molecule signal of isoprene and methacrolein at the octapole non-linear resonance (β_z = ½). The protonated molecule ion signal for methyl vinyl ketone shows an increase around β_z =0.45; however, at the octapole non-linear resonance the ion signal

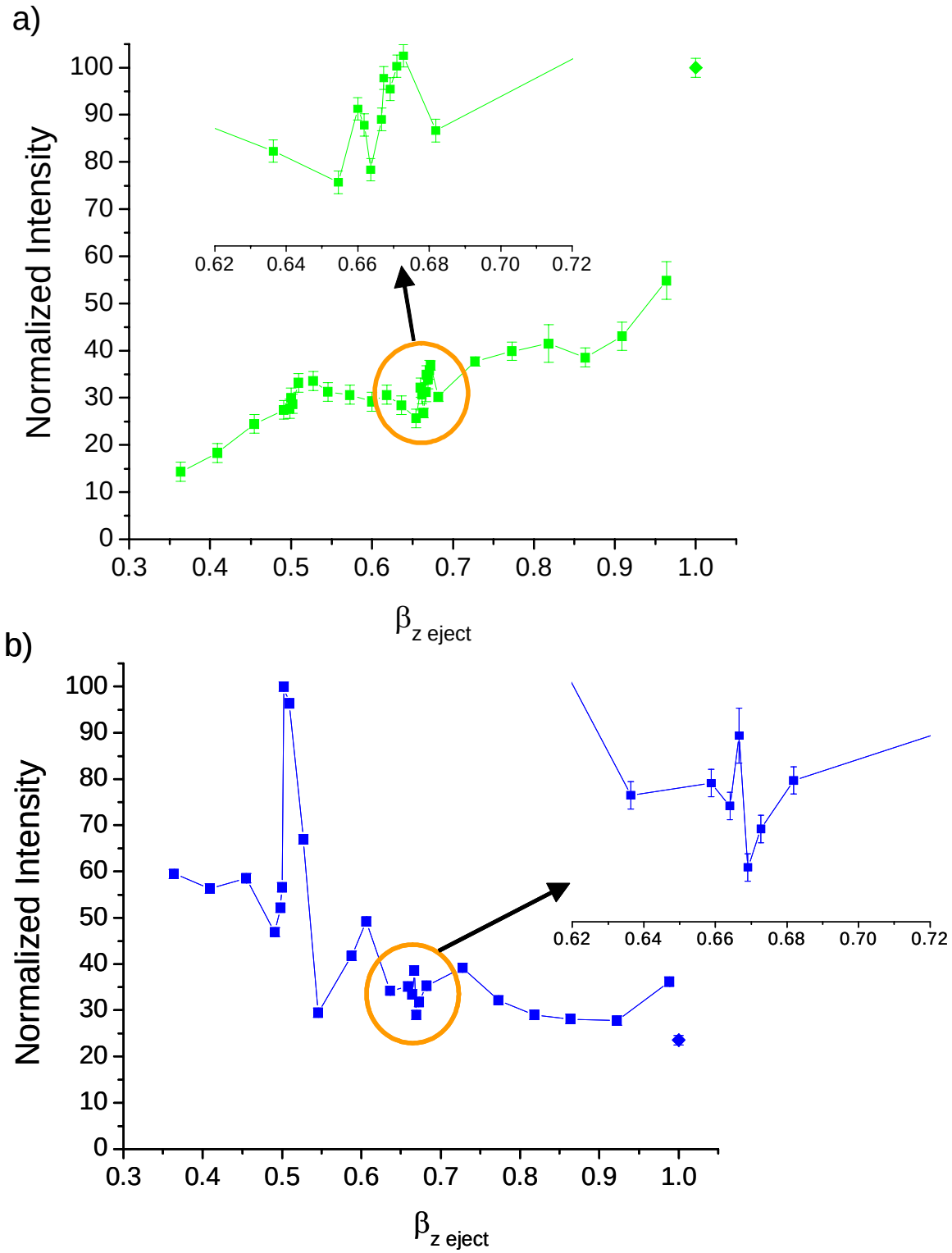

Figure 3.7 – Double resonance ejection of Isoprene $[M+H]^+$ at different β_z eject values in a) QITMS and b) CCIT. Zoom windows of hexapole resonance at $\beta_z = ⅔$. Unconnected point is with no resonance ejection.

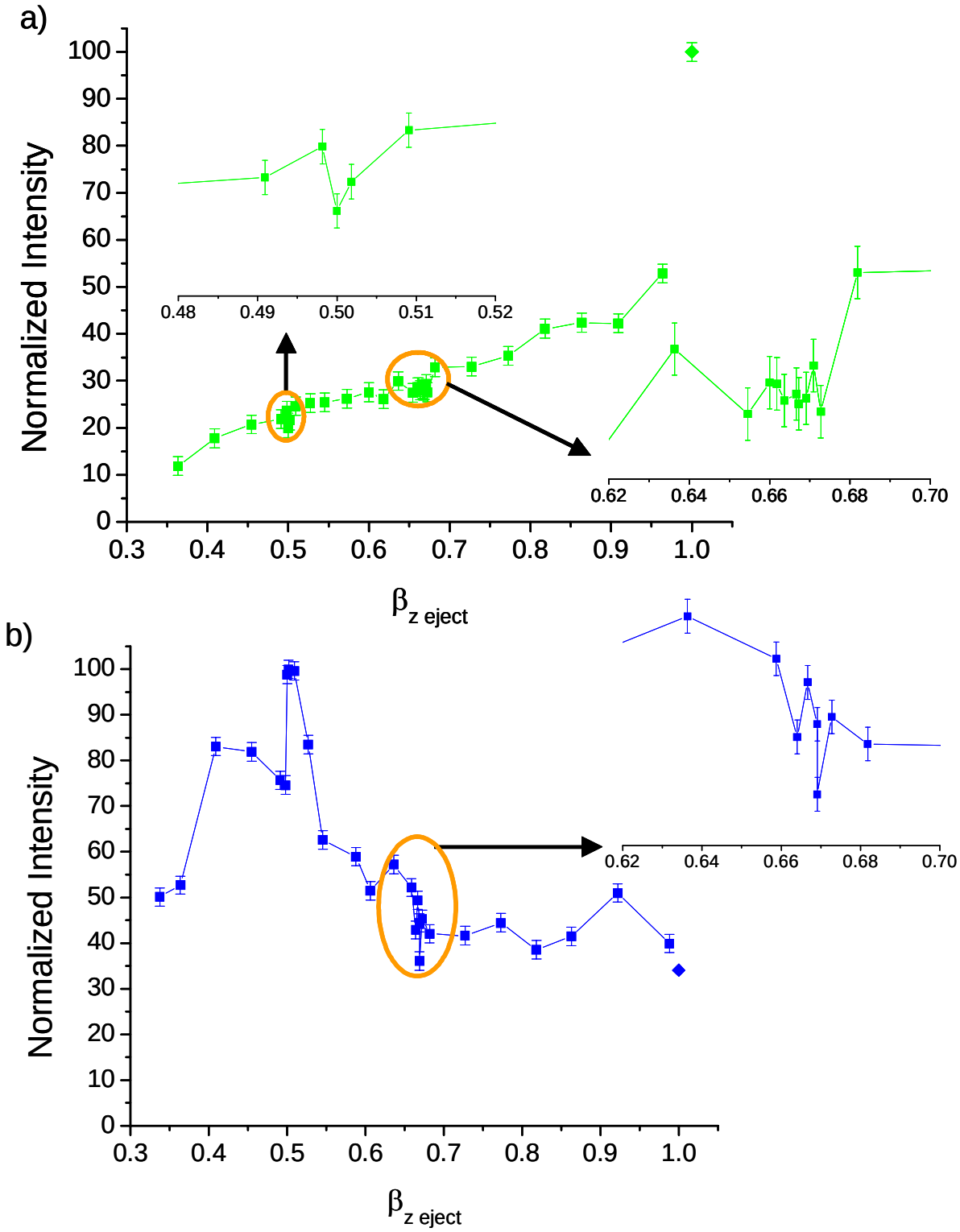

Figure 3.8 – Double resonance ejection of methacrolein $[M+H]^+$ at different β_z eject values in a) QITMS and b) CCIT. Zoom windows of hexapole resonance at $\beta_z = ⅔$ or octapole resonance at $\beta_z = ½$ Unconnected point is with no resonance ejection.

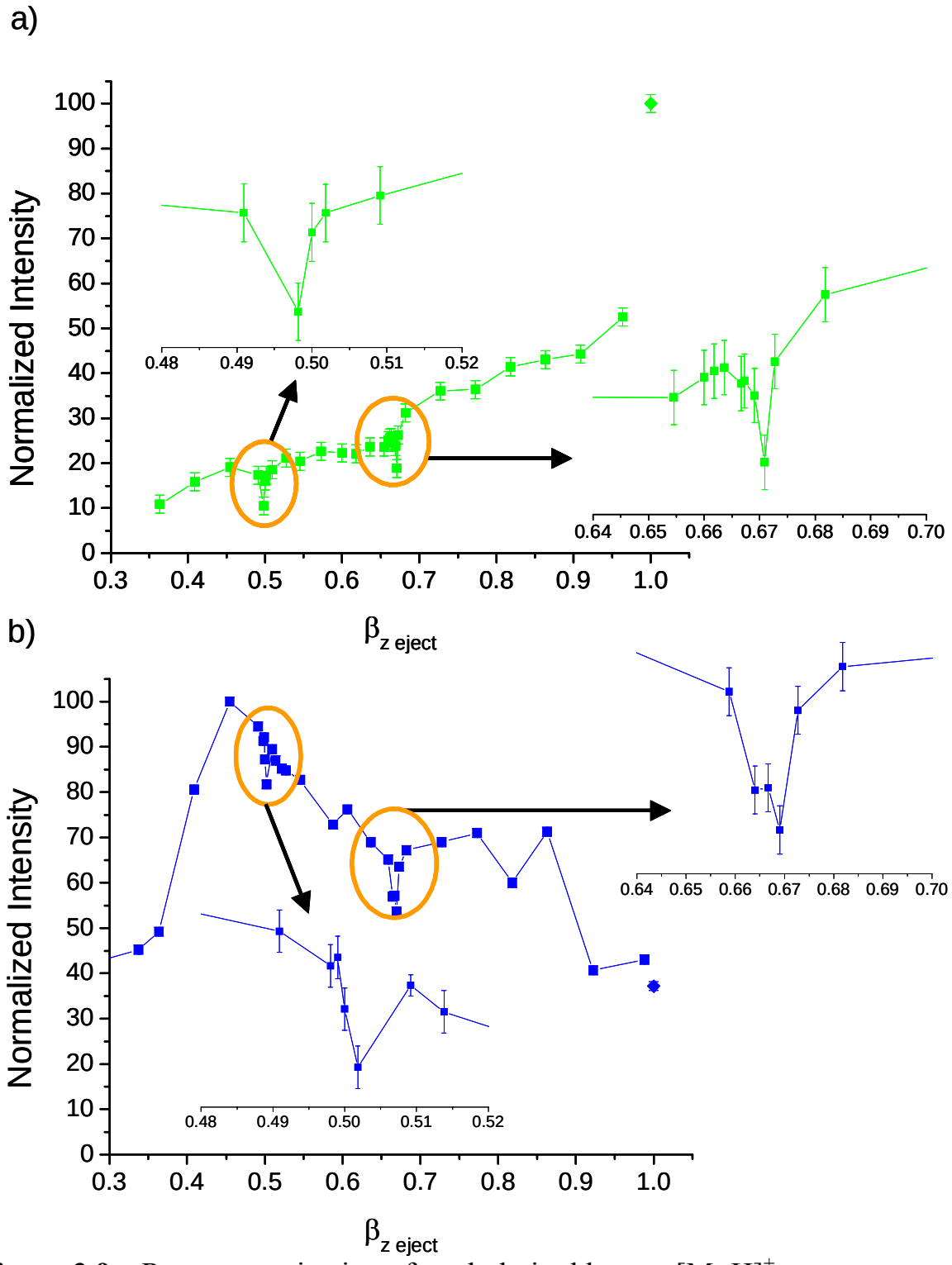

Figure 3.9 – Resonance ejection of methyl vinyl ketone $[M+H]^+$ at different β_z eject values in a) QITMS and b) CCIT. Zoom windows of hexapole resonance at $\beta_z = ⅔$ or octapole resonance at $\beta_z = ½$. Unconnected point is with no resonance ejection.

decreases. For the three compounds analyzed, the CCIT shows improvements in the observed signal at octapole non-linear resonances but a decrease in ion signal at the hexapole non-linear resonance. As was noted in the previous section the optimal detection method in the QITMS for all analytes was with no resonance ejection, meaning that ion signal is decreased with any resonance ejection voltage. Additional decreases in ion signal were then observed at both non-linear resonances. While the experiments were originally aimed at increasing ion signal with resonance ejection at non-linear resonances, the resulting ion losses are likely negative effects of higher order fields. The reasons for these ion losses are not clear. One possible explanation for ion losses is that ion motion, in the presence of higher order fields, is coupled in the radial and axial motion. Ion motion is coupled because, as described in **Section 1.4 Equation 1.35,** the electric potential with higher order fields has cross terms such as r^2z^2. The result of this coupling is that when ions are axially excited their radial motion also increases. Because the higher order fields are strongest closest to the end caps, this coupling of ion motion could result in ions striking an electrode because they are kinetically excited and because of the radial coupling from the non-linear resonance.

The difference in results between the two instruments can be related to the strength and location of the higher order field components. As previously stated, in the QITMS the higher order fields are localized and strongest near the end caps, whereas the higher order fields in the CCIT are present throughout the entire ion trap because of the cylindrical geometry. While it is still likely that the higher order fields in the CCIT are strongest near the endcaps, they are not localized higher order fields. Because of the location of the higher order fields in the QITMS, ions do not feel the effects of the higher order fields until they are close to the end caps where ions are lost because of the radial coupling of ion motion and

resulting increase in kinetic energy. Ions in the CCIT feel the effects of the higher order fields during more of their ejection time, thus radial coupling happens when ions are close to the center of the ion trap where there are no electrodes to strike. Additionally, the end caps of the CCIT are open and ions are less likely to strike an electrode surface than in the QITMS.

Resonance ejection at non-linear resonances affected methacrolein and methyl vinyl ketone differently. Methyl vinyl ketone showed a more pronounced effect at both non-linear resonances. In the CCIT, the methacrolein $[M+H]^+$ signal increased at the octapole non-linear resonance whereas methyl vinyl ketone decreased. It is well known that the kinetic energy gained from non-linear resonances can result in ion dissociation during ion ejection.[43] The result is usually a shift in the observed mass-to-charge ratio of the given ion, referred to as a mass shift, which was not observed. Mass shifts will be more thoroughly discussed in **Chapter 4**. Even though mass shifts were not observed, given that ion losses have already been noted with conventional resonance ejection, ion loss is still a possibility.

3.7.4 Heavy Buffer Gas

As discussed in **Section 3.4.2** the heavy buffer gas, which is present as air carrying the analyte, may be harmful to the overall experiment. The heavy buffer gas was also theorized to be a factor in ion losses in the QITMS. The heavy buffer gas was removed from the experiment by filling the Tedlar™ bag with helium and then injecting methyl vinyl ketone vapors into the bag (7 ppm). Ions were allowed to react with water reagent ions for 800 msec and then ions were resonantly ejected at various β_z eject values. The signal intensity of the protonated molecule was monitored at each β_z eject values. As shown in **Figure 3.10,** the optimal ion signal observed still occurred when no resonance ejection

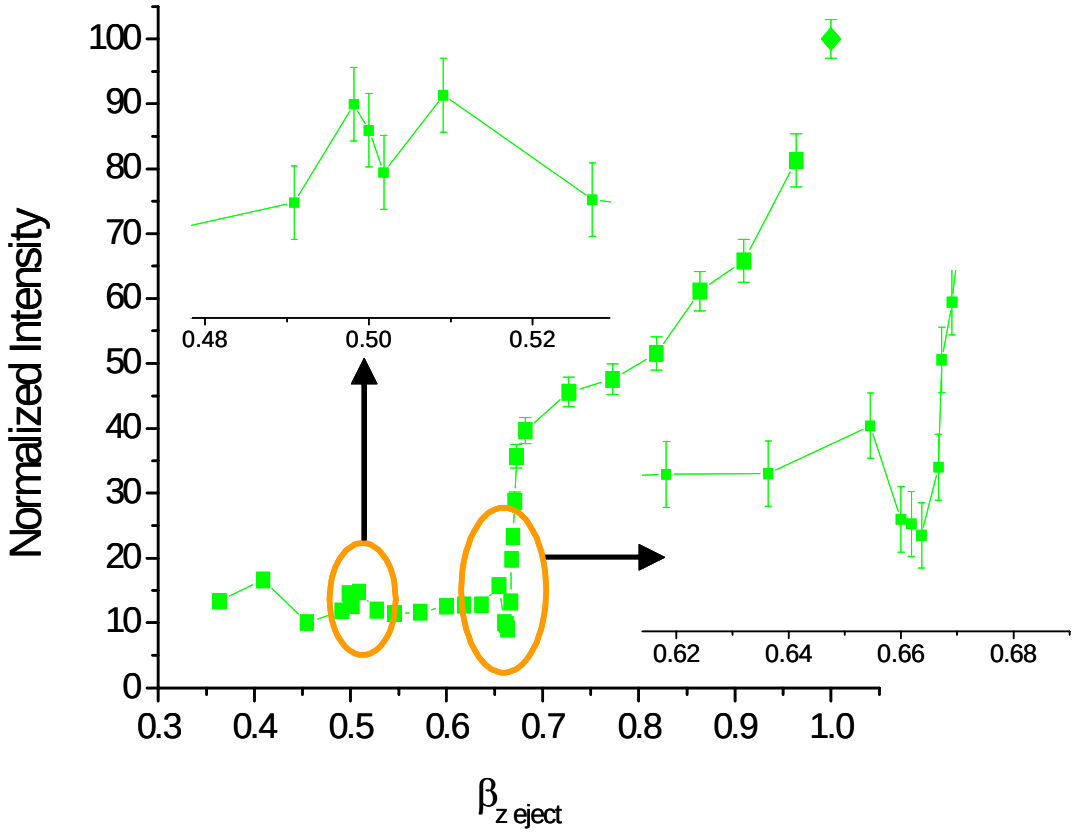

Figure 3.10 – Double resonance ejection of methyl vinyl ketone $[M+H]^+$ at different β_z eject values in QITMS with pure helium buffer gas. Zoom windows of hexapole resonance at $\beta_z = ⅔$ or octapole resonance at $\beta_z = ½$. Unconnected point is with no resonance ejection.

voltage was used. In the presence of heavy buffer gas almost half of the ion signal is lost between $\beta_{z\ eject} = 1$ (no resonance ejection) and $\beta_{z\ eject} = 0.96$ (see **Figure 3.9a**). With helium as the buffer gas, the ion signal only decreases about 20% from $\beta_{z\ eject} = 1$ (no resonance ejection) and $\beta_{z\ eject} = 0.96$. These results suggest that some of the ion losses observed in resonance ejection may be due to the presence of heavy buffer gas, but not all. A more pronounced decrease in the protonated molecule ion signal was observed at the hexapole non-linear resonance ($\beta_z = ⅔$) with helium than in the presence of the heavy buffer gas. Results at the octapole non-linear resonance ($\beta_z = ½$) were more comparable to the CCIT results (**Figure 3.9b)**, where there is an observed decrease in ion signal at the non-linear resonance but there is a more local increase in ion signal occurring before and after $\beta_z = ½$.

3.8 Conclusions

SICI of isoprene and its photooxidation byproducts methyl vinyl ketone and methacrolein was performed in a QITMS and a CCIT. The application of resonance ejection at octapole non-linear resonances in the presence of a heavy buffer gas mixture was shown to be successful at increasing ion signal in the CCIT, which will lead to improved sensitivities. At shorter reaction times (<800 msec) the CCIT may prove more sensitive for the detection of VOCs using resonance ejection at non-linear resonances. However, ion losses in the CCIT at long reaction times (> 2 seconds) due to non resonance ejection of ions will counteract any gained sensitivity from resonance ejection at non-linear resonances. Resonance ejection of ions in the QITMS caused a decrease in ion signal, with a further decrease in ion signal observed at non-linear resonances. Results from experiments in the QITMS without the heavy buffer gas showed that some of the ion losses during conventional resonance ejection

may be due to the presence of the heavy buffer gas. The effects of higher order fields was shown to be chemically dependant as methyl vinyl ketone showed more pronounced ion losses at non-linear resonances than its isomer methacrolein in both the QITMS and the CCIT, possibly due to ion fragmentation. If the ion losses due to non resonance ejection processes in the CCIT can be prevented, the CCIT may be an ideal ion trap for the detection of VOC's in conjunction with resonance ejection used at non linear resonances.

3.9 References

1. Atkinson, R., *Gas-Phase Tropospheric Chemistry of Volatile Organic Compounds.* Journal of Physical Chemistry Reference Data, 1997. 26(2): p. 215-290.

2. Doyle, M.; Sexton, K. G.; Jeffries, H.; Bridge, K.; Jaspers, I., *Effects of 1,3-Butadiene, Isoprene, and Their Photochemical Degradation Products on Human Lung Cells.* Environmental Health Perspectives, 2004. 112(15): p. 1488-1495.

3. Kuster, W. C.; Jobson, B. T.; Karl, T.; Riemer, D.; Apel, E.; Goldon, P. D.; Fehsenfeld, F. C., *Intercomparison of Volatile Organic Carbon Measurement techniques and Data at La Porte during the TexAQS2000 Air Quality Study.* Environmental Science and Technology, 2004. 38(1): p. 221-228.

4. Lindinger, W.; Hansel, A.; Jordan, A., *On-line monitoring of volatile organic compounds at pptv levels by means of Proton-Transfer -Reaction Mass Spectrometry (PTR-MS) Medical Applications, food control, and environmental research.* International Journal of Mass Spectrometry, 1998. 173: p. 191-241.

5. Prazeller, P.; Palmer, P.; Boscaini, E.; Jobson, T.; Alexander, M., *Proton Transfer Reaction Ion Trap Mass Spectrometer.* Rapid Communications in Mass Spectrometry, 2003. 17: p. 1593-1599.

6. Glish, G. L.; Van Berkel, G. L.; McLuckey, S. A. *Selected Ion Chemical Ionization Ion Trap Mass Spectrometry*. in *Proceedings of the 11th International Mass Spectrometry Conference*. 1988. Bordeaux, France.

7. Dalton, C. N. *Applications of Glow Discharge Ionization for Environmental Analysis* Doctoral, University of North Carolina, Chapel Hill, 2002.

8. Wendling, K. S.; Kaplan, D. A.; Glish, G. L. *Selected Ion Chemical Ionization in a Quadrupole Ion Trap Mass Spectrometer for the Detection of Volatile Organic Compounds*. in *Proceedings of the 53th American Society for Mass Spectrometry Conference on Mass Spectrometry*. 2005. San Antonio, TX.

9. Franzen, J.; Gabling, R.-H.; Heinen, G.; Weiss, G. Method for mass-spectroscopic examination of a gas mixture and mass spectrometer intended for carrying out this method. US Patent 5028777, 1991.

10. Danell, R. M.; Danell, A. S.; Glish, G. L.; Vachet, R. W., *The use of static pressures of heavy gases within a quadrupole ion trap.* Journal of the American Society for Mass Spectrometry, 2003. 14(10): p. 1099-1109.

11. Dempster, A. J., *A New Moethod of Positive Ray Analysis.* Physical Review A, 1918. 11: p. 316-324.

12. Munson, M. S. B.; Field, F. H., *Chemical Ionization mass spectrometry. I. General introduction.* Journal of the American Chemical Society, 1966. 88: p. 2621.

13. Herron, W. J.; Goeringer, D. E.; McLuckey, S. A., *Ion-Ion Reactions in the Gas Phase: Proton Transfer Reactions of Protonated Pyridine with Multiply Charged Oligonucleotide Anions.* Journal of the American Society for Mass Spectrometry, 1995. 6: p. 529-532.

14. Jakubowski, N.; Bogaerts, A.; Hoffmann, V., *Analytical Glow Discharges*, in *Atomic Spectroscopy in Elemental Analysis*; Cullen, M., Ed.; CRC Press: Boca Raton, 2004, pp 91-156.

15. McLuckey, S. A.; Glish, G. L.; Asano, K. G.; Grant, B. C., *Atmospheric Sampling Glow Discharge Ionization Source for the Determination of Trace Organic Compounds in Ambient Air.* Analytical Chemistry, 1988. 60: p. 2220-2227.

16. Rodriguez, J.; Pereiro, R.; Sanz-Medel, A., *Glow discharge atomic emission spectrometry for the determination of chlorides and total organochlorine in water samples via on-line continuous generation of chlorine.* Journal of Analytical Atomic Spectrometry, 1998. 13(9): p. 911-915.

17. Broekaert, J. A. C., *Glow Discharge Atomic Spectroscopy.* Appl. Spectrosc., 1995. 49(7): p. 12A.

18. Marcus, R. K. *Glow Discharge Spectroscopies*; Plenum Press: New York, 1993.

19. You, J.; Fanning, J. C.; Marcus, R. K., *Particle Beam Aqueous Sample Introduction for Hollow Cathode Atomic Emission Spectroscopy.* Analytical Chemistry, 1994. 66: p. 3916-3924.

20. Dalton, C. N.; Jaoui, M.; Kamens, R. M.; Glish, G. L., *Continuous real-time analysis of products from the reaction of some monoterpenes with ozone using atmospheric sampling glow discharge ionization coupled to a quadrupole ion trap mass spectrometer.* Analytical Chemistry, 2005. 77(10): p. 3156-3163.

21. Asano, K. G.; McLuckey, S. A.; Glish, G. L., *Comparison of Atmospheric Sampling Glow Discharge Ionization with Electron Ionization.* Spectros. Int. J., 1990. 6: p. 191-210.

22. Berberich, D. W.; Hail, M. E.; Johnson, J. V.; Yost, R. A., *Mass-Selection Of Reactant Ions For Chemical Ionization In Quadrupole Ion Trap And Triple Quadrupole Mass Spectrometers.* International Journal of Mass Sprectrometry and Ion Processes, 1991. 94: p. 115-147.

23. Strife, R. J.; Keller, P. R., *Ion Trap Chemical Ionization Mass Spectrometry - RF/DC for Isolating Unique Reactant Ions.* Organic Mass Spectrometry, 1989. 24: p. 2001-2204.

24. Tanner, D. J.; Jefferson, A.; Eisele, F. L., *Selected ion chemical ionization mass spectrometric measurement of OH.* J. Geophys. Res., 1997. 102: p. 6415-6425.

25. March, R. E.; Todd, J. F. J., Eds. *Quadrupole Ion Trap Mass Spectrometry*, 2nd ed.; John Wiley & Sons, Inc.: Hoboken, NJ, 2005.

26. Todd, J. F. J.; Waldren, R. M.; Mather, R. E., *The Quadrupole Ion Store (QUISTOR) Part IX. Space-Charge and Ion Stability. A Theoretical Background and Experimental Results.* International Journal of Mass Spectrometry and Ion Processes, 1980. 34: p. 325-349.

27. Cox, K. A.; Cleven, C. D.; Cooks, R. G., *Mass Shifts and Local Space Charge Effects Observed in the Quadrupole Ion Trap at Higher Resolution.* International Journal of Mass Spectrometry and Ion Processes, 1995. 144: p. 47-65.

28. McLuckey, S. A.; Glish, G. L.; Asano, K. G., *Coupling of an Atmospheric-Sampling Ion Source with an Ion-Trap Mass Spectrometer.* Analytica Chimica Acta, 1989. 225: p. 25-35.

29. Charles, M. J.; McLuckey, S. A.; Glish, G. L., *Competition Between Resonance Ejection and Ion Dissociation During Resonant Excitation in a Quadrupole Ion Trap.* Journal of the American Society for Mass Spectrometry, 1994. 5: p. 1031-1041.

30. Morand, K. L.; Cox, K. A.; Cooks, R. G., *Efficient Trapping and Collision-induced Dissociation of High-mass Cluster Ions Using Mixed Target Gases in the Quadrupole Ion Trap.* Rapid Communications in Mass Spectrometry, 1992. 6: p. 520-523.

31. Vachet, R. W.; Glish, G. L., *Effects of Heavy Gases on the Tandem Mass Spectra of Peptide Ions in the Quadrupole Ion Trap.* Journal of the American Society for Mass Spectrometry, 1996. 7: p. 1194-1202.

32. Wang, Y.; Franzen, J.; Wanczek, K. P., *The Non-Linear Resonance Ion Trap. Part 2. A General Theoretical Analysis.* International Journal of Mass Spectrometry and Ion Processes, 1993. 124: p. 125-144.

33. Franzen, J.; Gabling, R.-H.; Schubert, M.; Wang, Y., *Nonlinear Ion Traps*, in *Practical Aspects of Ion Trap Mass Spectrometry. Volume I. Fundamentals of Ion Trap Mass Spectrometry*; March, R. E., Todd, J. F. J., Eds.; CRC Press: Boca Raton, 1995; Vol. I, pp 49-167.

34. Alheit, R.; Kleineidam, S.; Vedel, F.; Vedel, M.; Werth, G., *Higher Order Non-Linear Resonances in a Paul Trap.* International Journal of Mass Spectrometry and Ion Processes, 1996. 154: p. 155-169.

35. Doroshenko, V. M.; Cotter, R. J., *Losses of Ions During Forward and Reverse Scans in a Quadrupole Ion Trap Mass Spectrometer and How to Reverse Them.* Journal of the American Society for Mass Spectrometry, 1997. 8(11): p. 1141-1146.

36. Guidugli, F.; Traldi, P., *A Phenomenological Description of a Black Hole for Collisionally Induced Decomposition Products in Ion-trap Mass Spectrometry.* Rapid Communications in Mass Spectrometry, 1991. 5: p. 343-348.

37. Morand, K. L.; Lammert, S. A.; Cooks, R. G., *Concerning 'Black Holes' in Ion-trap Mass Spectrometry.* Rapid Communications in Mass Spectrometry, 1991. 5: p. 491.

38. Guidugli, F.; Traldi, P.; Franklin, A. M.; Langford, M. L.; Murrell, J.; Todd, J. F. J., *Further Thoughts on the Occurrence of 'Black Holes' in Ion-trap Mass Spectrometry.* Rapid Communications in Mass Spectrometry, 1992. 6: p. 229-231.

39. Todd, J. F. J.; Penman, A. D.; Smith, R. D., *Some Alternative Scanning Methods for the Ion Trap Mass Spectrometer.* International Journal of Mass Spectrometry and Ion Processes, 1991. 106: p. 117-135.

40. Williams, J. D.; Reiser, H. P.; Kaiser, R. E.; Cooks, R. G., *Resonance Effects During Ion Injection into an Ion Trap Mass-Spectrometer.* International Journal of Mass Spectrometry and Ion Processes, 1991. 108(2-3): p. 199-219.

41. Moxom, J.; Reilly, P. T. A.; Whitten, W. B.; Ramsey, J. M., *Double Resonance Ejection in a Micro Ion Trap Mass Spectrometer.* Rapid Communications in Mass Spectrometry, 2002. 16(8): p. 755-760.

42. Kaplan, D. A.; Glish, G. L. *Development and Characterization of a Higher Order Field Ion Trap Mass Spectrometer*. in *Proceedings of the 52nd ASMS Conference on Mass Spectrometry and Allied Topics*. 2004. Nashville, TN.

43. Syka, J. E. P., *Commercialization of the Quadrupole Ion Trap*, in *Practical Aspects of Ion Trap Mass Spectrometry*; March, R. E., Todd, J. F. J., Eds.; CRC Press: Boca Raton, FL, 1995; Vol. I, pp 169-205.

Chapter 4

Fundamental Studies of Ion Injection and Trapping in Linear and Conventional 3-D rf Ion Traps

4.1 Introduction

Advances over the past 15 years in technology aimed at the quadrupole ion trap mass spectrometer (QITMS) such as the introduction of externally generated ions, automatic gain control, and ejection of larger mass ions above the nominal mass range have helped to make the QITMS one of the more robust mass analyzers in today's analytical laboratory.[1-5] Of these three advances perhaps the most important has been the introduction of externally generated ions. The first reports of externally generated ions being trapped in the QITMS were accomplished with ions generated in an electron ionization (EI) source and atmospheric sampling glow discharge ionization source similar to that described in **Chapter 3**.[1, 2] Development and further advancements of electrospray ionization, matrix assisted laser/desorption ionization, and atmospheric pressure chemical ionization have lead to the analysis of non-volatile samples in ion traps; e.g., biological samples.[6]

Early researchers showed that the injection of externally generated ions suffered from two major problems: mass bias and collision induced dissociation (CID).[1, 2] Researchers have extensively studied the effects of the QITMS's mass bias and reported methods to calibrate and minimize the effects of the mass bias.[1, 2, 7-10] There is some skepticism as to

whether ion dissociation is the result of collision induced dissociation, but regardless of the mechanism as ions enter the ion trap they can dissociate.[11-13] The result is a reduced molecular ion (or pseudomolecular ion) abundance, and increased abundance of fragment ions. Ions that undergo this dissociation are often termed fragile ions. One complexity with the fragile ion phenomena is that not all ions are fragile. While some compound classes such as n-alkanes are well known to be fragile, there are many compounds whose level of fragility is not known.[14, 15] The problem associated with fragile ions is that sometimes an analytical method is solely monitoring the ion abundance of the molecular ion and not fragment ions. Therefore ion traps are less sensitive to fragile ions. Fragile ion fragmentation is further complicated in instruments with EI sources because many of the fragment ions are also generated in the source. In addition to not always knowing which analytes are fragile or whether a fragment ion is formed from fragile ion fragmentation or source fragmentation, there is not a complete understanding as to what instrument factors influence fragile ion fragmentation. With the commercialization of the linear ion trap there is interest in studying fragile ions and comparing any observed fragmentation with the fragmentation observed in the conventional quadrupole ion trap.[16] The work described in this chapter will focus on fragile ions and factors that influence the amount of observed fragmentation in linear (2-D) and conventional (3-D) ion traps. The effects of the amplitude of the radio frequency (rf) voltage during ion injection, ion kinetic energy, and pressure were explored on a stand-alone 2-D ion trap and a stand-alone conventional 3-D ion trap with external EI ionization sources. The goal of these initial studies is to gain an understanding of how the above mentioned factors will impact the mass spectra that are generated in instruments that are commercially available. Some comparative studies that were conducted between the two instruments and a

quadrupole mass analyzer are also described. Because of the difficulty in determining whether a fragment ion was formed from as it entered the ion trap or in the source, a hybrid quadrupole 2-D ion trap and a hybrid quadrupole 3-D ion trap were constructed. These hybrid instruments allow fragile ions of a single mass-to-charge to be selected from the ion source and the amount of fragile ion fragmentation to be quantitatively observed in the mass spectra generated from the 2-D or 3-D ion trap. The effects of rf amplitude during ion injection, ion kinetic energy and pressure on fragile ion fragmentation were then explored on the hybrid quadrupole 2-D ion trap and hybrid quadrupole 3-D ion trap.

4.2 Background

4.2.1 Mass Shifts

When the quadrupole ion trap was commercially released in 1984 by the Finnigan Corporation, ions were created within the ion trap utilizing internal EI. Therefore fragile ion fragmentation during ion injection was not a concern; however, unwanted ion fragmentation was still a problem. Before the commercial release of the quadrupole ion trap, researchers at the Finnigan Corporation realized that mass spectrum of nitrobenzene acquired with a quadrupole ion trap was flawed.[17] The molecular ion of nitrobenzene was consistently recorded at 1 *m/z* lower than its actual value of *m/z* 123. Of the twenty or so compounds that were explored most did not have this problem but a select few suffered from this mass shift. Observed mass shifts were eventually reduced by axially stretching the distance between the end cap electrodes by 10.6%.[18] Since then, a lot of research has been devoted to the study of these mass shifts.[19-24] Research has separated mass shifts into two categories: ones of a chemical nature and ones that are not of a chemical nature. One example of a mass shift that

is not of a chemical nature is a mass shift resulting from ion/ion interactions, that is, exceeding the space charge limit (the number of ions that can fill the trap before degraded performance) of the ion trap. As the buffer gas pressure changes, ions will eject at slightly different rf voltages due to an increase or decrease in the number of collisions. The amplitude, frequency, and phase (relative to the operating frequency of the ion trap) of the supplemental ac voltage used for resonance ejection can all affect where ions are measured in the mass-to-charge scale. Chemical mass shifts are the result of ions fragmenting during the ejection process. These ions were also termed fragile ions. Because the fragmentation occurs during the ejection process, fragments of singly charged ions formed during ejection do not have stable trajectories and are ejected immediately. The fragmentation theory was definitively proven by researchers who created a hybrid 3-D quadrupole ion trap quadrupole mass spectrometer, where the quadrupole was used to mass analyze fragment ions that were created while ions are ejected from the ion trap.[24] Fragile ion fragmentation, as described in **Section 4.1**, is not just limited to the ion ejection process. Fragile ion fragmentation can also occur while ions are injected into the ion trap and it can also occur while using resonance ejection to isolate ions.

4.2.2 Fragile ion fragmentation

Some research has suggested that fragile ion fragmentation is the result of CID while other research suggests that it is the result of surface induced dissociation (SID).[2, 11, 12, 24] SID is generally a high energy process that results in fragmentation rich mass spectra, where as CID is gentler and results in fewer fragment ions than in SID. In either case, whether the collision is with a surface or a gas atom, the process involved is the conversion of the kinetic energy of an ion into internal energy. Dissociation occurs when the total internal energy of

an ion is sufficient to cause bond(s) to break, which will only be observed if this process can happen on the time scale of the experiment (before the ions strike the detector).

Fragile ion fragmentation during ion ejection (resonance ejection or mass selective instability) may be the result of kinetic excitation as a result of the linear excitation from the dipolar resonance ejection voltage that is applied to the endcap electrodes or the X-rods in the 3-D or 2-D ion trap respectively. Ions will "feel" the effects of this voltage when their axial motion is closest to endcap electrodes or X-rods; therefore, as ions are being ejected from the ion trap they are accelerated from the resonance ejection voltage. The ions kinetic energy is increased and the collisions with the buffer gas can result in dissociation. An additional explanation is that as ions are ejected they are kinetically excited due to non-linear fields that are present near the endcaps of the ion trap. As described in **Section 1.5**, these non-linear fields couple into the ion motion much more readily than quadrupole fields. The strength of the non-linear fields decrease rapidly as ions move toward the center of the ion trap, so ions only "feel" their effects near the endcaps. The strength of some non-linear fields was reduced by the axial stretch that was mentioned earlier, which reduced the observed mass shifts.

Fragile ion fragmentation that occurs during ion isolation occurs because the ions are gaining kinetic energy from the applied resonance excitation waveforms.[24] Even though the excitation waveform will not be in resonance with the ion, i.e. the waveform does not contain a frequency component equal to the ion secular frequency, the ion does gain some kinetic energy through off resonance excitation.[24, 25]

Ion fragmentation that occurs during the injection of externally generated ions is complicated by the fact that ions are not initially trapped. Ions must travel from the ion

source, through any ion optics, through the rf field, adopt their periodic motion and become trapped. During ion injection ions travel through rf fields that are not well defined, referred to as fringe fields. These fringe fields are the result of the rf voltage penetrating the holes in the entrance end caps. Once in the trapping volume, ions can be affected by higher order fields that are present near the endcaps. Additionally an ion may take several rf cycles after it has entered the ion trap to become completely trapped.[9, 26] During this period the ion's kinetic energy is being reduced through collisions with the buffer gas. These collisions can also result in CID. Therefore ions could fragment on the way into the ion trap, after they enter the ion trap but before their motion is stable, or possibly even after they have been trapped for several rf cycles. Fragile ion fragmentation during ion injection could depend on the ions kinetic energy before entering the ion trap, the pressure of the buffer gas, and/or the amplitude of the rf voltage during ion injection. Some research has been conducted on fragile ion fragmentation while injecting ions into a conventional 3-D ion trap, but no research has been conducted on the newer linear 2-D ion trap.[2, 11-13, 27] Most of the research suggests that when injecting ions at low kinetic energies (<20 eV) ion fragmentation is the result of CID.

4.2.3 Instrumental Concerns

As described in **Section 1.4.1.2**, the 2-D ion trap is a cross between the 3-D ion trap and the quadrupole mass filter. Geometrically, as with the quadrupole mass analyzer, the 2-D ion trap has 4 rods with a radio frequency (rf) potential of opposite phase and equal amplitude applied to every other rod. The commercial 2-D ion trap from Thermo Electron is separated into three sections, which can each have a dc offset potential applied to them in addition to the rf and dc voltage that are used to trap and eject ions.[16] The stand alone

version of this instrument that was used in the experiments in **Section 4.4** contains a curved prefilter that follows the ion source before the 2-D ion trap. The 3-D ion trap consists of two hyperbolic end cap electrodes and one hyperbolic torroidal ring electrode. The 3-D ion trap from Thermo Electron also has a dc offset applied to all three electrodes in addition to the rf and dc voltages used to trap and eject ions.

Similar to the 3-D ion trap the mass-to-charge (*m/z*) range of ions that are trapped in the 2-D ion trap is dependant upon the amplitude of the rf voltage and dc voltages applied to the trapping electrodes. Ions are ejected from the 2-D and 3-D ion traps using resonance ejection. In the 3-D ion trap the resonance excitation waveforms are applied to the end caps and ions are ejected out of either endcap; although only the exit endcap has a detector following it. In the 2-D ion trap ions are radially excited by applying the resonance excitation waveforms to the X rods, which have slots cut into them for ions to exit through. (See Figure 1.6 for picture of 2-D ion trap)

An additional difference between the 2-D and 3-D ion traps is in how the rf voltage affects the ion motion. In the 3-D ion trap the rf potential affects the ions motion in all dimensions. Because of the holes in the end cap electrodes, required for ions to enter and exit the ion trap, the rf potential is non-zero outside of the 3-D ion trap and ions must travel through this rf fringe field during ion injection. The fringe fields in radio frequency (rf) devices are the stray electric fields that can be observed outside the bounds of the devices. The presence of a fringe field means that an ion “feels” the effects of the rf potential before it enters the device. The fringe field gets larger as the amplitude of the rf voltage gets larger. Ions motion in a fringe field can be quite complicated and is not well understood; as rf fringe fields are difficult to model. In addition to the ions traveling through fringe fields, in the 3-D

ion trap they must have enough kinetic energy to overcome the amplitude of the rf voltage inside the ion trap. Therefore ions are only injected over a very small portion of the rf cycle. This results in fewer ions being trapped in the 3-D ion trap compared to the 2-D ion trap. In the 2-D ion trap and quadrupole analyzers, theoretically the rf voltage does not affect the ion's motion toward the detector (the ions' axial motion). The rf voltage does however affect the x and y motion of the ion. Thus, when the mass-to-charge of an ion is smaller than the lowest mass-to-charge that can be passed through the quadrupole the ion will likely hit a quadrupole or 2-D ion trap rod. Theoretically, because the rf voltage does not affect the ions' axial motion, ions are trapped over the entire rf cycle allowing for more ions to be trapped. In reality the slots in X-rods and non-idealities in the electrode geometry cause the rf voltage along the axial dimension to be non-zero. The separation between the prefilter and 2-D ion trap helps to minimize any fringe field; however, there is still some fringe field present. In general the dc potentials that are applied to the three sections of the 2-D ion trap are responsible for controlling the ion's axial motions; meaning the along with the radial effects of the rf potential ions must have sufficient kinetic energy to overcome the dc potential offset on the 2-D ion trap to be injected in to the 2-D ion trap. Understanding the similarities and differences between the 3-D and 2-D ion traps and the quadrupole mass analyzer will help to further identify what factors control fragile ion fragmentation.

4.3 Experimental

4.3.1 Analytes and Introduction Methods

Analytes explored during this work are the calibration gas perfluorotributylamine (FC-43), n-butylbenzene, tert-butylbenzene, nonane, xenon, and a mix of n-alkanes. The mix

of n-alkanes was diluted by 50% with hexanes from a mixture of n-alkanes that was 200 ng/mL of C_9H_{20}-$C_{26}H_{54,}$ $C_{28}H_{58}$, $C_{30}H_{62,}$ $C_{32}H_{66}$, $C_{34}H_{70}$, $C_{36}H_{74}$, $C_{38}H_{78}$, $C_{40}H_{82}$, and $C_{44}H_{90}$ for a sample concentration of 100 ng/mL. All of the analytes except the alkanes were directly introduced into the mass spectrometer's ion source by sampling the analytes' head space. Analytes introduced directly into the source were put into a vial enclosed with a septum and placed in an oven set at 50°C. Approximately 1.5 cm of a 1 m length section of a 0.25 μm inner diameter capillary gas chromatography (GC) column was inserted into the vial and the other end of the column section was connected to a metering valve (Magretti Avionics). The pressure of the analyte introduced could be varied by altering the temperature in the GC oven or by further opening or closing the metering valve. The metering valve was attached to a custom ion volume insertion/removal probe that was hollowed out and modified to connect to the leak valve. After the samples were prepared and connected to the insertion/removal probe, the connection was evacuated and then inserted into the mass spectrometer through the probe inlet of the instrument. The insertion/removal probe is conventionally used to insert and remove ion volumes from the ion source; however, this insertion/removal probe had a hollow core for neat volatile analyte introduction. The tip of the insertion/removal probe was positioned approximately 2.5 cm directly behind the ion source. The one meter section of column was changed and removable parts of the connection system were cleaned with acetone and heated after experiments with each compound.

4.3.2 Separation Methods

The mix of n-alkanes was run on a Focus GC (Thermo Electron, Austin TX) with the following method: The injector temperature was set to 275°C with a split/splitless (SSL) injected split flow of 20 mL/min, the mass spectrometer transfer line was set to 350°C, and

the ion source was set to 200°C. The GC was started at 60°C for 1 min and then ramped to 320°C at 25°C/min. The final temperature was held for 25 min. The carrier gas was held at 1 mL/min for the first 7.25 min and then ramped to 2 mL/min at a rate of 5 mL/min^2 and then held at 2 mL/min for the remainder of the GC run. The column for the 3-D ion trap (Polaris Q, Thermo Electron, Austin TX) and for the 2-D ion trap (Polaris LTQ, Thermo Electron, Austin Texas) was a 30 m column. The column for the quadrupole mass analyzer (DSQ, Thermo Electron, Austin TX) was a 15 m column; therefore, all the times for chromatography were halved from the 30 m column. Each instrument's election ionization source was set either to 50, 100, or 250 μA emission current and 70eV electron energy. During the separation of the analytes, the 2-D ion trap and 3-D ion trap were set to scan from 40-650 or 50-650 Da and 1-3 scans per mass spectrum were acquired. The single quadrupole was set to scan from 50-650 at a rate of 1603.4 Da/sec.

4.3.3 Injection rf Amplitude

Experiments designed to explore the effects of the amplitude of the rf voltage during ion injection were conducted in the 3-D and 2-D ion traps. During these experiments the injection rf amplitude was changed during ion ejection to a requested amplitude. The values requested were in terms of the low mass cut off (LMCO) or the lowest mass-to-charge ion that can be trapped in the instrument, which is directly related to the rf amplitude (**Equation 1.28**). In the 3-D ion trap the LMCO was varied from 4 -140 Da and in the 2-D ion trap the LMCO was varied from 4 Da to a value 10 Da greater than the mass-to-charge of the analyte ion. Following ion injection the LMCO was decreased to 50 Da for FC-43 ions and 35 Da for nonane, n-butylbenzene, and t-butylbenzene. In experiments with n-alkanes the LMCO was set to 40 in both ion traps and ions were acquired from 40-620 Da.

4.3.4 Ion Kinetic Energy

The kinetic energy of the ions is determined by the potential difference between the ion source and offset potential of the 3-D or 2-D ion trap. In the 2-D ion trap the ions spend the majority of their time in the center section of the ion trap; therefore the kinetic energy is determined by the potential difference between the source and the center section. Ions are generated between -2 and -3 V depending on the ion population in the EI source.[28] The prefilter before the 2-D ion trap has a dc offset which was set to -7 V. In experiments with the 2-D ion trap, following ion injection the front and back sections are raised to 0 V while the center section remains at the potential used for ion injection. The 2-D ion trap also has a lens following the last section which is set at + 10 V to prevent ions from axially ejecting out of the ion trap.

The trapping efficiency in both ion traps depends on the amount of kinetic energy that can be removed from the ion through collisions with the buffer gas so that ions will cool to the center of the ion trap and remain trapped. An additional concern in the trapping of ions in the 3-D ion trap is the pseudopotential well created by the rf voltage. This pseudopotential well is an estimate of an ion's kinetic energy as a function of the axial or radial dimension. At lower rf voltages the axial pseudopotential well ($\overline{D}_z$) can be calculated using **Equation 4.1**, where V is the amplitude of the rf voltage, Ω is the angular frequency of the rf voltage, and r_0 and z_0 are the radial and axial dimensions of the ion trap respectively.

$$\overline{D}_z = \frac{4eV^2 z_0^2}{m(r_0^2 + z_0^2)^2 \Omega^2} \qquad \textbf{EQ4.1}$$

If the initial kinetic energy of an ion is greater than pseudopotential well it must be cooled through collisions so that its kinetic energy is less than the pseudopotential well. If the

kinetic energy of the ions after collisions with the buffer gas is greater than the pseudopotential well then ion will continue through the rf trapping field and be ejected out of an endcap electrode. To remove effects of trapping efficiency, the LMCO (rf voltage during ion injection) was scaled with kinetic energy to ensure that the pseudopotential well depth was optimal for injection of ions at a given kinetic energy. In the 2-D ion trap the trapping potential well is created by the relative dc voltage on the center section compared to the back and front sections which are at 0 volts. A radial potential well does exist in the 2-D ion trap; however, this should not drastically affect trapping as it will in the 3-D ion trap. For consistency, the LMCO was scaled as a function of the kinetic energy for both the 2-D and 3-D ion traps.

4.3.5 General Experimental Conditions

The injection rf studies and ion kinetic energy studies in the stand alone 2-D and 3-D ion traps were performed using the selected ion monitoring (SIM) mode of the ion traps, which isolates the ion of interest after ion injection. Experiments in the hybrid instruments were done using the full scan mode, which has a short period of time following ion injection followed by ion ejection. The ion's abundance was then monitored as a function of the parameter being varied. Ten replicate scans were completed for each setting, averaged together, and the results stored in a database. The automatic gain control (AGC), which attempts to maintain a constant number of ions, was turned on for all experiments in both the stand alone and hybrid instruments. The AGC algorithms have a user input parameter called the "ion target", which relates to the number of trapped ions. The ion target for the 2-D trap was set to 5000 and for the 3-D trap the ion target was set to 5. The particular ion targets were chosen so that the number of ions trapped is small so that ions do not undergo space

charge effects, which can lead to degraded performance. The 2-D ion trap has a larger target because the maximum number of ions that can be trapped (without space charge effects) in the 2-D ion trap is greater than the 3-D ion trap.[16] More specifically AGC adjusts the time over which ions are gated into the ion trap. This is accomplished by performing a prescan, before the normal experimental scan, to determine the signal from a set gate time (typically 250 μsec). Based on this signal, the number of ions are determined, related back to the requested "ion target" number and the gate time during the normal experimental scan is readjusted. The prescan consists of a short ion injection time, followed by the quick ejection of back ground ions (*m/z 20 – 46)*, and finally the remaining ions are detected together in a non-mass selective manner by turning the rf voltage off. The overall prescan takes 1-2 msec. With AGC on, the number of ions in the ion trap is being controlled. Consider two separate experiments, both using AGC, (assuming a constant flux of ions from the source and the same requested ion target) in which one experiment required 2 msec to reach x number of ions, and the second experiment required 5 msec to reach the same number of ions. The ion injection in the experiment with 2 msec was more efficient because it required less time to trap the same number of ions.

4.4 Single Instrument Results

The study of fragile ion fragmentation is complicated by the fact that ions fragment both in the source and during ion injection. The effects of the amplitude of the rf voltage during ion injection and the initial kinetic energy on a few known fragile ions were conducted on stand-alone instruments, which can not easily separate the source fragmentation from fragmentation during ion injection. The results from these instruments

will be presented in this section to demonstrate the need for a hybrid quadrupole ion trap, one capable of differentiating between source and injection fragmentation.

4.4.1 Electron Ionization of n-alkanes

As mention in **Section 4.1**, analysis of externally generated ions in the QITMS is known to suffer from mass bias and fragile ion fragmentation during ion injections. Implications of these effects can be seen in the differences in mass spectra generated by QITMSs with external electron ionization (EI) sources and quadrupole mass analyzers with similar EI sources. The main advantage of EI is that it is a very reproducible ionization technique. Thus, EI mass spectra are compiled and libraries are created for verification of known compounds and identification of unknown analytes using the known library mass spectra. Quite often EI libraries do not state the mass analyzer used to acquire the mass spectrum, which is usually a quadrupole or sector instrument. Unfortunately, confidence in the instrumentation can decline when the produced mass spectra do not match library spectra. If a compiled EI library was taken with QITMS, the mass spectra may be comparable with mass spectra taken with other QITMSs; provided all instrument conditions are the same. However, QITMS EI libraries are not commercially available.

Straight chain alkanes are known to produce a low amount of molecular ion signal in quadrupole mass analyzers and an even lower amount in 3-D ion traps. The percent of the total ion current (%TIC) that is comprised of the molecular ion will be used as a measure of the level of the molecular ion signal present. For the purpose of these discussions the molecular ion %TIC will be referred to as the $M^{+\bullet}$(%TIC). This is calculated by taking the ratio of the area of the TIC chromatogram for a given compound's retention time and the area from the selected ion chromatogram for the molecular ion (^{12}C and ^{13}C). Below in **Figure**

4.1 (note: connected lines are for visual aesthetics, they do not denote a trend) is a comparison of the $M^{+\bullet}$(%TIC) of n-alkanes on the three different mass analyzers. The quadrupole mass analyzer detected more molecular ion signal for all of the n-alkanes in the mixture. Comparable molecular ion signals were observed in the 2-D ion trap and 3-D ion trap. The 3-D ion trap from dodecane (C_{12}) to nonadecane (C_{19}) appears to be producing more molecular ion signal than the 2-D ion trap. The inset plot in **Figure 4.1** shows that the precision for the 3-D trap was poorer than the 2-D ion trap. Under the optimal conditions for the two instruments, the 3-D trap from $C_{12}H_{26}$ to $C_{19}H_{40}$ showed more molecular ion signal.

The National Institute of Standard's (NIST) data in **Figure 4.1** is an average of 3-5 different replicate spectra in the NIST and Wiley databases. The quadrupole mass analyzer data had significantly more molecular ion than the NIST data over most of the range of alkanes. The NIST data had at least 2 fold greater molecular ion relative abundances than the 3-D or 2-D ion traps.

4.4.2 Storage Time

Fragile ion fragmentation may not occur during ion injection but rather several rf cycles following the initial trapping of the ions. To explore this possibility, the ion accumulation time was reduced to 10 μsec and a cool period of 10 μsec – 200 msec was added before ions were ejected. Because of instrumentation requirements the shortest time from the initial introduction of ions to the beginning of ion ejections was 750 μsec. This experiment was conducted on the 2-D ion trap while introducing nonane vapors into the EI source. Over the full time range no decrease in the molecular ion signal or increase in the fragment ion signal was observed. Instead the molecular ion signal increased as a function of time, most likely due to ion molecule reactions with the neutral analyte. The analyte is

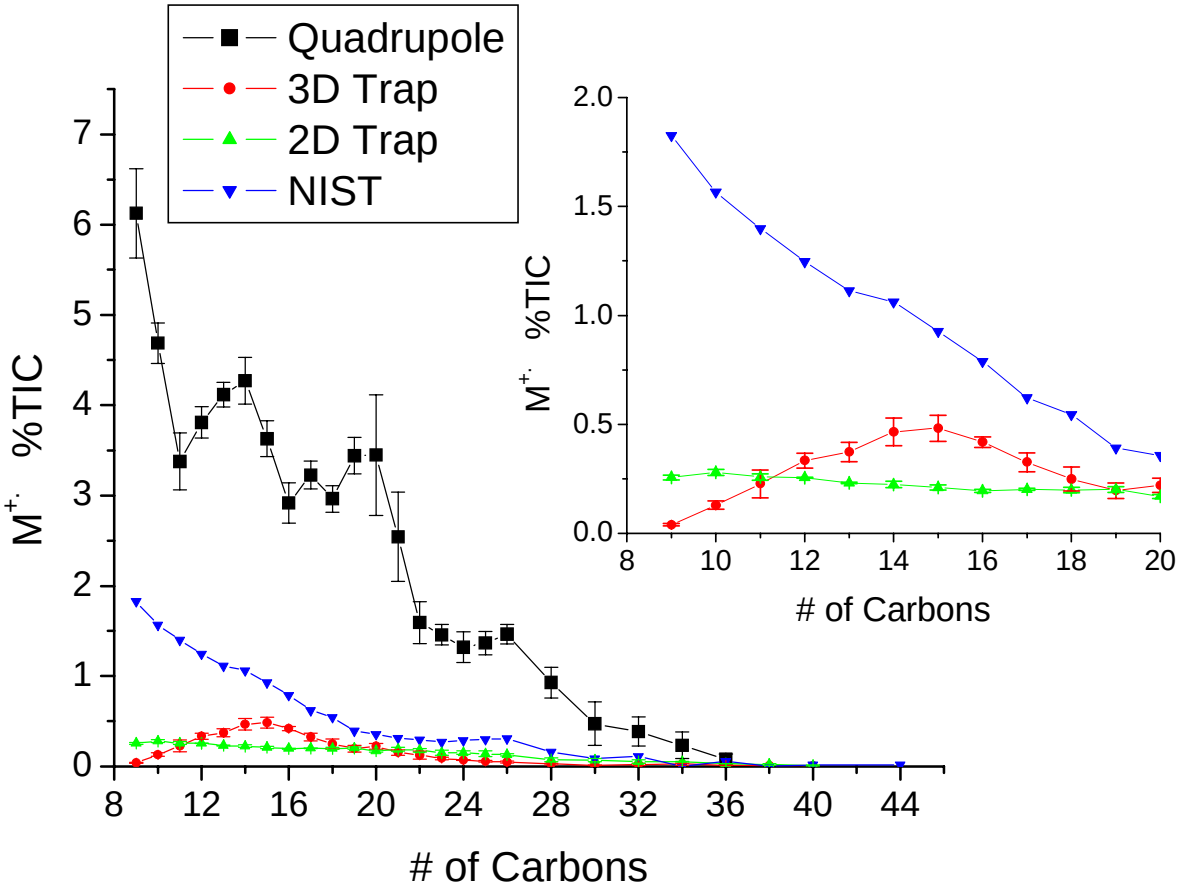

Figure 4.1- Plot comparing the molecular ion %TIC of n-alkanes on three different mass analyzers and NIST data. Source emission currents: 2-D ion trap 50 μA, 3-D ion trap 250 μA, and Quadrupole 50 μA.

present in the ion trap because its vapors are introduced into an open ions source, so there is nothing preventing the neutral analyte from entering the ion trap. Analyte vapor pressures were as low as possible so as to reduce the possibility of ion/molecule reactions, but they did still occur. Because of the long time between ion injection and ejection it can not definitively be stated that time is not a factor but above 750 rf cycles there does not appear to be a increase in the amount of fragmentation.

4.4.3 LMCO During Ion Injection

The LMCO (amplitude of the rf voltage) during ion injection has been previously shown to affect fragile ion fragmentation in 3-D ion traps.[1] As the LMCO is increased, the axial pseudopotential well depth increases allowing ions to absorb more kinetic energy from the rf voltage. The peak area of the fragments ions of FC-43 with *m/z* 69, 100, 131, 219, 264, 314, 414, 502 and 614 were monitored as a function of the LMCO during ion injection. To simplify the plot only the peak areas of *m/z* 69, 131, 219, 414, 502, and 614 were plotted as a function of the LMCO in **Figure 4.2**. In the 2-D ion trap, **Figure 4.2a**, ions should be injected from some threshold LMCO value until the LMCO is equal to the mass-to-charge ratio of the ion of interest. The threshold LMCO increases linearly as a function of mass-to-charge ratio as has been reported in the literature for 3-D ion traps.[2] Injection over the full range of LMCO was not observed for all ions, ions above *m/z* 400 were not trapped above LMCO 350. Most of the ions have a sharp increase in abundance above some threshold LMCO and then quickly drop ~35% in abundance and then slowly decrease until the ions are no longer trapped. The LMCO at which the area was reduced by 50% for a given ion is plotted as a function of the mass-to-charge ratio of all of the FC-43 fragment ions **Figure 4.3**. From this plot it is clear that *m/z* 209 and *m/z* 502 ions are affected more by higher amplitude

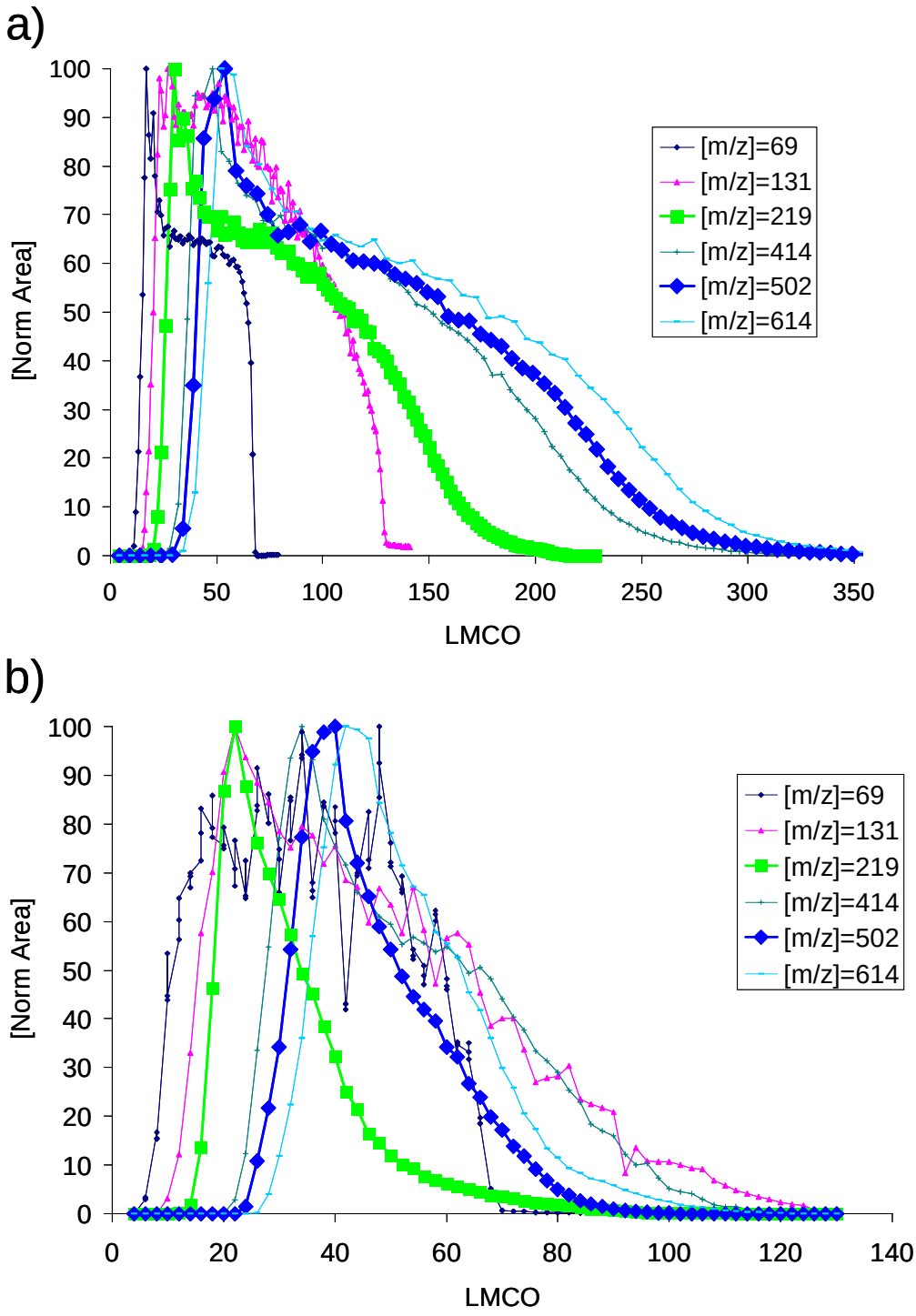

Figure 4.2- Effect of LMCO during ion injection. Ions of *m/z* 219 and 502 are highlighted to show the differences between these fragile ions from more stable ions. a) 2-D trap data b) 3-D trap data.

rf amplitudes than the other FC-43 fragment ions, although the difference observed for *m/z* 502 is less than *m/z* 219. These two ions are known fragile ions from FC-43. Another important observation from **Figure 4.2a** is that *m/z* 131 does not have the same shape as the other ions. Specifically, the peak area does not decrease after the initial spike. This increased peak area suggests that some ions are fragmenting to *m/z* 131 during ion injection; however, this instrumental set up will not allow for the determination of which ions are fragmenting to *m/z* 131.

As shown in **Figure 4.2b**, when the LMCO during ion injection is increased in the 3-D ion trap, the observed peak area for ions of *m/z* 502 and 219 decreased faster than smaller mass-to-charge ions. Research has shown that heavier mass-to-charge ions inject over a narrower range of LMCO than lighter mass-to-charge ions, because collisional cooling is not as effective due to the mass difference between the ion and the collision gas.[2] This effect explains why *m/z* 614 was injected over a narrower range of LMCO compared to *m/z* 414. However, the effect does not account for the narrower injection range that was observed for *m/z* 219 and 502 because *m/z* 414 and 614 were both injected over wider range of LMCO. As with the 2-D ion trap, some of the *m/z* 131 peak area may be the result of fragile ion fragmentation resulting in the ion appearing to be injected over a broader range of LMCO. In connection with *m/z* 131 possibly being injected over a wider range of LMCO and *m/z* 219 and 502 being injected over a narrower range of LMCO there is likely fragile ion fragmentation occurring in the 3-D ion trap. However, it is difficult to truly determine how much fragmentation is occurring because all the ions decrease in abundance well before their mass-to-charge is equal to the LMCO during ion injection.

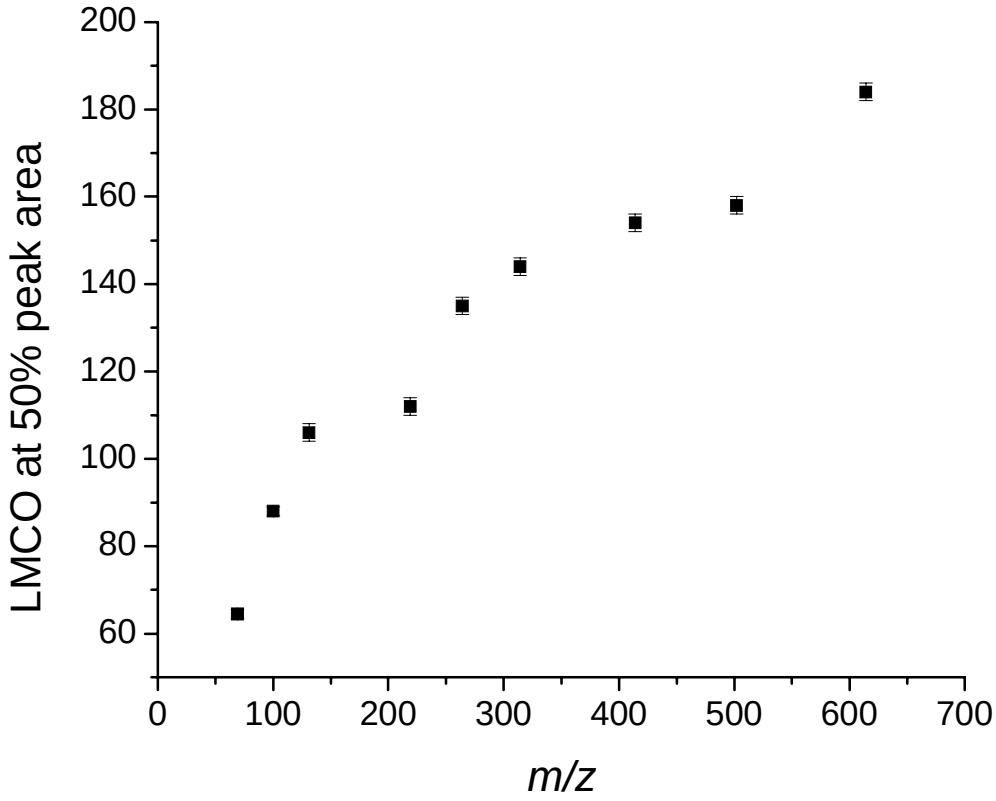

Figure 4.3 – LMCO during ion injection in 2-D ion trap when ion peak area was reduced 50% after maximum peak area.

The injection rf experiments with n-butylbenzene and nonane had similar results compared to FC-43 ions; however, the source fragment ions for these analytes are lower in mass-to-charge than most of the FC-43 ions so the ions are ejected at lower LMCO. Thus higher rf amplitudes are not reached, which would increase the amount of fragmentation observed.

4.4.4 Initial Ion Kinetic Energy

The initial kinetic energy of an ion is adjusted by changing the dc offset voltage of the 3-D ion trap or the dc offset of the center section of the 2-D ion trap. These dc offsets will be referred to as the trap offset. When the trap offset was varied while injecting FC-43 fragment ions *m/z* 69, 100, 131, 219, 264, 314, 414, 502, and 614 the observed results are quite similar to those described for the LMCO varied during ion injection in **Section 4.4.2**. As shown in **Figure 4.4**, in both instruments the ions of *m/z* 219 and 502 stand out from the other ions. In the trap offset curves the 219 and 502 *m/z* ions increase in abundance until the trap offset reaches -10V and then they quickly decrease. The other ions, such as the ion of *m/z* 69, continue to increase until -30 V in the 2-D ion trap and -40 V in the 3-D ion trap. The normalized areas for *m/z* 69 ion and other ions continue to increase at more negative trap offsets because higher mass-to-charge ions are fragmenting to these ions, such as *m/z* 502 and 219 ions. Larger kinetic energies, as set by the more negative trap offset voltage, lead to significantly more fragmentation. This is likely the result of increased CID because of the increased kinetic energy. Determining which ions are fragmenting to *m/z* 131 and *m/z* 69 is not possible in these instrument; however, it will be possible when the source fragment ions are removed from the mass spectrum

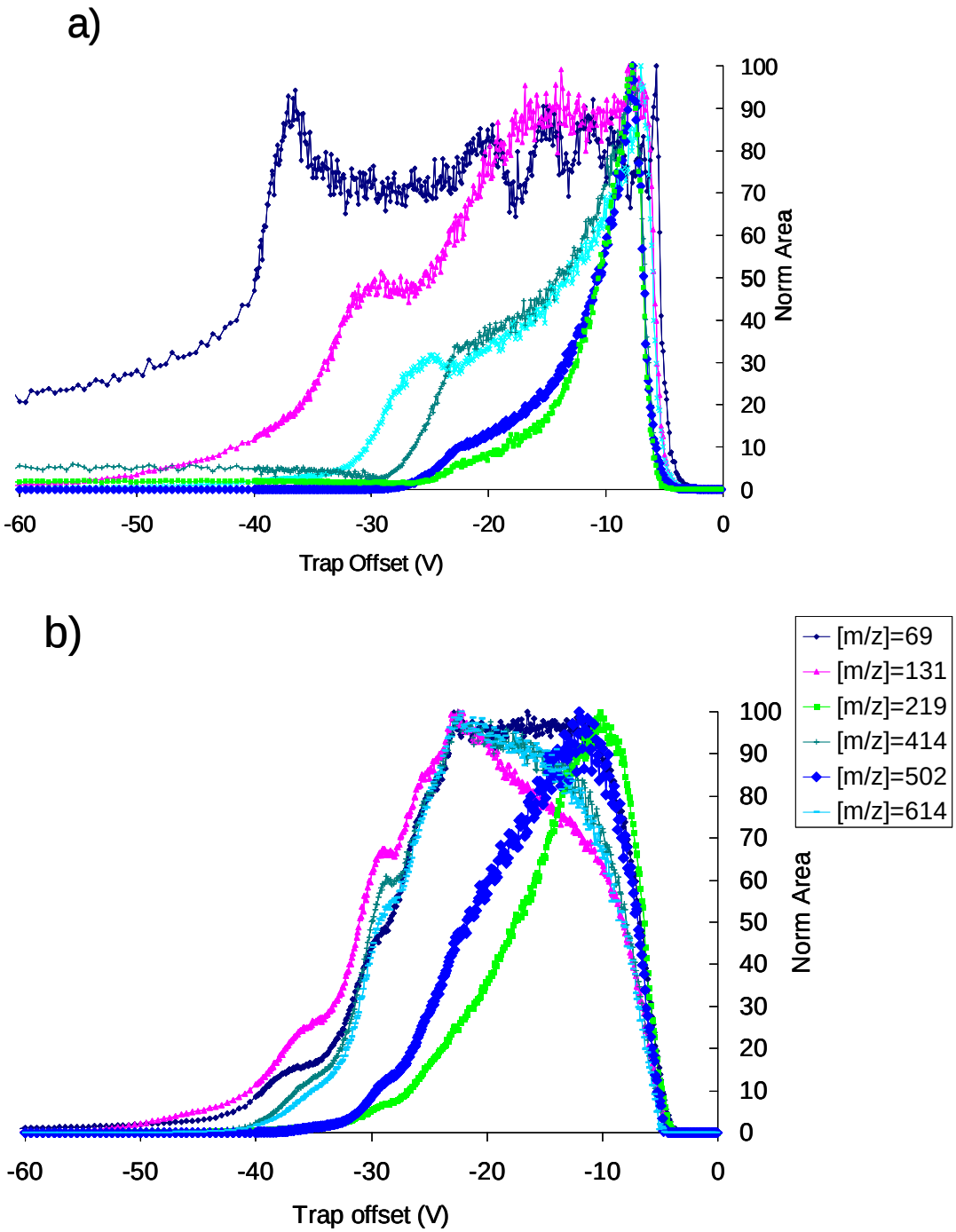

Figure 4.4 – Effect of trap offset voltage on injection of FC-43 ions in a) 2-D ion trap data and b) 3-D trap data.

Trap offset experiments run with n-butylbenzene, t-butylbenzene and nonane, which are all fragile ions, yielded similar results as the FC-43 ions. As the trap offset was decreased the molecular ion abundance with all of these analytes increases very quickly until about -10 V and then quickly decreases. Similarities in the curves between these three different compounds and the FC-43 fragment ions *m/z* 502 and 219 compared to the non-fragile ions of FC-43, i.e. *m/z* 131, suggest that the shape of the trap offset curve can be used as a benchmark for the ions' fragility.

4.5 Hybrid Instrumentation

4.5.1 Motivation

One problem that all of these above experiments have is that any comparisons between the 3-D trap, 2-D ion trap, and quadrupole are all convoluted by that fact that only the 2-D ion trap and quadrupole mass filter have a bent prefilter following the ionization source before the mass analyzer. In studying fragile ions, there needs to be a way to observe improvements to the amount of fragile ion fragmentation. A second problem arises because many of the fragments that the fragile ions make are also generated in the source. Therefore determining the genealogy of fragment ions can be quite challenging. The best solution to both of these problems is to design and build an instrument that will allow for the study of fragile ions by selecting one ion from the ionization source and observing what fragments appear in the mass spectrum. This instrument will also allow for better comparisons between 2-D and 3-D ion traps because the instrument will have the same ionization source and ion transfer optics in both configurations.

As illustrated in **Figure 4.5**, this hybrid mass spectrometer consists of an ion source, prefilter, quadrupole mass analyzer and then either a 3-D trap or a 2-D trap. This instrument was designed by Joe Weick, Scott Quarmby, and Brody Guckenberger; and I contributed toward the end of the design work.

4.5.2 Instrument Construction, Operation, and Tuning

The quadrupole mass analyzer was first put into the system with a detector to be tuned and tested. There were minimal problems with tuning the quadrupole and getting it to operate properly in the larger vacuum manifold. The larger manifold is compromised of a modified vacuum manifold for the Polaris Q (Thermo Electron, Austin TX) QITMS and the DSQ (Thermo Electron, Austin TX) single quadrupole. These two vacuum manifolds are held together with a set of four M4 screws and a seal is created by an o-ring between the two manifolds. After optimizing the performance of the quadrupole, the detector was removed. An exit lens with an aperture size of 1.5 mm, for efficient ion transfer to the 3-D trap, was installed at the quad exit. During operation the quad exit lens was held at the same potential as lens 3 of the ion source. The 3-D ion trap was then installed and pushed up against the quadrupole exit lens, which was electrically isolated with a ceramic spacer. The ceramic spacer had sufficient holes to allow for out-gassing. The electron multiplier detector used for the quadrupole was also used for the 3-D ion trap. To tune the ion trap the quad was set to rf only mode by installing a switch to turn on and off the dc to the quadrupole rod driver. The ion trap was mass calibrated and went through waveform calibration at Helium flow rates of 0.3, 0.6, 1.0, 1.6 and 2 mL/min (pressures reported with data). Following the calibration, trap offset experiments and injection rf experiments at several trap offsets were run at various pressures. The instruments communicated using a spare analog input on the quadrupole mass

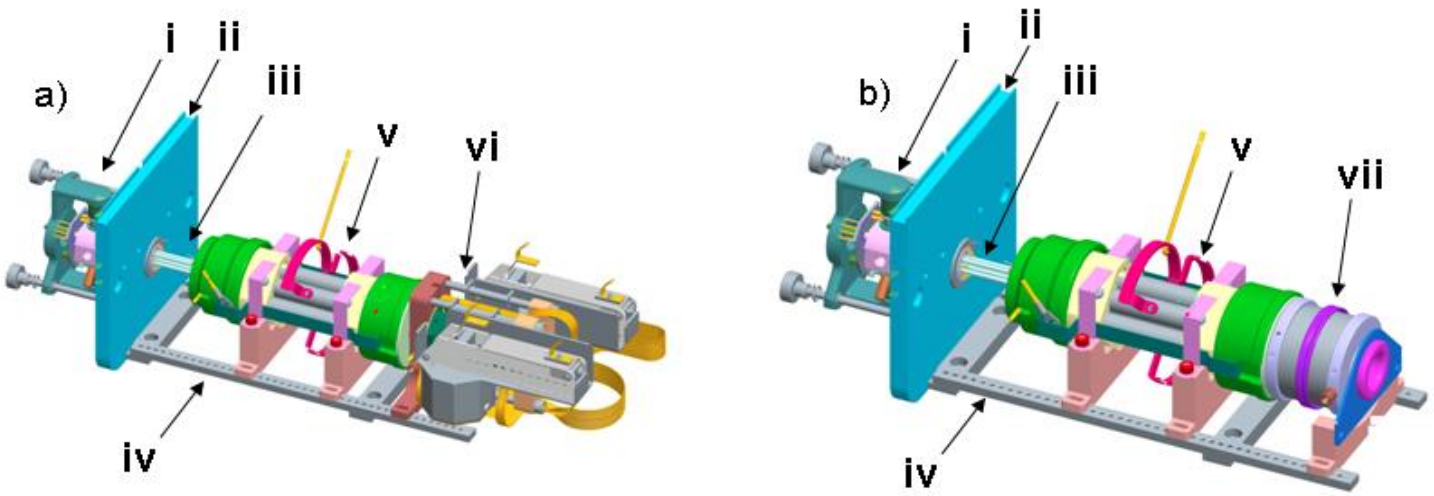

Figure 4.5 – Images of hybrid mass spectrometer constructed during internship at Thermo Electron a) Quad 2-D ion trap and b) Quad 3-D ion trap. The labeled components of each instrument are i) EI source, ii) baffle wall, iii) prefilter, iv) mounting assembly, v) quadrupole mass filter and assembly, vi) 2-D ion trap and assembly, and vii) 3-D ion trap and assembly. Parts i-v are the same parts in both instruments.

analyzer analog board. A voltage sent from the 3-D trap's analog board set the voltage of the analog input. A custom program, written in Visual Basic 6, running on the quadrupole mass analyzer read the input voltage and fed the value into a calibration which sets the rf/dc voltages to determine which mass-to-charge ion to pass through the quadrupole. The width of the mass-to-charges that was passed through the quadrupole was 0.01 Da and the dwell time was 4 seconds. Following experiments with the 3-D ion trap, it was removed and the 2-D trap was installed. The quad exit lens was exchanged for a larger 3.96 mm aperture lens, which is slightly larger than the aperture of the entrance lens of the 2-D ion trap. The electronics were updated with appropriate parts for the 2-D ion trap. There were some problems with the rf voltage being picked up on the anode wire of the detectors for the 2-D ion trap, but once this wire and all the connections to the anodes were shielded the noise was minimized. The 2-D ion trap was tuned at the same Helium flow rates as the 3-D ion trap and the full set of experiments were repeated.

4.6. Hybrid Instrumentation Results

4.6.1 Comparisons of 2-D and 3-D ion traps

One of the goals of this work was to make comparisons between the 2-D ion trap and the 3-D ion trap when the ion sources are the same. The work described thus far has shown that fragile ion fragmentation occurs in both the 2-D and 3-D ion traps. What has not been addressed is how much fragmentation is occurring. Selecting ions of one mass-to-charge from the source allows for a quantitative analysis of how much of the selected ion signal is fragmenting. Additionally, the mass spectra produced will show what ions are generated as a result of the fragile ion fragmentation. **Figure 4.6a** and **Figure 4.6b** are the mass spectra

acquired with the 2-D and 3-D ion traps when the FC-43 fragment ion of *m/z* 502 was selected from the ion source. If there was no fragmentation, the mass spectrum would be just the ion of *m/z* 502. What was observed was that in the 2-D ion trap mass spectrum the *m/z* 502 ion signal was 39 %TIC and 69 %TIC in the 3-D ion trap mass spectrum. Both mass spectra show that the major fragment of the *m/z* 502 ion is the *m/z* 264 ion, which were 56 and 24 %TIC in the 2-D and 3-D ion traps respectively. When the product and molecular ion signals are added they are greater than 93 %TIC in both instruments. The data suggests that the *m/z* 502 fragile ion is fragmenting more in the 2-D ion trap. While this is likely qualitatively correct, the amount of fragmentation may be artificially high. In the description of the hybrid quadrupole 2-D ion trap, it was stated that the anode was shielded to minimize the pick up of rf voltage. Despite the shielding, at larger amplitude rf voltages (larger mass-to-charge ions) the anode was still picking up rf voltage. The rf voltage that was picked up manifested itself as a dc bias in the electrometer, which raised the background. The auto zero algorithm then removed this elevated baseline which removed some level of the high mass-to-charge ion signal. Therefore, the *m/z* 502 ion signal may be slightly reduced increasing the observed relative amount of fragmentation. Further instrument modifications are necessary to completely remove the rf pickup from the anode of the multiplier.

Resultant mass spectra created when nonane molecular ions (*m/z* 128) were selected from the source are illustrated in **Figure 4.6c** for the 2-D ion trap and **Figure 4.6d** for the 3-D ion trap. As previously stated, the molecular ion signal of n-alkanes in an EI source should be low. However, this data shows that the nonane molecular ion signal was reduced 90% by fragile ion fragmentation. The molecular ion signal from the 2-D ion trap mass spectrum was 10.4 %TIC and 6.5 %TIC from the 3-D ion trap mass spectrum. The molecular ions of

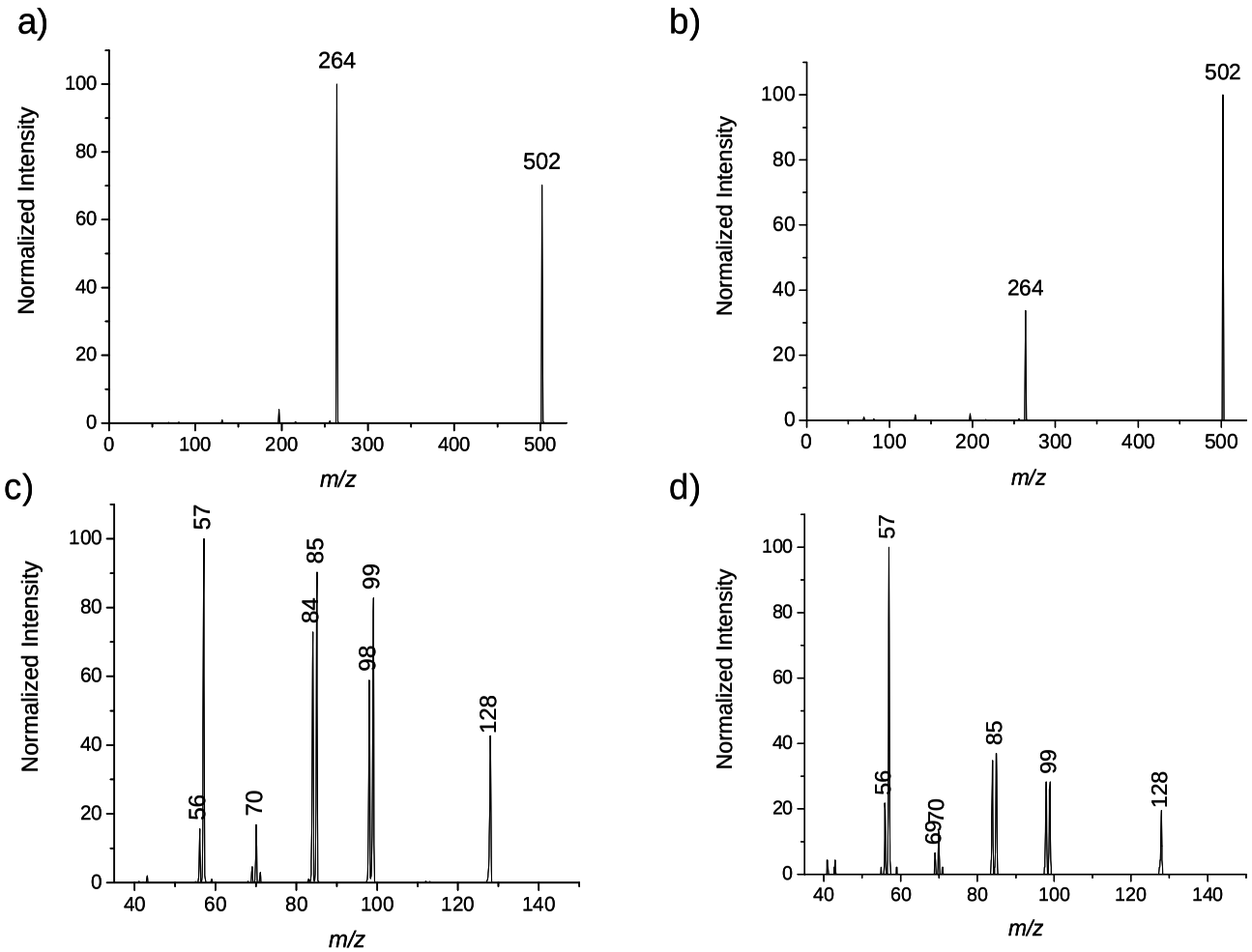

Figure 4.6 – Mass Spectra illustrating the amount of fragmentation observed when selecting the 502 *m/z* fragment of FC-43 or the 128 *m/z* molecular of nonane from the source. a) 2-D ion trap 502 *m/z* , b) 3-D ion trap 502 *m/z*, c) 2-D ion trap nonane, d) 3-D ion trap nonane

n-butylbenzene and t-butylbenzene (*m/z* 134) were selected from the source and the observed %TIC results from both instruments are summarized in **Table 4.1**. In addition to the *m/z* 502 fragments of FC-43, 24 other fragment ions were also individually selected from the source and the observed %TIC from both instruments are summarized in Table 2. For several of the ions that were analyzed, the differences in fragile ions fragmentation in the 2-D and 3-D ion traps are not statistically significant (%TIC reported are $\pm$ 3%). When the results are statistically significant ions less than *m/z* 500 are fragmenting more in the 3-D ion trap. Higher mass-to-charge ions are fragmenting more in the 2-D ion trap; however, the actual difference between the two instruments may be smaller than the values in **Table 4.2**.

Instrument	n-butylbenzene	t-butylbenzene	Nonane
2-D Ion Trap	81.6	58.1	10.4
3-D Ion Trap	80.4	56.0	6.5

Table 4.1- Molecular ion %TIC for hybrid instruments.

m/z	2-D Ion Trap	3-D Ion Trap
69	97.8	97
114	91.8	77.7
119	3.3	4.1
131	99.2	93.8
145	85.8	71.1
150	43.9	36.4
169	13.1	2.4
214	70.2	72.1
219	<0.1	0.7
226	67.5	56.4
264	91.4	88.4
276	76.3	48.8
314	89.7	79.1
319	0.7	0
326	87	63.7
352	53.3	68.1
364	85.4	62.3
376	69.2	42.8
402	2.1	34.4
414	93.6	92.6
426	58.2	40.7
452	0.1	23.9
464	78.2	71.5
502	39.4	69.0
614	0.1	56.0

Table 4.2 – Summary of %TIC for FC-43 ions in hybrid instruments.

Comparisons of ion injection times between the two instruments were performed. The molecular ion of t-butylbenzene was passed through the quadrupole and the injection time was monitored while varying the LMCO during ion injection (injection rf). The pressure of the analyte was the same in the two experiments. AGC ion target for both instruments was 1/10 of the default target, 5 for the 3-D trap and 5000 for the 2-D ion trap. The maximum injection time for AGC was set to 250 msec. As described in **Section 4.3.5**, with the AGC on, ion injection is more efficient if the injection time is shorter; assuming the same sample concentration and ion flux from the source. Conversely when the instruments have injection times at the maximum 250 msec, they are not likely to reach the set ion targets and thus are not trapping efficiently. As can be seen in the inset figure in **Figure 4.7**, the injection time

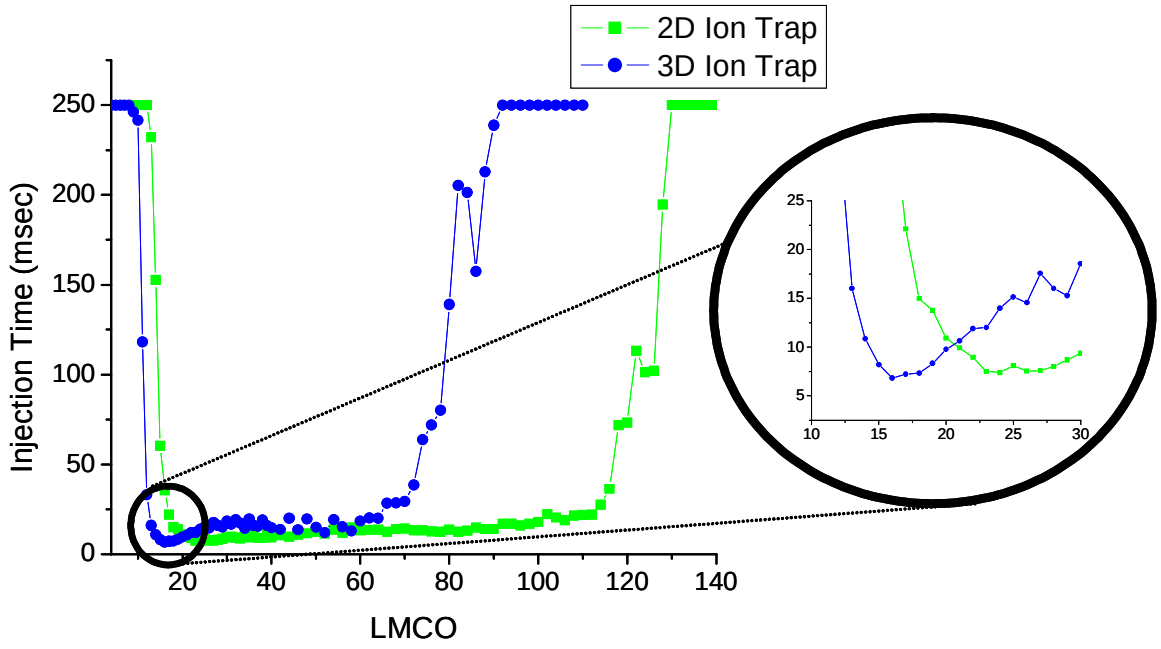

Figure 4.7 – Plot of inject times as a function of the LMCO during ion injection of the molecular ion of t-butylbenzene. Source emission currents: 2-D ion trap 50 μA, 3-D ion trap 250 μA AGC Targets: 2-D ion trap 5000, 3-D ion trap 5

for both instruments reaches a minimum of about 5 msec. In addition to the 2-D ion trap having a larger trapping volume, the 2-D ion trap stores ions during the entire rf duty cycle; therefore, the 2-D ion trap has more ions trapped than the 3-D ion trap in the same injection time. The 3-D trap and 2-D trap reach their minimum injection time about 5 Da apart, the 3-D trap around a LMCO of 18 Da and the 2-D around a LMCO of 23 Da. The LMCO during ion injection that is chosen for a given mass-to-charge ion is related to the ion's kinetic energy, the geometry of the ion trap, and the pressure of the buffer gas. The small difference in the LMCO for trapping is due to differences in the geometries between the two instruments. The algorithm that is used to determine what LMCO was used during ion injection of a given mass-to-charge ratio ion did not take into account these geometric differences. This small issue will only affect the data in the 2-D ion trap when ions are injected at low LMCO; the actual value depends on the mass-to-charge ratio of the ion.

4.6.2 Xenon Control Studies

An important comparative analysis is to explore what happens to non fragile ions while investigating the effects of the rf amplitude during ion injection, helium buffer gas pressure, and ion kinetic energy. The 132 isotope of xenon is an ideal control ion because it is similar in mass-to-charge to the molecular ion of n-butylbenzene (*m/z* 134), t-butylbenzene (*m/z* 134), and nonane (*m/z* 128), which removes the mass bias of the 3-D ion trap. Results of injection rf experiments (plotted as LMCO) and kinetic energy experiments as a function of pressure in the 2-D and 3-D ion traps are shown in **Figure 4.8** and **Figure 4.9** respectively**.** The dotted line in **Figure 4.8a** illustrates how the plot for ion injection as a function of injection rf (LMCO) should theoretically appear. The height of the dotted line is arbitrary but the result is that once ions are able to be injected into the 2-D ion trap they should be

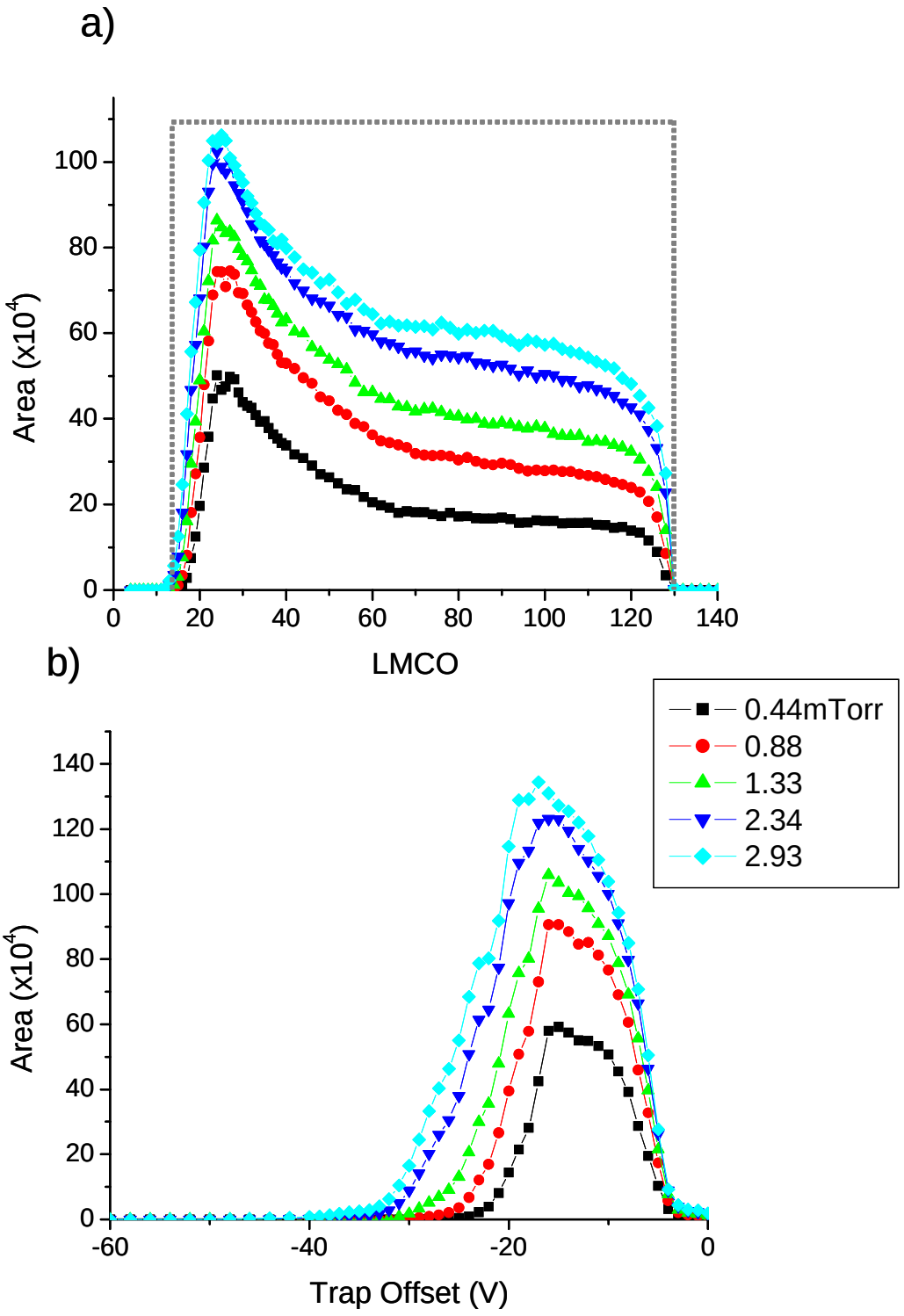

Figure 4.8 – Hybrid 2-D ion trap xenon control studies a) LMCO during ion injection b) trap offset voltage

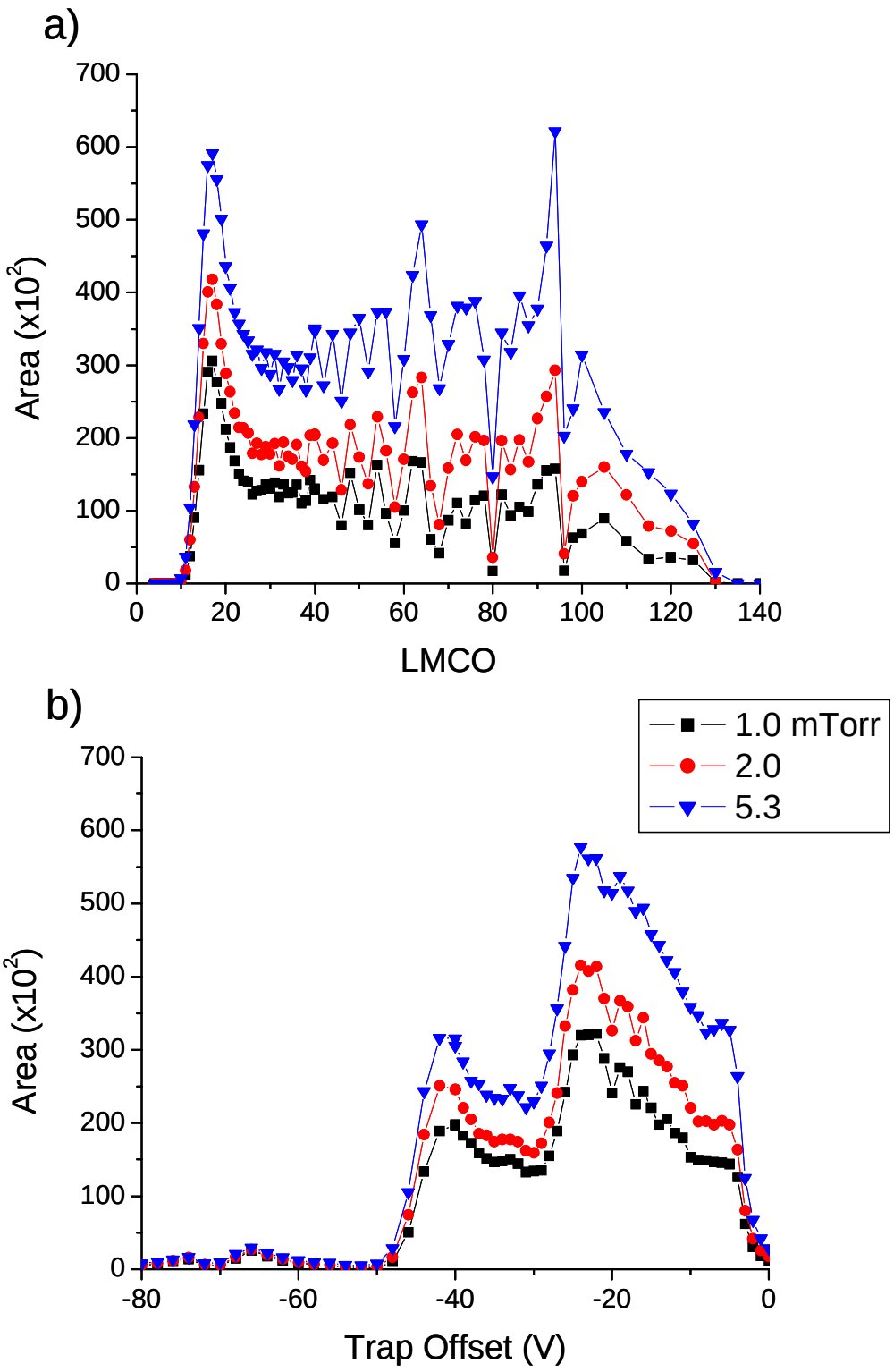

Figure 4.9 – Hybrid 3-D ion trap xenon control studies a) LMCO during ion injection b) trap offset voltage

indiscriminately injected until the LMCO during ion injection is equal to *m/z* 132. Xenon ions were found to be optimally injected from LMCO 19-25 Da. Ion injection efficiency then decreases, levels off from LMCO of 60-120 Da, and then falls off rapidly from 120-132 Da. As shown in **Figure 4.8a,** the xenon ion increased in abundance at higher pressures across all LMCO. The dc potential applied to the center section of the 2-D ion trap controls the axial kinetic energy of the ions. As shown in **Figure 4.8b**, at 0.44 mTorr xenon ions reach a maximum injection at a trap offset of -17 V. Ion intensities then quickly decrease at trap offsets more negative than -20 V. By – 40 V almost no ions were observed. A possible explanation for this is that the ion's axial kinetic energy is so large that radial ejection and detection is not very efficient. As the pressure was increased the trap offset voltage where the maximum ion abundance was observed got more negative, i.e. greater kinetic energies. This is because greater kinetic energy ions can be further cooled at higher pressures, thus allowing them to be more efficiently trapped.

Injection of externally generated ions into a 3-D ion trap is more complicated than in a 2-D ion trap because in the 3-D ion trap the rf voltage affects motion in all three dimensions. [10] As described in section 4.4.2 the range of rf amplitudes over which ions can be injected into the 3-D ion does depend on the mass-to-charge of that ion. Ions with mass-to-charge values below 150 Da can often be injected over a range from LMCO of 10 Da to the LMCO of that ion. As shown in **Figure 4.9a**, xenon ions were optimally injected from LMCO of 16-18 Da. Drastic decreases in ion abundances were observed at several LMCO. As discussed in **Section 4.2.1** and **Chapter 3**, these decreases can be attributed to nonlinear resonances, which cause the ion to be inefficiently trapped.[10] As a function of pressure the ion abundance increases at all LMCO. At constant injection rf amplitude, low kinetic energy

(low trap offset voltages) ions are not able to overcome the rf potential barrier and thus are not efficiently trapped. Ions with high kinetic energies can have too much kinetic energy and once they overcome the injection rf potential barrier they are not sufficiently cooled through collisions with the buffer gas and they hit an electrode or are ejected out of the ion trap. As described in **Section 4.3.4**, the LMCO during ion injection was scaled with the kinetic energy of the ions to minimize losses in ion injection efficiency. The optimal trap offset for the injection of xenon ions at 1 mTorr, as shown in **Figure 4.9b**, was -22 V. If a fragile ion was injected at -22 V the ion would likely fragment. The amount of xenon ions increased as a function of pressure at all kinetic energies; however unlike the 2-D ion trap the optimal trap offset voltage did not change as a function of pressure.

4.6.3 LMCO During Ion Injection

n-butylbenzene has been used for many years as a thermometer compound because the kinetics and energetics of its fragmentation are well understood. Using the quadrupole to transmit only the molecular ion of n-butylbenzene, the area of the molecular ion and its fragments were monitored as a function of LMCO during ion injection. The 2-D ion trap had very little observed change in the %TIC for any of the ions as the LMCO was increased above LMCO of 15 Da, as can be seen from **Figure 4.10a**. In the 2-D ion trap, the data below LMCO of 15 Da is artificially large as a result of an instrument artifact that will be discussed shortly. Theoretically, because the rf voltage should not affect the ion's axial motion in the 2-D ion trap, ions should not fragment as a function of the rf amplitude during ion injection. The amount of fragmentation can be described as 100 minus the molecular ion %TIC. Meaning that with n-butylbenzene in the 2-D ion trap the molecular ion loses roughly 20% of its abundance due to fragmentation, so there is 20% fragmentation. This level of

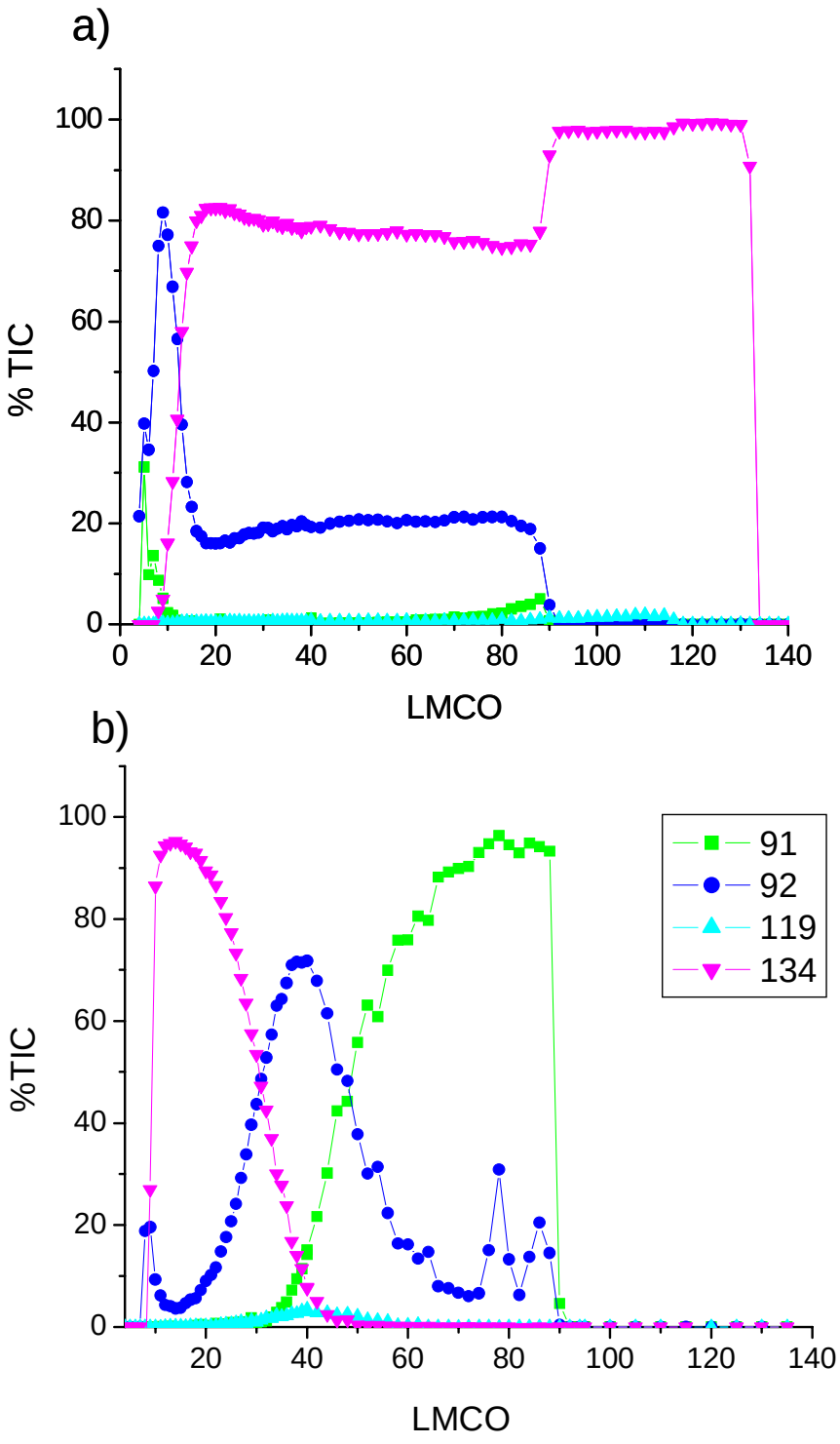

Figure 4.10 – Plot comparing the effects of LMCO on the % TIC of n-butylbenzene molecular ion (*m/z*=134) a) 2-D ion trap b) 3-D ion trap.

fragmentation seems to be a baseline fragmentation. It could be occurring in the quadrupole mass analyzer which was held at a constant rf potential during the entire experiment. However, this fragmentation is not likely occurring in the quadrupole because it was not observed in the hybrid 3-D ion trap, which uses the same quadrupole. In fact, in the 3-D ion trap at LMCO of 13 Da the molecular ion %TIC was 95%. The baseline fragmentation in the 2-D ion trap may therefore be a result of the electric field imperfections because of the slits in the X rods of the 2-D ion trap. These field imperfections will create a non-zero rf potential along the z axis, which is termed a field imbalance. This field imbalance will cause the rf potential to slightly affect the ions axial motions, which will get worse with increasing rf voltage. These effects are most obvious as the radial motion of the ion increases rapidly just before the LMCO is equal to the ion's mass-to-charge ratio. As can be seen in **Figure 4.10a**, the amount of fragmentation begins to increase above an injection LMCO of 70 Da and more rapidly above LMCO of 80 Da, which can be seen by the increase in the *m/z* 91 and 92 fragment %TICs. Another possible explanation for the baseline fragmentation is CID, which may not occur in the 3-D because of differences in the ion injection process.

A significant amount of fragmentation occurs as a result of the rf amplitude during ion injection in the 3-D ion trap. As illustrated in **Figure 4.10b**, at low injection rf amplitudes (LMCO < 15 Da) there is a small amount *m/z* 92 signal. This fragment ion's signal starts increasing above a LMCO of 15 Da. At LMCO of 35 Da there was almost a 50% reduction of the molecular ion signal. Above LMCO of 40 Da higher energy fragmentation occurs and the fragment ion of *m/z* 91 was the predominant ion. The fragment ion of *m/z* 92 is the rearrangement fragment ion. The *m/z* 91 ion can be either the simple cleave fragment of the molecular ion (*m/z* 134) and/or the simple cleavage of the *m/z* 92

fragment.[29, 30] The rearrangement ion takes more time to form and usually occurs at lower internal energies. The fragment ion of *m/z* 91 forms at higher internal energies and likely forms rapidly. The optimal LMCO for trapping a *m/z* 134 ion in the 3-D ion trap will range from 15-35 Da depending on pressure and kinetic energy. During the experiment in **Section 4.6.1**, ions were injected in two segments each at a different LMCO (also conventional method used in standalone instruments); e.g., LMCO 35 and LMCO 18. When the molecular ion %TIC at these two values are averaged the %TIC is about 80%, which agrees with the %TIC of 80% reported in **Table 4.1**. For n-butylbenzene, operating at slightly lower rf amplitudes (< LMCO 18) during ion injection decreases the amount of fragile ion fragmentation.

The 2-D ion trap data in **Figure 4.10a** has two artifacts that can be explained. First, the discrete stair steps that are present at LMCO of 91 Da are artifacts as a result of *m/z* 91 and 92 ions being ejected because the LMCO is greater than or equal to the mass-to-charge of the ion; therefore, the %TIC of all ions that are still trapped immediately increase. The second artifact is present in the data below LMCO of 10 Da. This artifact is the large increase and then decrease in the %TIC of the *m/z* 92 fragment. None of the ions are being efficiently trapped at LMCO < 10 Da so the ion abundances are low, which can make the %TIC calculation be biased to lower mass-to-charge ions that will be trapped more efficiently before higher mass-to-charge ions. Additionally the 2-D ion trap does not start to trap *m/z* 134 efficiently until LMCO of 13 Da as shown in **Figure 4.7**. The 3-D ion trap data in **Figure 4.10b** does not have the same shape as the 2-D ion trap data in **Figure 4.10a** because the 3-D ion trap starts trapping *m/z* 134 about 5 Da before the 2-D ion trap. If the 3-D ion trap data in **Figure 4.10b** is examined closely at LMCO 8 Da, similar results

compared to the 2-D ion trap are observed. The observed quick increase in the *m/z* 92 fragment is observed to a much smaller extent than in the 2-D because the *m/z* 134 is being trapped LMCO > 10 Da. Differences in the LMCO at which the two ion traps begin to trap *m/z* 134 are a result of differences in the injection algorithms for the two instruments as described in **Section 4.6.1**. Following the completion of this work theses differences were remedied.

4.6.4 Pressure

The role of helium pressure in fragile ion fragmentation was explored with all of the analytes, but one of the more clear examples of the effect of pressure on fragile ion fragmentation is seen with the molecular ion of n-butylbenzene in the 2-D ion trap. As can be seen in **Figure 4.11**, the fragment ion *m/z* 92 area increased with pressure; however, the molecular ion signal did not increase above pressures of 0.88 mTorr. At pressures above 1.33 mTorr the area of *m/z* 92 fragment ions did not increase at the same rate as lower pressures and in fact the curve flattened out at greater LMCO. This suggests that as the pressure is increasing, more of the molecular ion is fragmenting to *m/z* 92 at greater LMCO. At smaller LMCO the molecular ion signal increased with pressure first due to improved trapping. Above 1.33 mTorr the molecular ion signal at a given LMCO decreased with pressure but only up to 2.34 mTorr. The decrease in molecular ion signal in connection with the corresponding increase in fragment ion signal suggests that n-butylbenzene is further fragmenting with increase helium pressures. The fact that the xenon ion abundance at a given LMCO did not decrease as a function of pressure, further suggests that for n-butylbenzene, higher pressure increases the amount of fragmentation in the 2-D ion trap. Nonane, showed similar trends as those observed with n-butylbenzene. In the 2-D ion trap

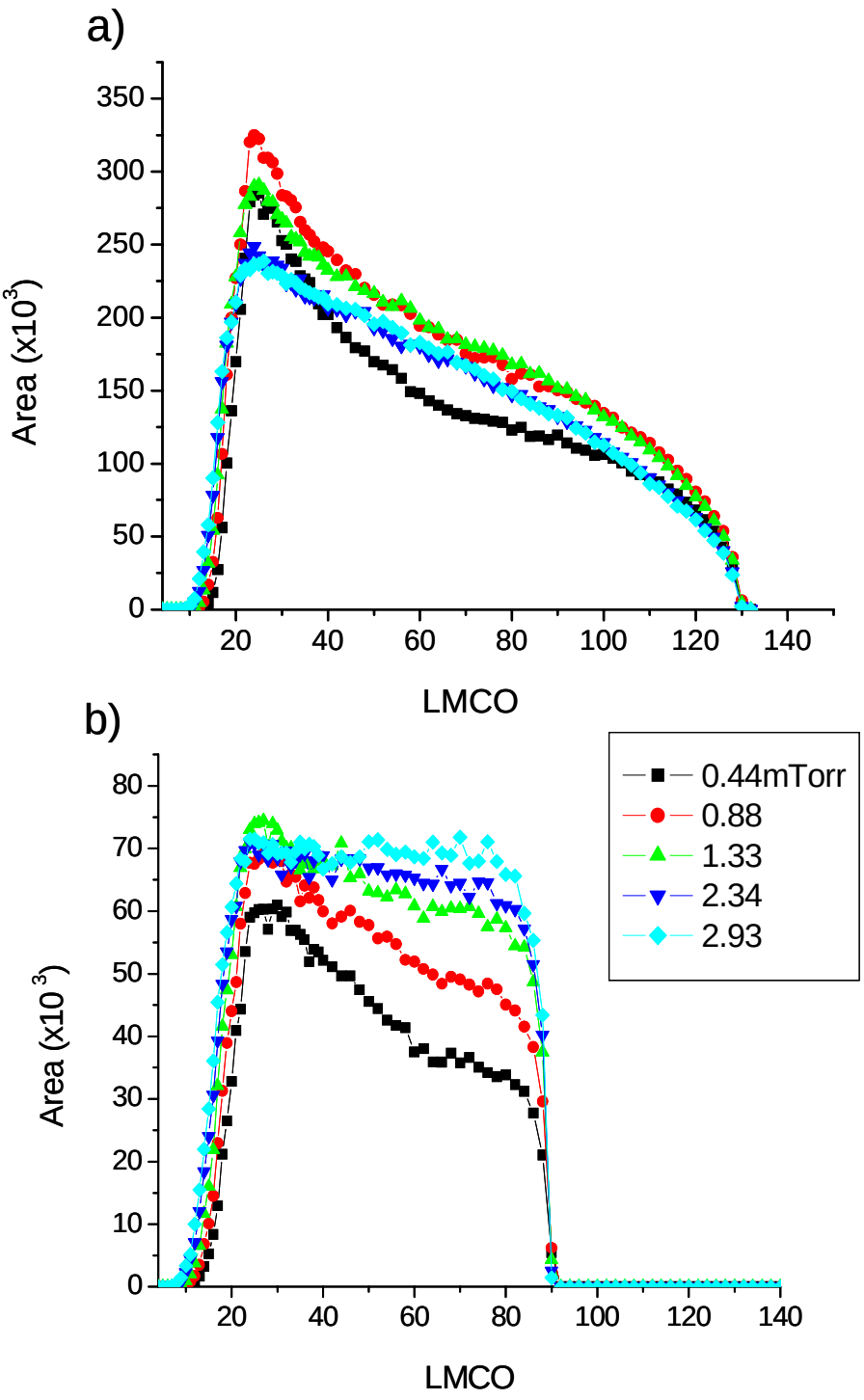

Figure 4.11 – 2-D ion trap n-butylbenzene fragmentation as a function of LMCO during ion injection and pressure a) Molecular ion *m/z* =134, b) Fragment ion *m/z*=92.

the nonane molecular ion abundance decreased as a function of pressure and several of the fragment ion abundances increased as a function of pressure (data not shown).

Collisions with the helium buffer gas can kinetically cool ions as well as cause dissociation. The effects of pressure on the molecular ion signal of n-butylbenzene in the 3-D ion trap were less pronounced than those in the 2-D ion trap. The effects of pressure on the molecular ion signal of t-butylbenzene were more pronounced in the 3-D ion trap and are illustrated in **Figure 4.12**. As pressure was increased in the 3-D ion trap both the molecular ion signal and the fragment ion signal increase. The molecular ion abundance is increasing due to more efficient trapping as a result of kinetic cooling. More molecular ions should then lead to an increase in the abundance of the fragment ion. However, from 2.0 mTorr to 5.3 mTorr the fragment ion area increased by a factor of 1.75 where as the molecular ion signal only increased by 1.2 suggesting that increasing the buffer gas pressure is causing more fragmentation. As with the 2-D ion trap data in **Figure 4.8**, xenon control studies with the 3-D ion trap showed that xenon ion abundances increase with pressure. The relative increase in peak area of xenon ions in the 3-D ion trap from 2.0 mTorr to 5.3 mTorr was 1.4, which is more than the molecular ion but less than fragment ion. This subtle difference further suggests that t-butylbenzene is fragmenting but to a small extent. Because pressure also improves trapping efficiency, the results of n-butylbenzene in the 3-D ion trap are not as clear. As a function of increasing pressure, the molecular ion abundance and fragment ion abundance increased at about the same rate for n-butylbenzene in the 3-D ion trap. Therefore it is not clear whether n-butylbenzene is fragmenting as the result of higher helium pressures.

Differences in %TIC for the molecular ions of n-butylbenzene (80 %TIC) and t-butylbenzene (56 %TIC) suggest that t-butylbenzene is more fragile; therefore, the pressure

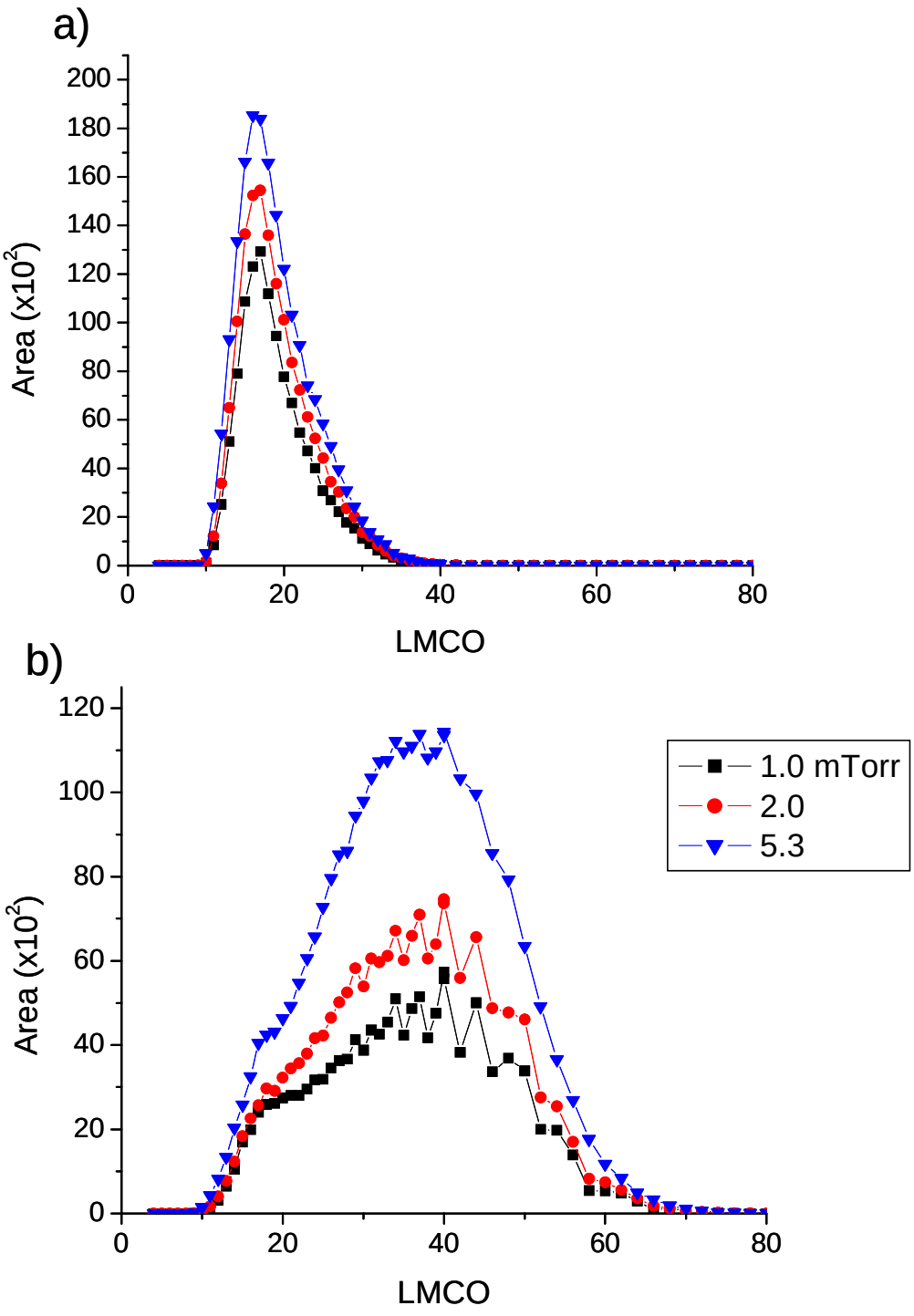

Figure 4.12 – 3-D ion trap t-butylbenzene fragmentation as a function of LMCO during ion injection and pressure a) Molecular ion *m/z* =134, b) Fragment ion *m/z*=119.

of helium may affect fragile ions at varying levels depending on the fragility of the analyte. The exact role of pressure in fragile ion fragmentation is not clear but the subtle differences in the data suggest that increases in pressure do not cause a significant change in ion fragmentation. Because ion traps ion trap performance deteriorates at lower pressures due to a lack of collisions and its performance deteriorates at higher pressures due to too many collisions, the full impact of pressure on fragile ion fragmentation may not be completely understood.

4.6.5 Kinetic Energy

The effects of kinetic energy on n-alkanes and the FC-43 ions, previously discussed, showed that increasing the ions' kinetic energy decreases the amount of observed molecular or analyte ion. Fragile ion fragmentation may not be the only source for the reduced ion signal, the reduced signal could be due to poor trapping efficiency. If the kinetic energy is too large, ions will not be contained by the rf trapping field in the 3-D trap or the dc trapping potential in the 2-D ion trap. The data illustrated in **Figure 4.13** was taken by varying the trap offset voltage of the 2-D ion trap and 3-D ion trap. The default operating trap offset voltage for both instruments was -10 V, which resulted in almost a 45% fragmentation of molecular ions. The molecular ion was completely fragmented by -25 V in the 2-D ion trap and by -30 V in the 3-D ion trap. At more negative potentials the collisions can be much more energetic and n-butylbenzene fragments to the *m/z* 91 ion, which may have resulted from the molecular ion directly and/or the *m/z* 92 fragment ion. The ion signal was drastically reduced at trap offsets more negative than -52 V in the 3-D ion trap, which was most likely being caused by inefficient trapping as described above.

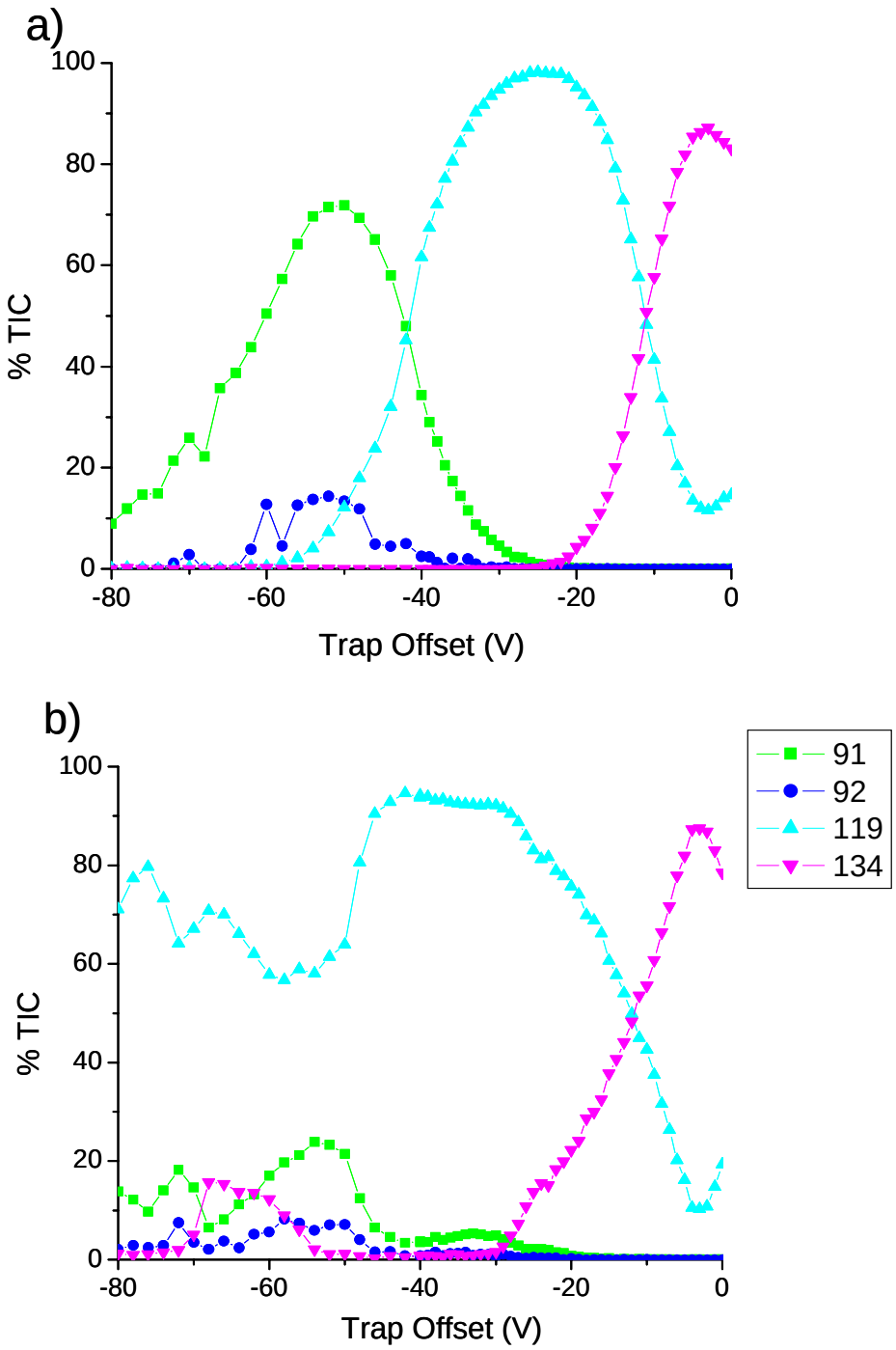

Figure 4.13 – Plot comparing the effects of trap offset voltage on the %TIC of t-butylbenzene molecular ion (m/z=134) a) 2-D ion trap b) 3-D ion trap.

In both instruments the amount of fragmentation can be reduced from 45% to 15% by decreasing to trap offsets to -7 V. The kinetic energy of the ion was the only factor which had enough control to cause complete ion fragmentation and also decrease the amount of fragmentation.

Decreasing an ions' kinetic energy clearly helps reduce fragmentation of an ion such as t-butylbenzene. But how much does decreasing the kinetic energy help an extremely fragile ion, like nonane, which has more than 90% fragmentation at a -10 V trap offset voltage? As shown in **Figure 4.14a**, the nonane molecular ion has a significant amount of fragmentation as a function of trap offset. If the 2-D ion trap was operated with a trap offset of -6 V, as opposed to -10 V, the molecular ion %TIC would rise from 10% to 25%. The area data in **Figure 4.14b** shows that this %TIC increase was not an artifact; the nonane ion abundance was really increasing. A non-fragile ion, xenon, under the same conditions decreased in intensity when the trap offset was made more positive from -10 V to -7 V as seen in **Figure 4.8b**. The fact that a non-fragile ion was decreasing in abundance and a fragile ion was increasing means the increase in %TIC is not due to better trapping, but rather a decrease in the fragmentation. Increasing the trap offset to more positive potentials will help to further decrease fragmentation; however, at potentials more positive than -4 V the ions lack the kinetic energy to over come the potential barriers of the ion trap. Therefore if the trap offset goes above -4 V the ions drop to too low of an abundance and sensitivity suffers.

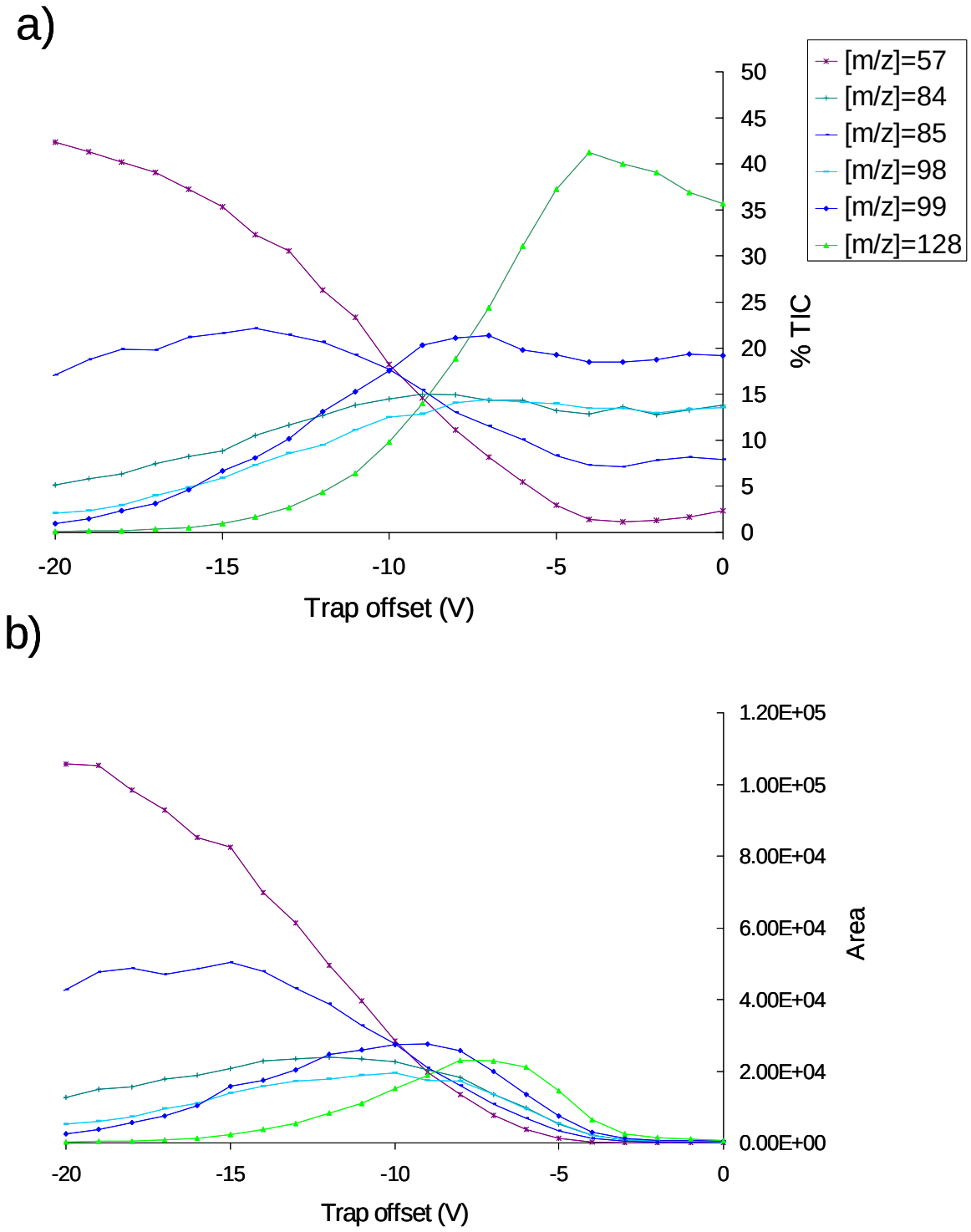

Figure 4.14 –Nonane $M^{+\bullet}$ fragmentation in 2-D ion trap as a function of trap offset voltage a) %TIC of molecular ion and trapped fragments b) Area of molecular ion and trapped fragments.

4.7 Conclusions:

Fragile ion fragmentation during the injection of externally generated ions is a problem in both the 3-D and 2-D ion traps, and is the main reason for the differences in the mass spectra taken with quadrupole mass analyzers and quadrupole ion traps. The fragmentation appears to be occurring as ions are entering the trap or immediately following ions entering the ion trap. No additional fragmentation was observed at longer storage times. Fragile ion fragmentation in standalone 2-D and 3-D quadrupole ion traps can be identified using experiments that vary the LMCO during ion injection. In these experiments ions that are injected over a narrower LMCO range than ions that have a lower mass-to-charge ratio are fragile. Additionally when varying the kinetic energy of ions, fragile ions have a narrower range of kinetic energies allowed for ion injection; compared to non-fragile ions.

In general, utilizing the current optimal operating conditions for the 2-D and 3-D ion traps, the 2-D ion trap has less fragile ion fragmentation than the 3-D ion trap. The data from the hybrid instrument shows the 2-D ion trap is capable of storing significantly more ions in the same amount of time, thus reducing the over all scan time. The 2-D ion trap is also capable of injecting ions over a much broader range of injection rf amplitudes with minimal change in fragmentation.

Pressure, rf amplitude during ion injection, and ion kinetic energy all affect the amount of fragmentation that is observed to some degree in both instruments. The effects of pressure in both instruments are not significant and the sensitivity loss in reducing the helium pressure to minimize fragmentation is more harmful than the sensitivity gained with reduced fragmentation. The rf amplitude during injection is a significant factor in fragile ion fragmentation in the 3-D ion trap. When the LMCO is equal to *m/z* 30, fragile ions almost

always fragment. Decreasing the rf amplitude will result in a decreased amount of fragmentation. There may be some loss to sensitivity with this decrease depending on the mass-to-charge of the analyte. The rf amplitude during ion injection does not significantly affect fragile ions in the 2-D ion trap. For n-butylbenzene, fragmentation does not increase until the injection LMCO is greater than 70 Da. However, a baseline level of fragmentation in the 2-D ion trap was observed, which may be a result of the field imbalance caused by the slots in the X rods or simply CID. The kinetic energy of the ions effects the fragile ion fragmentation significantly in both the 2-D and 3-D ion traps. When the kinetic energy is sufficiently high the ion can completely fragment in both instruments. As shown with none by reducing the trap offset in the 2-D ion trap by a few voltage the fragmentation can be reduced by 15-20 % with out significant loss to the sensitivity, due to poor trapping efficiency at lower kinetic energies. In both instruments the trap offset voltage should be made more positive by several volts to minimize fragmentation.

4.8 References

1. McLuckey, S. A.; Glish, G. L.; Asano, K. G., *Coupling of an Atmospheric-Sampling Ion Source with an Ion-Trap Mass Spectrometer.* Analytica Chimica Acta, 1989. 225: p. 25-35.

2. Louris, J. N.; Amy, J. W.; Ridley, T. Y.; Cooks, R. G., *Injection of Ions into a Quadrupole Ion Trap Mass Spectrometer.* International Journal of Mass Spectrometry and Ion Processes, 1989. 88: p. 97-111.

3. Kaiser, R. E. J.; Louris, J. N.; Amy, J. W.; Cooks, R. G., *Extending the Mass Range of the Quadrupole Ion Trap Using Axial Modulation.* Rapid Communications in Mass Spectrometry, 1989. 3: p. 225-229.

4. VanBerkel, G. J.; Glish, G. L.; McLuckey, S. A., *Electrospray Ionization Combined with Ion Trap Mass Spectrometry.* Analytical Chemistry, 1990. 62: p. 1284-1295.

5. Schwartz, J.; Zhou, X.; Bier, M. E. Method of increasing the dynamic range and sensitivity of a mass spectrometer. US Patent 5572022, 1996.

6. Glish, G. L.; Vachet, R. W., *The basics of mass spectrometry in the twenty-first century.* Nature Reviews Drug Discovery, 2003. 2(2): p. 140-150.

7. Yoshinari, K., *Theoretical and Numerical Analysis of the Behavior of Ions Injected Into a Quadrupole Ion Trap Mass Spectrometer.* Rapid Communications in Mass Spectrometry, 2000. 14: p. 215-223.

8. Appelhans, A. D.; Dahl, D. A., *Measurement of external ion injection and trapping efficiency in the ion trap mass spectrometer and comparison with a predictive model.* International Journal of Mass Spectrometry, 2002. 216: p. 269–284.

9. Quarmby, S. T.; Yost, R. A., *Fundamental Studies of Ion Injection and trapping of Electrosprayed Ions on a Quadrupole Ion Trap.* International Journal of Mass Spectrometry, 1999. 190/191: p. 81-102.

10. Kofel, P., *Injection of Mass Selected Ions into the Radio Frequency Ion Trap*, in *Practical Aspects of Ion Trap Mass Spectrometry*; March, R. E., Todd, J. F. J., Eds.; CRC Press: Boca Raton, FL, 1995; Vol. II, pp 51-87.

11. Schwartz, J., *A Sector/Ion Trap Hybrid Mass Spectrometer of BE/Trap configuration.* Int. J. Mass Spec. Ion Processes, 1990. 98: p. 209-224.

12. Morand, K. L.; Horing, S. R.; Cooks, R. G., *A Tandem Quadrupole-Ion Trap Mass Spectrometer.* Int. J. Mass Spec. Ion Processes, 1991. 105: p. 13-29.

13. VanBerkel, G. J.; McLuckey, S. A.; Glish, G. L., *Electrospray Ionization of Porphyrins Using a Quadrupole Ion Trap for Analysis.* Analytical Chemistry, 1991. 63(11): p. 1098-1108.

14. Bortolini, O.; Traldi, P., *Evaluation of the Polarizability of Gaseous Ions*, in *Practical Aspects of Ion Trap Mass Spectrometry*; March, R. E., Todd, J. F. J., Eds.; CRC Press: Boca Raton, FL, 1995; Vol. II, pp 145-159.

15. Traldi, P.; Favretto, D.; Catinella, S.; Bortolini, O., *Mass Displacements in Quadrupolar Field Analysers.* Organic Mass Spectrometry, 1993. 28: p. 745-751.

16. Schwartz, J. C.; Senko, M. W.; Syka, J. E. P., *A two-dimensional quadrupole ion trap mass spectrometer.* Journal of the American Society for Mass Spectrometry, 2002. 13(6): p. 659-669.

17. Syka, J. E. P., *Commercialization of the Quadrupole Ion Trap*, in *Practical Aspects of Ion Trap Mass Spectrometry*; March, R. E., Todd, J. F. J., Eds.; CRC Press: Boca Raton, FL, 1995; Vol. I, pp 169-205.

18. Louris, J. N.; Schwartz, J.; George C. Stafford, J.; Syka, J. E. P.; Taylor, D. *The Paul Ion Trap Mass Selective Instability Scan: Trap Geometry and Resolution*. in *The 40th ASMS Conference on Mass Spectrometry and Allied Topics*. 1992. Washington, DC.

19. Li, H.; Plass, W. E.; Patterson, G. E.; Cooks, R. G., *Chemical mass shifts in resonance ejection experiments in the quadrupole ion trap.* Journal of Mass Spectrometry, 2002. 37(10): p. 1051-1058.

20. Cox, K. A.; Cleven, C. D.; Cooks, R. G., *Mass Shifts and Local Space Charge Effects Observed in the Quadrupole Ion Trap at Higher Resolution.* International Journal of Mass Spectrometry and Ion Processes, 1995. 144: p. 47-65.

21. Cleven, C. D.; Cox, K. A.; Cooks, R. G.; Bier, M. E., *Mass Shifts due to Ion/Ion Interactions in a Quadrupole Ion-Trap Mass Spectrometer.* Rapid Communications in Mass Spectrometry, 1994. 8: p. 451-454.

22. Wells, J. M.; Plass, W. R.; Patterson, G. E.; Ouyang, Z.; Badman, E. R.; Cooks, R. G., *Chemical Mass Shifts in Ion Trap Mass Spectrometry: Experiments and Simulations.* Analytical Chemistry, 1999. 71(16): p. 3405-3415.

23. Wells, J. M.; Plass, W. R.; Cooks, R. G., *Control of Chemical Mass Shifts in the Quadrupole Ion Trap Through Selection of Resonance Ejection Working Point and rf Scan Direction.* Analytical Chemistry, 2000. 72: p. 2677-2683.

24. McClellan, J. E.; Murphy, J. P.; Mulholland, J. J.; Yost, R. A., *Effects of Fragile Ions on Mass Resolution and on Isolation for Tandem Mass Spectrometry in the Quadrupole Ion Trap Mass Spectrometer.* Analytical Chemistry, 2002. 74: p. 401-412.

25. Goeringer, D. E.; McLuckey, S. A., *Evolution of Ion Internal Energy During Collisional Excitation in the Paul Ion Trap: A Stochastic Approach.* Journal of Chemical Physics, 1996. 104(6): p. 2214-2221.

26. O, C. S.; Schuessler, H. A., *Confinement of Ions Created Externally in a Radio-Frequency Ion Trap.* Journal of Applied Physics, 1981. 52(3): p. 1157-1166.

27. Murphy, J. *Fundamental Studies of the Quadrupole Ion Trap Mass Spectrometer: Compound-Dependent Mass Shifts and Space Charge* Doctoral Dissertation, University of Florida, Gainesville, FL, 2002.

28. Clay, D.; Guckenberger, B.; Quarmby, S.; McCauley, E.; Schoen, A. *Elimination of Neutral Noise from a GC/MS Quadrupole Mass Spectrometer*. in *98th Gulf Coast Conference*. 2002. Galveston Island, TX.

29. Wong, R. L.; Robinson, E. W.; Williams, E. R., *Activation of protonated peptides and molecular ions of small molecules using heated filaments in fourier-transform ion cyclotron resonance mass spectrometry.* International Journal of Mass Spectrometry, 2004. 234(1-3): p. 1-9.

30. Basic, C.; Yost, R. A., *Collision-induced dissociation breakdown surfaces for n-alkylbenzene molecular ions in a quadrupole ion trap mass spectrometer.* International Journal of Mass Spectrometry, 2000. 194(2-3): p. 121-132.

Chapter 5

A Novel Octapole Ion Trap Mass Spectrometer: Theory, Prototype, and Comparison Studies

5.1 Introduction

Throughout this dissertation higher order fields have been described as minor field components of a predominantly quadrupole trapping field. One of the most utilized higher order fields in quadrupole ion traps has been the octapole field. As described in **Chapter 4**, the mass shifts discovered during the commercialization of the 3-D ion trap were removed by introducing an axial stretch to the electrode geometry.[1] The inherent symmetry involved with this stretch introduced even higher order fields, notably octapole fields. Octapole non-linear resonances are known to enhance resolution and sensitivity as was shown in **Chapter 2** and **Chapter 3**. Octapole fields are also known to improve trapping efficiency and theoretically improve MS/MS efficiency.[2-4] Recently researchers have used octapole fields in linear traps to enhance the efficiency of tandem mass spectrometry (MS/MS) and ion ejection.[5-7] Literature suggests that for optimal operation of a quadrupole ion trap, higher order fields are best used in moderation.[2, 8] Therefore octapole fields make up about 2%, and the remaining higher order fields make roughly 8%, of the over all field in modern 3-D quadrupole ion traps.[2]

The advantages of octapole fields when used as minor field components have been extensively studied. However, there have been very few studies of ion traps with

predominantly octapole fields There is one instance in the literature where a three dimensional octapole ion trap was used to study the spectroscopy of barium ions; however, no mass analysis was conducted.[9] Developing an ion trap with predominately octapole fields is advantageous because of the enhanced sensitivity due to improved trapping efficiency and because of improved MS/MS efficiencies. In this chapter the theory, ion trajectory modeling, and proof of principle experiments for a cylindrical octapole ion trap mass spectrometer are presented.

5.2 Octapole Fields

5.2.1 Importance of Octapole Fields

One advantage of octapole fields is an improved trapping or storage efficiency. The electric potentials in an octapole field and in a quadrupole field are described by **Equation 5.1** and **Equation 5.2** respectively.

$$\phi(r,\varphi,z) = A_4 \frac{\left(0.375r^4 - 3r^2z^2 + z^4\right)}{\left(.5r_0^{\,2} + z_0^2\right)^2} + A_0 \qquad \textbf{EQ5.1}$$

$$\phi(r,\varphi,z) = A_2 \frac{\left(0.5r^2 - z^2\right)}{\left(r_0^{\,2} + 2z_0^2\right)} + A_0 \qquad \textbf{EQ5.2}$$

In these equations, the A_4, A_2, and A_0 are weighting terms for the octapole, quadrupole, and monopole field respectively. As described in **Section 1.4**, the electric field (E) is the derivative of the electric potential over all dimensions and the corresponding force (F) is the charge (q) of an ion multiplied by the electric field (**Equation 5.3**).

$$F = \textbf{-qE} = \textbf{-q}\nabla\phi \qquad \textbf{EQ5.3}$$

A plot showing how the force varies axially with distance from the center of the ion trap is shown in **Figure 5.1**. For a quadrupole field, the restoring force varies linearly as an ion

moves axially away from the center of the trap. Compared to the quadrupole field, the octapole field has a larger region in the center of the trap where ions are not affected by a restoring force. However, as ions travel axially away from the center they are affected by a larger force. Thus octapole fields often aid in confining ions to the center of an ion trap. The result of the wide-spread minimal force in the center of the ion trap is that theoretically more ions can be trapped in an octapole field, which will impact an ion trap's sensitivity and can lead to an improved limit of detection.

Another advantage of octapole fields is an increase in MS/MS efficiency, which is the ratio of the sum of product ion abundances over the initial precursor ion abundance. An ion's motion in an octapole field is quite different from an ion's motions in a quadrupole field. First, the secular frequency of an ions motion is dependent on the amplitude of its radial and axial motion.[4] This dependence is the result of the cross term (r^2z^2) in the electric potential, as shown in **Equations 5.1** and **Equation 5.2**. Because of this cross term, an ion's motion is coupled in the radial and axial dimensions. When an ion is axially excited during resonance excitation in an octapole field, its axial motion increases but some of the gained kinetic energy is transferred into the radial motion. Because the secular frequency is dependant on the amplitude of the ion's axial motion, the secular frequency of the ion changes; this alteration causes a phase shift between the frequency of the resonance excitation voltage and the secular frequency. As the phase shift becomes greater, the ion's secular frequency is no longer in resonance with the applied waveform and the kinetic energy of the ion decreases. As the kinetic energy of the ion lessons it will come back into resonance and the ion will begin gaining kinetic energy again. If the amplitude of the

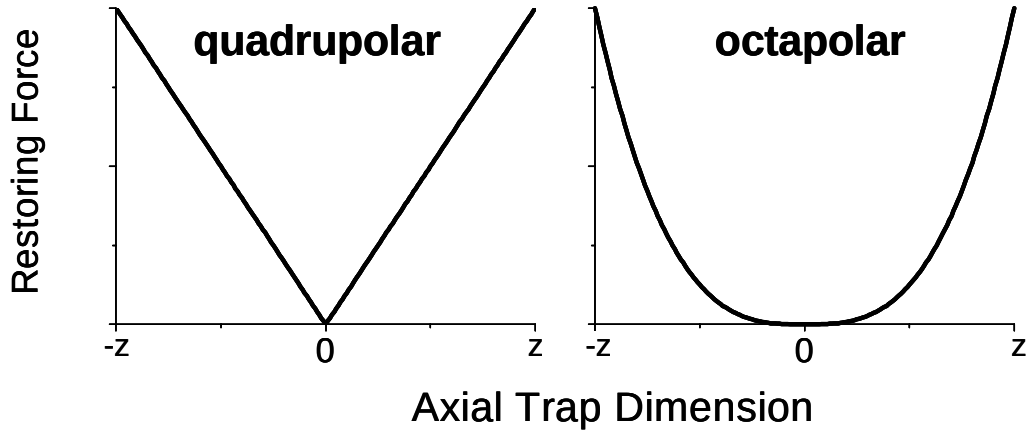

Figure 5.1 – Restoring force for quadrupole and octapole fields.

resonance ejection voltage is insufficient for ion ejection and the ion is incapable of dissociation (e.g., Xenon) the ion would be indefinitely trapped in the octapole field. Alternatively, when this same ion is resonantly excited in a quadrupole field, the ion's motion in the axial and radial dimensions are uncoupled and the ion's axial secular frequency stays the same and the ion does not fall out of resonance. Thus as the ion's kinetic energy increases only its axial motion increases and in the absence of collisions from the buffer gas the maximum amplitude of the ion's axial trajectory will continue to increase until the ion is ejected from the ion trap. When an ion has bonds and is thus able to have internal (vibration/rotation) energy, an ion's ions kinetic energy can be converted into internal energy through collisions with the buffer gas. Ions will dissociate when the gained internal energy is greater than the critical energy for a given dissociation process. This process will occur regardless of the field type. However, in the quadrupole field, ions can be ejected from the ion trap before they can gain sufficient internal energy for dissociation. This competition between excitation and ejection reduces the MS/MS efficiency because precursor ions are lost during the excitation process. In the presence of octapole fields, the competition between ejection and excitation should be minimized because ion ejection is decreased from the ions going in and out of resonance. The practical results are that ions can be excited for a longer period of time and at higher amplitude resonance excitation voltages, which will lead to more product ions and improved MS/MS efficiency.

5.2.2 Creating the Octapole Ion Trap

The octapole ion trap is a five electrode device with two endcap electrodes and three ring electrodes. One may wonder where are the eight poles in an octapole ion trap? Or further, where are the four poles of a quadrupole ion trap? An analogy between the

quadrupole mass filter and the quadrupole ion trap will help to better understand why the octapole ion trap adopts this electrode geometry. The quadrupole mass filter, shown in **Figure 5.2a**, is a four electrode array where a rf voltage of equal amplitude but 180 degrees out of phase is applied to alternating electrodes. Imagine the electrodes of the 3-D ion trap being created by "bending" the shaded electrodes together to create the ring electrode, shown in **Figure 5.2b**, and "bending" each of the non-shaded electrodes around itself to create the endcap electrodes. The 3-D quadrupole ion trap (**Figure 5.2b**) is a three electrode device which can operate with an rf voltage of equal amplitude but 180 degrees out of phase applied to alternating electrodes. However, the endcap electrodes are usually grounded resulting in half the over all electric potential relative to the quadrupole mass filter. The 3-D octapole ion trap electrode geometry follows from the linear octapole in the same way the 3-D quadrupole ion trap follows from the quadrupole mass filter. The linear octapole (**Figure 5.2c**), which is often used as an ion guide for transmitting ions into mass analyzers, consists of an eight electrode array with an rf voltage of equal amplitude but 180 degrees out of phase applied to alternating electrodes. Imagine the electrodes for the 3-D octapole ion trap are created by "bending" the shaded and center non-shaded electrodes together to create the three ring electrodes, shown in **Figure 5.2d**. The 3-D octapole ion trap is then a five electrode system with an rf voltage of equal amplitude but 180 degrees out of phase applied to alternating electrodes. Just as with the 3-D quadrupole ion trap, the 3-D octapole ion trap is best operated with the endcaps and consequently the center ring electrode grounded. The 3-D quadrupole ion trap and the 3-D octapole ion trap are not operated with the endcaps having rf voltage applied to them because it is not efficient to inject ions through the high amplitude voltage.

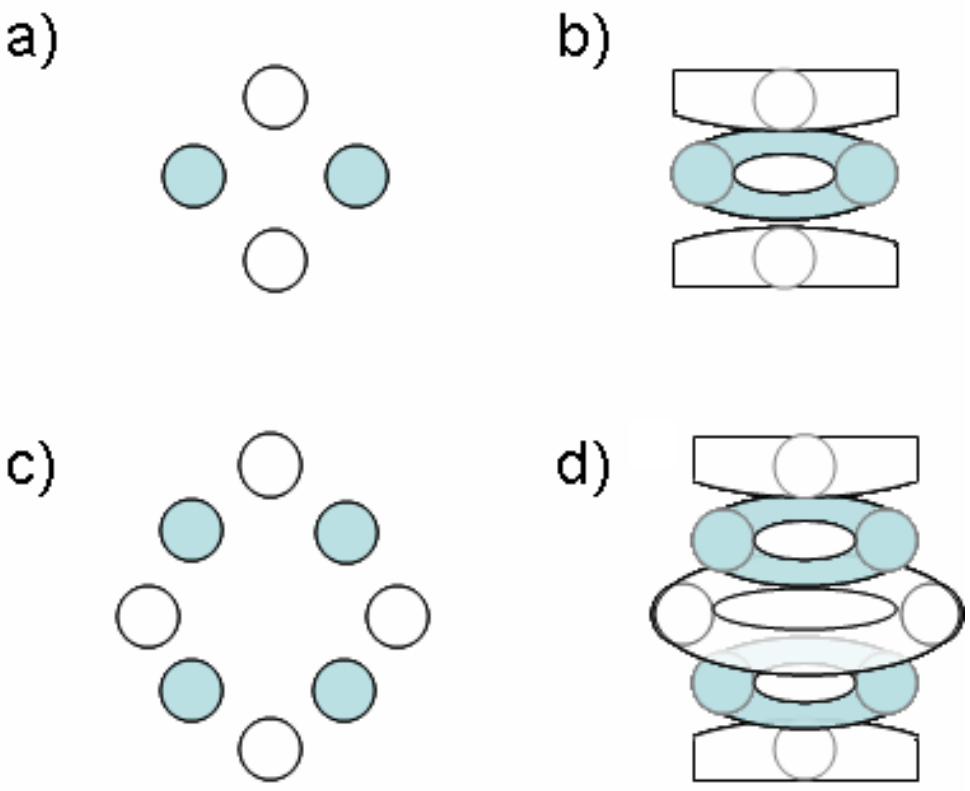

Figure 5.2 – Representation of a) Quadrupole mass filter, b) 3-D quadrupole ion trap, c) Octapole ion guide and d) 3-D octapole ion trap. Shaded color demotes different phase but equal amplitude.

In the octapole ion trap electrode geometry, the two smaller diameter ring electrodes are called "intermediate" ring electrodes and the larger diameter ring electrode is called the "central" ring electrode. An "ideal" octapole ion trap has a characteristic geometric relationship (*s*) between the radii of these two sets of electrodes, which is described in **Equation 5.4**.[9] In this equation, r_0 is half the inner diameter of the central ring electrode and r_{in} is the shortest distance from the intermediate ring electrode's surface to the trap center at the polar angle equal to arcos($\sqrt{3}/7$).[9] Similar to the 3-D quadrupole ion trap, the "ideal" 3-D octapole ion trap ring electrodes have hyperbolic surfaces.

$$s^4 = \frac{3}{8} r_0^4 + \frac{3}{7} r_{in}^4 \qquad \textbf{EQ5.4}$$

The compensated cylindrical ion trap (CCIT) described in **Chapter 2**, is a five electrode cylindrical ion trap with three ring electrodes and two end cap electrodes. This quadrupole ion trap geometry is operated with a separate and independent rf voltage for each ring electrode. An octapole cylindrical ion trap (OCIT) can be implemented by simply grounding the central ring electrode. The radii of the three ring electrodes are equal and the geometry is cylindrical so **Equation 5.4** will not be satisfied. As a result, the primary octapole field will be combined with minor field components such as quadrupole, hexapole, and dodecapole fields. **Figure 5.3** shows the differences in the electric fields when the instrument is operated as a CCIT versus the OCIT. Each curve in the figure is an isopotential curve, with the greatest magnitude isopotential curves closest to the electrode surfaces.

5.2.3 Ion Motion in an Octapole Field

The time dependant electric potential for an octapole field is described in **Equation 5.5**, where z_0 is the shortest distance between the endcap electrodes and $V_0 \cos\Omega t$ is the rf voltage applied to the intermediate ring electrodes. For this analysis, no dc voltage will

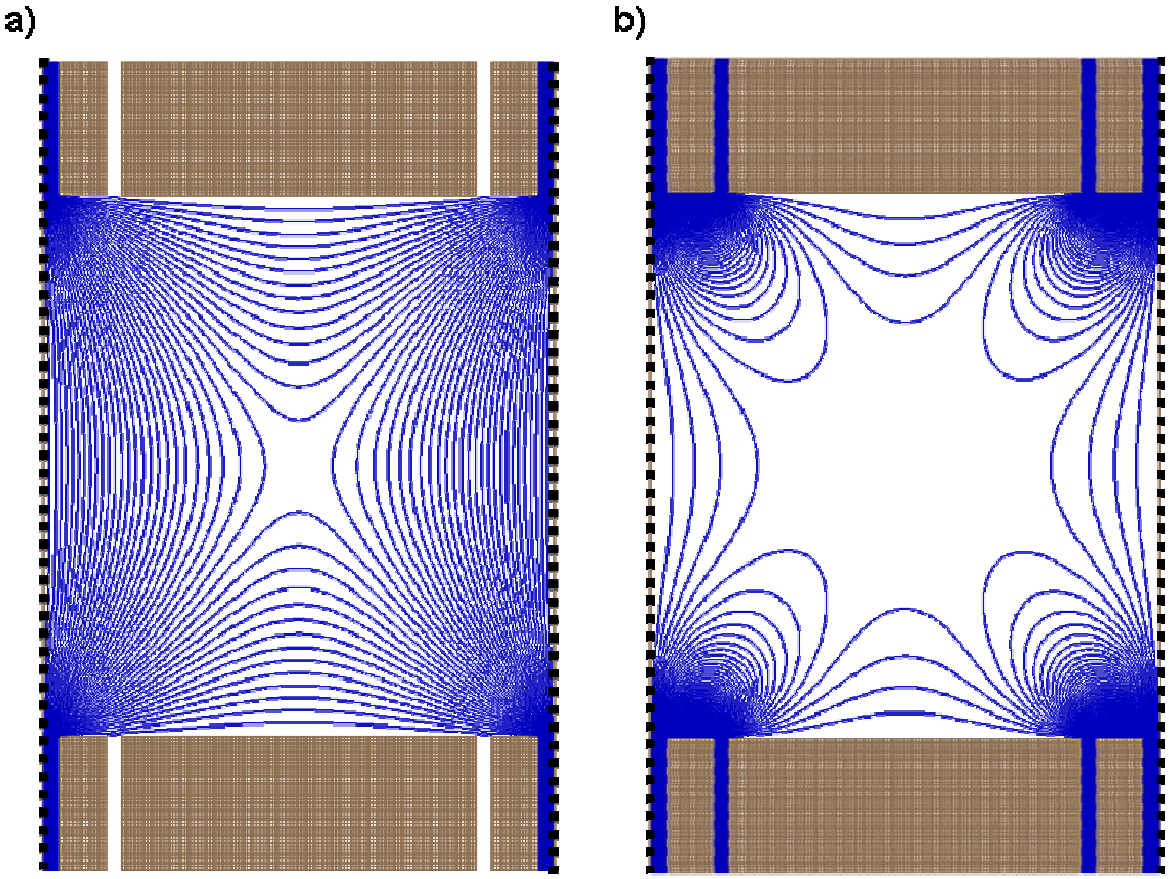

Figure 5.3 – Isopotential curves for a) CCIT “quadrupole ion trap” and b) OCIT “octapole ion trap”.

be applied to the ring electrode and the central ring and endcap electrodes are set at electrical ground.

$$\phi(r,\varphi,z,t)=\frac{V_0\cos\Omega t}{2z_0^4}\left(0.375r^4-3r^2z^2+z^4\right) \qquad \textbf{EQ 5.5}$$

In the derivation of ion motion in a quadrupole field (**Section 1.2.2** and **Section 1.3.2**) the equations describing the electric field and the force acting on an ion were simplified because the ion's motion in the x, y or r, z dimensions were independent. Because the electric potential in an octapole field has cross terms, the motion of an ion in the r or z dimension can not be decoupled. Therefore **Equation 5.6** and **Equation 5.7** are two coupled, nonlinear, time dependant second order differential equations which when solved describe the trajectory of a single ion in an octapole field (knowing initial conditions).[9]

$$\frac{d^2r}{d\zeta^2}=2q_4\cos(2\zeta)\frac{3r}{s\sqrt{2}}\left(\frac{r^2}{2s^2}-2\frac{z^2}{s^2}\right)+\frac{2M_z^2}{m^2\Omega^2r^3s} \qquad \textbf{EQ5.6}$$

$$\frac{d^2z}{d\zeta^2}=2q_4\cos(2\zeta)\sqrt{2}\frac{z}{s}\left(3\frac{r^2}{z^2}-2\frac{z^2}{s^2}\right) \qquad \textbf{EQ5.7}$$

$$\zeta=\frac{t\Omega}{2} \qquad \textbf{EQ5.8}$$

$$q_4=2\sqrt{2}\frac{eV}{m\Omega^2s^2} \qquad \textbf{EQ5.9}$$

$$M_z=mr^2\varphi \qquad \textbf{EQ5.10}$$

In **Equation 5.6** and **5.7** the term ζ is a unitless parameter described in **Equation 5.8**, s, r and z are geometric terms, Ω is the angular frequency of the rf voltage in radians, and *m* is the mass of the ion of interest in kilograms. The q_4 term is analogous to the q_z Mathieu parameter for quadrupole devices and is described in **Equation 5.9**. As described in

Section 3.5, the radial motion in an octapole field contains an angular momentum term (M_z), which is shown in **Equation 5.10** where φ is the tangential angular velocity of the ion.[9, 10] As previously mentioned in **Section 3.5**, the angular momentum is considered to be negligible or zero. This is because the tangential velocity is zero. As long as the electrodes are symmetrical the tangential angular velocity will remain zero.[9, 10] When this angular momentum term was previously mentioned in **Section 3.5**, the octapole field was a minor field component and the angular term was considered negligible.[10] In a predominantly octapole field, the same assumption is valid as long as the electrodes have rotational symmetry.[9]

5.2.4 Octapole Ion Trap Operation

While **Equations 5.6** and **5.7** do take a similar form to the Mathieu equation that is described in **Equation 1.10**; the fact that these equations are not independent results in very complex solutions. There is currently no known literature describing the stability diagram for the 3-D octapole ion trap. The operation of the octapole ion trap is simplified by the fact that no dc potential is used in these experiments; meaning the only concern is the stability diagram along the q axis. Therefore all that is needed is the maximum q_u value ions can have and still have a stable trajectory in the 3-D octapole ion trap. As will be described later, this value can be ascertained through ion trajectory modeling. But for the purposes of understanding how the octapole ion trap operates an estimate of these q_u values will be helpful.

The Mathieu stability diagrams for the quadrupole mass filter and the 3-D quadrupole ion trap have some important similarities. In both instruments, when no dc voltage is used (a_u=0) the stability diagrams are identical along the q-axis. In both instruments, ions that

have a q_u value greater than 0.908 do not have stable trajectories. If the linear octapole and 3-D octapole ion trap have a similar correlation in their stability diagrams, then the ions that have a q_z value greater than 50 will not have stable trajectories and will not be trapped.[11] In a 3D quadrupole ion trap with a radius of 1 cm operated at 1.1 MHz, 7.5 $kV_{0\text{-}p}$ is necessary to eject a 650 Da ion at a q_z of 0.908. In a 3-D octapole ion trap, 375 $kV_{0\text{-}p}$ would be required to eject the same 650 Da ion, assuming similar dimensions and operating conditions. The required high voltage means that mass selective instability is not going to be a practical mode of operation. Instead, resonance ejection will have to be employed to eject ions from the octapole ion trap. The resonance ejection voltage could be applied to both the endcap electrodes with the central ring still grounded, to both endcaps and the central ring, to solely one end cap or the central ring with the other two electrodes grounded, or the central ring and either the entrance or exit endcap electrodes with the unused endcap electrode grounded. Resonance ejection could be performed with a static frequency in conjunction with a mass selective instability scan, as described in **Section 1.3.4**, which would eject ions over a portion of the full mass-to-charge range that can be trapped. Alternatively, the rf voltage could be held static and the frequency of the resonance ejection voltage varied to resonantly eject ions over the entire mass-to-charge range; e.g., to eject out ions in increasing order of mass-to-charge decrease the frequency from $\Omega/2$ to some lower value.

5.3 Methods

5.3.1 Ion Trajectory Simulations

5.3.1.1 Creating the Model

Ion trajectory simulations were performed using the simulation program SIMION 3D 7.0. In this program ion trajectories are modeled moving through an electric field. The electric field is created from an electric potential array which describes the potential as a function of the distance from the electrode surface (or the potential gradient). This potential array is constructed from the geometry of the electrodes, which was entered with the electrode dimensions and spacing as outlined in **Chapter 2**. The spatial resolution of the potential array is defined in mm/grid unit, which for these simulations was 0.1 mm/grid unit. The potential array for each electrode, which is in volts/grid unit, was 108,000 pts. The over all potential array had dimensions of 360x300x300 grid units. The potential gradients are calculated by solving Laplace's equation using the finite difference method approach (small step sizes), which is referred to as refining the potential array in SIMION.[12] The conditions for refining the potential array that were used were a maximum iteration limit of 20,000 steps, max-over relaxation factor of 0.90, historical memory factor of 0.70, and a convergence of $5x10^{-3}$.[12] These conditions define how long the refining process takes and the accuracy of the potential array.[13]

Laplace's equation describes an electrostatic condition; therefore the potential arrays are normalized such that they can be updated for any voltage applied to the electrode. A user program, supplied with SIMION, was modified for the simulation of ions in the CCIT and the OCIT.[13] The CCIT and the OCIT contain three ring electrodes and two endcaps to which each can have an rf voltage applied. The program was customized to allow an rf voltage to

be applied to any of the five electrodes. The program adjusts the voltage on the electrodes at a given time interval (<<1 μsec). The program includes the addition of a supplemental ac voltage to the endcap electrodes for resonance excitation and also includes calculations to simulate collisions with a buffer gas. During simulations with the OCIT, either the central ring and endcap electrodes were grounded with the rf voltage applied to the intermediate ring electrodes or vice versa.

5.3.1.2 Pressure Calculations

The pressure model used for these simulations is a simple hard sphere collision model that simulates elastic "head on"/frontal collisions with a stationary buffer gas. At each time step the distance an ion has traveled is calculated from the ion's velocity. The resultant value and another, called "mean free path", are used to calculate a collision factor, termed CF (**Equation 5.11)**. The mean free path term (MFP) the distance traveled between collisions. The collision factor is compared to a random number between 1 and 0.

$$CF = 1 - e^{\frac{-d}{MFP}} \qquad \textbf{EQ5.11}$$

If the random number is greater than the CF then a collision occurs and the ion's velocity is readjusted using **Equation 5.12**, where v_{old} is the initial velocity of the ion, m_{ion} is the mass of the ion, m_{buffer} is the mass of the buffer gas, and v_{new} is the final velocity.

$$v_{new} = v_{old}\left(\frac{m_{ion} - m_{buffer}}{m_{ion} + m_{buffer}}\right) \qquad \textbf{EQ5.12}$$

This collision model does not take into account collisions that might increase the velocity of an ion. The value of the MFP term used in these experiments was 40 mm and the mass of the buffer gas was 4 Da. Researchers have shown that the MFP of 40 mm using this model corresponds to a pressure of 15 mTorr (collisional cross section of 50 $Å^2$) when modeled in

different trajectory simulation software; however, it is believed that this pressure is two large.[12] The calculated MFP corresponds to a pressure of approximately 0.6 mTorr assuming a 50 $Å^2$ collision cross section. The correlation between modeled pressure and actual with this pressure model has not been determined but it is hope that the model will correlate to a pressure close to 1 mTorr.

5.3.1.3 Simulation Conditions

The simulations conducted modeled two experiments: ion storage and resonance ejection. In each of these simulations a *m/z* 100, 500, 1000, 5000, and 10000 ion was individually modeled with an initial kinetic energy of 0.1eV. During one set of resonance ejection simulations, an ion representing xenon's most abundant isotope (*m/z* 132) was also modeled. For each set of simulations five replicates were conducted. Unless otherwise stated the initial position of the ions was in the geometric center of the ion trap. Additionally, the simulations were conducted for 10000 μsec and at each 5 μsec interval, an ion's simulation time, x position, y position, z position, v_x, v_y, and v_z were recorded to a comma delimited file for data analysis. In the ion storage simulations, ions were stored at various rf voltages ranging from 200 $V_{0\text{-}p}$ to 25 $kV_{0\text{-}p}$; if an ion's motion was still stable after 10000 μsec the ion was said to be "trapped". Resonance ejection simulations were performed with a 3, 5, 8 or 15 $V_{0\text{-}p}$ resonance ejection voltage which had a frequency ranging from 1 to 400 kHz.

5.3.2 Experimental Implementation of the Octapole Ion Trap

The cylindrical octapole ion trap was implemented by grounding the center ring electrode of the CCIT electrodes and driving the intermediate ring electrodes with the rf voltages generated from the circuitry of rf_2 and rf_3 (**Chapter 2**). To minimize rf pickup on

the central ring electrode, the ground connection should be directly at the electrode; however, doing this prevents simple conversion back to the CCIT operation. Therefore the ground wire and ground connection to the rf circuitry enclosure were made as close as possible to the high voltage feed-through. Resonance ejection voltages were generated with a Stanford Research systems DS345 function generator (Sunnyvale, CA). This function generator is capable of a linear frequency sweep over a set range at a given scan rate which determined the frequency resolution of the ramp. The function generator outputs a voltage with the beginning frequency of the ramp until the linear frequency sweep is initialized with a trigger. Following the sweep the function generator returns to the original voltage. Because the function generator is always outputting a voltage, the output needed to be switched on or off. A circuit, shown in **Figure 5.4**, was designed to gate the application of the waveform so that it was only applied to the endcap electrodes during ion ejection. Following the gate (ADG411 solid state relay Analog Devices, Norwood, MA), a non-inverting input operational amplifier (AD811, Analog Devices, Norwood, MA) is used to double the amplitude of the resonance ejection voltage. The output of this circuit drives a balun, which protects the circuit and the function generator from rf feedback and outputs two equal amplitude but 180 degrees out of phase voltages that are the same frequency as the input voltage.

The analyte used in these experiments was Xenon. Vapors were introduced into an EI source using a metering valve with an analyte pressure of $9x10^{-7}$ torr. The EI source conditions were identical to those listed in **Section 2.5**. The dynode and guard ring were held at -7 kV and -400 V respectively. The resonant frequency of the rf system was 746 kHz with the central ring grounded. The rf voltages on the intermediate ring electrodes were held at

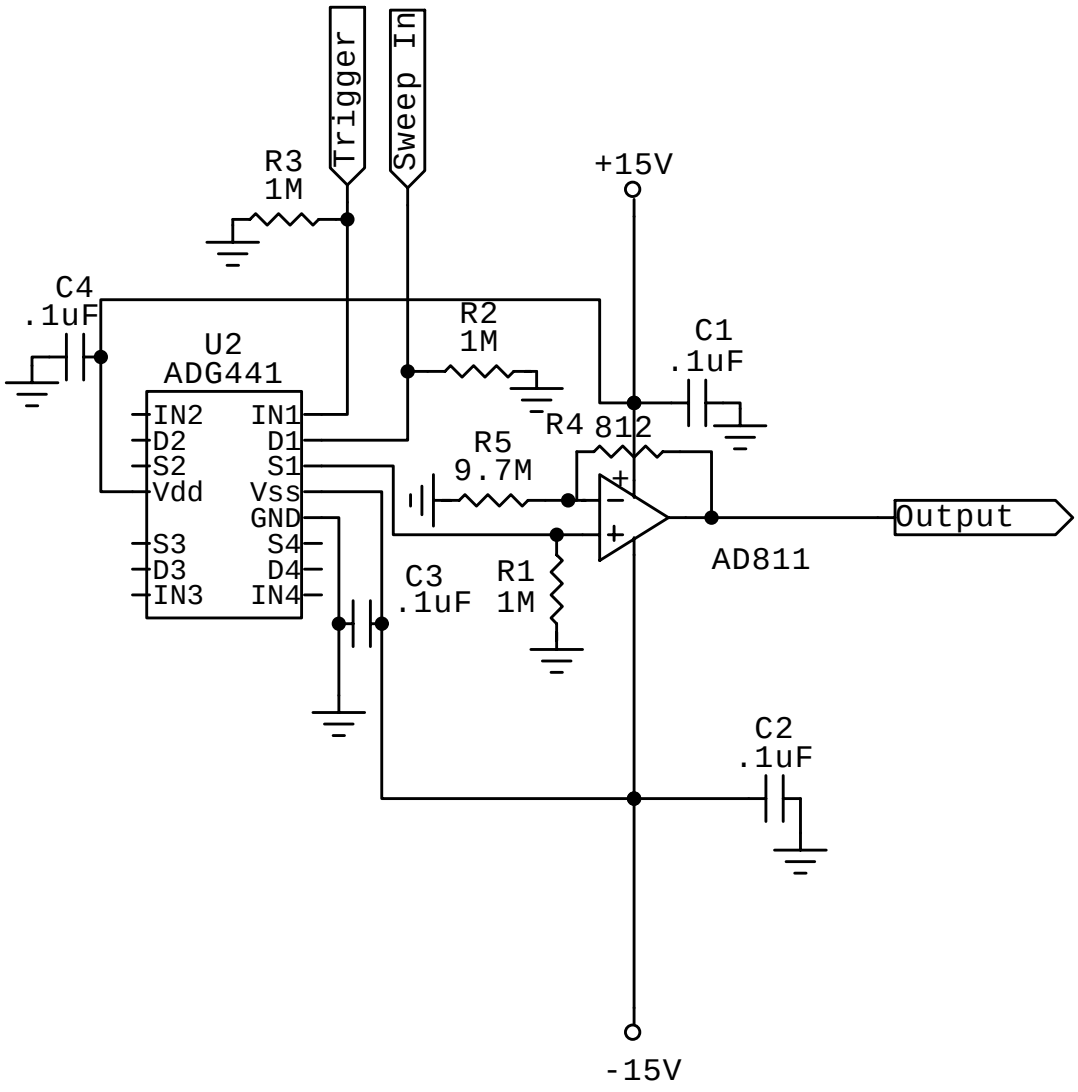

Figure 5.4 – Gate circuit for applying resonance ejection voltage to endcap electrodes.

$1000V_{0\text{-}p}$ during the entire experiment. The time table for the resonance ejection experiments was as follows: The rf voltages were allowed to initialize for 35 msec. Ions were then injected into the ion trap for 2 msec (unless otherwise noted). The electron multiplier was subsequently allowed to equilibrate for 80 msec. The equilibration time is to give the power supply enough time to reach its full voltage. During resonance ejection experiments the full frequency sweep required about ~130 msec.

The maximum storage capacity of an ion trap is the maximum number of ions that can be put into the ion trap. Experiments to compare the maximum storage capacity of the OCIT and CCIT were performed by varying the time that ions were injected into the ion trap from 1 msec to several seconds. Following the electron multiplier warm up time, ions were then ejected by turning off the rf voltage, which takes about 200 μsec to fully decay. Ion extraction was aided by the large negative voltages on the dynode and the guard ring.

5.3.3 CCIT Comparison Experiments

The OCIT instrumental setup can be converted back to the CCIT simply by removing the ground wire, which was attached to the high voltage feed through connected to the central ring electrode, and reconnecting the rf circuitry for the center ring. The rf voltages of all three electrodes will be equal so that the CCIT is essentially a CIT with one large ring electrode. The CCIT operated in this manner will allow for comparisons of a 3-D quadrupole ion trap with cylindrical geometry to a 3-D octapole ion trap with cylindrical geometry. Analyte pressures, source conditions, and the voltages applied to the guard ring and dynode for the CCIT experiments were consistent with those listed for the OCIT. After reconnecting the center coil (see **Chapter 2**) the resonant frequency of the system was found to be 759 kHz. The time table for resonance ejection experiments was as follows: the rf voltage was

allowed to initialize for 5 msec, ions were injected into the ion trap at a LMCO of 20 for 2 msec, the LMCO was reduced to 16 Da and the ions cooled for 20 msec. For ion ejection, the electron multiplier warmed up for 80 msec, and ions were resonantly ejected at $\beta_z = ½$ for 175 msec while increasing the LMCO from 16-140 Da. Comparison experiments to estimate the maximum storage capacity of the CCIT were conducted using the same ion ejection method described in **Section 5.3.2**. The difference between the experiments is only that the rf voltage (LMCO) is varied in the CCIT whereas it is constant in the experiments for the OCIT.

5.4 Results and Discussion

5.4.1 Ion Storage

The range of voltages over which ions have stable trajectories in the CCIT and OCIT was modeled. As shown in **Figure 5.5,** 8000 $V_{0\text{-}p}$ is necessary to trap the full mass-to-charge of ions that were modeled in the OCIT, whereas only 570 $V_{0\text{-}p}$ is necessary in the CCIT. This voltage difference is most likely because of the rapid rate at which the octapole field declines in the ion trap as a function of the axial distance; a larger amplitude voltage is necessary to achieve sufficient rf voltage near the center of the ion trap.

The maximum rf voltage at which ions have a stable trajectory in the ion trap (with no dc voltage) should be the right edge of the Mathieu stability diagram. As described in **Section 5.2.4** if the 2-D octapole ion trap stability diagram is similar to the 3-D octapole ion trap, just as the 2-D quadrupole is similar to 3-D quadrupole ion trap, then the maximum rf voltage for stable ion trajectory should be ~50 times greater in the OCIT than in the CCIT. As shown in **Figure 5.6**, the maximum rf voltage in the OCIT is much greater than in the

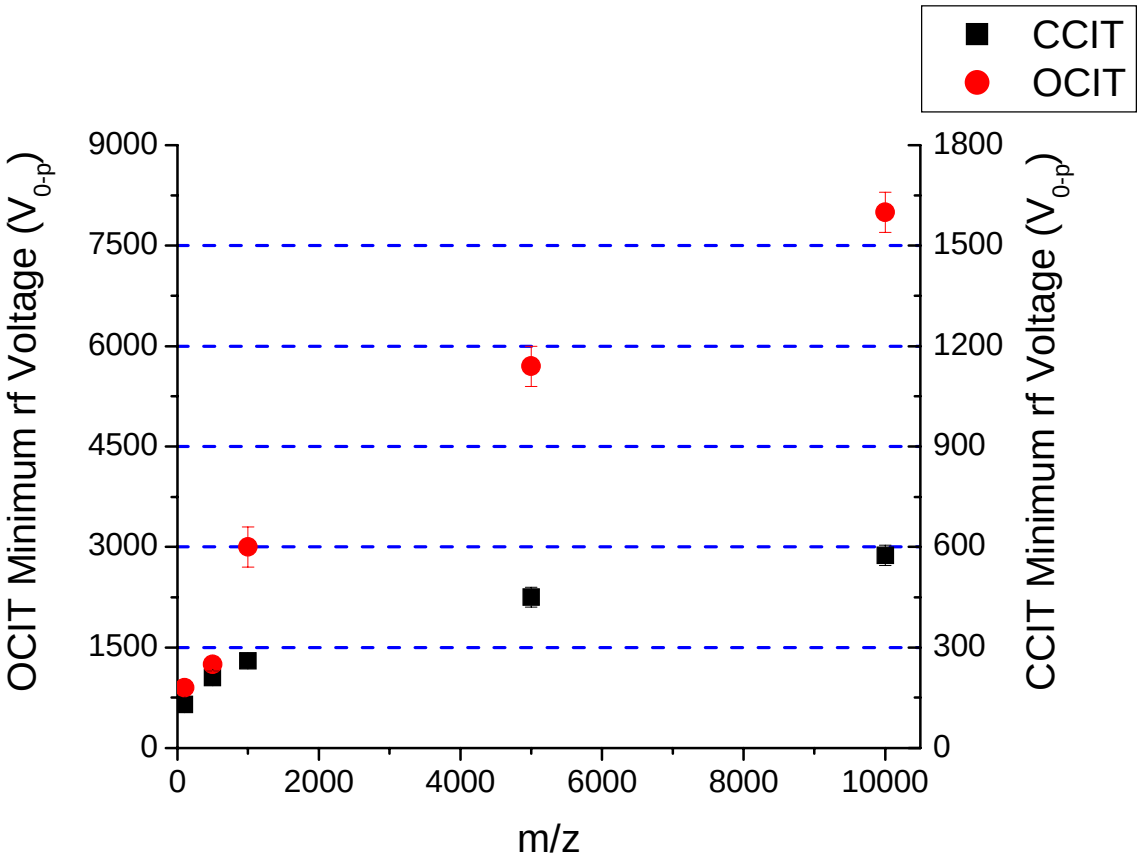

Figure 5.5 – Minimum rf voltage required for ions to have a stable trajectory in the CCIT and the OCIT.

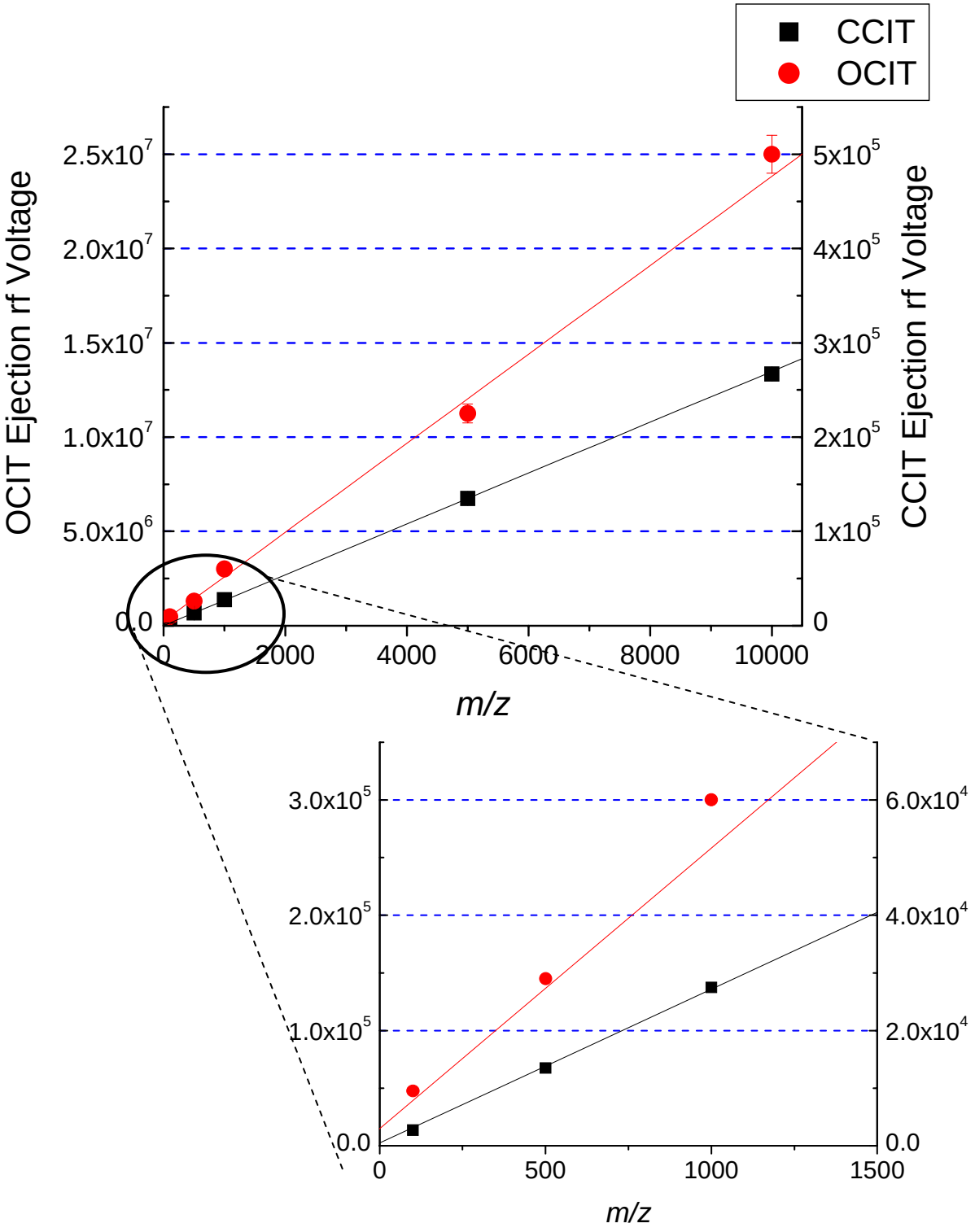

Figure 5.6 – Maximum rf voltage allowed for ions to have a stable trajectory in the CCIT and the OCIT

CCIT. The slopes of the lines shown in **Figure 5.6** are 980 V/(*m/z*) and 27 V/(*m/z*) for the OCIT and the CCIT respectively, which means the octapole ion trap needs a 36 times larger voltage to eject an ion of the same mass-to-charge ratio compared to the quadrupole ion trap. This value is close to the predicted value of 50 times greater voltage described in **Section 5.2.4**, based on the maximum q_u of 50 for the OCIT and 0.908 for the CCIT. The OCIT data is not perfectly linear which is contrary to what is predicted from **Equation 5.9,** where the q_4 is directly proportional to the rf voltage. The simulation data is only non-linear with the lighter mass-to-charge ratio ions. Specifically, the *m/z* 100 ion has a stable trajectory until 190 $kV_{0\text{-}p}$ in the OCIT and until 2500 $V_{0\text{-}p}$ in the CCIT; these voltages differ by a factor of 70. All of the other ions modeled have factors around 35 ± 2.

5.4.2 Resonance Excitation

As described in **Section 5.2.1** there should be an improvement in MS/MS efficiencies using octapole fields because the competition between excitation and ejection is reduced by the cross terms in the equations of motion. Most of the reports in the literature on this enhancement have been conjecture; however, researchers have recently experimentally verified the theory in a linear ion trap with added octapole fields.[6] Both these experiments and the theoretical improvements due to octapole fields occur in a field that is predominantly quadrupole. There are no literature reports of ion excitation in a predominantly octapole field. Resonance excitation of a *m/z* 500 ion was simulated in both the CCIT and the OCIT "operated" at 800 kHz. In the CCIT, at a $q_z = 0.17$, the *m/z* 500 ion was resonantly excited with a 500 mV_{pp} 47.4 kHz excitation voltage. As shown in **Figure 5.7**, the ion was ejected after 3 msec at a kinetic energy of 35 eV. In the OCIT, at a $q_4 = 0.17$, the ion was resonantly excited with a $10V_{pp}$ 38.4 kHz excitation voltage for 50 msec and, as shown in **Figure 5.8,**

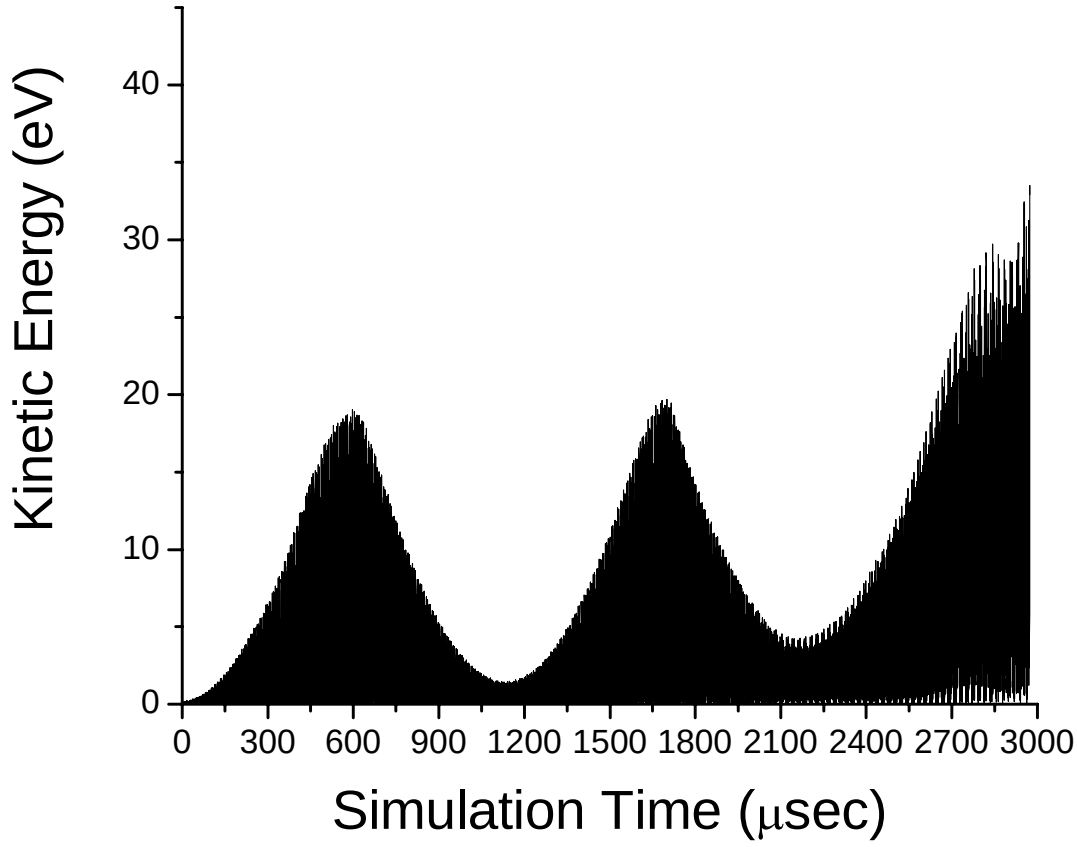

Figure 5.7 – Simulation of resonance excitation of *m/z* 500 ion in a CCIT $q_z = 0.17$, 500 mV_{pp} 47.4 kHz resonance excitation voltage.

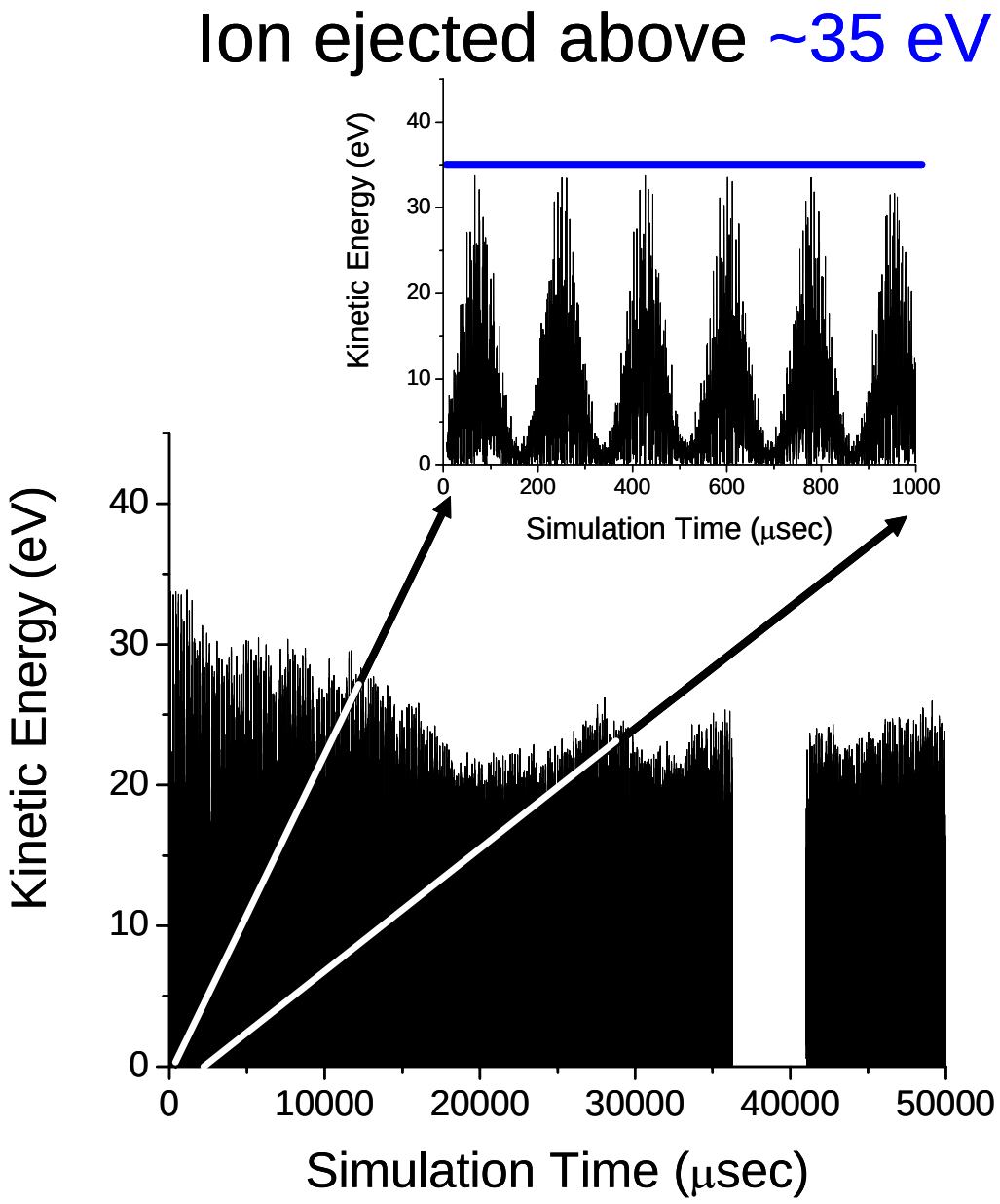

Figure 5.8 – Simulation of resonance excitation of a *m/z* 500 ion in a octapole cylindrical ion trap at $q_z = 0.17$, 10 V_{pp} 38.4 kHz resonance excitation voltage.

was not ejected. The ion's kinetic energy starts out just below 35 eV (inset figure of **Figure 5.8**) and then (due to the cross terms) the ion's motion goes out of resonance with the excitation voltage and the ion is cooled down. The ion then goes back into resonance and is continually excited and cooled for the entire 50 msec period, virtually removing any competition between ion ejection and excitation. These simulations for the excitation of an ion in a predominantly octapole field are consistent with the theory that has been described for the octapole field as a minor field component.

5.4.3 Resonance Ejection

5.4.3.1 Single Frequency

Theoretically in an octapole field, all ions of the same mass-to-charge ratio that have been cooled to the center of the ion trap should have a single secular frequency at a constant applied rf voltage, which is represented by the dotted line in **Figure 5.9**. Ions will typically absorb power from resonance ejection voltages over a small range of frequencies, which is referred to as off resonance excitation. This range of frequencies over which ions will absorb power from the resonance ejection voltage can broaden because space charge effects and/or thermal variances. In 3-D quadrupole ion traps this range can be larger than several kHz.[14] When resonance ejection was experimentally performed at a range of separate frequencies, shown by black square data points in **Figure 5.9,** Xenon ions were resonantly ejected over a range of frequencies from 500 Hz to 70 kHz. A large peak area means that ions were resonantly ejected. Therefore Xenon ions were not resonantly ejected above 75 kHz. Simulations of resonance ejection of Xenon ions, shown by the circle points in **Figure 5.9**, also yielded ejection (low simulation times) over a similar range of frequencies to those experimentally observed. The two overlaid plots of experimental (black square) and

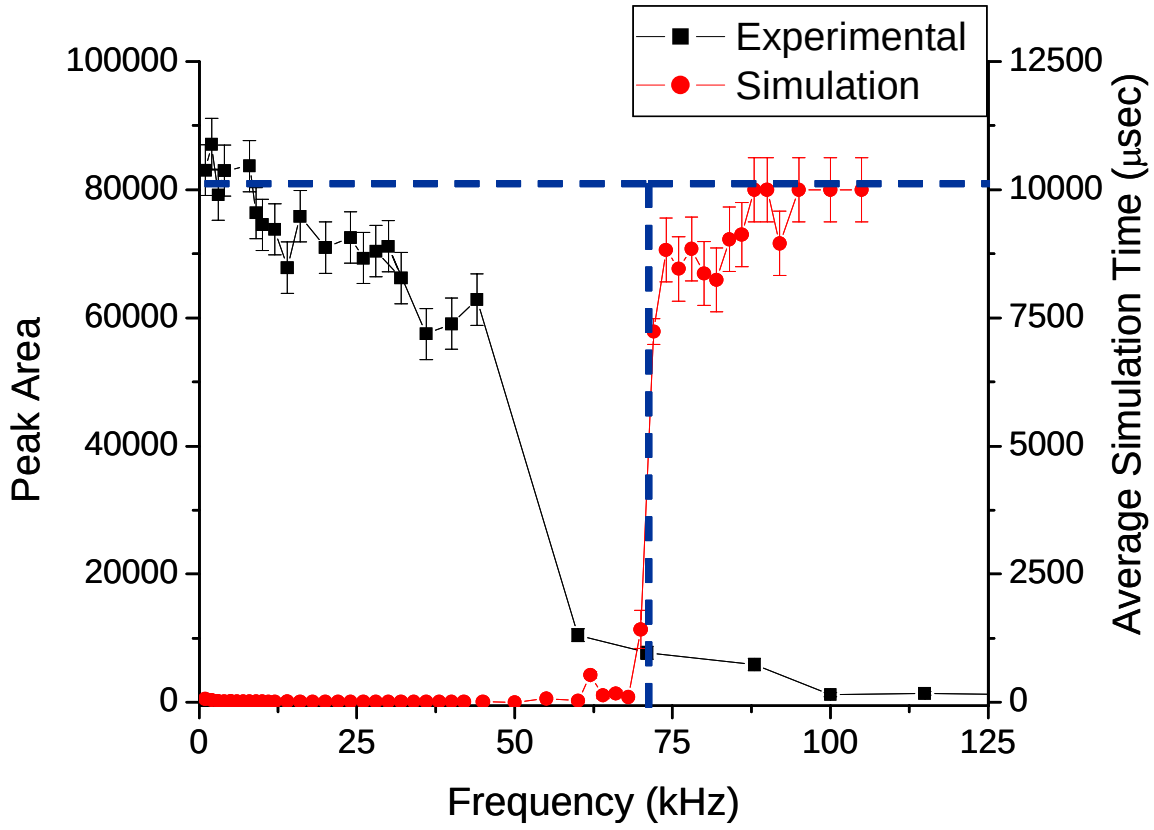

Figure 5.9 – Experimental and simulated resonance ejection of xenon ion *m/z* 132. Dotted line is the theoretical secular frequency of the ion at 73.4 kHz. Low simulation times mean ions were ejected.

simulation results (red circle) appear to be the reciprocal of one another; however, low simulations times from ejected ions correlate to large peak areas from ejected ions in the experimental observations. Simulation of resonance ejection of higher mass to charge ions showed that these ions were also ejected below resonance ejection voltage frequencies of 200 kHz.

Both simulations and experimental observations suggest ions are ejected because of a non-resonant process. In this process ions actually adopt the frequency of the resonance ejection voltage, even though it is not the ions' theoretical secular frequencies. In some instances the ions are not all ejected at the same time and are instead ejected in packets which are temporally separated by a period equal to the frequency of the resonance ejection voltage. When a 5 kHz resonance ejection voltage was applied to the end caps, as is shown in **Figure 5.10a**, ions were not all ejected in the first cycle of the resonance ejection voltage. During each subsequent cycle the intensity of the ion signal decreases. When the amplitude of the resonance ejection voltage was increased all of the ions can be ejected in one packet. If the resonance ejection voltage was linearly increased during the ejection time, the ions were ejected in multiple packets as shown in **Figure 5.10b**. The over all ejected ion packets had a global Gaussian shape, with the maximum ejection occurring at the amplitude necessary to eject more than 75% of the ions trapped. Simulations of resonance ejection with lower amplitudes also showed that ions were not ejected in one packet and subsequent packets of ions occurred at a time corresponding to the period of the resonance ejection voltage.

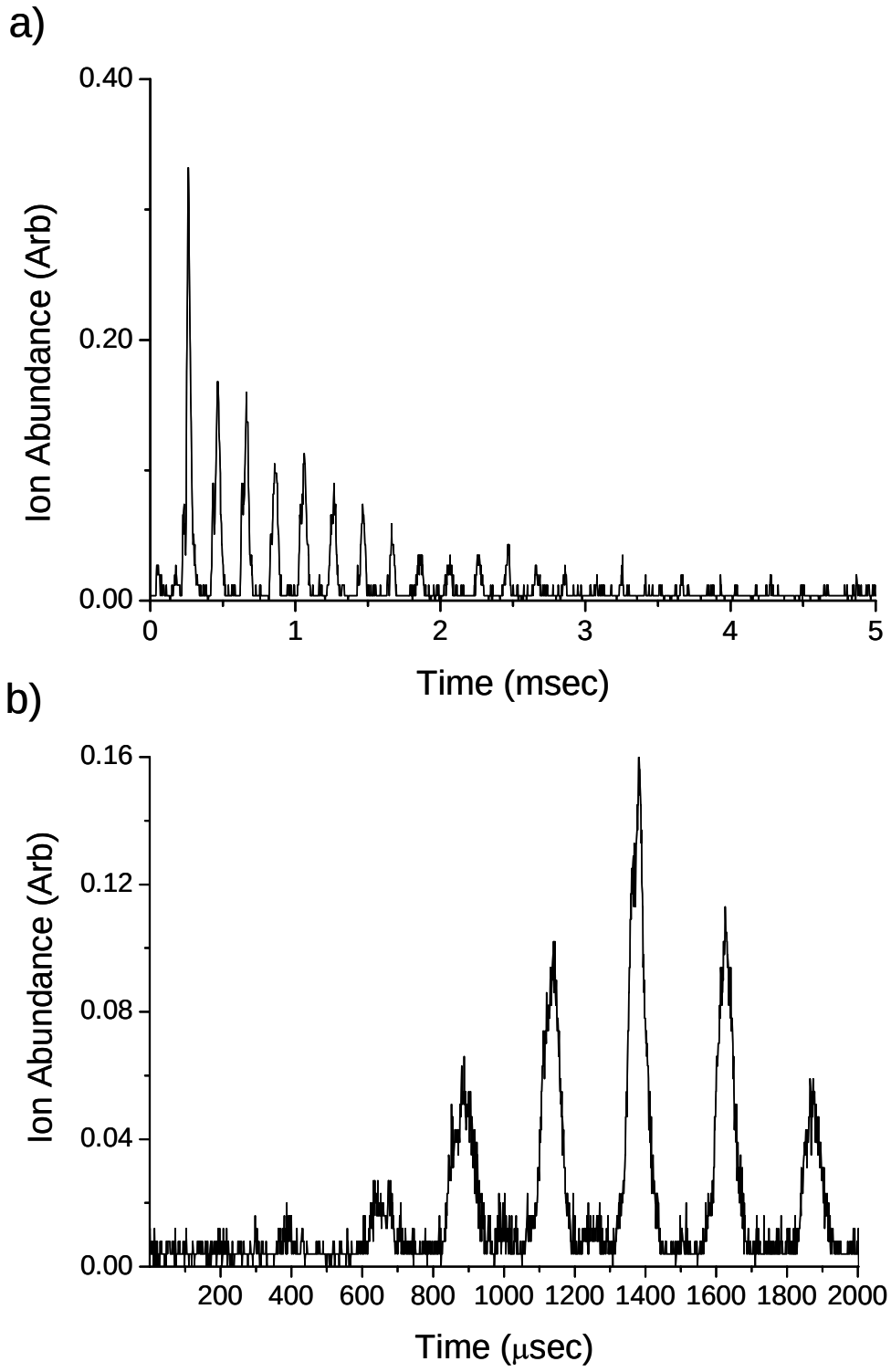

Figure 5.10 – Experimental Resonance ejection of xenon at a) 10 $V_{0\text{-}p}$ 5 kHz for 5 msec and b) Linear ramp of amplitude 0-10 $V_{0\text{-}p}$ 5 kHz for 2 msec.

5.4.3.2 Frequency Sweep

Xenon has multiple isotopes and should produce ions at *m/z* 128, 129, 130, 131, 132, 134, and 136. The most abundant ion is the *m/z* 132 ion. Each of these ions should have its own secular frequency. At a constant applied rf voltage, performing a linear increase of the resonance ejection voltage frequency should theoretically eject the ions in order of their increasing mass-to-charge ratios. When this linear sweep was performed from 200 - 30 kHz and from 100 – 30 kHz, ions were ejected over a range of 70 - 80 kHz in one unresolved peak. If the linear sweep was reversed in direction, from 30 – 200 kHz, ejection occurred from 30-40 kHz. These results agree with the non-resonance ejection that was observed with a single frequency.

5.4.3.3 Resonance ejection in the CCIT

In a 3-D quadrupole ion trap as the rf voltage is increased, the secular frequency of ions of a given mass-to-charge ratio should increase. Over a range of rf voltages corresponding to q_z less than 0.4 this increase is linear. The plot in **Figure 5.11a** shows how the secular frequency of a xenon molecular ion (*m/z* 132) should theoretically change as a function of rf voltage. Secular frequencies were calculated using **Equation 1.29** and **Equation 1.30**. When resonance ejection was performed at an amplitude comparable to that used in the OCIT, resonance ejection of xenon ions was observed over two voltage regions in the same mass spectrum. Resonance ejection voltage frequencies below 40 kHz caused all xenon ions to be ejected, similar to the non resonance ejection observed in the OCIT. **Figure 5.11b** shows a two-dimensional representation of the mass spectra acquired at different resonance ejection voltage frequencies. The pseudo third-dimension in the plot, ion abundance, is represented by the color scale where red is the most abundant ion signal. In

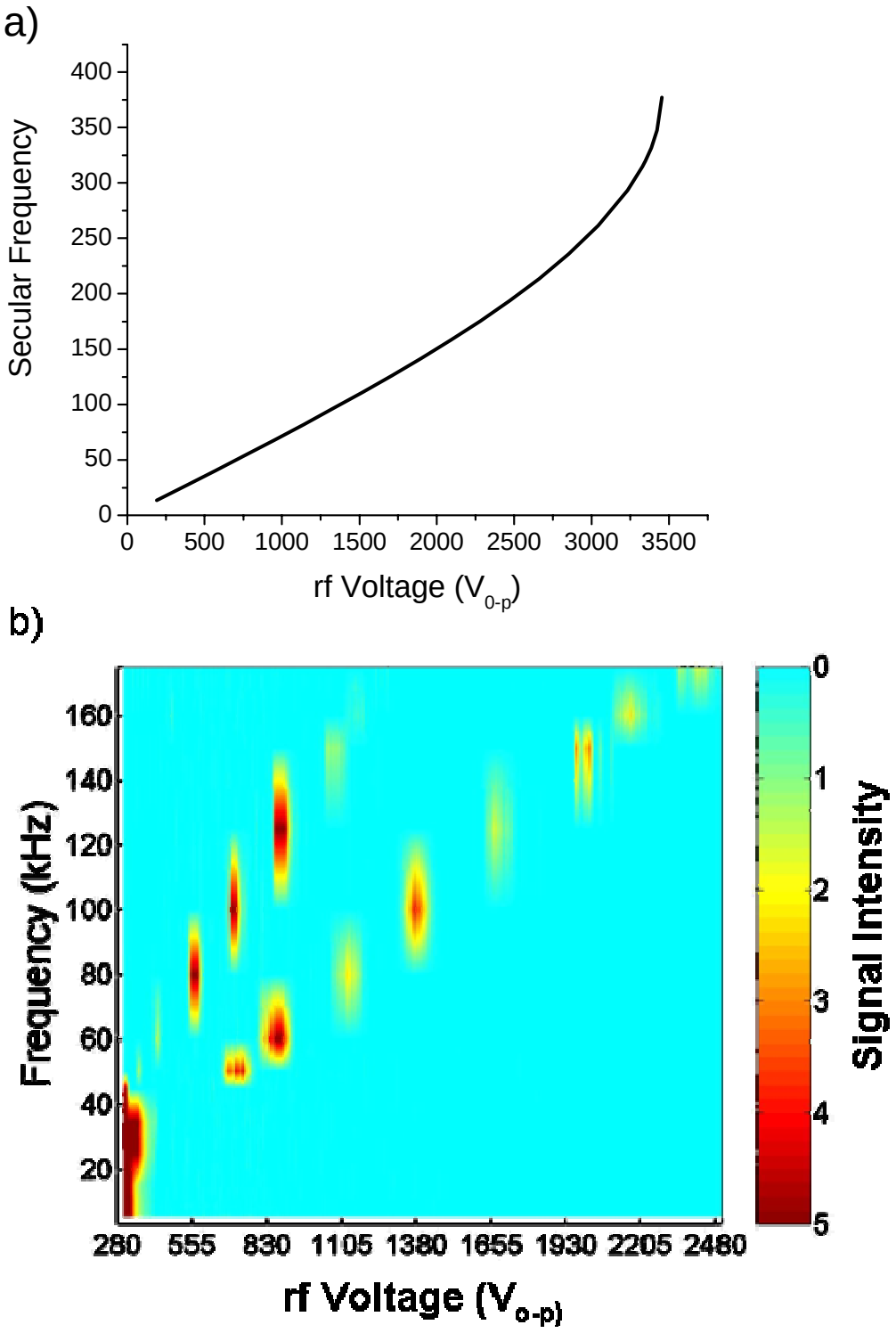

Figure 5.11 - a) Calculated secular frequency of a xenon *m/z* 132 ion b) Resonance ejection experiments of xenon in CCIT.

any one mass spectrum the observed resonance ejection occurring at the larger voltages is close to the calculated secular frequency of the xenon molecular ions at that given ejection voltage. The plot is not a continuous line like the theoretical calculation because mass spectra were not acquired at every possible frequency of the resonance ejection voltage. The ions ejected at the smaller rf voltages occur at half the voltage of the larger ejection point, which could be ions corresponding to the 2^+ charge state of Xenon. These ions are not believed to be the 2^+ charge state of the xenon ion because as the amplitude of the resonance ejection voltage is increased, the ion abundances observed at the larger voltages begin to decrease. These secondary ejection points are more likely due to spurious ejection or "ghost" peaks that have been reported in the literature with quadrupole ion traps that have a greater percentage higher order fields than a conventional 3-D ion trap.[2] Simulations of resonance ejection in the CCIT, shown in **Figure 12a** and **Figure 12b**, were performed at 5 $V_{0\text{-}p}$ and 15 $V_{0\text{-}p}$. Resonance ejection simulations at $5V_{0\text{-}p}$ do not show the secondary ejection at lower rf voltages**,** as shown in **Figure 5.12a**. Simulations were attempted at $8V_{0\text{-}p}$ as well with no observed second ejection; however at the lower amplitudes resonance ejection does occur when the frequency of the resonance ejection voltage is below 40 kHz. The second ejection point is observed in the simulations at 15 $V_{0\text{-}p}$. These simulations show that the model that is being used does agree with experimental observation in the CCIT.

5.4.4 Maximum Storage Capacity

As the number of ions trapped in an ion trap is increased, ions will undergo space charge; the effects of which are described in **Section 3.4.2**. When the number of ions in the ion trap reaches a critical value, no more ions will be able to be put into the ion trap because of columbic repulsions. This critical value is referred to as the maximum storage capacity.

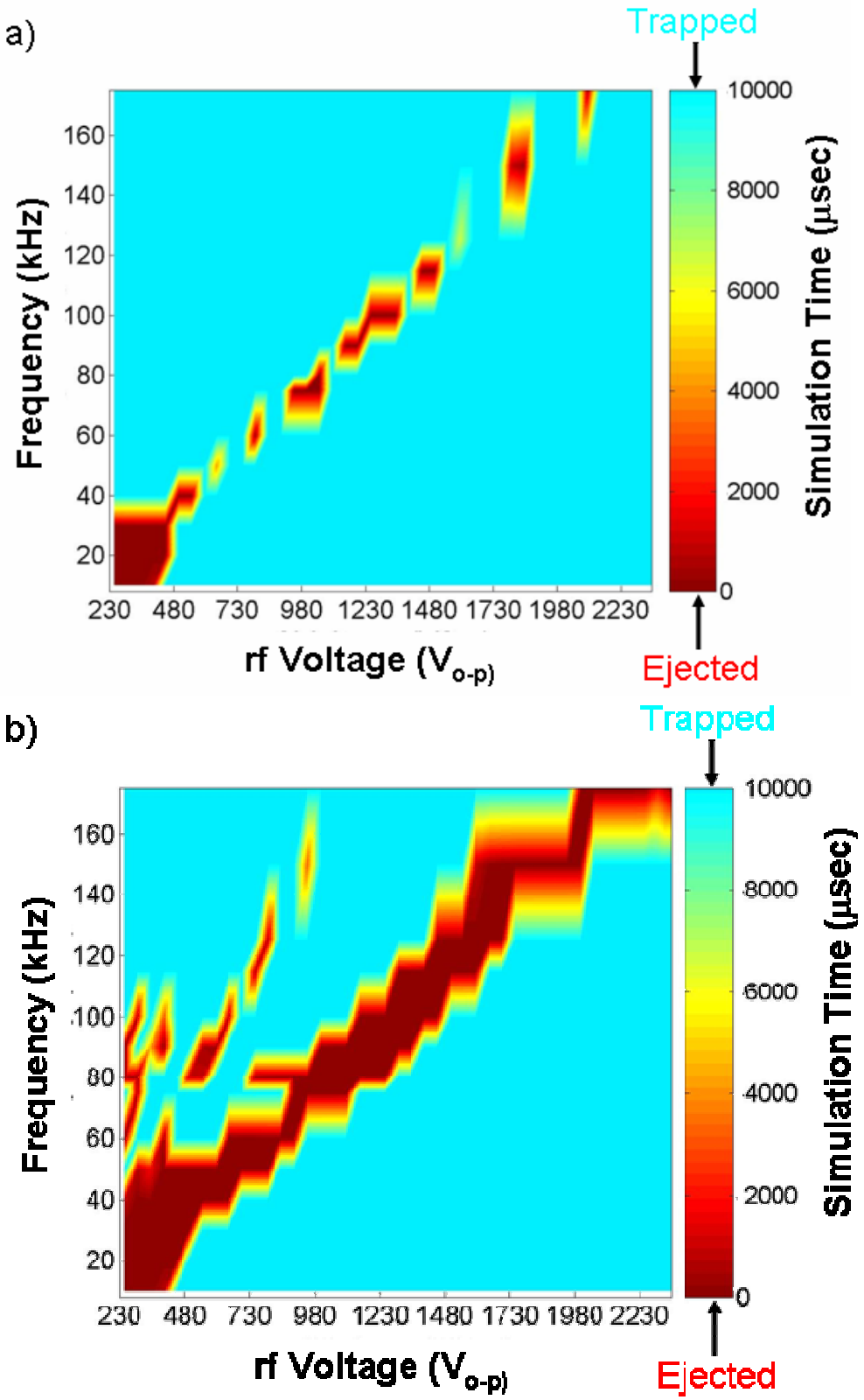

Figure 5.12 – Simulated resonance ejection in a CCIT at a) $5V_{0\text{-}p}$ b) 15 $V_{0\text{-}p}$.

It is not advisable to operate an ion trap at the maximum storage charge capacity but it is useful to know its value and where the ion abundance detected as a function of gate time becomes non-linear. If a device can trap more ions from the same analyte concentration in the ionization source, the ion trap can have a lower limit of detection for analytes and possibly an improved sensitivity. Results from the experiments exploring the maximum storage capacity in the OCIT and the CCIT are shown in **Figure 5.13a.** As a function of injection time ions can be injected into the OCIT with an observed linear increase from 0.5 to 500 msec. At longer injection times ions can still be put into the ion trap, although the increase begins to level off. The CCIT only has an observed linear range from 0.5 – 5 msec. The ion signal then levels off completely by 200 msec, which means that the CCIT has reached its maximum storage capacity. The OCIT did not level off; however, comparing the maximum observed total ion current (TIC) from the two instruments shows that the octapole ion trap (OCIT) has at least a 50 times greater maximum storage capacity than the quadrupole ion trap (CCIT). Comparing the total ion current in the range of times where the CCIT signal increase is linear, shown in **Figure 5.13b,** the OCIT still has almost 2.5 greater observed ion current than the CCIT. This means that in a region where both instruments are not under space charge conditions the OCIT is at least 2.5 more sensitive than CCIT.

5.5 Conclusions

Ion trajectories were simulated in a 3-D octapole ion trap with a cylindrical electrode geometry. Ions of *m/z* 100-10,000 were found to have stable trajectories with rf voltages ranging from 750-3x10^7 $V_{0\text{-}p}$. The minimum voltage necessary to trap *m/z* 10,000 ions (8000 $V_{0\text{-}p}$) was much higher than the rf voltages necessary for *m/z* 100 ions (750 $V_{0\text{-}p}$). Rf

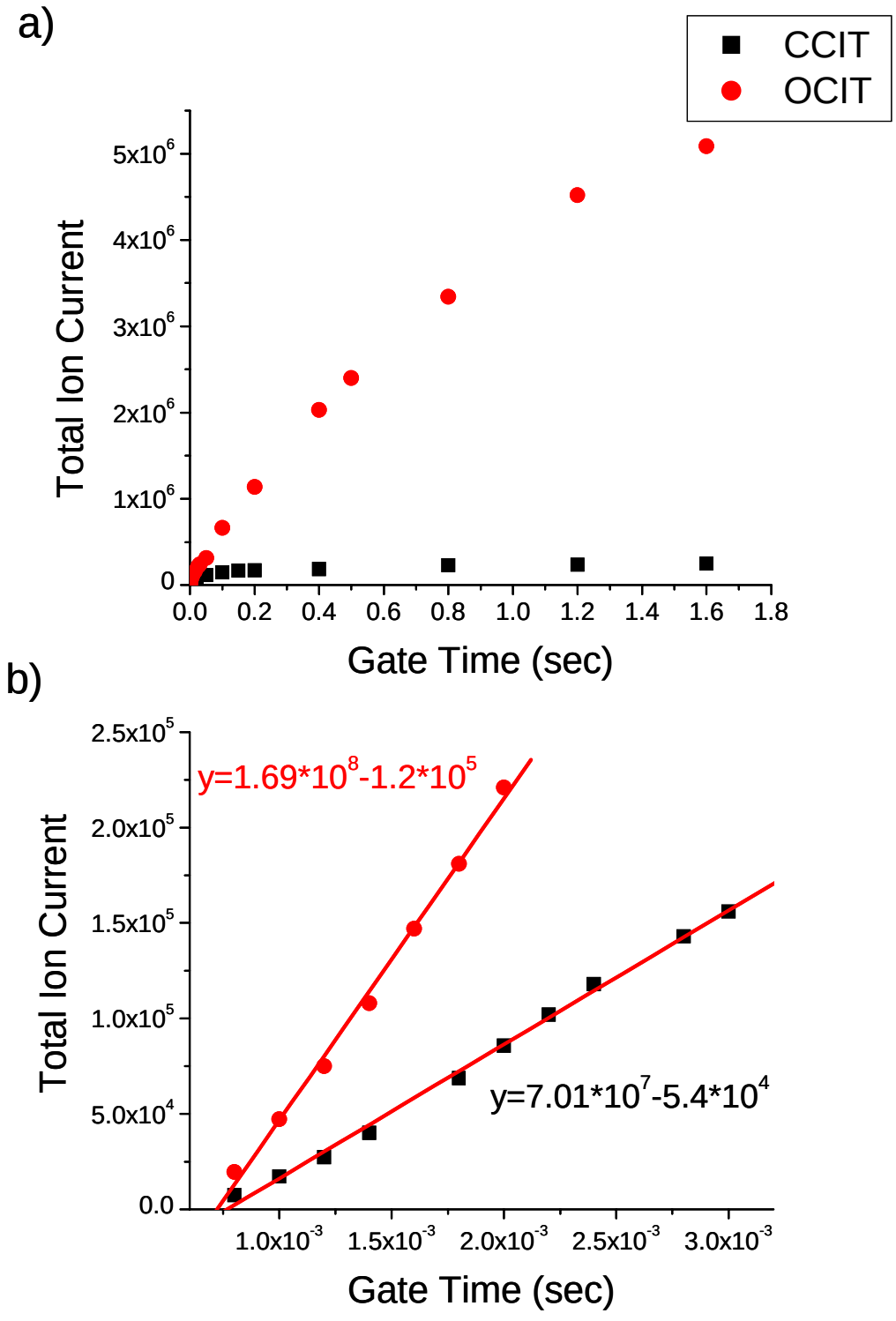

Figure 5.13 – Comparisons of a) Maximum storage capacity b) Sensitivity in linear region of CCIT.

voltages necessary to eject ions out of the octapole ion trap were 36 times greater than the voltages necessary to eject ions out of a 3-D quadrupole ion trap with identical electrode geometry. Mass analysis in the cylindrical octapole ion trap is not possible because resonance ejection simulations showed that at a constant rf voltage, ions were ejected over a broad frequency predicted by ion trajectory simulations. Resonance ejection of xenon ions occurred at all frequencies below 75 kHz. During resonance ejection ions adopt the resonance ejection voltage frequency and are ejected in packets at a rate corresponding to the period of the resonance ejection voltage. When the amplitude of the resonance ejection voltage is sufficient ($> 10V_{0\text{-}p}$) ions were ejected in as short of a time as 8 μsec. Because resonance ejection occurred over a broad frequency range the octapole cylindrical ion trap is not capable of mass analysis by resonance ejection.

Simulations performed for the 3-D quadrupole ion trap with identical geometry to the OCIT, showed that ions were ejected at all frequencies below a resonance ejection frequency of 40 kHz. Additionally, simulation data showed that at larger amplitude resonance ejection voltages, a secondary resonance ejection point was observed. Experimentally, ions resonantly ejected in the cylindrical 3-D quadrupole ion trap were ejected at resonance ejection frequencies below 50 kHz and the secondary ejection point was observed. Ion ejection at all frequencies below 50 kHz is not the manner in which a quadrupole ion trap should operate. The model might be questioned; however, the agreement with ion trajectory simulations and experimental observation in both the octapole ion trap and the quadrupole ion trap verify the accuracy of the models used. The fact that both experimental results and simulations show the ions ejecting at all frequencies below 50 kHz suggests that the geometry (spacing and thickness) of the cylindrical electrodes is the reason for the ejection.

One of the reported advantages of octapole fields is that they should be able to focus and confine ions more efficiently than quadrupole fields. Theoretically this should lead to more ions being trapped. Experiments looking at the maximum storage capacity of the cylindrical octapole ion trap and the cylindrical quadrupole ion trap show that the octapole ion trap is capable of storing at least 50 times more ions than the quadrupole ion trap. Additionally when the two instruments are compared in a region where they both have linear increases in ion abundance with increasing time, the octapole ion trap is 2.5 times more sensitive than the quadrupole ion trap.

Even though mass analysis is not possible due to the geometry of the octapole ion trap presented in this chapter, ions were still able to be ejected quickly using non-resonance ejection. Because of its greater storage capacity and higher sensitivity, the octapole ion trap could be used as a storage device or reaction chamber in the front of another analyzer such as a TOF. Other electrode geometries such as adjusting the ring radius of the central ring electrode or adjusting the width of the central ring electrodes may help make the octapole ion trap capable of mass analysis.

5.6 References

1. Louris, J. N.; Schwartz, J.; George C. Stafford, J.; Syka, J. E. P.; Taylor, D. *The Paul Ion Trap Mass Selective Instability Scan: Trap Geometry and Resolution*. in *The 40th ASMS Conference on Mass Spectrometry and Allied Topics*. 1992. Washington, DC.

2. March, R. E.; Todd, J. F. J., Eds. *Quadrupole Ion Trap Mass Spectrometry*, 2nd ed.; John Wiley & Sons, Inc.: Hoboken, NJ, 2005.

3. Franzen, J.; Gabling, R.-H.; Heinen, G.; Weiss, G. Method for mass-spectroscopic examination of a gas mixture and mass spectrometer intended for carrying out this method. US Patent 5028777, 1991.

4. Franzen, J., *Simulation Study of an Ion Cage with Superimposed Multipole Fields.* International Journal of Mass Spectrometry and Ion Processes, **1991**. 106: p. 63-78.

5. Hager, J. W., *Performance optimization and fringing field modifications of a 24-mm long RF-only quadrupole mass spectrometer.* Rapid Communications in Mass Spectrometry, **1999**. 13(8): p. 740-748.

6. Collings, B. A., *Increased fragmentation efficiency of ions in a low pressure linear ion trap with an added dc octopole field.* Journal of the American Society for Mass Spectrometry, **2005**. 16(8): p. 1342-1352.

7. Sudakov, M.; Douglas, D. J., *Linear Quadrupoles with Added Octapole Fields.* Rapid Communications in Mass Spectrometry, **2003**. 17: p. 2290-2294.

8. Franzen, J.; Gabling, R.-H.; Schubert, M.; Wang, Y., *Nonlinear Ion Traps*, in *Practical Aspects of Ion Trap Mass Spectrometry. Volume I. Fundamentals of Ion Trap Mass Spectrometry*; March, R. E., Todd, J. F. J., Eds.; CRC Press: Boca Raton, 1995; Vol. I, pp 49-167.

9. Walz, J.; Siemers, I.; Shubert, M.; Neuhauser, W.; Blatt, R.; Teloy, E., *Ion Storage in the rf Octupole Trap.* Physical Review A, **1994**. 50: p. 4122-4132.

10. Wang, Y.; Franzen, J.; Wanczek, K. P., *The Non-Linear Resonance Ion Trap. Part 2. A General Theoretical Analysis.* International Journal of Mass Spectrometry and Ion Processes, **1993**. 124: p. 125-144.

11. Hägg, C.; Szabo, I., *New Ion-Optical Devices Utilizing Oscillatory Electric Fields. III. Stability of Ion Motion in a Two-Dimensional Octopole Field.* International Journal of Mass Spectrometry and Ion Processes, **1986**. 73: p. 277-294.

12. Forbes, M.; Sharifi, M.; Croley, T.; Lausevic, Z.; March, R. E., *Simulation of ion trajectories in a quadrupole ion trap: a comparison of three simulation programs.* Journal of Mass Spectrometry, **1999**. 34: p. 1219-1239.
13. Dahl, D. A., 7.0 ed.; Idaho National Engineering Laboratory: Idaho Falls, 1999.

14. Vedel, F.; Vedel, M., *Nonlinear effects in the detection of stored ions.* Physical Review A, **1990**. 41: p. 2348-2351.

Chapter 6

Octapole Ion Trap Fourier Transform Mass Spectrometer: Theory, Prototype, Simulations, and Initial Experiments

6.1 Introduction

The octapole ion trap described in **Chapter 5** was determined to be 2.5 times more sensitive and capable of trapping more than 50 times the number of ions as compared to a quadrupole ion trap with similar geometry. Due to ions being ejected by a non resonance ejection process, the octapole ion trap was not capable of mass analysis. Similar non resonance ejection was also observed in the 3-D quadrupole ion trap with the same geometry, both experimentally and through simulation. This similarity suggested that non resonance ejection is the result of the electrode geometry. There are two main concerns with the first generation octapole ion trap electrode geometry. The first generation octapole ion trap's endcap electrodes were cylindrical electrodes covered with an 88% transmission Ni plated wire mesh. The purpose of this mesh was to help create a uniform electric field. These mesh electrodes however, do truncate the electric fields. The other concern is that the intermediate ring electrodes are four times shorter (axially) compared to the central ring electrode. Because the rf voltage in the first generation trap was applied to the shorter intermediate ring electrodes, the larger grounded central ring electrode created a non-ideal octapole electric field. A new geometry for the octapole ion trap has been realized, which has more quadrupole field characteristics and will have improved resonance ejection properties. This

second generation geometry octapole ion trap is also thought to be capable of a non-destructive detection technique, which includes the acquisition and Fourier transform of an image current from the trapped ions in the ion trap. In this chapter the theory, ion trajectory modeling, and initial experiments with this second generation octapole ion trap are presented.

6.2 Second Generation Octapole Ion Trap

6.2.1 Electrode Geometry

A second generation octapole ion trap was developed based on an open endcap cylindrical ion trap proposed by Gabrielse et al.[1] This geometry, as shown in **Figure 6.1,** addresses both of the concerns from the first generation geometry. The endcap electrodes are open (no mesh) and the length (z_e) is such that any fringe fields and/or field truncation should be minimized. The central ring length (z_c) was reduced from 2.5 cm to a length that is less than the intermediate ring electrodes. The dimensions for the second generation octapole ion trap are as follows:

$$r_0 = 1.0 \text{ cm}$$

$$z_0 = 2.7 \text{ cm}$$

$$z_e = 2.1 \text{ cm}$$

$$z_c = 0.11 \text{ cm}$$

$$\Delta z_c = 0.36 \text{ cm}$$

$$z_g = 0.1 \text{ cm}$$

The radius of the ion trap (r_0) and the axial length of each of the electrodes were reduced by half from the dimensions described in the literature; reasons for this will be described in **Section 6.3.4**. With the addition of the open end cap electrodes, the distance from the end of

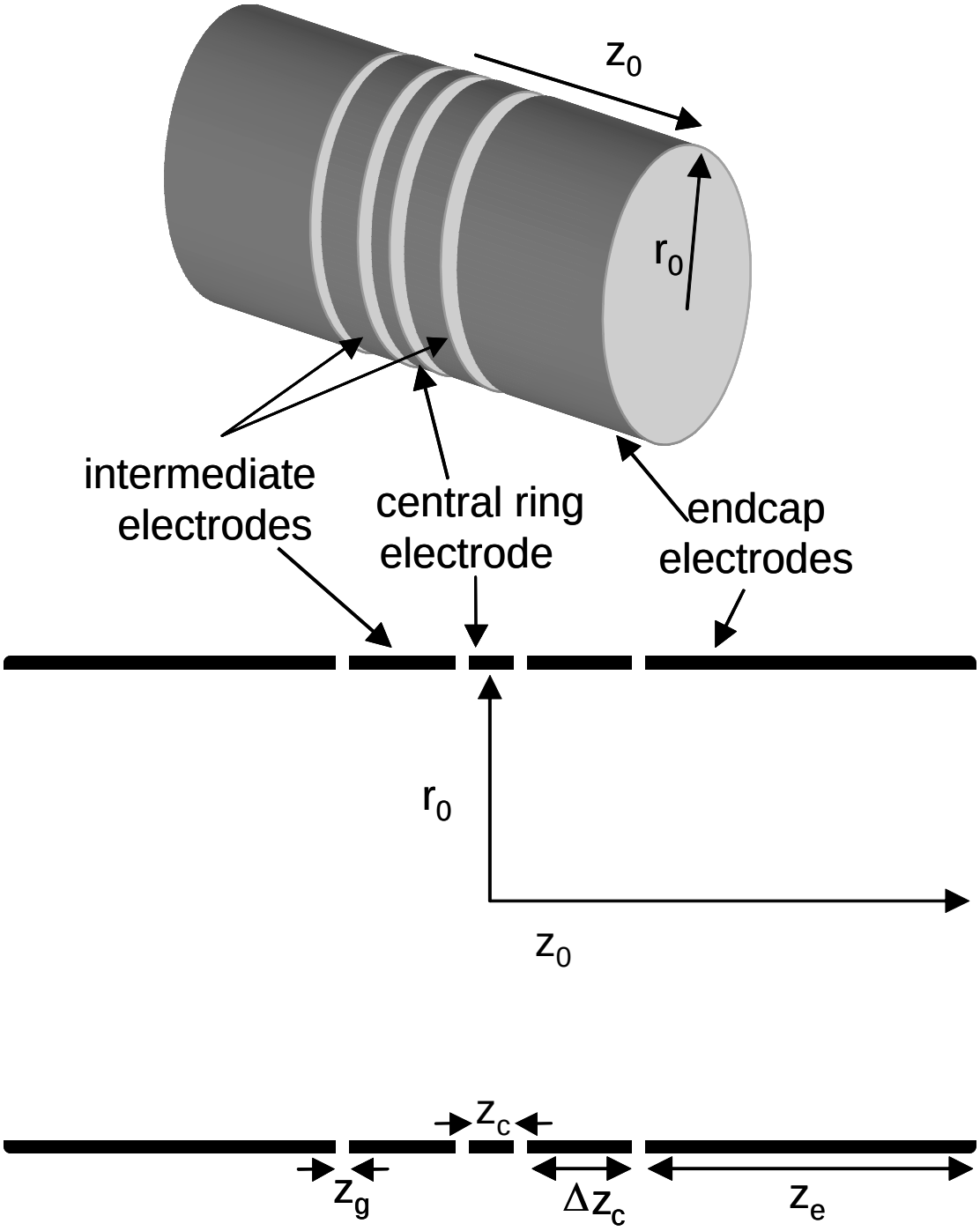

Figure 6.1 – 3-D image of Open Endcap Octapole Cylindrical Ion Trap and a 2-D cross section of electrodes. (Not drawn to scale)

the endcap electrode to the center of the ion trap (z_0) was increased by 1 cm. The gap between the electrodes (z_g) is the same distance as in the first generation electrode geometry. Because of the electrode shape, the second generation octapole ion trap will be referred to as the open endcap octapole cylindrical ion trap (OEOCIT) while the first generation will be referred to as the octapole cylindrical ion trap (OCIT).

6.2.2 Electric Fields

The result of decreasing the length of the central ring electrode is that the voltage applied to the intermediate ring electrode has a large affect on the overall electric field in the octapole ion trap. As shown in **Figure 6.2a**, the electric fields in the OEOCIT are quite different from those of the OCIT (**Figure 5.3**). The electric fields in OEOCIT have more quadrupole fields in the center of the ion trap than the OCIT. However, the relative octapole field is still much greater than a conventional 3-D quadrupole ion trap or a cylindrical quadrupole ion trap with the same geometry. As shown in **Figure 6.2b**, when the rf voltage is applied to all three ring electrodes the quadrupole field is quite different from that of the octapole-rich field shown in **Figure 6.2a.** When the rf voltage is applied all three ring electrodes, the geometry will be referred to as the open endcap quadrupole cylindrical ion trap (OEQCIT).

6.2.3 Operation

The OEOCIT will be operated using the same methods that were used in the OCIT, as outlined in **Section 5.2.4.** The main detection method implemented with the OCIT was resonance ejection at a constant rf voltage. The amplitudes of the rf voltage necessary to trap and eject ions in the OEOCIT will be different from the OCIT because the electric fields are

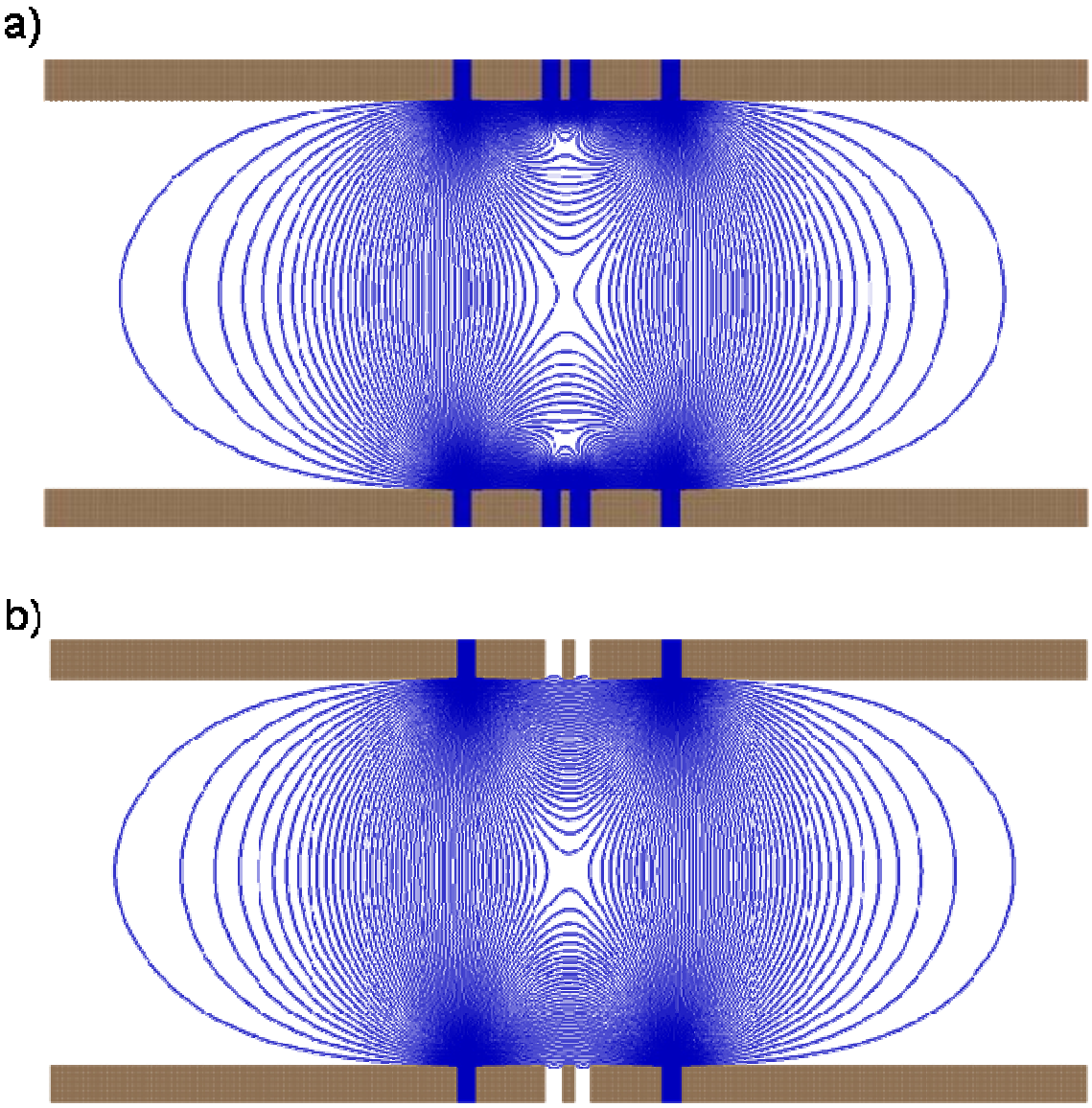

Figure 6.2 – 2-D cross section of a) OEOCIT with isopotential curves, b) OEQCIT with isopotential curves.

different. More specifically, the amplitudes in OEOCIT are likely to be less because both the axial and radial dimensions of the OEOCIT are less than the OCIT.

In addition to resonance ejection, a non-destructive ion detection technique will be implemented. Ion trajectory modeling showed that when ions were not resonantly excited the maximum amplitude of their radial and axial motion was close to the electrodes. With the ions motion being close to the electrode surfaces it may be possible to detect a current resulting from the ion's motion. The time based current, referred to as an image current, can be Fourier transformed to determine the frequency of the ion's motion. If ions of the same mass-to-charge ratio have the same secular frequency, then a correlation between mass-to-charge and frequency can be determined. Fourier transform techniques will be discussed in more detail in **Section 6.3**. The OCIT was able to trap more than 50 times the number of ions compared to a quadrupole ion trap of similar geometry. Because the strength of the image current improves with the number of ions trapped, FT detection can be a very sensitive technique in the octapole ion trap. The number of ions trapped in the OEOCIT is likely to be less than the OCIT because the OEOCIT has a smaller trapping volume. However, with the octapole fields present in the OEOCIT the number of ions that are trapped should be greater than a quadrupole ion trap with a similar geometry.

6.3 Fourier Transform Mass Spectrometers

6.3.1 Benefits of Fourier Transform Mass Spectrometry

As mentioned in **Section 6.2.3**, Fourier transform mass spectrometry is generally considered a non destructive technique. As will be addressed shortly, one of the largest advantages of Fourier transform mass spectrometry is the high mass resolving power that is

achievable (>1,000,000). Additionally because FTMS is z non-destructive detection method, it can be repeated several times to improve the sensitivity. Non-destructive techniques also allow for experiments to be performed on the same of ions following the initial ion detection. Subsequent experiments can include dissociation methods or ion molecule reactions. An additional advantage of Fourier transform experiments in a rf ion trap, is that the detection method removes the need for the high voltage power supplies of the electron multiplier (2 kV) and the dynode (10 kV).

6.3.2 Background

The first Fourier transform ion cyclotron resonance mass spectrometer (FT-ICR) was introduced in 1976.[2] In the FT-ICR, ions are stored in a low pressure (10^{-10} – 10^{-11} torr) segmented trapping cell located inside a high field electro-magnet. The trapping cell is a segmented cube where each of the six electrodes is electrically isolated. A dc voltage is applied to the electrodes of the cube that are orthogonal with the ion source, which axially confines the ions. All ions in the magnetic field have a cyclotron motion and the frequency of that motion is different for each ion with a different mass-to-charge ratio. Even though ions of the same mass-to-charge have the same frequency their motion may not be coherent because they enter the ICR at different time during ion injection. The radius of the ion's motion can be increased by applying a supplemental ac voltage with the same frequency as the cyclotron frequency of an ion, to two parallel electrodes of the trapping cell.[3] This supplemental voltage also makes the ions motion coherent. The parallel electrodes, which the excitation voltage is applied to, are two of the four remaining electrodes that are not orthogonal with the ion source. The supplemental ac voltage is then switched off and an induced current is differentially detected on the last two parallel electrodes of the segmented

trapping cell. Differentially detecting the image current helps to improve the signal to noise ratio of the image current signal.[4] Following excitation, the detected ion's signal slowly decays as a result of collisions with any background gas, which cause the ion's motion to be incoherent. Over extended periods of time the ion's radius of motion will also begin to decrease. This time dependant signal, referred to as the transient signal, can then be Fourier transformed and the cyclotron frequencies of ions can be determined. Using **Equation 6.1**, the ion's mass-to-charge ratio can be calculated from the measured cyclotron frequency, where ω is the cyclotron frequency, B is the magnetic field strength, m is the mass of the ion and z is the charge.

$$\omega = \frac{zB}{m} \qquad \textbf{EQ 6.1}$$

Tandem mass spectrometry can be performed in the ICR by pulsing in a collisions gas; however, the collision gas must be allowed to evacuate so that the pressure in the cell is not too high during ion detection. If the pressure in cell is too high the transient will decay too quickly. Some commercial FT-ICR instruments have other mass analyzers, such as a linear ion trap, before the ICR for ion accumulation and MS/MS capabilities. Other tandem mass spectrometry methods, such as infrared multiphoton photo dissociation or electron capture dissociation, are also possible in the ICR cell. The resolving power of the FT-ICR is typically 500,000-600,000 and can be much greater.[2, 4] The strength and uniformity of the magnetic field is the biggest factor in determining the mass resolving power of the FT-ICR. The electromagnets available today can range from 4 – 12T and can cost well over $1,000,000.[2, 4] In addition to cost, these electromagnets are difficult to maintain because they have to be cooled with liquid helium and liquid nitrogen.

Until 2005, the FT-ICR was the only commercially available Fourier transform mass spectrometer (FTMS). In 2005, the Orbitrap™ FTMS (Thermo Electron, SanJose, CA) was commercially released.[5-8] This instrument uses curved electric fields, generated from a spindle shaped electrode operated with an electrostatic dc voltage of -3 to -5kV, to trap ions in a low pressure (10^{-10} – 10^{-11}) ion trap. Ions of different mass-to-charge ratios moving around the spindle electrode have a characteristic oscillation frequency. While ions are being injected into the Orbitrap the voltage on the spindle is slowly made more negative, thus "squeezing" the ions radially toward the spindle electrode. This prevents ion losses during ion injection into the Orbitrap. Ions are injected over very small dimensions thus making the ion packet coherent. An image current is then detected from the ions' axial motion with respect to the spindle electrode on an split outer barrel-like electrode.[5] The commercial instrument also has a linear ion trap before the Orbitrap, which allows for tandem mass spectrometry experiments (MS/MS). The Obritrap™ has been shown to be capable of mass resolving powers of up to 200,000 without the large, expensive electromagnet.[5-7] The Orbitrap's resolving power is not as impressive as the FT-ICR but it is still greater than the typical resolving power of most conventional 3-D ion traps (<5,000). Although, resolving powers up to 1,000,000 have been observed in the 3-D ion trap, it is not typical.

6.3.3 Fourier Transform Radio Frequency Quadrupole Ion Traps

Image current Fourier Transform detection has been reported in rf 3-D and rf 2-D quadruple ion traps.[9-16] The first theoretical report of Fourier transform experiments in a 3-D quadrupole ion trap proposed a detection process analogous to the detection methods used in FT-ICRs. In this method, ions are first resonantly excited, the excitation voltage is then turned off, and finally the image current of ions is detected on the endcap electrodes. Because

detection occurs at the endcap electrodes, the axial secular frequency of the ions will be measured. The resonance excitation voltage selected in this theoretical analysis was intended to excite a narrow mass-to-charge range of ions. With the development of broadband excitation techniques such as stored waveform inverse Fourier transform (SWIFT), a wider range of mass-to-charge ions could be resonantly excited at once.[3, 17] Using SWIFT, researchers were able to resonantly excite a broad mass-to-charge range of ions and detect an image current, thus creating the first experimental FT 3-D quadrupole ion trap.[9, 12, 14] The endcap electrodes were found to pick-up as much as 600 V_{pp} of the rf voltage applied to the ring electrode.[9] Thus, the fundamental drive frequency must be filtered out of the time-based image current signal so that it does not dominate the Fourier transformed signal. The lower the pick-up voltage on the endcap electrodes, the more efficient the filtering process will be. To reduce the voltage on the detector electrode, the quadrupole ion trap used in this report was modified to have an electrically isolated pin electrode inserted in one endcap electrode.[9, 14] The pin electrode extended about 0.5 mm above the endcap electrode surface and was used to detect the image current. The rf voltage picked up by the pin electrode was reduced to less than 40 V_{pp}. The mass resolving power reported was on the order of 1000. An improvement to the detection method was suggested in which a detector pin would be inserted into both endcaps and the image current would be detected differentially between the two endcaps.[9] However, inserting this second pin electrode makes trapping ions more complicated because ions are injected through the endcap electrodes. Ions therefore can be generated internally in the ion trap using electron ionization with the electrons injected through a hole in the ring electrode. Alternatively the ions could be generated externally and

injected through a hole in the ring electrode. These proposed modifications have never implemented.

Recently Fourier transform experiments were described in a 2-D quadrupole ion trap patent.[11] This patent contained several possible embodiments of the FT 2-D ion trap. In one embodiment a set of four rods were used as the detector electrodes. These detector rods were present in addition to the 2-D quadrupole ion trap's four standard rods, As shown in **Figure 6.3**, the top pair of rods (shaded) and the bottom pair of rods (diagonal lines) were connected together electrically. The sets of rods can be used to differentially detect the image current. The ions' motion is thus detected in the X direction. A slightly different configuration was used for the experimental implementation of the FT 2-D quadrupole ion trap. This configuration replaced the detection rods with a set of four flat plates to detect the image current instead of the detection rods as in the previous example. The quadrupole rods in this configuration had a modified hyperbolic geometry. These modifications made the field a more ideal quadrupole field. The resolving power of the FT 2-D quadrupole ion trap was approximately 7000, which is slightly better than the resolving power observed in the FT 3-D quadrupole ion trap.

6.3.4 Fourier Transform 3-D Octapole Ion Trap

6.3.4.1 Methodology

The example of the FT 2-D quadrupole ion trap shown in **Figure 6.3** is very similar to the 2-D octapole described in **Section 5.2.2**. If all four of the rods of the quadrupole were driven in phase and the four detector rods were electrically grounded (as they are in **Figure 6.3**) the device would be a FT 2-D octapole. If this configuration is translated to a 3-D octapole ion trap as shown in **Figure 6.4a**, the detector electrodes are the intermediate

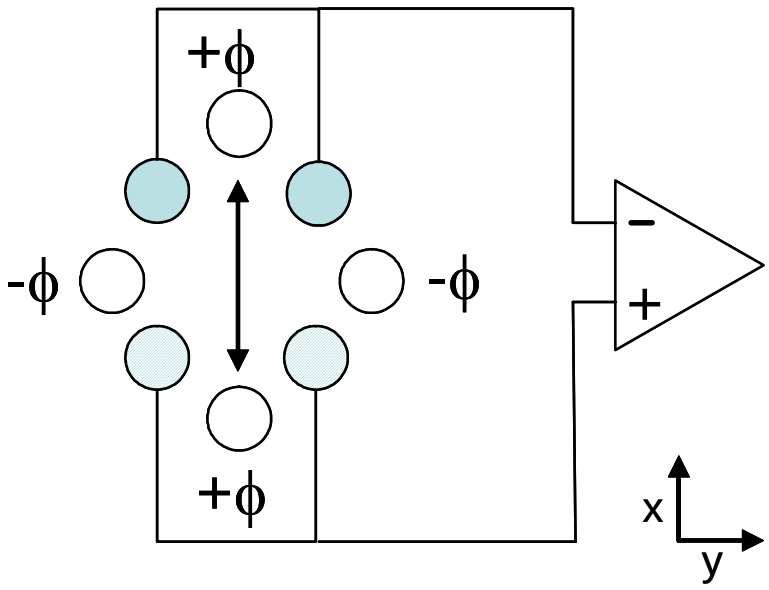

Figure 6.3 Experimental design for FT experiments in a 2-D quadrupole ion trap.

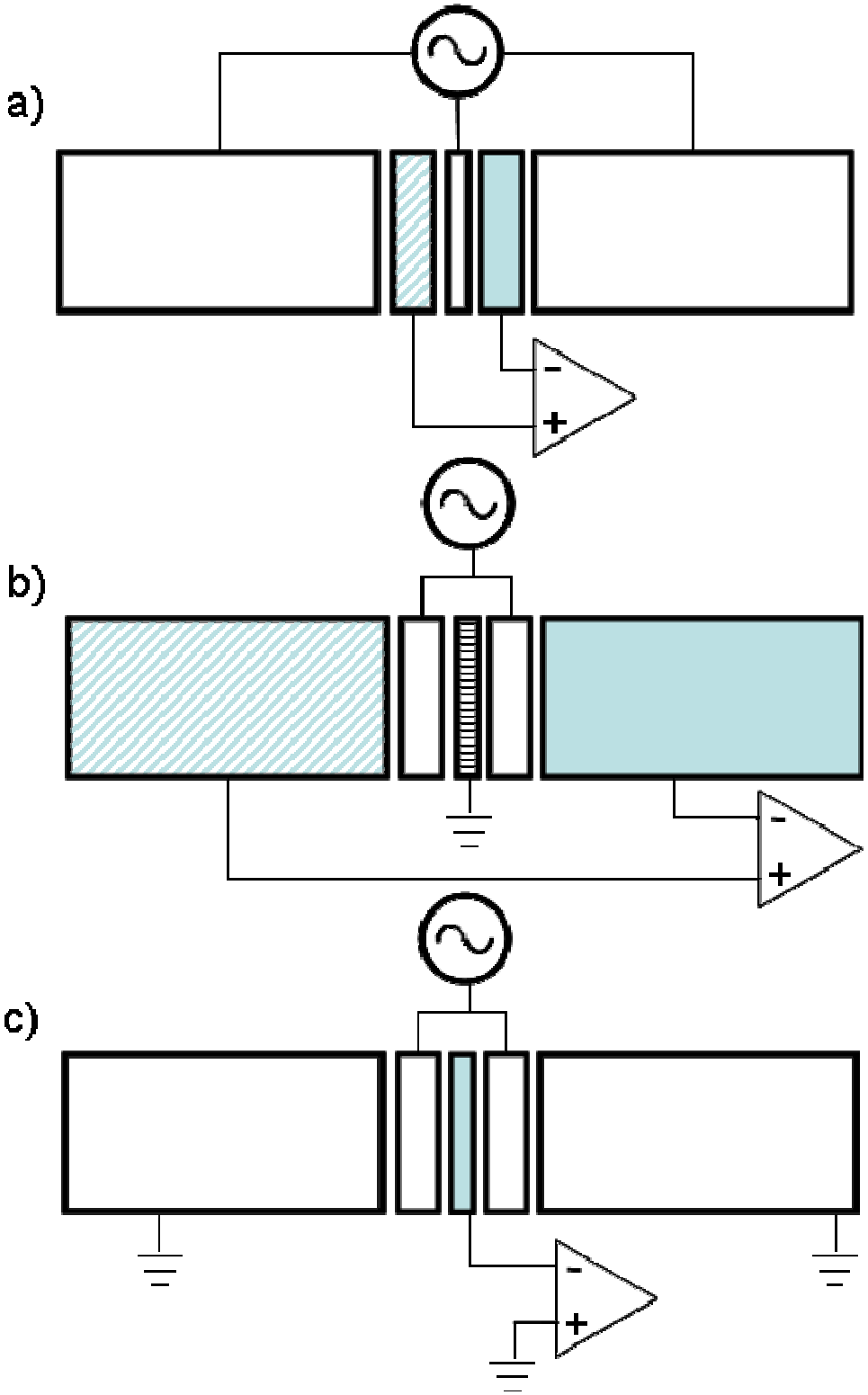

Figure 6.4 – FT OEOCIT with a) Intermediate ring electrodes or b) end cap electrodes c) central ring as detector electrode.

electrodes and the rf voltage is applied to the endcap electrodes and the central ring electrode. This configuration is not ideal for the operation of the octapole ion trap because injecting ions through the high amplitude rf voltage on the end cap electrodes would be inefficient. An improved operation method, shown in **Figure 6.4b**, uses the endcap electrodes as the detector electrodes and the rf voltage is applied to the intermediate ring electrodes while the central ring electrode is grounded. A third detection method, shown in **Figure 6.4c**, is accomplished by detecting the image current single ended on the central ring electrode. The rf voltage would be applied to the intermediate ring electrodes and the endcap electrodes would be grounded. As mentioned in **Section 6.3.3**, single ended detection methods are more prone to noise. An additional potential drawback to this method is that the central ring electrode may be more prone to rf pickup than the endcap electrodes. The image current detected in any of these three methods will detect the axial frequency of the ions.

6.3.4.2 Experimental Concerns

Fourier transform experiments in the 3-D octapole ion trap will suffer some of the same challenges as the 3-D and 2-D quadrupole ion trap FT experiments. The operating frequency of the rf voltage needs to be filtered out of the image current signal. Researchers have shown that the rf frequency can be removed with minimal losses to the lower frequency data.[10, 13, 14] In one report researchers used a compensation circuitry network to add a low rf voltage signal to the detector pin electrode that is 180 degrees out of phase with the fundamental rf voltage.[10] This voltage helps to remove any rf voltage that is picked up by the detector electrodes. The detection circuit also contains a low noise charge amplifier followed by a simple network of operation amplifiers that contains an active low pass filter. The circuit has a bandwidth of 200 kHz and a gain of 500. Rf voltage that is picked up on the endcap or

central ring electrodes can therefore be removed by using circuitry similar to that described above.

Space charge effects and ion coherence are two factors that affect all FT instruments. As more ions are trapped, the number of ion/ion interactions increases, resulting in the broadening of the secular frequency of ions of the same mass-to-charge ratio. The 3-D octapole ion trap can trap more ions than a 3-D quadrupole ion trap with a similar geometry. As discussed in **Section 5.4.4,** as ions were injected into the 3-D octapole ion trap the observed signal intensity followed a linear trend over a wide range of injection times. This trend suggests that the octapole ion trap can trap more ions than a 3-D quadrupole ion trap without suffering from space charge effects except at very long injection times. Under the experimental conditions discussed in **Section 5.3.4**, space charge effects were observed at injection times greater than 1 second.

Establishing ion coherence is vital to ion image current detection.[4, 13] If the ion packet is not coherent, ions of the same mass to charge will approach the electrode surfaces at different times. The ions will have the same frequencies but different phases, which can result in deconstructive interference where a given frequency component is reduced. Ion coherence in FT-ICR, 3-D quadrupole ion trap, and 2-D quadrupole ion trap instruments is commonly established by broad band resonance excitation. In these instruments the resonance excitation voltage also serves to increase the trajectory of the ions to bring them closer to the electrode surfaces. In the work presented here, the electrode dimensions of the 3-D octapole ion trap were reduced to ensure that the ion cloud is closer to the surfaces of the electrodes, minimizing the need for resonance excitation. The role of ion coherence and resonance excitation in the 3-D octapole ion trap will be further addressed in **Section 6.5**.

6.4 Methods

6.4.1 Ion Trajectory Simulations

6.4.1.1 Creating the Model

Ion trajectory simulations were performed using the simulation program SIMION. Two sets of potential arrays were constructed from the electrode geometry using the electrode dimensions and spacing described in **Section 6.2.1.** The first array is created with the exact listed electrode dimensions and spacing and the second with twice the listed dimensions and the same electrode spacing. For the purposes of discussion this larger geometry will be referred to as the 2xOEOCIT. The sizes of these potential arrays were 525x120x120 and 1050x240x240 for the OEOCIT and 2xOEOCIT respectively, with both potential arrays using a 0.1 mm/grid unit. The methods for creating and refining a potential array are discussed in **Section 5.3.1**. The user program used to simulate ion motion in an rf trapping field was the same as that described in **Section 5.3.1**. Simulations of a cylindrical quadrupole ion trap with the same geometry as the OEOCIT were performed for comparison purposes. This was accomplished by modifying the user program to apply the rf voltage to the central ring as well as to the intermediate ring electrodes. The OEQCIT was modeled and was not experimentally implemented. Although the OEQCIT could be implemented by applying the rf voltage to the intermediate and central ring electrodes of the OEOCIT.

6.4.1.2 Simulation Conditions

The simulations conducted modeled three experiments: ion storage, resonance ejection, and image current detection. In each of these simulations a *m/z* 100, 500, 1000, 5000, and 10000 ion was individually modeled with an initial kinetic energy of 0.1eV. During one set of resonance ejection simulations, an ion representing xenon's most abundant

isotope (*m/z* 132) was also modeled. For each set of simulations five replicates were conducted. Unless otherwise stated the initial position of the ion was in the geometric center of the ion trap. The simulations were conducted for simulations times of 10000 μsec and at every 5 μsec interval the ion's simulation time, x position, y position, z position, v_x, v_y, and v_z were recorded to a comma delimited file for data analysis. In the ion storage simulations, ions were stored at various rf voltages ranging from 50 $V_{0\text{-}p}$ to 400 $kV_{0\text{-}p}$; if an ion's motion was still stable after 10000 μsec the ion was said to be "trapped". Resonance ejection simulations were performed with an 8 $V_{0\text{-}p}$ resonance ejection voltage which had a frequency ranging from 1 to 400 kHz.

The induced current detected during an FT octapole ion trap experiment is assumed to decrease as a function of the reciprocal of the ion's 3-D distance from an electrode. Following the ion trajectory simulation (no resonance ejection used), the ion's x and y positions were used to calculate a radial distance from the detector electrodes. The electrode in the x and y dimension is a circle and therefore will have an infinite number of distances to calculate. With a resolution of 0.01 mm, the radius (r) of the electrodes and **Equation 6.2** was used to create a 2-D array that represented the coordinates of the detector electrode. Any row in this 2-D array represents a (x_e, y_e) coordinate point on the electrode surface. The ion's distance at each element in the array was calculated using **Equation 6.3**, where x_i and y_i are the Cartesian coordinates of the ion's position, and x_e and y_e are Cartesian coordinates on the electrode surface. The shortest distance was taken to be the actual radial distance of the ion from the electrode.

$$x_e^2 + y_e^2 = r_e^2 \qquad \textbf{EQ6.2}$$

$$r = \sqrt{(x_i - x_e)^2 + (y_i - y_e)^2} \qquad \textbf{EQ6.3}$$

A 1-D array was created that contained the axial coordinates for the detector electrode. The shortest axial distance was calculated in a similar manner by using **Equation 6.4**, where z_e is the axial coordinate of the detector electrode and z_i is the axial coordinate of the ion. The shortest 3-D distance (d) was calculated using **Equation 6.5**.

$$z = z_i - z_e \qquad \textbf{EQ6.4}$$

$$d = \sqrt{(r)^2 + (z)^2} \qquad \textbf{EQ6.5}$$

Differential image current detection was simulated by setting the center of the ion trap as d = 0. All ion positions that were to the left of the center had a negative distance and those to the right had a positive distance. A distance was calculated for each point in time and the resultant distance vs. time data was fast Fourier transformed to obtain the frequency based spectrum. The time interval between recorded ion positions in the simulations was decreased from 5 μsec to 0.5 μsec so that the secular frequencies were not aliased. By decreasing this time interval the position of an ion is recorded more often. According to Nyquist theorem, a frequency based signal must be sampled by at least twice the frequency of the signal to be accurately characterized, which would mean than the minimum frequency that can be determined in this method is 1 MHz. The maximum frequency for an ion when the ion trap is operated at 800 kHz should be 400 kHz. FTMS simulations in a 3-D octapole ion trap were performed using the three detection methods shown in **Figure 6.4**. Additionally a single-ended detection method was simulated using the entrance endcap as the detector electrode. FT simulations were performed for *m/z* 100, 500, and 1000 ions. The secular frequencies of m/z 100 and 1000 ions were simulated as a function of the rf voltage.

6.4.2 Experimental Implementation of the OEOCIT

The OEOCIT electrodes were designed and machined according to the mechanical drawings in **Appendix II**. A 2-D representation of the electrode stack is shown in **Figure 6.5**. The central ring electrode was grounded through a small connection rod that was spot welded to the electrode. The connection rod is threaded for a 4/40 screw so that a wire can be attached for grounding. A wire going from each of the intermediate ring electrodes was connected into one electrical connecter. Each of the endcap electrodes had a separate connector which was attached to an electrical feed-through in a 6" conflat flange.

The rf circuitry described in **Chapter 2** and **Chapter 5** was modified for the operation of the OEOCIT. The rf circuits used to control the intermediate electrodes (rf_2 and rf_3) were disconnected from the high voltage feed-throughs. The connections were removed and holes in the rf enclosures were electrically sealed with copper tape. The remaining rf circuit (rf_1) was connected to one high voltage feed-though and both intermediate ring electrodes were connected inside the vacuum housing to the wire attached to the high voltage feed-through. With two electrodes being driven by one rf circuit, the capacitance of the circuit increased. A 55pF parallel capacitor was removed to compensate for the added capacitance. Using methods described in **Chapter 2**, the resonant frequency of the circuitry was measured to be 757.5 kHz.

Resonance ejection and maximum storage capacity experiments were performed using the methods described in **Section 5.3.2** and **Section 5.3.3**. Minor adjustments to these methods are described below. The analyte used in these experiments was xenon. Vapors were introduced into an EI source using a metering valve with an analyte pressure of $9x10^{-7}$ torr. The voltages in the EI source were modified slightly from previous experiments. The ion

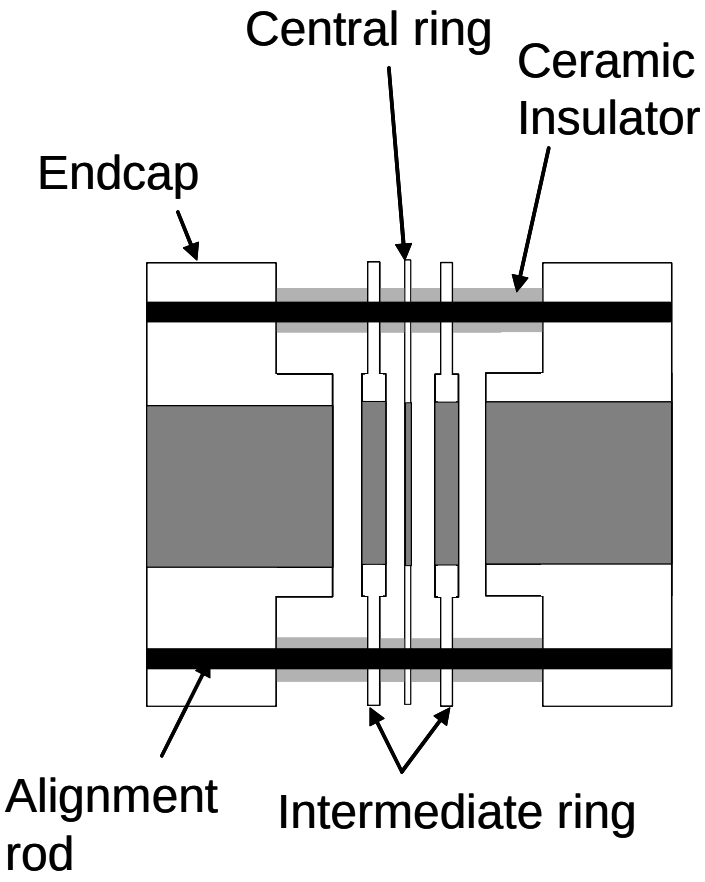

Figure 6.5 – OEOCIT electrode stack.

block was set to 8 V and the first, second and third Einzel lenses were set to -33 V, -200 V, and -36 V respectively. The dynode and guard ring were held at -7 kV and -400 V, respectively. The high voltage power supply for the electron multiplier was replaced with a supply having a 1 msec rise time (MS1021, K&M, West Springfield, MA). Because of this short rise time, a few sections of the experiment were decreased. The rf voltages on the intermediate ring electrodes were held at $500V_{0\text{-}p}$ during the entire experiment. The new time tables for resonance ejection experiments are as follows: The rf voltages were allowed to initialize for 5 msec. Ions were then injected into the ion trap for 4 msec, unless otherwise noted. The ions were then allowed to cool for 30 msec. During the last 5 msec of this cool period the voltage applied to the electron multiplier was allowed to equilibrate. Resonance ejection was performed for 5 msec. The rf voltage was then turned off in 1 msec. Data was acquired on a Tektronix DS420 digital oscilloscope. Ions that were not ejected during resonance ejection were detected when the rf voltage was turned off.

Recalling section **5.3.4**, the maximum storage capacity of an ion trap is the maximum number of ions that can be put into the ion trap. Experiments to study the maximum storage capacity of the OEOCIT were performed by varying the time that ions were injected into the ion trap from 1 msec to several seconds. Following the 30 msec cool time, ions were then ejected by turning off the rf voltage, which takes about 200 μsec to fully decay. Ions were detected while the rf voltage was turned off. Ion extraction was aided by the large negative voltages on the dynode and the guard ring.

6.5 Results and Discussion

6.5.1 Ion Storage

The range of voltages over which ions have stable trajectories were modeled for the OEOCIT, the OEQCIT and the 2xOEOCIT. As shown in **Figure 6.6,** 650 $V_{0\text{-}p}$ is necessary to trap the full mass-to-charge range of ions that were modeled in the OEOCIT, whereas only 400 $V_{0\text{-}p}$ is necessary in the OEQCIT. The larger 2xOEOCIT required 1000$V_{0\text{-}p}$ to trap the full mass-to-charge range of ions. The voltage difference between the OEOCIT and OEQCIT is most likely due the OEOCIT having more octapole field component than the OEQCIT. The voltage differences between the OEOCIT and the 2xOEOCIT geometries are the result of decreasing the 2xOEOCIT geometry.

As described in **Section 5.2.4,** the maximum rf voltage at which ions have a stable trajectory in the ion trap (with no dc voltage) should be the right edge of the Mathieu stability diagram. The maximum rf voltage needed for stable ion trajectory should be ~50 times greater in an octapole trap than in a quadrupole ion trap. As shown in **Figure 6.7**, the maximum rf voltage in the OEOCIT is greater than in the OEQCIT. The slopes of the lines shown in **Figure 6.7** are 8.0 V/(*m/z*) and 6.1 V/(*m/z*) for the OEOCIT and the OEQCIT respectively, which means that the octapole ion trap needs a 1.33 times larger voltage to eject an ion of the same mass-to-charge ratio compared to the quadrupole ion trap. This value is much less than the predicted value of 50 times greater voltage based on the maximum q_u of 50 for the OEOCIT and 0.908 for the OEQCIT. As described in **Section 6.2.1**, the OEOCIT has more quadrupole fields than the first generation OCIT. The addition of quadrupole fields to the octapole trap reduces the differences between the OEOCIT and the OEQCIT.

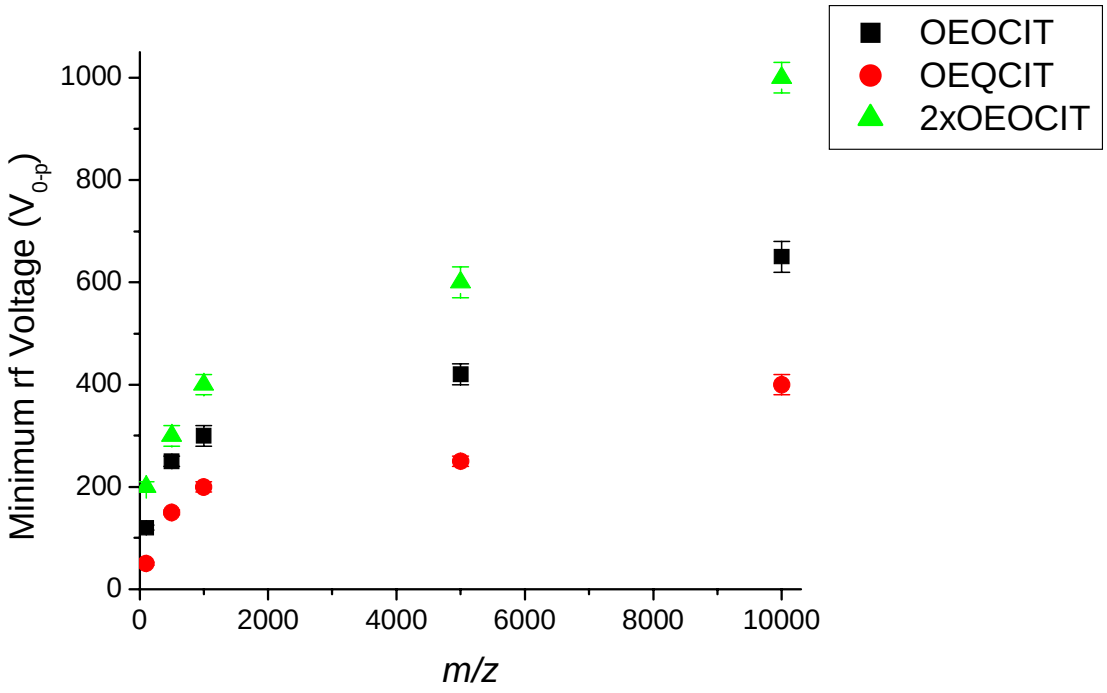

Figure 6.6 – Minimum rf voltage required to trap ions in the OEOCIT, OEQCIT, and the 2xOEOCIT.

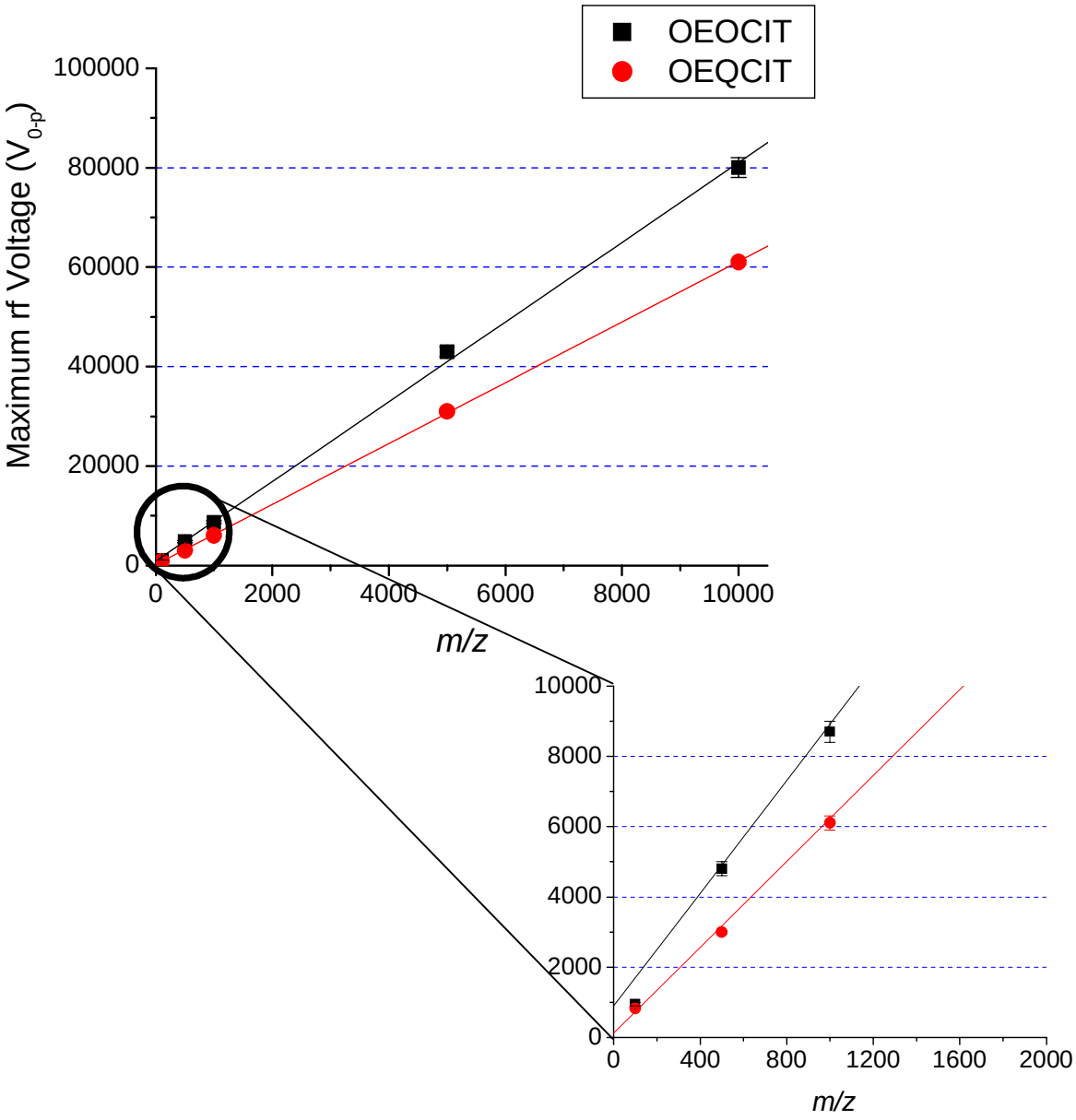

Figure 6.7 – Maximum rf voltage allowed for ions to have a stable trajectory in OEOCIT and OEQCIT.

The 2xOEOCIT geometry that was adapted from the literature was reduced in half to improve the proposed FT experiments. Reducing the radius and axial dimensions of the trap should result in lower voltages needed to eject ions out of the OEOCIT. From **Equation 5.9**, decreasing the radius in half should result in approximately a four times lower voltage required to eject ions from the OEOCIT. As shown in **Figure 6.8**, the voltage required to eject ions from the 2xOEOCIT is much greater than the OEOCIT. The slopes of the lines shown in **Figure 6.8** are 34.1 V/(*m/z*) and 8.0 V/(*m/z*) for the 2xOEOCIT and the OEOCIT respectively. The relative ratio of these two slopes agrees with the expected difference of four from the reduced electrode dimensions.

6.5.2 Resonance Ejection

In an octapole field, all ions of the same mass-to-charge ratio that have been cooled to the center of the ion trap should theoretically have a single secular frequency at a constant applied rf voltage. This theoretical secular frequency for the most abundant xenon ion at *m/z* 132 is represented by the dotted line in **Figure 6.9**. When resonance ejection was experimentally performed at a range of separate frequencies (8 $V_{0\text{-}p}$ for all voltages), as shown by the square data points in **Figure 6.9,** xenon ions were resonantly ejected over a range of frequencies from 55 kHz to 90 kHz, with the maximum number of ions detected at 80 kHz. Xenon ions were not resonantly ejected above 100 kHz. A small resonance ejection region was also observed from 30 to 40 kHz, with the maximum peak area detected at 38 kHz. This resonance ejection region corresponds to half the frequency of the 55 to 90 kHz resonance ejection region. Another ejection region occurs from 19.5 to 20.5 kHz, which is roughly half the frequency of where the maximum peak area was observed in the 30 to 40 kHz ejection region. When the resonance ejection amplitude was reduced from 8 to 3 $V_{0\text{-}p}$

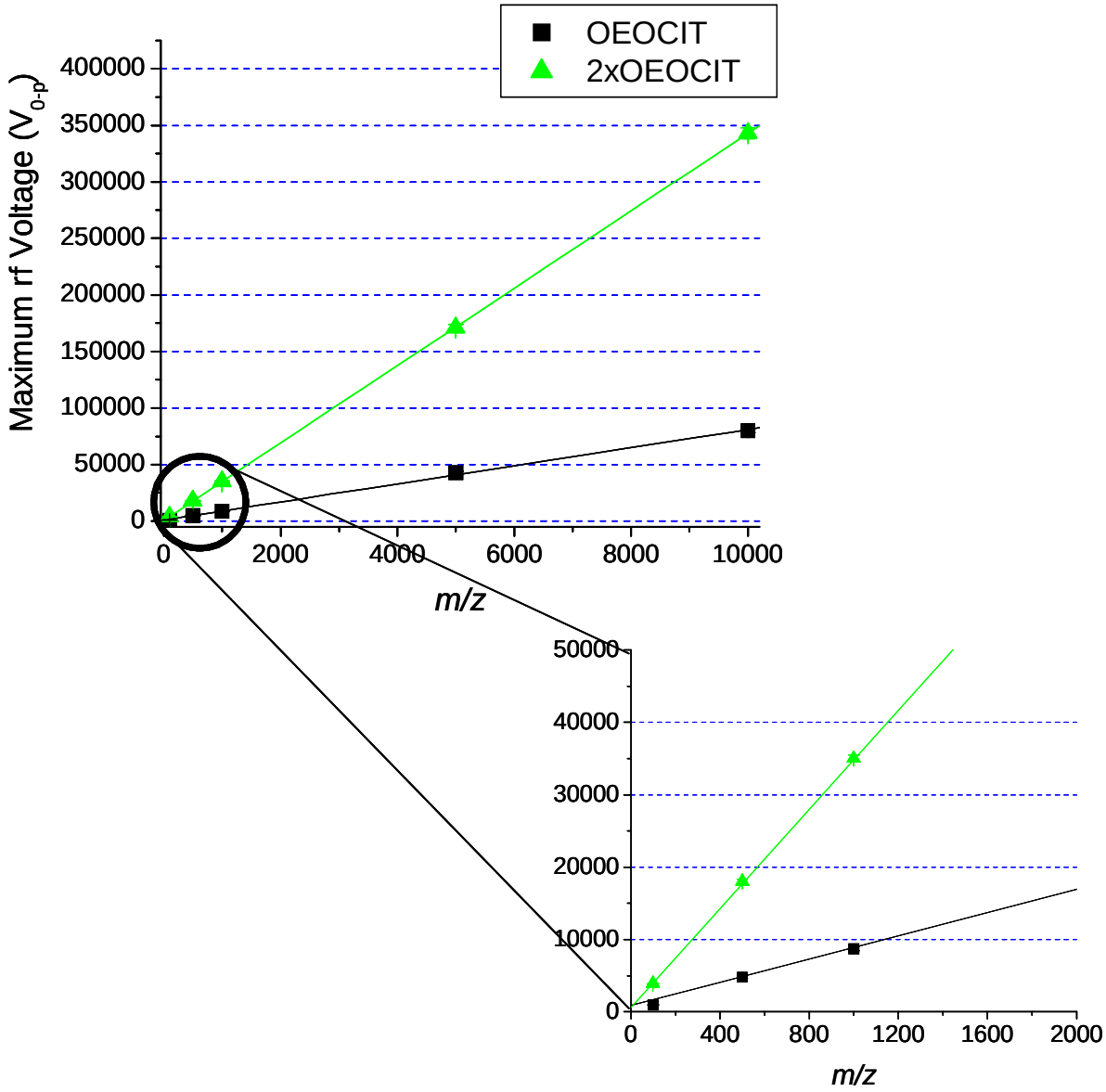

Figure 6.8 – Maximum rf voltage allowed for ions to have a stable trajectory in OEOCIT and 2xOEOCIT.

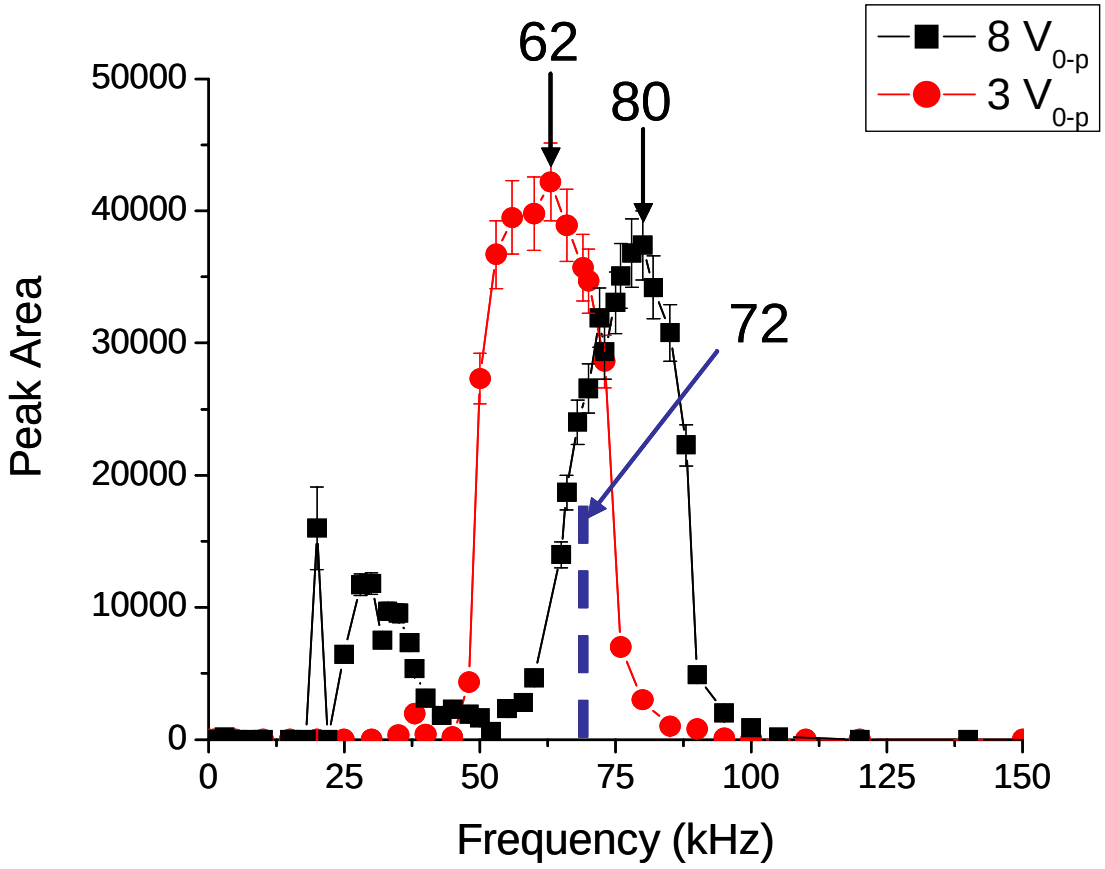

Figure 6.9 –Resonance ejection of xenon ions in OEOCIT with resonance ejection voltage amplitudes of 8 $V_{0\text{-}p}$ and 3 $V_{0\text{-}p}$. Dotted line represents theoretical secular frequency of *m/z* 132 ion.

the ejection at the two smaller regions was not significant, as shown by the circular data points in **Figure 6.9**. The center of the resonance ejection also shifts from 80 kHz to 62 kHz. This shift in the secular frequency is probably due to the fact that in an octapole field the secular frequency of ions depends on the amplitude of their motion. The larger amplitude causes the ions to be resonantly excited at different positions along their trajectory (different radial and axial positions in the ion trap) and thus the secular frequency will be slightly different. Without the presence of a resonance ejection voltage, ions should still have one secular frequency because they will have reached a steady state motion when located in the center of the ion trap. When the rf voltage was increased from 500 $V_{0\text{-}p}$ to 1000 $V_{0\text{-}p}$ ions were resonantly ejected with a 8 $V_{0\text{-}p}$ resonance ejection voltage from 137.5 – 155 kHz and other ejection regions were not observed.

Following resonance ejection the rf voltage was turned off and the ions that were not resonantly ejected were detected. The peak area as a function of the frequency of the resonance ejection voltage should therefore be the inverse of the plots from resonantly ejected ions shown in **Figure 6.9** (rf voltage is 500 $V_{0\text{-}p}$). As shown in **Figure 6.10**, this was inverse relation ship was not observed in experiments with an 8 $V_{0\text{-}p}$ resonance ejection voltage. During resonance ejection experiments ions were not ejected from frequencies of 40-50 kHz. Consequently these ions that were not resonantly ejected should be detected and a resultant peak observed; however, ions were not detected from 40 to 50 kHz by turning off the rf voltage after resonance ejection. At frequencies lower than 28 kHz the ion current begins to increase as expected, with the exception of the ejection which occurs at 20 kHz. A possible explanation for the ejection at 20 kHz is that ions are being resonantly excited from 40 to 50 kHz but not ejected. When the rf voltage is turned off, ions' excited motion causes

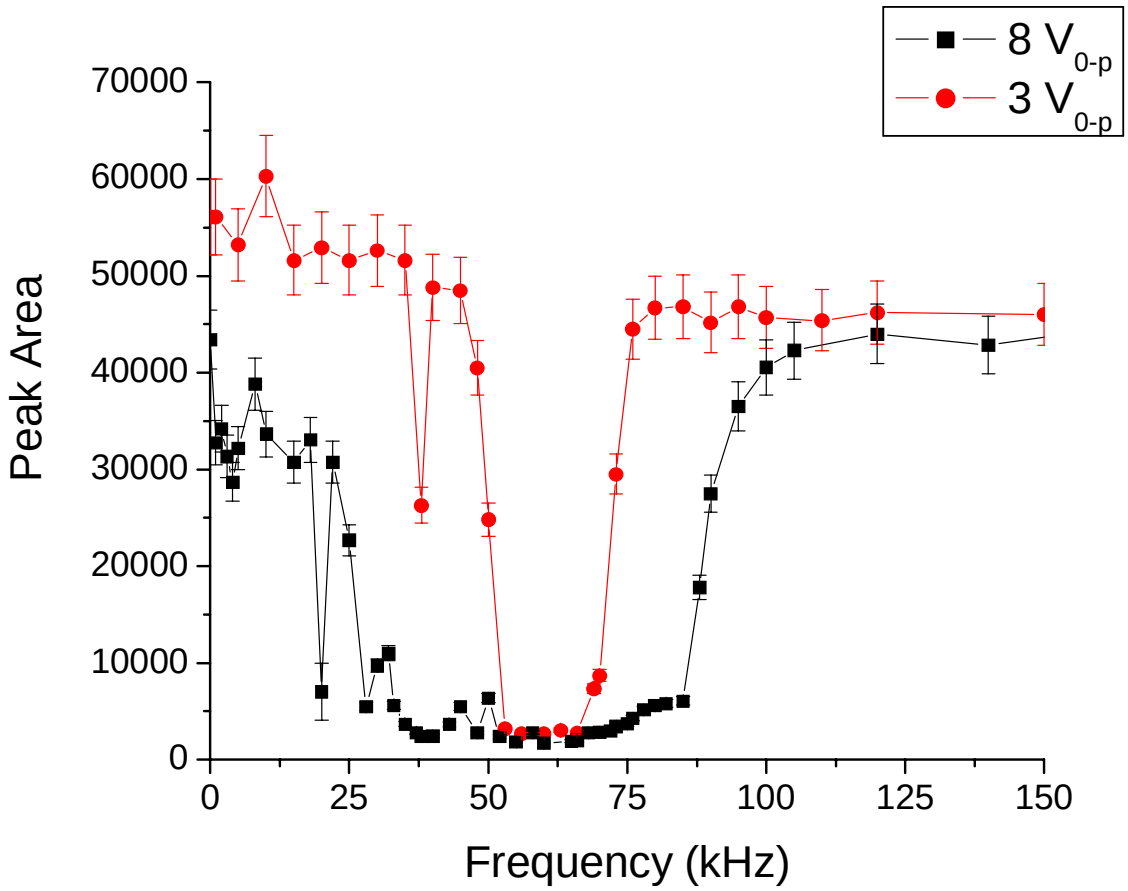

Figure 6.10 – Peak area detected from ions that were not resonantly ejected.

them to not be extracted efficiently by the dynode and guard ring voltages, thus they are not detected. The plot for 3 $V_{0\text{-}p}$ shown in **Figure 6.10** is the inverse of the 3 $V_{0\text{-}p}$ plot in **Figure 6.9**. This means ions that were not resonantly ejected in the experiments illustrated in **Figure 6.9** were detected by shutting off the rf voltage after resonance ejection, as shown in **Figure 6.10**. There is, however, a decrease in the ion signal at 38 kHz, which is much larger than the slight increase in ion signal, observed with resonance ejection experiments at 38 kHz. As with the data from resonance ejection with 8 $V_{0\text{-}p}$, the decrease in detected signal at 38 kHz, suggests that not all of the resonantly excited ions are ejected at 38 kHz.

Simulations of resonance ejection of xenon ions in the OEOCIT geometry, shown by the green triangle points in **Figure 6.11a**, also yielded ejection over a similar range of frequencies to those experimentally observed (black square points). As noted in **Section 6.4.1.2**, when an ions simulation time is less than 10,000 μsec, the ion is said to be ejected. The two overlaid plots of experimental (black square) and simulation results (green triangle) appear to be the reciprocal of one another; however, low simulation times from ejected ions correlate to large peak areas from ejected ions in the experimental observations. There is some disagreement in the experimental results with resonance ejection occurring at lower frequencies and over a slightly broader range of ejection frequencies compared to the simulations. At lower resonance ejection voltage amplitudes there is good agreement with the experiments and modeling. As shown in **Figure 6.11b**, when examining the peak area of ions not ejected during resonance ejection at 3 $V_{0\text{-}p}$ the frequency range that ions were ejected is very similar to the resonance ejection simulations.

Ion trajectory simulations of higher mass-to-charge ratio ions in the 2xOEOCIT geometry, operated at 4 $kV_{0\text{-}p}$, showed that ions were ejected in a non resonance ejection

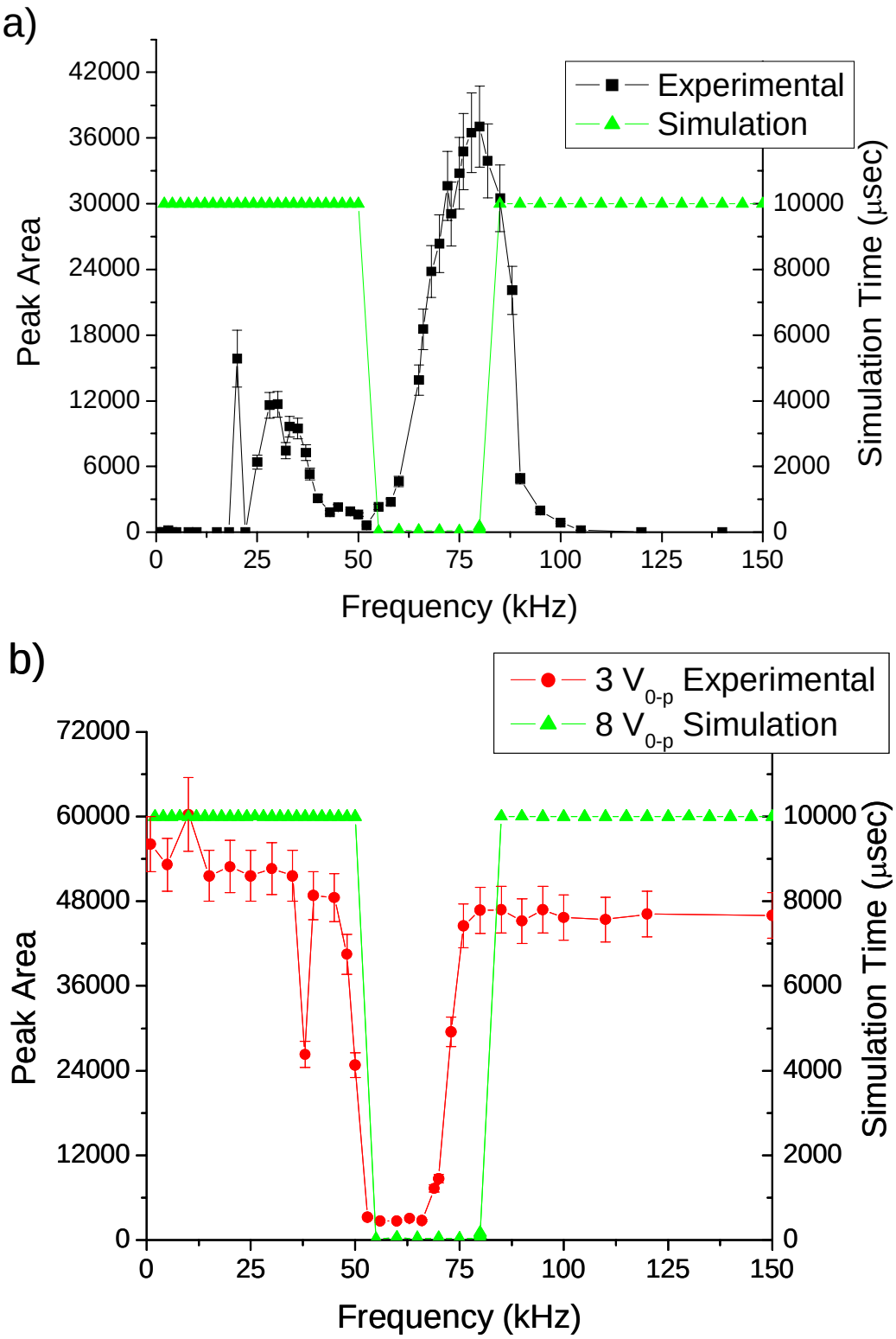

Figure 6.11 – a) Resonance ejection experiments and simulations at 8 $V_{0\text{-}p}$ b) Peak area of ions not ejected from resonance ejection at $3V_{0\text{-}p}$ with simulation at $8V_{0\text{-}p}$. Low simulations times correlates to ejected ions.

process at frequencies below 30 kHz. When the rf voltage is increased above 4 kV_{0-p} the ions are only ejected with the frequency of the resonance ejection voltage similar to the secular frequencies of the ions. Simulations in the OEOCIT showed that at rf voltages below 1 kV_{0-p} ions experienced non-resonance ejection below 20 kHz. Above 2 kV_{0-p} the non resonance ejection was not observed.

6.5.3 Maximum Storage Capacity

As the number of ions trapped in an ion trap is increased, ions will be affected by space charge; which was described in **Section 3.4.2**. The theory and importance of the maximum storage capacity is described in **Section 5.4.4**. As ions are injected into the ion trap, the increase in observed ion abundance should be linear. As the increase in ion signal becomes non-linear and finally no longer increases, the ion trap has reached its maximum storage capacity. Results from the experiments exploring the maximum storage capacity in the OEOCIT are shown in **Figure 6.12.** As a function of injection time, ions can be injected into the OEOCIT with an observed linear increase from 0.5 to 500 msec. At longer injection times ions can still be brought into the ion trap, but the ion signal asymptotically approaches a limit. Comparing the maximum total ion current (TIC) reached to the first generation OCIT in **Section 5.4.4**, the OEOCIT is trapping on average eight to ten times fewer ions than the OCIT. Some of this trapping difference is due to the decrease in the trapping volume. In the quadrupole ion trap with similar geometry to the OCIT, described in **Section 4.4.4,** the maximum total ion current was $2.5x10^5$, which is two to three times less than in the OEOCIT. The pressure of xenon in the source was the same; however, the ion block and einzel lenses voltage were slightly different, which may cause ions to be focused to a different position in the volume of the ion trap. The initial position, with respect to the center

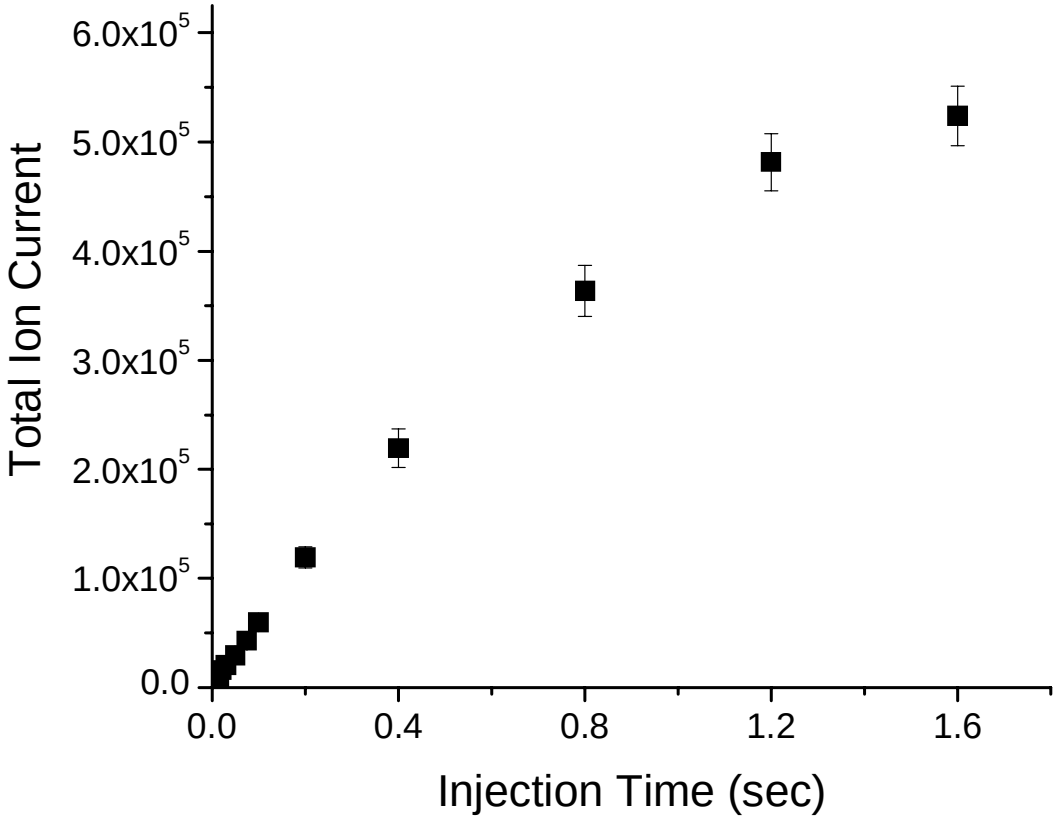

Figure 6.12 – Maximum storage capacity results in an OEOCIT.

of the ion trap can affect the ions stability in the presence of higher order fields.[18] Therefore some of the difference may also be due to trapping or transmission efficiency differences between the devices.

6.5.4 Image Current Simulations and Fourier Transform Calculations

Single ended detection was simulated on the entrance endcap electrode for a *m/z* 500 ion with an rf voltage of 4 $kV_{0\text{-}p}$ in the 2xOEOCIT geometry. As shown in **Figure 6.13a** the secular frequency of the ion was observed at 44100 kHz. The first, second, and third harmonics were also observed. At the fundamental and the harmonic frequencies, an additional frequency was observed. These frequencies correspond to the axial and radial frequencies of the ion. The detection method should only detect the axial frequencies of the ion; however, because the algorithm used calculates a 3-D distance, both the radial and axial directions are taken into account. If the results of **Equation 6.3** and **Equations 6.4** are each Fourier transformed, then the axial and radial components can be separated, as shown in **Figure 6.13b** and **Figure 6.13c**. Note that amplitude of the radial component is less than the axial component. As shown in **Figure 6.13d**, when the differential detection mode was simulated only the axial frequency was observed and only even harmonics were observed. During these experiments no resonance ejection was performed. The simulation was only performed with one ion at a time so it is not clear whether or not the ion cloud will be coherent. Coherence could easily be established with a low amplitude resonance excitation voltage applied to the central ring electrode, while detecting the image current on the end caps. Alternatively the resonance excitation voltage could be applied to the endcaps, while detecting on the central ring electrode. It also important to note that unlike image current detection in a conventional 3-D quadrupole ion trap no resonance excitation method was

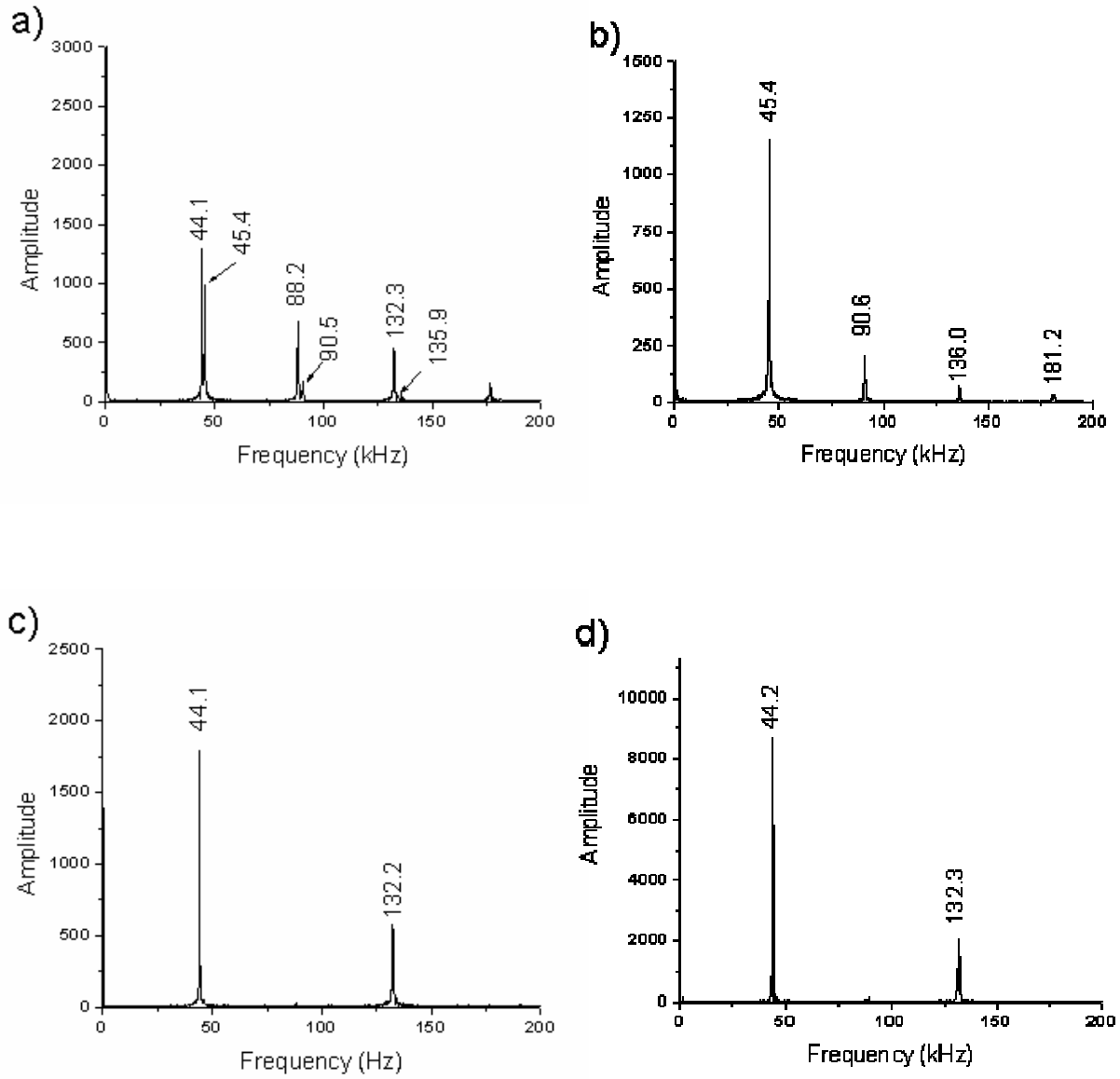

Figure 6.13 – Secular frequencies of *m/z* 500 ion from FT of calculated reciprocal distances in a) Single ended detection method b) Decoupled radial frequency c) Decoupled axial frequency d) Differential detection mode.

used during this simulated technique and yet a simulated FT signal was still able to be calculated. Resonance excitation in a 3-D quadrupole ion trap serves to establish ion coherence and to increase the ion's trajectory so that the ions are closer to the endcap electrodes. Ions motion is incoherent in the 3-D ion trap because ions are injected over several rf cycles. Only one ion was modeled at a time; therefore, the necessity for ion coherence was not addressed. Ions may need to be resonantly excited in the OEOCIT to establish ion coherence and it is not clear whether the ions motion will be close enough to endcap electrodes to detect an image current without resonance excitation.

Ion trajectories were simulated for a *m/z* 100 and 1000 ion while varying the rf voltage from 500 to 4000 $V_{0\text{-}p}$. The ion's reciprocal distance from the end cap electrodes as a function of time was Fourier transformed and the secular frequency calculated at each rf voltage. As shown in **Figure 6.14** the secular frequencies, determined using the differential detection method, were linear over the full range of rf voltages. The secular frequencies calculated at each rf voltage agreed with the secular frequencies determined during the simulation of resonance ejection. As described in **Section 5.4.3.3** this linear response is expected. The linear response was also experimentally observed in **Section 6.5.2** when the central frequency of the resonance ejection region doubled from 77 kHz to 144 kHz when the rf voltage was increased from 500 to 1000 $V_{0\text{-}p}$.

It is arguable whether or not the image current will be sufficient when detected on the endcap electrodes in the 2xOEOCIT. To improve the relative proximity of the ions to the electrode surfaces, the OEOCIT electrodes were designed to be half the dimensions of the modeled system. Two alternative detection methods were also simulated. The first was with the intermediate electrodes as the detection electrodes with the rf voltage applied to the

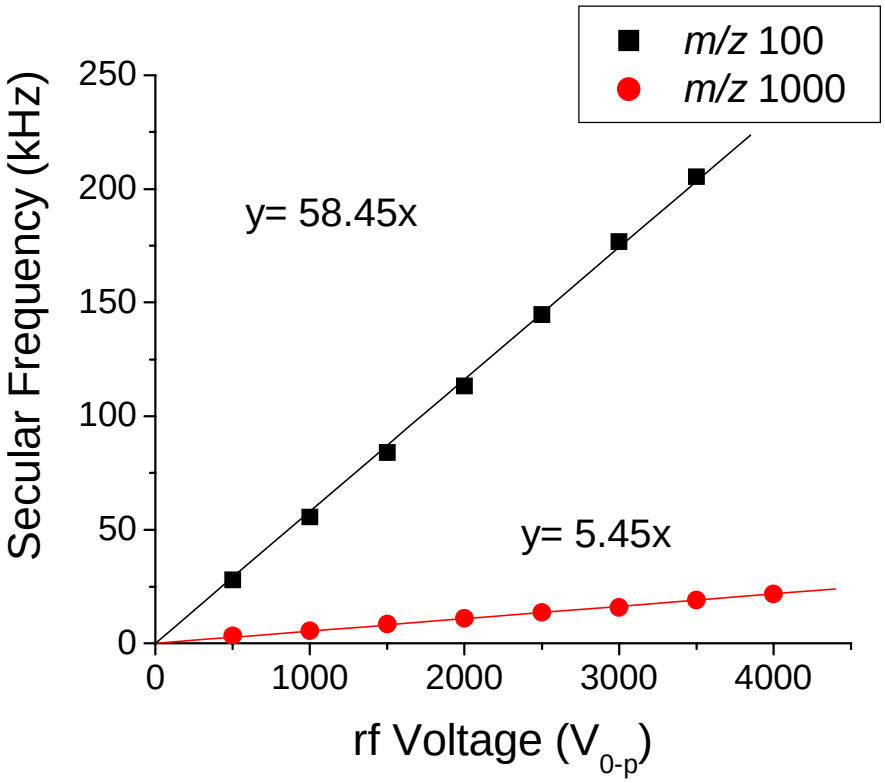

Figure 6.14 – Secular frequencies of *m/z* 100 and 1000 determined in simulated FT experiments in the 2xOEOCIT.

endcaps and central ring electrodes. This simulated method gave a larger FT response than detection on the endcap electrodes. As previously mentioned the electrical configuration when detecting an image current on the intermediate electrodes, is not ideal for the operation of the octapole trap because of the high voltage that is applied to the endcap electrodes. The second alternative that was explored was to detect the image current on the central ring electrode. The simulated image current detected in this mode also gave a better response than when the endcap electrodes were used as the detection electrodes, but this electrode may be more prone to picking up rf voltage because of its relative size and location to the intermediate ring electrodes. In general, the agreement of the experimental results and the ion trajectory modeling suggests that image current detection and subsequent Fourier transformation of that signal seems to be a viable detection method that can be implemented on an octapole ion trap.

6.6 Conclusions

Ion trajectories were simulated in a second generation open end cap 3-D octapole ion trap with a cylindrical electrode geometry. Ions of *m/z* 100 to 10,000 were found to have stable trajectories with rf voltages ranging from 100 - 8×10^5 $V_{0\text{-}p}$. The minimum voltage necessary to trap *m/z* 10,000 ions (650 $V_{0\text{-}p}$) was much more comparable to the voltage necessary for *m/z* 100 ions (100 $V_{0\text{-}p}$) than in the first generation geometry. The rf voltages necessary to eject ions out of the OEOCIT were 1.33 times greater than the voltages necessary to eject ions out of a 3-D quadrupole ion trap with identical electrode geometry.

The OEOCIT electrodes were designed and constructed. Initial resonance ejection experiments showed that xenon ions were ejected over a range of frequencies from 55 to

90 kHz. At larger resonance ejection amplitudes a secondary resonance ejection region was observed from 33 to 40 kHz, which is roughly half the frequency of the 55 to 90 kHz ejection region. Ions were not resonantly ejected from 40 to 50 kHz. Ions that were not resonantly ejected were detected by turning off the rf voltage following resonance ejection. In these experiments, ions were not observed from 40 to 50 kHz, suggesting that ions which were not resonantly ejected are still being resonantly excited in this frequency range. The ion excited motion is then preventing an efficient extraction following turning off the rf voltage. At lower resonance ejection amplitudes, experimental results agreed with resonance ejection simulations. The relatively narrow resonance ejection is an improvement over the first generation octapole ion trap; however, the ejection region is still too broad for mass analysis by resonance ejection.

One of the reported advantages of octapole fields is that they should be able to focus and confine ions more efficiently than quadrupole fields. Theoretically this should lead to more ions being trapped. Experiments looking at the maximum storage capacity of the OEOCIT showed that ions were injected over a broad range of injection times with a linear increase in ion abundances. Compared to the first generation OCIT the OEOCIT is trapping fewer ions; however, the electrode geometry was reduced in half. The observed TIC was still three to four times greater than a cylindrical quadrupole ion trap with a larger electrode geometry.

Even though mass analysis via resonance ejection was not ideal, an alternative non-destructive detection method was proposed. Detection of an ion image current was simulated in the OEOCIT by calculating the reciprocal distance of an ion from a detector electrode during ion trajectory simulations. The image current was then subsequently Fourier

transformed. The endcap electrodes, intermediate ring electrodes, and a split central ring electrode were all simulated as detector electrodes. The intermediate ring electrodes gave the greatest response followed by the central ring and the end cap electrodes. The most practical of all three methods to implement is the image current detection on the endcap electrodes. The axial secular frequency of a *m/z* 100, 500, and 1000 ion were calculated and found to agree with the secular frequencies determined during resonance ejection simulations. The secular frequencies of a *m/z* 100 and *m/z* 1000 ion were determined to be linear as a function of the rf voltage. Agreements with modeling and experimental resonance ejection results suggest that the proposed Fourier transform method is a viable, non-destructive detection method for the second generation open endcap octapole ion trap with cylindrical geometry.

6.7 References

1. Gabrielse, G.; Haarsma, L.; Rolston, S. L., *Open-Endcap Penning Traps for High Precision Experiments.* International Journal of Mass Spectrometry and Ion Processes, 1989. 88: p. 319-332.

2. Comisarow, M. B.; Marshall, A. G., *Theory of Fourier-Transform Ion-Cyclotron Resonance Mass-Spectroscopy .1. Fundamental Equations and Low-Pressure Line-Shape.* Journal of Chemical Physics, 1976. 64(1): p. 110-119.

3. Marshall, A. G.; Wang, T.-C. L.; Ricca, T. L., *Tailored Excitation for Fourier Transform Ion Cyclotron Resonance Mass Spectrometry.* Journal of the American Chemical Society, 1985. 107(26): p. 7893-7897.

4. Marshall, A. G.; Hendrickson, C. L.; Jackson, G. S., *Fourier Transform Ion Cyclotron Resonance Mass Spectrometry: A Primer.* Mass Spectrometry Reviews, 1998. 17: p. 1-35.

5. Makarov, A., *Electrostatic Axially Harmonic Orbital Trapping: A High-Performance Technique of Mass Analysis.* Analytical Chemistry, 2000. 72: p. 1156-1162.

6. Hu, Q. Z.; Noll, R. J.; Li, H. Y.; Makarov, A.; Hardman, M.; Cooks, R. G., *The Orbitrap: a new mass spectrometer.* Journal of Mass Spectrometry, 2005. 40(4): p. 430-443.

7. Olsen, J. V.; de Godoy, L. M. F.; Li, G. Q.; Macek, B.; Mortensen, P.; Pesch, R.; Makarov, A.; Lange, O.; Horning, S.; Mann, M., *Parts per million mass accuracy on an orbitrap mass spectrometer via lock mass injection into a C-trap.* Molecular & Cellular Proteomics, 2005. 4(12): p. 2010-2021.

8. Hardman, M.; Makarov, A., *Interfacing the Orbitrap Mass Analyzer to an Electrospray Ion Source.* Analytical Chemistry, 2003. 75: p. 1699-1705.

9. Frankevich, V.; Soni, M.; Nappi, M.; Santini, R. E.; Amy, J. W.; Cooks, R. G. Non-Destructive Ion Trap Mass Spectrometer and Method. US Patent 5625186, 1997.

10. Aliman, M.; Glasmachers, A., *A novel electric ion resonance cell design with high signal-to-noise ratio and low distortion for Fourier transform mass spectrometry.* Journal of the American Society for Mass Spectrometry, 1999. 10(10): p. 1000-1007.

11. Senko, M. W. Linear Quadrupole Mass Spectrometer. US Patent 6403955 B11, 2002.

12. Soni, M. H.; Wong, P. S. H.; Cooks, R. G., *Notched Broad-Band Excitation of Ions in a Bench-Top Ion Trap Mass Spectrometer.* Analytica Chimica Acta, 1995. 303: p. 149-162.

13. Badman, E. R.; Patterson, G. E.; Wells, J. M.; Santini, R. E.; Cooks, R. G., *Differential Non-destructive Image Current Detection in a Fourier Transform Quadrupole Ion Trap.* Journal of Mass Spectrometry, 1999. 34: p. 889-894.

14. Soni, M.; Frankevich, V.; Nappi, M.; Santini, R. E.; Amy, J. W.; Cooks, R. G., *Broad-Band Fourier Transform Quadrupole Ion Trap Mass Spectrometry.* Analytical Chemistry, 1996. 68: p. 3314-3320.

15. Nappi, M.; Frankevich, V.; Soni, M.; Cooks, R. G., *Characteristics of a broad-band Fourier transform ion trap mass spectrometer.* International Journal of Mass Spectrometry and Ion Processes, 1998. 177: p. 91-104.

16. Syka, J. E. P.; Fies, W. J. J. Fourier Transform Quadrupole Mass Spectrometer and Method. US Patent 1988.

17. Guan, S.; Marshall, A. G., *Stored Waveform Inverse Fourier Transform Axial Excitation/Ejection for Quadrupole Ion Trap Mass Spectrometry.* Analytical Chemistry, 1993. 65(9): p. 1288-1294.

18. Hägg, C.; Szabo, I., *New Ion-Optical Devices Utilizing Oscillatory Electric Fields. III. Stability of Ion Motion in a Two-Dimensional Octopole Field.* International Journal of Mass Spectrometry and Ion Processes, 1986. 73: p. 277-294.

Chapter 7

Conclusions and Future Directions

7.1 Summary

Over the past two decades the quadrupole ion trap mass spectrometer has become one of the more heavily used mass spectrometers in today's analytical laboratory. It is known for its sensitivity, high MS/MS efficiency, and for being relatively inexpensive. The electrodynamic field used to trap ions in the ion trap is theoretically a pure quadrupole field. In reality, however, this field contains minor contributions from higher order fields that are a result of non-idealities in the ion trap electrodes. The experiments described in this dissertation were designed to study higher order fields and their impact on the operation of quadrupole ion traps. Additional studies exploring ion fragmentation during ion injection in 2-D and conventional 3-D quadrupole ion traps were also described. Lastly a higher order field ion trap was developed, proof of principle experiments performed, and a second generation geometry was described with Fourier transform detection possibilities. The results obtained from each of these experiments and future directions of this work are discussed in this chapter.

7.2 Radio Frequency Circuitry Development and Characterization of a Compensated Cylindrical Ion Trap Mass Spectrometer

The development of a compensated cylindrical ion trap (CCIT) to study the effects of higher order fields in quadrupole ion traps was described in **Chapter 2**.[1, 2] Several properties of the CCIT were determined and optimized. The CCIT was capable of producing mass spectra via resonance ejection with a mass resolving power of 110. The optimum results for resonance ejection occurred at the octapole non-linear resonance of $\beta_z = ½$. Mass resolution was improved by decreasing the scan rate of the rf voltage during mass analysis.

Experimental flaws found in the first generation rf circuitry led to the development of a new resonant rf system consisting of three resonant LC circuits, where the inductor in each circuit was a simple autotransformer. The rf circuits were matched and tuned so that the overall rf system had one resonant frequency. Following optimization, the rf circuitry was capable of generating voltages of 100 - 2500 $V_{0\text{-}p}$ and the system was tunable for resonant frequencies from 730 to 1050 kHz This second generation circuitry was more robust and efficient than the first generation rf circuitry.

The original goal of the CCIT was to electro-dynamically introduce higher order fields by independently controlling the amplitude of the rf voltages on the compensating ring electrodes and the center ring electrode. However, when the rf voltages on the compensating ring electrodes were increased relative to the amplitude of the voltage on the center ring electrode, the voltages on all three ring electrodes increased. Further exploration of this occurrence showed that the electrodes were capacitively coupled. Off resonant operation was attempted to reduce the effects of the capacitive coupling. When the rf circuitry was operated in an off resonant mode, the amplitudes of the voltage on all three electrodes were able to be independently controlled. When circuits were operated off resonant, the amplitude

of the rf voltage was found to be less than 200 $V_{0\text{-}p}$, which is insufficient for any useful mass spectrometry experiments. Inserting electrically grounded shielding electrodes between the compensating ring electrodes and the center ring electrodes was successful at reducing the effects of the capacitive coupling. Varying the voltage on the center ring electrode relative to the compensating ring electrodes was more effective at maintaining an independent control of the rf voltages. When the voltages on the three ring electrodes were not equal, the phase of the rf voltages shifted. The phase of the voltage on the compensating ring electrodes shifted as much as 50 degrees relative to the voltage on the center ring. The full implications of this phase shift have not yet been determined.

Experiments intending to introduce octapole fields during ion injection were performed by applying an equal amplitude rf voltage to the compensating ring electrodes and varying that voltage relative to the voltage on the center ring electrode and vice-versa. Mass spectra acquired suggested that there were improvements to the injection efficiency over a broad range of rf voltages. The introduced phase shift as well as any changes to axial dimensions due to the presence of the shielding electrodes makes it difficult to determine the exact contributions of higher order field components that were introduced. Also, the phase shifts and any changes to the electrode geometry invalidate the electrostatic calculations of the electric fields used to determine the percentage of HOF introduced.[2] Electrostatic modeling of the electric fields with the elongated electrode geometry and the phase changes will need to be completed to gain an understanding of what voltage ratios are required to introduce different higher order field content. Further improvements to the amplitude control may be achieved with the introduction of a feedback loop to monitor and actively control the amplitude of the rf voltages in the three LC circuits. With a greater understanding of the

introduced higher order fields and a better control of the amplitude of the rf voltage, the stability diagram of the CCIT can be explored. By systematically varying the rf voltages on the compensating and center ring electrodes, the effects of introducing higher order fields during ion injection, ion ejection, and during MS/MS experiments can be studied. The results from these experiments will lead to a greater understanding of the optimal higher order field contributions during each portion of a mass spectrometry experiment. The fact that amplitude control is possible with the shielding electrodes makes electro-dynamically introduced higher order fields a possibility in the future to study the effect of higher order field content in ion traps.

7.3 Impact of Non-Linear Resonances on Environmental Applications

The work described in **Chapter 3** simulated online air sampling techniques by direct sampling from an 80-L Tedlar™ bag that was filled with a low ppm concentration of the analyte in air. Isoprene, methacrolein, and methyl vinyl ketone in air were successfully ionized via selected ion chemical ionization. Resonance ejection at non-linear resonances was performed to counteract the negative side effects of the analyte being present in air, which is harmful to ion trap performance due to scattering effects.[3] These experiments were conducted in a compensated cylindrical ion trap and a conventional 3-D quadrupole ion trap mass spectrometer (QITMS). Improvements to the observed ion abundance were noted in the CCIT when resonance ejection was performed at octapole non-linear resonances ($\beta_z = ½$) for all analytes. In the QITMS, when resonance ejection was performed at the octapole non-linear resonance, decreases in ion abundances were observed. Decreases in ion abundance were observed at hexapole non-linear resonances ($\beta_z = ⅔$) in both the CCIT and the QITMS.

In addition to the decreases in ion signal at non-linear resonances in the QITMS, decreases in ion signal were observed in conventional resonance ejection. Results from experiments in the QITMS without the heavy buffer gas (air) showed that there was a less dramatic loss in ion signal during conventional resonance ejection. Therefore, some of the ion losses during conventional resonance ejection may be due to the presence of the heavy buffer gas.

In the CCIT, ion losses due to non-resonance ejection were observed at long reaction times (<2 sec). These losses counteracted any gained sensitivity due to resonance ejection at the non-linear resonances. The effect of resonance ejection at non-linear resonances appeared to be more pronounced for methyl vinyl ketone as compared to its isomer methacrolein. These results suggest that there may be a chemical specificity to the effects of higher order fields, which has been suggested in the literature.[4, 5] Exploring a wider class of compounds may help to further understand the chemical nature of these effects. Using analytes with a larger molecular weight, such as alpha-pinene or bornyl acetate, would also be of interest to see if the effects of the heavy bath gas are as pronounced.

There are potential improvements to the CCIT that may improve its performance for the analysis of VOCs. The ion losses that were observed during long reaction times in the CCIT were believed to be the result of the electrode geometry. Altering the mesh-covered endcap geometry may be a good starting point for improving the electrode geometry. The electrode geometry was originally adapted from a cylindrical ion trap that was designed for an ICR cell. This cylindrical ion trap contained a unique set of open endcap electrodes. Introducing these open endcaps instead of the mesh endcap electrodes may prevent ion losses by removing any truncation of the electric fields caused by the mesh-endcap electrodes. When these open endcap electrodes were used in the octapole ion trap described in **Chapter 6**, non-

resonance ejection was not observed. A thorough ion trajectory simulation of the CCIT and modifications to the geometry would aid in finding the optimal geometry to prevent ion losses. Modifications to the geometry of the CCIT to prevent ion losses would help make the CCIT an ideal ion trap for the detection of VOCs in conjunction with resonance ejection used at non linear resonances.

7.4 Fundamental Studies of Ion Injection and Trapping in Linear and Conventional 3-D rf Ion Traps

Experiments exploring the differences in fragile ion fragmentation during ion injection in 2-D and 3-D rf ion traps were described in **Chapter 4**. A hybrid quadrupole 2-D quadrupole ion trap and a hybrid quadrupole 3-D quadrupole ion trap were constructed to deconvolute molecular ion fragmentation during ion injection and molecular ion fragmentation that occurs in an EI source. The effects of initial ion kinetic energy, rf amplitude during ion injection, and buffer gas pressure on ion fragmentation were explored. The analytes studied were nonane (*m/z* 128), n-butylbenzene (*m/z* 134), t-butylbenzene (*m/z* 134), and FC-43 fragment ions (*m/z* 219 and *m/z* 502). In the 3-D ion trap, the rf voltage during ion injection was found to drastically effect ion fragmentation. For most of the analyte ions a lower rf voltage reduced fragmentation. However, decreases in the total ion current were observed at the lower rf voltages because of the mass bias that occurs during ion injection in the 3-D ion trap. In the 2-D ion trap, the rf voltage during ion injection was not a factor until just before the ion's trajectory was unstable. Increasing the initial kinetic energy of ions in both instruments was found to increase fragmentation. Fragmentation was reduced in both instruments by adjusting the kinetic energy of ions to 3 - 5 eV, which is 5 - 7 eV less than the optimal kinetic energy used with non-fragile ions. A baseline fragmentation of as

much as 30% was observed in the 2-D ion trap, which could not be reduced. The fragmentation of n-butylbenzene and t-butylbenzene could be reduced to 5% of the total ion current in the 3-D ion trap at reduced kinetic energies and a lower rf voltage. Increasing the buffer gas pressure in both instruments resulted in subtle increases of the amount of observed fragmentation. The effects of reducing the pressure of the buffer gas on fragile ion fragmentation could not be determined because of the decrease in sensitivity at lower buffer gas pressures. In general, utilizing the standard operating conditions for the 2-D and 3-D ion traps, the 2-D ion trap has less fragile ion fragmentation than the 3-D ion trap. When conditions were optimized less fragmentation was observed in the 3-D ion trap than the 2-D ion trap. As suggested in the literature, the main mechanism of fragile ion fragmentation is collision induced dissociation.[5-8]

Differences in the relative amount of observed fragmentation between n-butylbenzene, t-butylbenzene, and nonane further suggest that there is a strong chemical nature to fragile ion fragmentation. Because this set of analytes is not a diverse group of compounds, it would be useful to explore fragmentation during ion injection with several different classes of compounds. Some interesting classes of compounds are polychlorinated biphenyls, polyaromatic hydrocarbons, n-alkanes, n-alkenes, and volatile organic compounds similar to those used in **Chapter 3**. These compounds are of analytical interest because of their impact on the environment and use in petroleum applications. The goal of this work was to understand the effects affects of instrumental factors on fragile ion fragmentation. If a relative level of fragility could be established for these compounds, then analytical methods could be developed based on the work presented here that would reduce fragmentation and improve quantitative analysis in 2-D and 3-D quadrupole ion traps.

7.5 Development and Characterization of an Octapole Ion Trap

Theory, ion trajectory simulations, and proof of principle experiments for a novel octapole ion trap were described in **Chapter 5**. A novel cylindrical octapole ion trap was created by grounding the center ring electrode of the CCIT described in **Chapter 2**. Results from ion trajectory simulations showed that 36 times the rf voltage was required to mass selectively eject an ion from the octapole ion trap as compared to a quadrupole ion trap with the same electrode geometry. The rf voltage in the CCIT necessary to eject a *m/z* 500 ion was 13.5 $kV_{0\text{-}p}$, where as the octapole ion trap required more than 475 $kV_{0\text{-}p}$ to eject the same ion. Because of the impracticality of achieving the very large voltages necessary to mass selectively eject ions out of the octapole ion trap, mass analysis must be performed with resonance ejection.

Ions were successfully trapped in the cylindrical octapole ion trap. Experiments looking at the maximum storage capacity of the cylindrical octapole ion trap and the cylindrical quadrupole ion trap show that the cylindrical octapole ion trap is capable of storing at least 50 times more ions than the quadrupole ion trap. Additionally when the two instruments are compared in a region where they both have linear increases in ion abundance with increasing accumulation time, the octapole ion trap is 2.5 times more sensitive than the quadrupole ion trap.

Mass analysis in the cylindrical octapole ion trap is not possible because resonance ejection simulations show that at a constant rf voltage, ions were ejected over a broad frequency as predicted by ion trajectory simulations. Experiments in the prototype cylindrical octapole ion trap showed that resonance ejection of xenon ions occurred at all frequencies below 75 kHz, which agreed with the simulation results. Ions were ejected due

to a non-resonance ejection process, which was also observed in the compensated cylindrical quadrupole ion trap. The fact that experimental results and simulations in both instruments show ions ejecting at all frequencies below 75 kHz suggests that the geometry (spacing and thickness) of the cylindrical electrodes is the cause of the ejection.

Alternative geometries to the prototype cylindrical octapole ion trap geometry will need to be simulated and constructed. In a 3-D octapole ion trap the central ring electrode radius should theoretically be larger than the intermediate ring electrodes.[9] The theoretical relationship between the electrode radii, described in **Chapter 5**, is based on the electrodes having a hyperbolic surface.[9] The electrodes of the prototype cylindrical octapole trap are cylindrical so this relationship will not be satisfied. Modeling the electric fields of several electrode geometries with varying central ring electrode radii may help to find the optimal electrode geometry for the octapole ion trap. The relative thicknesses of the intermediate ring electrodes and the central ring electrode are also a concern. Two possible variations would include making the central electrode the same thickness as the intermediate ring electrodes and making the central ring electrode thickness smaller than the thickness of the intermediate ring electrodes. The last modification to the electrode geometry would be replacing the mesh covered endcap electrodes with an open endcap electrode. This electrode geometry has been used in cylindrical ion traps for penning ion traps. A second generation electrode geometry was proposed in **Chapter 6**; however, variations of the suggested modifications above will also need to be performed.

7.6 Development, Construction, and Characterization of a Second Generation Octapole Ion Trap Capable of Non-Destructive Detection Methods

The design, development, and characterization of a second generation octapole ion trap were described in **Chapter 6**. The second generation geometry contained open endcap electrodes and the central ring electrode length was reduced so that it was shorter than the intermediate ring electrodes. The new geometry, referred to as the open endcap octapole cylindrical ion trap (OEOCIT) had electric fields with a greater magnitude quadrupole field component than the previous geometry. The improvements to the electrode geometry should allow for improved resonance ejection. Additionally, a non-destructive detection technique was described. In this technique, the image current from the motion of trapped ions is monitored on the endcap electrodes and subsequently Fourier transformed. The mass spectrum is then generated by correlating the calculated frequencies with the secular frequencies of ions based on the trapping conditions.

Ion trajectory simulations of ion storage, resonance ejection, and several image current detection methods were performed. Ion trajectory simulations in the OEOCIT showed that only 650 $V_{0\text{-}p}$ was necessary for *m/z* 100 - 1000 ions to have a stable trajectory, which is less voltage than that required in the first generation octapole ion trap. During ion storage simulations, the rf voltage necessary to eject ions was only 1.33 times greater in the OEOCIT than in a quadrupole ion trap with the exact same electrode geometry. Resonance ejection simulations showed a more narrow range of frequencies necessary for resonance ejection of xenon ions than in the first octapole ion trap geometry. Additionally non-resonance ejection processes were not observed in the simulations. Three Fourier transform detection methods were simulated. In the first method the image current was differentially detected on the intermediate ring electrodes, while the rf voltage was applied to the endcaps

and central ring electrode. In the second method the image current was differentially detected on the endcap electrodes, while the rf voltage was applied to the intermediate ring electrodes and the central ring electrode was grounded. Finally, in the last method, the image current was detected on single ended on the central ring electrodes, while the rf voltage was applied to the intermediate ring electrodes and the endcaps were grounded. Detecting the image current on the intermediate ring electrodes gave the largest simulated response, followed by the central ring, and finally the endcap electrodes. Because it is impractical to operate the octapole ion trap with the rf voltage on the endcap electrodes, the first method can not be used. The second method offers mechanical and electrical challenges in the implementation; therefore, it will not be the first method attempted. Detecting the image current on the endcap electrodes is the most practical method to implement, even though it gives the lowest response of the three simulated methods. During the designing of the OEOCIT the dimensions of the electrode geometry were reduced by half to improve image currents that will be obtained.

The OEOCIT was constructed and characterized. Studies exploring the maximum storage capacity showed that the OEOCIT stores approximately 10 times fewer ions than the first generation octapole ion trap. This decrease was expected because the electrode geometry was reduced in half; however, the OEOCIT stored four times as many ions as the larger- radius quadrupole cylindrical ion trap described in **Chapter 5**. Resonance ejection of xenon ions showed agreement with resonance ejection simulations. During these experiments, increasing the amplitude of the resonance ejection voltage caused a shift in the frequency of the resonance ejection voltage that was needed to eject ions. At larger amplitudes the secular frequency of the ions appeared to shift by almost 18 kHz. Although

experiments agreed with the simulations, mass analysis via resonance ejection was still not possible because of the broad frequency range over which ions were resonantly ejected. The agreement of the resonance ejection experiments with the simulations does, however, suggest that the Fourier transform detection methods that were simulated are feasible.

The OEOCIT needs further characterization. Reports on linear octapole devices state that the location of the ion beam as it enters the device will affect the stability of an ion's trajectory through the device.[10] It would be useful to look at the positional dependence of ions on the trapping efficiency in the octapole ion trap. There may be improved conditions for ion injection that will result in more ions being trapped in a shorter period of time.

The circuitry designed to filter the rf voltage out of the image current described in **Chapter 6** needs to be constructed and characterized. Once this circuitry is constructed initial image current detection experiments can be performed. Resonance excitation may need to be used to establish ion coherence before the detection of the image current signal. If the detected image current is not sufficient then it may be necessary to construct the split central ring electrodes and differentially detect the image current between these electrodes.

7.7 **Conclusions**

The work presented in this dissertation is intended to serve as a basis for improved ion trap performance through the judicious use of higher order fields. The results presented herein may prove useful in the development of instruments capable of obtaining higher quality mass spectra (e.g., better resolution, sensitivity, MS/MS efficiency, etc.) for a wide variety of samples. The positive impact of the research with the compensated cylindrical ion trap mass spectrometer will give a better understanding of the improvements that can be

made through the use higher order fields. Additionally, the development of a novel octapole ion trap shows promise, and may lead to instrumentation that is capable of lower detection limits than those demonstrated by currently available 3-D quadrupole ion traps. Results obtained from a second generation octapole ion trap suggest the possibility of a new, inexpensive Fourier transform ion trap mass spectrometer. The increased storage capacity and sensitivity of the first generation octapole ion trap, coupled with the potential Fourier transform detection methods of the second generation octapole ion trap, indicates that this area of research will have a promising future. Finally, the instrumentation developments presented are but the first few steps toward the creation of the next generation of ion trap mass spectrometers. Operational improvements in the coming years will certainly continue to advance and improve the capabilities of the ion trap mass spectrometer, and consequently ensure its crucial role as a powerful analytical tool in many new and exciting areas of chemical and biological research.

7.8 References

1. Danell, R. M., *Advances In Ion Source And Quadrupole Ion Trap Design And Performance.* Ph.D. Thesis, University of North Carolina, 2001.

2. Ray, K. L. *New Approaches to Tandem Mass Spectrometry on a Quadrupole Ion Trap* Doctoral, The University of North Carolina, Chapel Hill, 2000.

3. Danell, R. M.; Danell, A. S.; Glish, G. L.; Vachet, R. W., *The use of static pressures of heavy gases within a quadrupole ion trap.* Journal of the American Society for Mass Spectrometry, 2003. 14(10): p. 1099-1109.

4. Bortolini, O.; Traldi, P., *Evaluation of the Polarizability of Gaseous Ions*, in *Practical Aspects of Ion Trap Mass Spectrometry*; March, R. E., Todd, J. F. J., Eds.; CRC Press: Boca Raton, FL, 1995; Vol. II, pp 145-159.

5. McClellan, J. E.; Murphy, J. P.; Mulholland, J. J.; Yost, R. A., *Effects of Fragile Ions on Mass Resolution and on Isolation for Tandem Mass Spectrometry in the Quadrupole Ion Trap Mass Spectrometer.* Analytical Chemistry, 2002. 74: p. 401-412.

6. Louris, J. N.; Amy, J. W.; Ridley, T. Y.; Cooks, R. G., *Injection of Ions into a Quadrupole Ion Trap Mass Spectrometer.* International Journal of Mass Spectrometry and Ion Processes, 1989. 88: p. 97-111.

7. McLuckey, S. A.; Glish, G. L.; Asano, K. G., *Coupling of an Atmospheric-Sampling Ion Source with an Ion-Trap Mass Spectrometer.* Analytica Chimica Acta, 1989. 225: p. 25-35.

8. VanBerkel, G. J.; McLuckey, S. A.; Glish, G. L., *Electrospray Ionization of Porphyrins Using a Quadrupole Ion Trap for Analysis.* Analytical Chemistry, 1991. 63(11): p. 1098-1108.

9. Walz, J.; Siemers, I.; Shubert, M.; Neuhauser, W.; Blatt, R.; Teloy, E., *Ion Storage in the rf Octupole Trap.* Physical Review A, 1994. 50: p. 4122-4132.

10. Hägg, C.; Szabo, I., *New Ion-Optical Devices Utilizing Oscillatory Electric Fields. III. Stability of Ion Motion in a Two-Dimensional Octopole Field.* International Journal of Mass Spectrometry and Ion Processes, 1986. 73: p. 277-294.

Appendix I

Software for Experiment Design, Data Acquisition, and Data Analysis

AI.1 Overview

The software necessary to perform experiments on an ion trap mass spectrometer can be separated into three main components: experiment design software, run time instrument control software for data acquisition, and data analysis software. Each of these components was designed to operate as a separate entity or to operate in communication with the other components. A general description of the organization and operational details for each of these pieces of software is presented in this Appendix. All of the software was written in the programming language G for National Instruments Lab VIEW, which is a unique fully graphical program language with an integrated compiler. As with any software project, e.g. Microsoft Windows, new problems are always found and revisions are never ending. The descriptions in this appendix serve to give the current status of each piece of the overall instrument control software that was developed over the coarse of the dissertation work..

AI.2 Experimental Design Software

The experimental design software was originally written for the compensated cylindrical ion trap described in Chapter 2. The software was then later adapted for the operation of a 3-D quadrupole ion trap mass spectrometer (QITMS). The concepts behind this software were adapted from the ICMS^{TM} that is available only for IBM 386 computers and was designed to operate a Finnigan ITMS^{TM}. The objective of this software is to allow the user to construct a “Scan Function” through a graphical user interface (GUI). The scan

function describes the amplitude of the rf voltage (typically in terms of the low mass cut off) that will be applied to the ring electrode(s) during each section of the experiment. Each portion of the scan function is called a scan segment. During any segment the user may select to also apply a waveform to the endcap electrodes, trigger various power supplies and lenses, and acquire data. There can be only one data acquisition segment per scan function. The end result, once the user is finished constructing the scan function, is a point by point 2-D array that will be used by the run time software to communicate with the appropriate analog output cards. Additionally the full waveform is constructed for the arbitrary waveform generator. **Figure AI.1** and **Figure AI.2** are the user interfaces for the CCIT and QITMS versions of the software respectively. The hierarchies of the main programs are shown in **Figure AI.3** and **AI.4**. A list of the main subprograms used by the experimental design programs for the CCIT and the QITMS are in **Table AI.1** and **Table AI.2** respectively.

AI2.1 CCIT Build Scan Function.llb

The scan function that is constructed with this program is an n × 19 array where n is the number of segments. The 19 positions along one row of the array are rf_1, rf_2, rf_3, dc_1, dc_2, dc_3, gate, multiplier, acquire, waveform, TTL1, TTL2, TTL3, TTL4, Wave Form Type, $V_{0\text{-}p}$, Frequency, Phase, and Swift Path. A version of the scan function is located in a comma delimited file, which contains the array and a comment for the scan function. Once the scan function is read in by the subprogram, “CSV into SF.vi”, the array is segmented and the 19 values from the first row are written to the appropriate objects on the user interface. The program then operates in a while loop, polling to see if the user has pushed a button or changed a value of an object on the GUI. After the user has performed some task the values

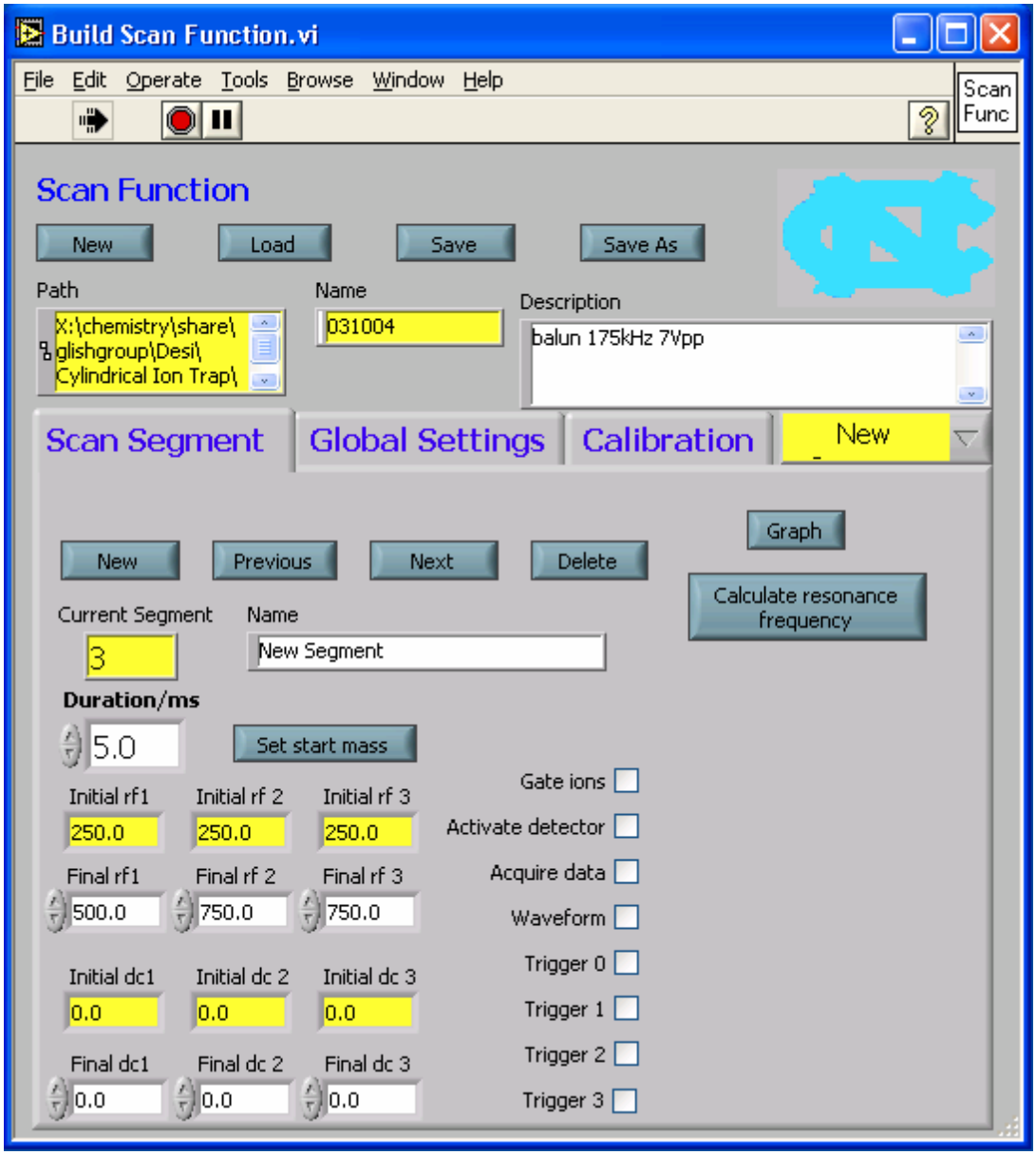

Figure A1.1 – GUI for experimental design software for CCIT.

a)

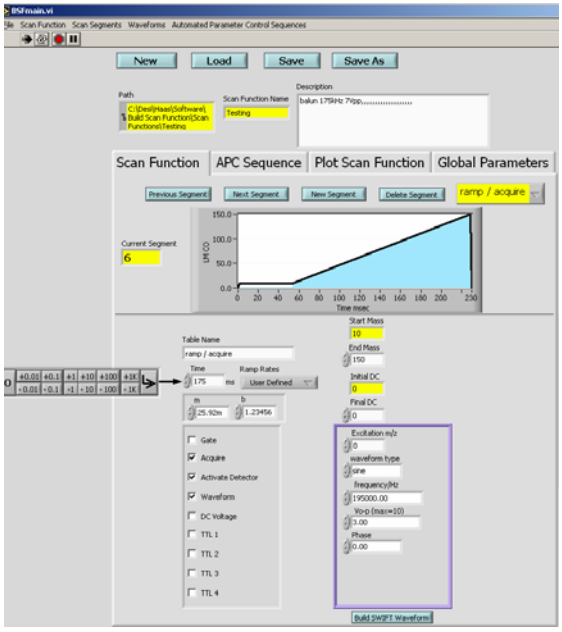

b)

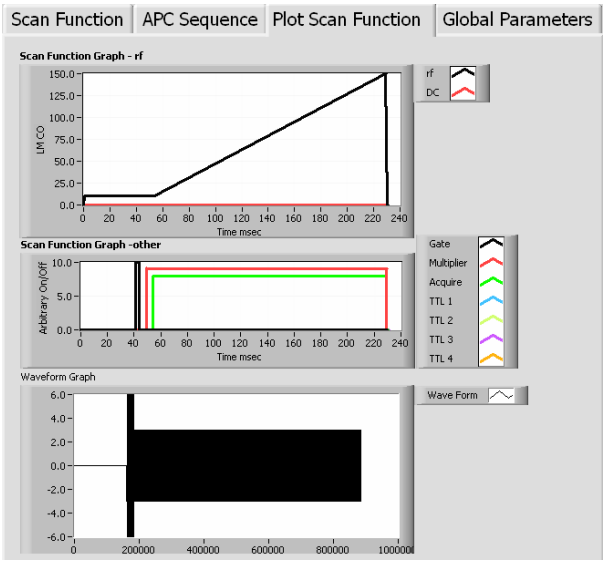

c)

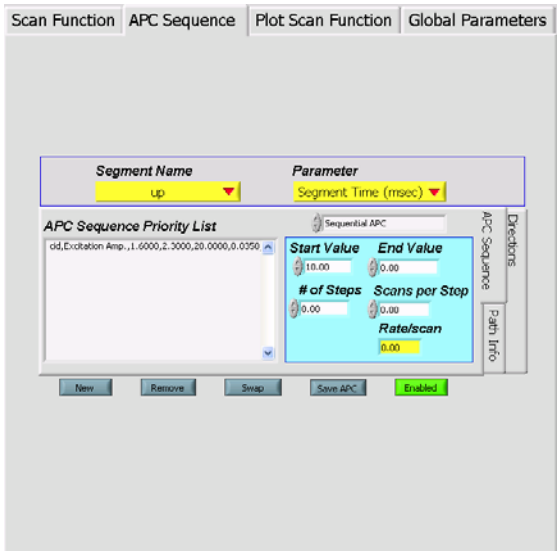

d)

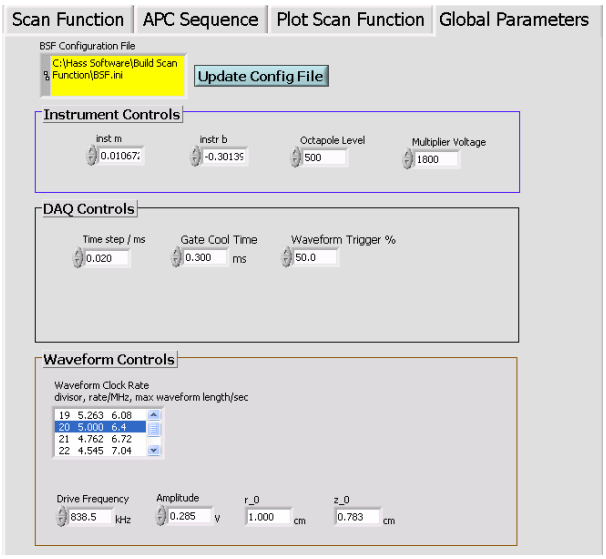

Figure A1.2 – GUI for experimental design software for QITMS
a) User Interface b) Plot scan function tab c) APC sequence tab and d) Global parameters tab.

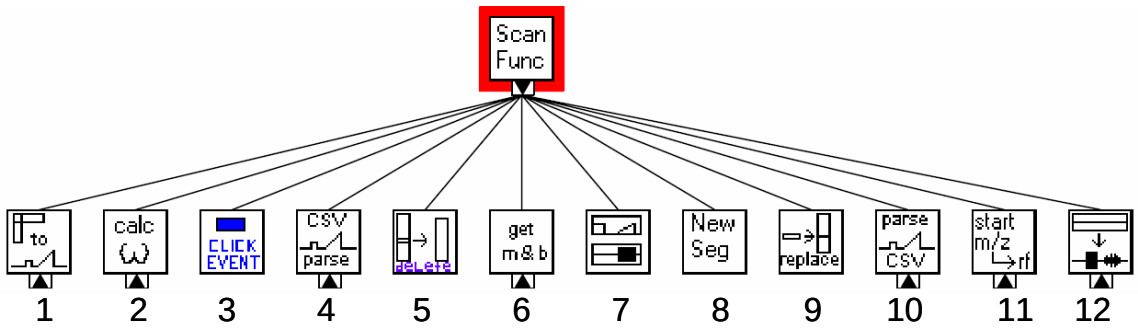

Figure A1.3 – Hierarchy for experimental design software for CCIT.

#	Program name	Description
1	Build scan function array.vi	Builds the n x 8 array with all of the points for the scan function and saves to binary file
2	calc resonance frequency.vi	Calculates the secular frequency of an ions given the rf voltage and m/z of the ion
3	click_event.vi	Determines what button or action was taken by the user, output is string
4	CSV into scan function.vi	Loads scan function from comma delimited file
5	delete segment.vi	Deletes a row of the scan function of the array
6	getm&b.vi	loads the calibration from the calibration file
7	Graph.vi	Displays the full scan function in a pop up window
8	new segment2.vi	Inserts a new row to the scan function array
9	replace segment.vi	Updates the array using the values from the GUI
10	save as CSV scan function.vi	Saves scan function array to a comma delimited file
11	start mass value to rf.vi	converts mass of an ion to rf voltage
12	waveform define and generate.vi	Constructs all of the waveforms for the scan function and saves them to a file

Table AI.1 – List and description of subprograms for **Figure A1.3.**

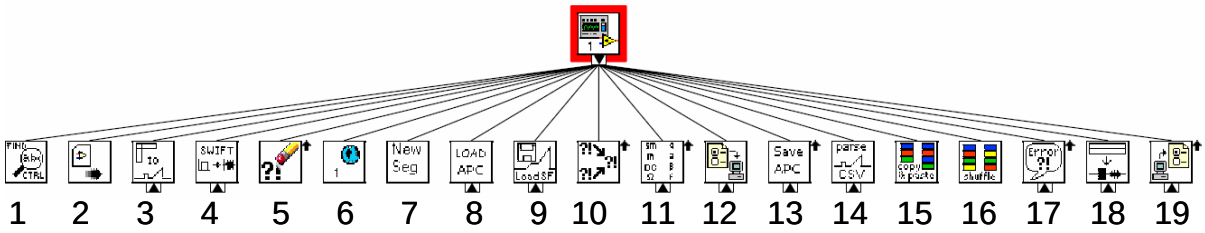

Figure AI.4 – Hierarchy for experimental design software for QITMS.

#	Program name	Description
1	BSF_Findcontrolbyname.vi	Allows for communication between APC and small plot of scan function
2	BSF_Loadandrun.vi	Calls APC program and Small scan function plot
3	Build Scan Function Array.vi	Builds all of the points for the n x 4 array and writes to global variables
4	Build SWIFT_Output(2.0).vi	Creates a SWIFT waveform (pop up standalone program)
5	Clear Errors.vi	General error handling
6	Global Variable.vi	Global variables used by Runtime and other programs
7	insert Segment.vi	Creates new segments; inserting new row into array
8	Load APC.vi	Starting an Automated Parameter Control
9	Load SF.vi	Loading a Scan Function
10	Merge Errors.vi	General error handler
11	Parameter Calculator_BSF.vi	Ion Trap parameter calculator
12	Read_config_BSF.vi	Reads user variables and set global variables from BSF.ini file
13	Save APC.vi	Saves APC and attaches it to a scan function
14	Save short SF.vi	Saves short version of scan function
15	Segment Copy	Allows user to copy and paste scan segments (pop up)
16	Segment Shuffle	Allows user to shuffle scan segments (pop up)
17	Simple Error Handler	General error handling
18	waveform define and generate_BSF_2.vi	Creates the points for the waveforms requested by user in step 15
19	Write_config_BSF	Writes user setting and global variable to BSF.ini file

Table AI.2 – List and description of subprograms for **Figure A1.4.**

of the array are updated, the screen is refreshed, and the program returns to the while loop. When a scan function is saved two binary files are created in addition to the short comma delimited version of the scan function. The first file is for the n x 8 scan array, where n is the number of points determined by the analog output rate (200kHz) and the length of the scan function. The eight values of the array are three dc control voltages for the rf voltages, three dc control voltages for the ion traps dc voltages, gate control voltage, and the electron multiplier control voltage. The second file contains all of the points for the waveform(s) that are applied to the endcap electrodes. These three files are saved in one folder and the entire contents of the folder are necessary to perform an experiment. Many of the variables are kept in the computer memory as global variables so that they are quickly accessible by the run time instrument control program. This prevents the run time program from needing to load the scan array and waveform from disk.

AI2.2 QITMS Build Scan Function.llb

AI2.2.1 Operation

The general purpose of the experimental design program for the QITMS is the same as the program for the CCIT, which is to create a scan function. The functionality of the program is also very similar. The program reads the scan function in from a comma delimited file. The 20 values from this file are segment name, time (ms), end mass, dc, dc on, gate, multiplier, acquire, ramp rate, waveform, TTL1, TTL2, TTL3, TTL4, Wave Form Type, Excite mass, $V_{0\text{-}p}$, Frequency, Phase, Swift. The values from the file are then put in an array and the individual elements of the first row of the array (or scan segment) are written to the controls on the GUI. The program then operates in a while loop waiting for the user to push a button or change a value. When the user saves the scan function, a comma delimited file is

created for the scan function. The scan array and waveforms are no longer saved, as they were in the old version. This was done because they are created and written to a global variable each time a scan function is loaded. The scan function folder will only contain the files named “scan function.csv” and “Automated Squence.csv”, which will be described in **Section AI2.2.3**.

When the scan array is created it is a n x 13 array, where the n values are determined by the analog output rate and the length of the scan function. The array contains four outputs that are for the rf voltage, the dc voltage, the electron multiplier voltage, and an auxiliary dc control voltage. The rest of the array is for the four TTLs, waveform trigger, two gate triggers, a multiplier trigger, and an acquire trigger. These nine columns from the scan array are used in the digital waveform. If each of these columns represents a bit of a 9 bit (0..8) number, then the 2-D n × 9 array can be turned into a 1-D array. This array will have n elements because each 9 bit binary number can be converted into a decimal number. This decimal number can be written to a digital output device as one number and all nine digital channels will assume the appropriate (0 or 1) output. See **Section AI3.3** for more details on the specific program that performs this operation.

AI.2.2.2 Program Updates and Additions

Several of the program structures were updated in QITMS version of the build scan function.llb. The programming structure for determining what action the user has performed was updated to a more efficient process called an “Event Structure”. This new process is built into Lab VIEW and allows the processor to more efficiently look at the value of objects in the GUI to determine if they have changed. The program contains four tabs. The first tab is the GUI for updating the scan function. The second and third tabs are for creating an

automated parameter control sequence (**Figure AI2.b**) and for plotting the scan function/waveforms (**Figure AI2.c)**. The automated parameter control (APC) will be discussed shortly. These two tabs are unique because they contain a programming element called a subpanel. The subpanel is essentially a link to a sub program. This subprogram can run simultaneously with the build scan function program. Subpanels prevent the need for pop up programs, which prevent access to the build scan function.llb until the pop up has been closed. Another subpanel also exists on the first tab. This subpanel is the small plot in **Figure AI.2a,** which represents the LMCO as a function of time. Only one instance of the subprogram can run at a time. Thus if the program is already open, it will can not be put into the subpanel. The last tab is for updating global variables and user settings, as shown in **Figure AI2.d**. The default values for the global variables and user settings are stored in an .ini file (BSF.ini). Retrieving these values from a .ini file allows the program to have different default settings on an individual computer basis without having to change, save, and recompile the program with new default values. If no .ini file is present one is created with the compiled program's default values.

In addition to updating the operating structure and adding subpanels, several of the user inputs (controls) were updated, removed, or added. The second and third rf voltages were removed because the QITMS only has one ring electrode. The values for the rf voltage are now input in terms of the low mass cut off (LMCO) (Da) instead of the voltage. The user inputs the value to be set at the end of the scan segment. The end LMCO ("end mass") of the previous scan segment becomes the beginning LMCO ("start mass") for the next scan segment. When the acquire check box is clicked a drop down listbox appears that allows the user to select specified scan rates or a custom scan rate. The last addition is a set of buttons

which allow the user to quickly increment the input values of an object; e.g. the end mass. These buttons appear when the user hovers over an object that has a numerical input.

AI2.2.3 Plot Scan Function and Automated Parameter Control Programs

The graph.vi is a program that plots the overall scan function including the rf and dc voltages, the digital triggers, and the waveforms. The rf voltage is plotted as a function of the LMCO and the time axis created from each of the scan segments' times. The level of the digital triggers is scaled so that they are discernable from one another. The waveforms are constructed and put together as one continuous waveform so that they can be plotted. This waveform construction can be time consuming. The program is used by the build scan function.llb and the runtime.llb.

The APC program allows the user to specify a parameter or parameters to be systematically varied by the run time.llb program. The APC program is linked to the scan function because the user must specify which scan segment a given parameter is varied on. The user specifies the start value, the end value, the number of steps, and the number of scans (mass spectra) to be acquired at each step. These values are stored in a comma delimited file, "Automated Sequence. csv", which also contains the path of the scan function that is associated with the APC sequence. The sequences can be enabled or disabled. A scan function will run in the runtime.llb regardless of whether the APC is enabled or disabled. This feature will be further discussed in **Section AI3.3**.

AI.3 Instrument Control and Data Acquisition Software

AI3.1 Controlling an Ion Trap

This section describes the newly developed control system for a QITMS. The necessary electronics and voltages to operate a quadrupole ion trap mass spectrometer are the rf voltage, dc trapping voltage, high voltage dc supplies for the multiplier and dynode, power supplies for ion optics, fast switching voltage for a gate lens to stop ions, supplemental ac voltage for ion manipulation, and several TTLs for other additional triggering capabilities. In addition to controlling the ion trap an oscilloscope or data acquisition device is required to record the mass spectrum. Several of the power supplies, such as the dynode and ion optic supplies, are static during most experiments and therefore their voltages can be set using their own internal potentiometer controls. The ion gate supply and the multiplier do need to be turned on and off during the experiment. As described in **Chapter 2** the amplitude of the low amplitude rf voltage is modulated with a dc voltage. The power supply for the dc trapping voltage is also controlled with a low voltage dc voltage. The instrumentation to operate these necessary control voltages are two function generators, an analog output device with multiple channels, a digital output device with multiple channels, and an analog input device.

AI3.2 Hardware Specifics

The hardware chosen for the instrument control is a National Instruments Peripheral Component Interconnect (PCI) eXtensions for Instrumentation (PXI) system, which is a PC-based platform for measurement and automation systems. The system is essentially a dedicated computer that is intended for instrumentation. The PXI controller consists of 1.26 GHz Pentium^{TM} III processor with 512MB of RAM and a 30 GB hard drive for data storage. The controller is run under a Windows^{TM} operating system. All of the data acquisition and

waveform generator cards are controlled using a standard PCI bus. Unlike a computer with standard PCI cards, these PXI cards can communicate between each other using a dedicated bus line that has its own independent 100MHz clock. This dedicated triggering system allows for absolute control over all timing in a given experiment. In addition to the windows platform, National Instruments programming platform LabView is loaded onto the hard drive. The instrumentation control software coordinates the different cards and the timing of their outputs and inputs. The PXI controller is a computer with capabilities for a monitor and for other USB devices.

The specific PXI cards chosen are the PXI-m6289 data acquisition (DAQ) device, the PXI-5401 function generator, and the PXI-5412 arbitrary waveform generator. The PXI-m6289 DAQ has four 16 bit analog output channels capable an output rate of 2 megasample/sec , 32 analog input channels capable of 500 kilosamples/sec, 48 digital inputs/outputs, and two 32 bit 80 MHz clocks. The output connectors of the PXI-m6289 are two 68 pin connectors. For easy access to analog output and input channels a breakout box was constructed from a standard 19" rackmount box (Jameco). The face of the box was milled out for the PXI-6289 connector cables and 16 British Naval Connectors (BNCs). A diagram of the face plate is shown in **Figure AI.5**. Two 68LPR connectors were installed in the box. These connectors have screw terminals that give access to the different channels from the PXI-m6289. Wires screwed into the 68LPR connectors were soldered to the BNCs. The PXI-5401 is a 16MHz function generator with 9.31 mHz resolution. The PXI-5412 is a 100 MHz 14 bit arbitrary waveform with 32 MB of buffer memory. **Figure AI.6** shows how the different PXI cards in the PXI system are used to control an ion trap and its power supplies.

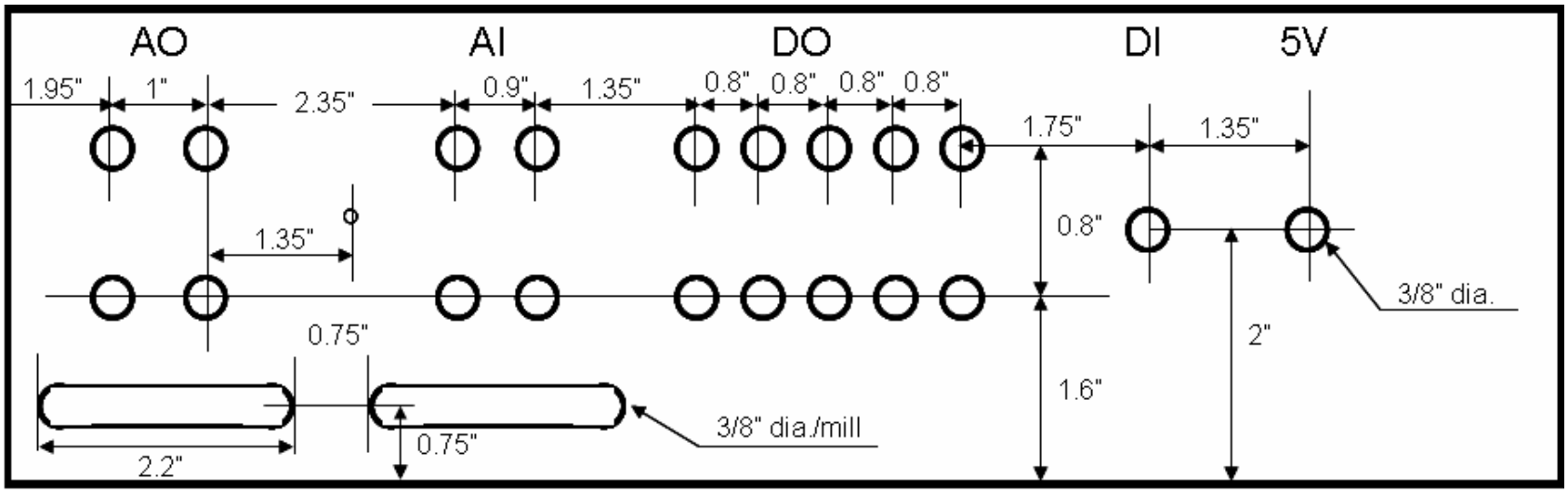

Figure AI.5 – Face plate of break out box for PXI system

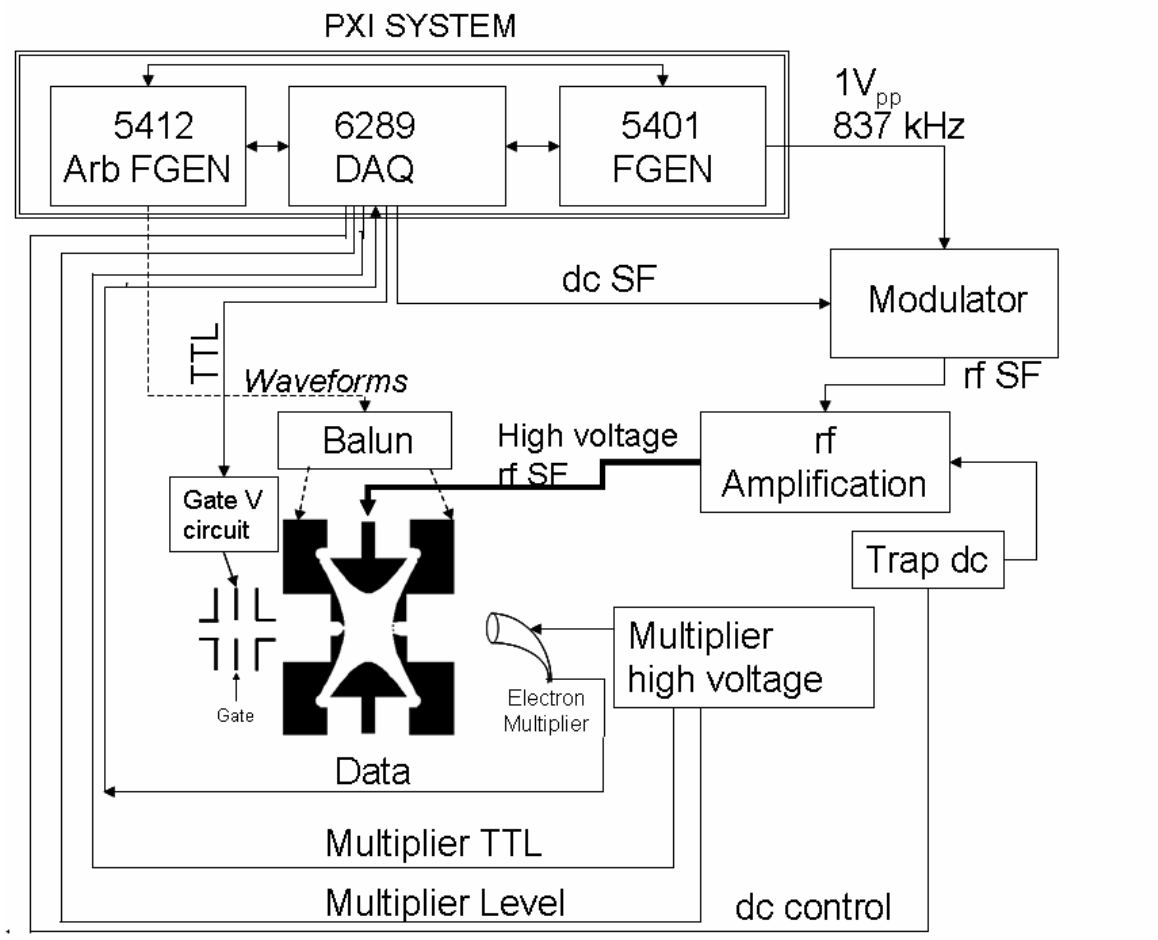

Figure AI.6 – Block diagram of instrument control system.
SF-scan function

The timing and synchronization of the PXI-cards is an important aspect of instrument control. The PXI-5401 is treated as a stand alone device during this software. Ideally this card would be synchronized with the scan function and the PXI-5412; however, due to device driver limitations this was not possible. The analog output, digital output, and the analog input must each be separately configured even though they are all performed from the same device. The analog output is generated from a n × 4 array that is written to the memory of the analog output card. The values for this array are described in **Section AI2.2.1.** The digital output is configured so that all 32 lines are set with one number. As described in **Section AI2.2.1**, an array of nine bit numbers representing TTLs and other digital triggers is generated from the full scan array. By writing to all of the digital lines at once (n element 1-D array) instead of all lines separately (n x 9 2-D array) the random access virtual computer memory used and the time it takes to write the array to memory is drastically reduced. The analog output and digital output operate using the analog output sample clock. The digital output starts when the analog output clock starts. The analog input can be configured to use the analog output clock or the analog input clock. When the analog output clock is used the input data rate is forced to be the same as the analog output rate, which may result in more points per peak than are necessary. The number of points can be decreased by changing the analog input to use a slower clock. The analog input is triggered with one of the digital output lines (PO.3). This digital line is wired on the 68LPR terminal block to the programmable function input (PFI.0), which is what the analog input is triggered with. Because the digital lines are output using the analog output clock, mis-triggers can occur when the analog input does not use the analog output clock. To remove mis-triggers the analog output is read back in and compared to the output. If they do not match then the scan

is restarted until the output and input match. The waveforms for the PXI-5412 are loaded onto the card individually. Each output from the PXI-5412 is then triggered with a digital output. This digital trigger corresponds to the user having "checked" the waveform to be on during a particular scan segment.

AI3.3 Runtime.llb

AI3.3.1 Runtime GUI

The instrument control and data acquisition software, Runtime.llb, is designed to allow the user to stop and start the scan function, acquire the mass spectrum, display the real time data, save the data, update the scan function, update the waveforms, and calibrate the mass spectrum. The GUI for the program is shown **Figure AI.7**. The GUI has a window for displaying the full mass spectrum and zoom window to show a selected range. Below these windows are a set of four tabs: scan function editor (**Figure AI7a**), acquire (**Figure AI7b**), waveform editor (**Figure AI7c**), and plot scan function (See **Section AI2.2**). The build scan function editor tab, waveform editor tab, and plot scan function tab contain a subpanel that links to the appropriate program. The build scanfunction.llb and plot scan function.vi were described in **Section AI.2.2**. The waveform editor.llb will be described in **Section AI3.3.3**.

AI3.3.2 Software operation

When the software is run a popup window appears from "operator start2_0".vi, which allows the user to select the operator. This subprogram uses a .ini file to store the file paths for data, waveform, and scan function directories used by each user. After the user is selected, the runtime program reads from the BSF.ini to determine the operating frequency of the rf voltage. The PXI-5401 is then configured and started. The scan function is then

a)

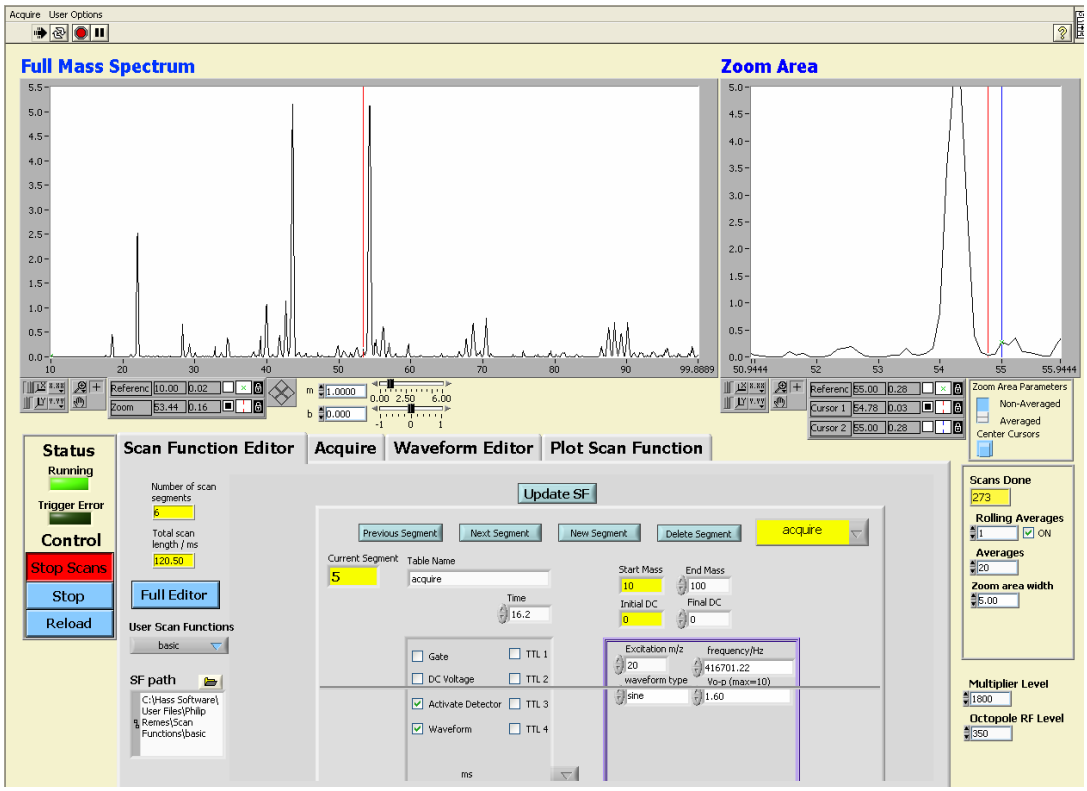

b)

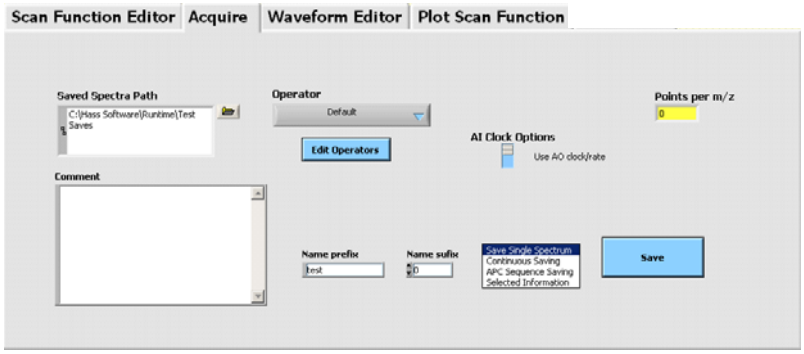

c)

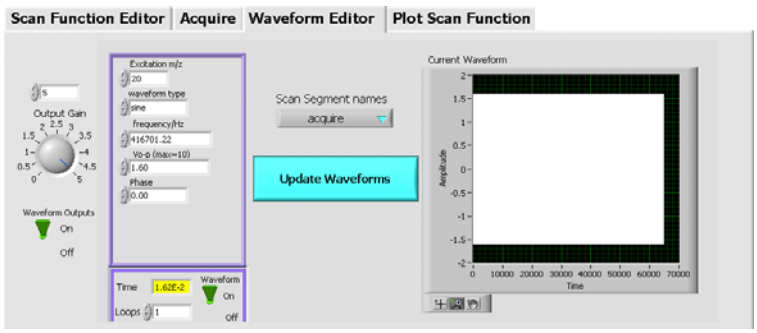

Figure AI.7 – GUI for Instrument Control and Data Acquisition Software a) Scan function editor tab, b) acquire tab, and c) waveform editor tab.

loaded, the scan array is created and the digital waveforms are created from a portion of the scan array as described in **Section AI2.2.** The program then operates in a while loop and using a “click event” waits for the user to start the scan. Once the “Start Scans” button is pushed, the PXI-cards are configured and if no errors are found the PXI-cards are started. The analog output function is started last because the digital output starts with the analog output, and both the waveforms and the analog input are triggered with digital outputs. The mass spectra that are acquired are averaged and displayed in the mass spectrum and zoom windows. The user can save a single mass spectrum or a continuous file of mass spectra. The user can also start an APC scan which automatically updates the scan function and acquires the data in predetermined incremental values as described in **Section AI.2.3**. When an APC is enabled, the user can save an APC sequence set of data, if it is disabled this saving option is not enabled. By clicking over to the scan function editor tab the user can manually update the scan function. After updating the scan function the user can click the update SF button. This button triggers a “click_event” that the runtime.llb program recognizes because this click event is a global “click_event”. This event causes the runtime.llb to stop scanning, reload the scan function, and the return to acquiring mass spectra. The system will run continuously until the user pushes “Stop Scans”. The user may then stop the program or start scanning again. The hierarchy of the subprograms used by the runtime.llb is in **Figure AI.8**. **Table AI.3** contains a list and description of the subprograms used by the runtime.llb program.

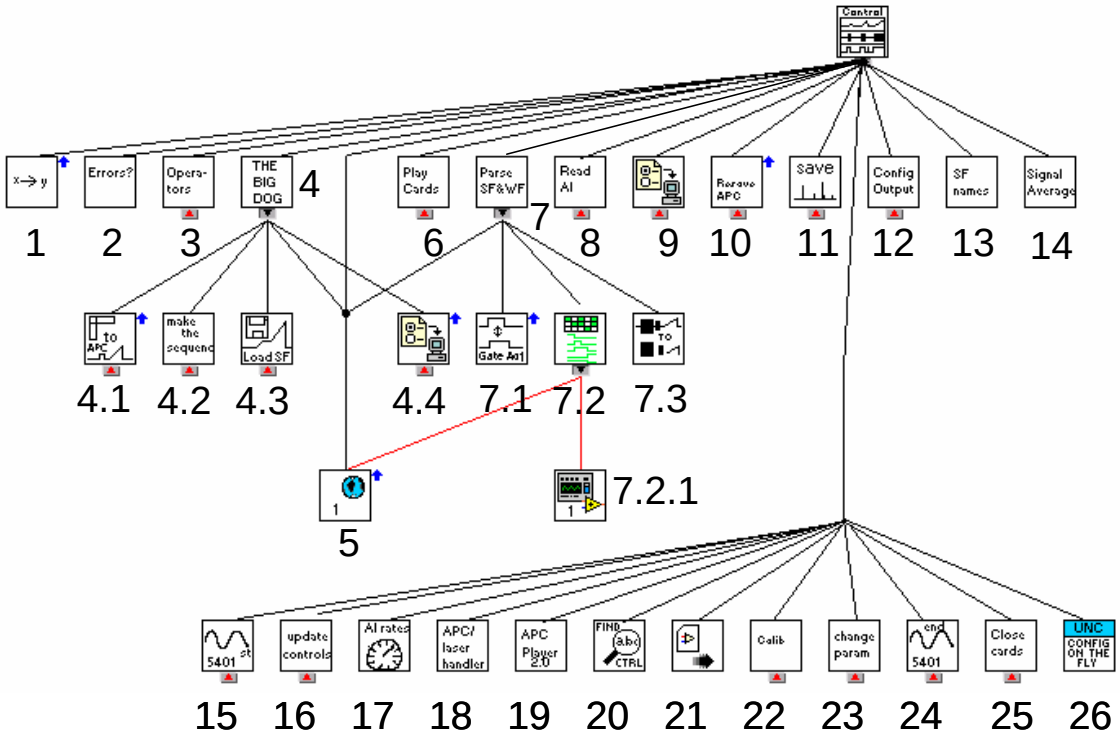

Figure AI.8 – Hierarchy for instrument control and data acquisition software.

#	Program name	Description
1	Converter.vi	Corrects mass scale using input calibrations
2	Errors.vi	General Error Handler
3	Operator_start2.0	Select User and Scan Functions (Pop up)
4	Load and Build all.vi	Opens scan function, APC sequence, and other calibration settings
4.1	Update SA and WF_2.vi	Creates scan array and builds waveforms
4.2	APC generator_2.vi	Creates the steps and APC array
4.3	LoadSF.vi	Opens the scan function.csv
4.4	reac_config_BSF.ini	Reads BSF.ini file which has user variables and default global variables
5	Global Variables	Globabl Variables written from build scan function
6	Play cards.vi	Starts the analog, digital, and waveform cards
7	Parse SF_4.vi	Separates out the nx13 array into a nx4 and nx9 array
7.1	Gate Adjust.vi	Adds a set amount of time (300 msec def.) to any segment with Gate checked
7.2	Generate DW_2.0.vi	Converts nx9 array of 1 and 0's to a 1x9 array of binary numbers (see text)
7.2.1	Gate_waveform adjust.vi	Removes the small time added by Gate adjust from the digital waveforms, also adjust length of waveform triggers to a % requested by user from .1 - 100% allowed
7.3	Waveform_pullout_2	Segments individual waveforms out of full concatenated waveforms. Also returns number of points in each waveform
8	Readi_ai3_0.vi	Reads data from analog input as binary, converts to decimal outputs header information and 2-D data array. Also checks that the input ramp matches the AO, if not then send out Boolean for mis-trigger.
9	Read_Operater.vi	Reads in directory paths from the operator.ini file
10	Resave APC for copying.vi	Opens APC sequence and resaves it with the copied scan function name
11	Save Spectrum 3_0.vi	Saves the data for single save, continuous save, and APC save modes
12	Setup Output.vi	Configures the analog out, analog input, digital output, and arbitrary function generator.
13	SF directories.vi	Changes the path of the scan function directory and verifies that the SF exists in the new directory
14	Signal Averaging.vi	Averages input data using standard averaging or rolling averages
15	Start 5401.vi	Configures and Starts the rf Function Generator
16	Update controls.vi	Updates the screen displays of the multiplier and octapole voltages from the dc control voltage in the analog output

17	AI possible rates.vi	Determines the possible AI rates based on the AO rate. The only possible AI rates are ones that are divisible into the AO with no remainders
18	APC and Laser Boolean Handler.vi	This vi checks to see if an APC is active and if the SF needs to be updated The output Boolean is sent to the vi # 19
19	Automated paramter control player 2.0.vi	Determines the next set of variables to be changed in a APC sequence
20	BSF_Find Controlbyname.vi	Allows for communication between APC and small plot of scan function
21	BSF_LoadandRun.vi	Calls BSF, waveform editor, plot scan function for subpanels
22	Calibration.vi	Calibrates the mass scale based on the cursor positions I the zoom window 1 point calibration
23	Change Parameter.vi	Updates the scan function when using APC and updates the voltages when multiplier or octapole voltages are changed by user
24	Close 5401.vi	Closes the handler for the rf function generator and stops it from running
25	Close Card.vi	Closes and stops the 6289 and 5412 cards.
26	Config on the fly_UNC.vi	Allows the user to update the amplitudes of all of the waveforms in real time

Table AI.3 - List and description of subprograms for **Figure A1.8**.

AI3.3.3 Waveform editor programs

These two programs are only used by the runtime.llb program. They are displayed in subpanels on the waveform editor and calibrate tabs in the runtime.llb program. The waveform editor shows the waveforms associated with each scan segment, regardless of whether they are turned on or off. The user can then quickly adjust the amplitude of the individual waveform, change the waveform type, and turn on or off an individual waveform. When the user is done, the update waveforms button is pushed. This button triggers a global "click_event", which causes the runtime.llb to stop scanning, reload the scan function, and return to acquiring mass spectra.

AI.4 Data Analysis Software

The data analysis software allows the user to quickly display and analyze the data that was saved with the data acquisition software. Two versions of the data analysis software were written to analyze the two different data formats that are acquired using the software described in **Section AI.3**. The first data format is just a single mass spectrum, and is a simple comma delimited or space delimited file. The second data format is from continuously saving mass spectrum. In this file the ion abundance data is stored in a continuous stream and is saved in a binary format to keep the file sizes small. The two versions of the software are called Data Analysis for single mass spectrum and Data Analysis Chronogram for continuous mass spectra. **Figure AI.9, Figure AI.10, Figure AI.11** are the GUIs for the Data Analysis, Data Analysis Chronogram programs and extra tabs, respectively. Each of the programs are separate and are not directly integrated with the experimental design or the instrument control software. An additional feature of these two programs is that they were modified to read in data from other instruments in the Glish Lab. The instrumental data that can be analyzed with this software are the CCIT, Finnigan ITMS^{TM}, Bruker Esquire, and the custom QITMS described in **Section AI.3**.

AI4.1 Data Analysis.llb

This program has several features beyond displaying the mass spectrum. Some features are only available for the custom QITMS and the CCIT. The user can recalibrate the mass scale, average several mass spectrum together, batch process several mass spectra, automatically detect peaks in the mass spectrum, manually add peaks to a list of peaks, remove peaks from that list of peaks, save the calibrated mass spectrum, save the peak list,

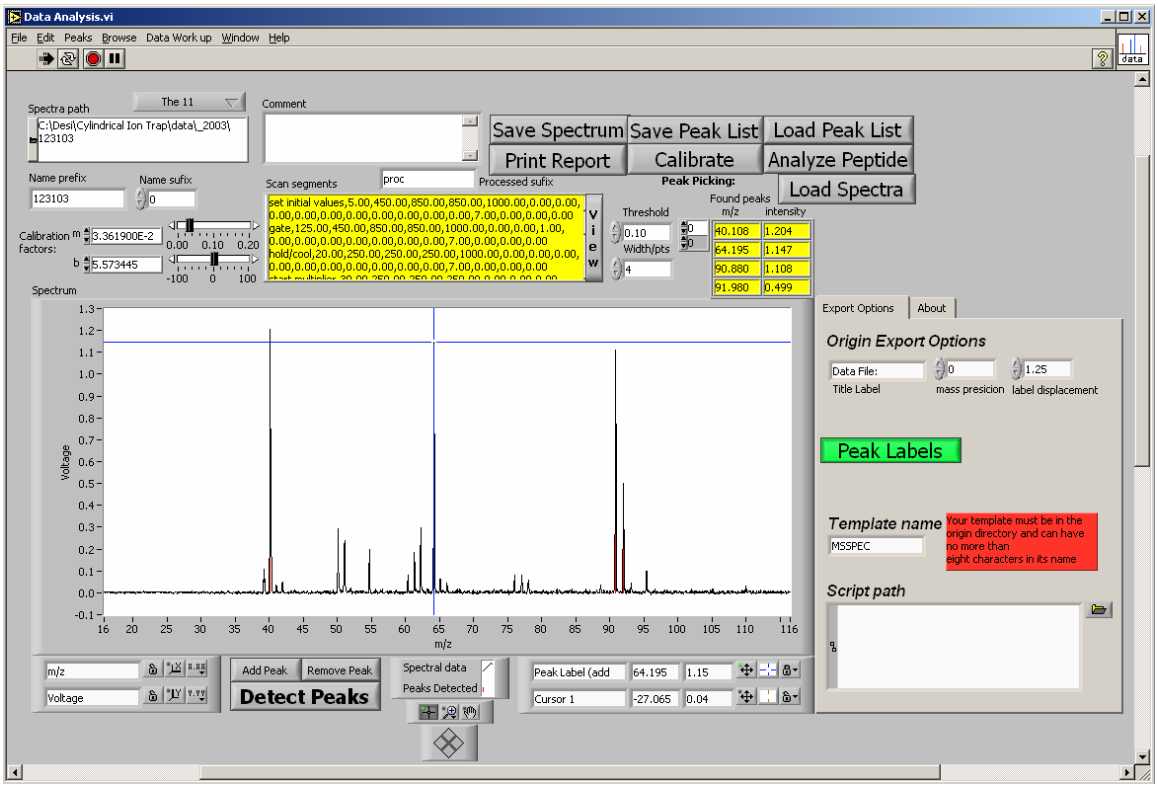

Figure AI.9 – GUI for data analysis software.

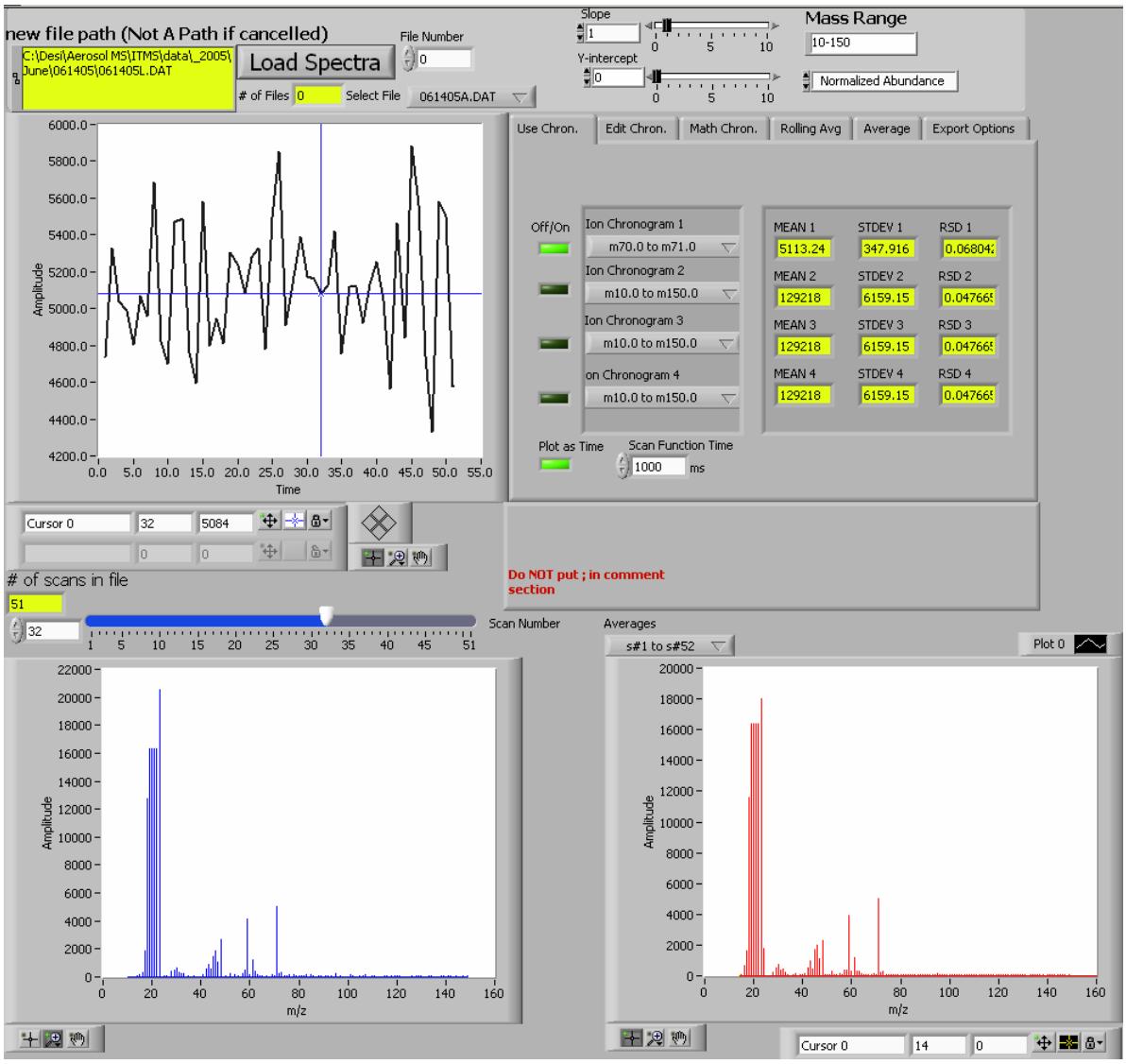

Figure A.10 – GUI for Data Analysis Chronogram.llb illustrating the “use chron.” tab.

a)

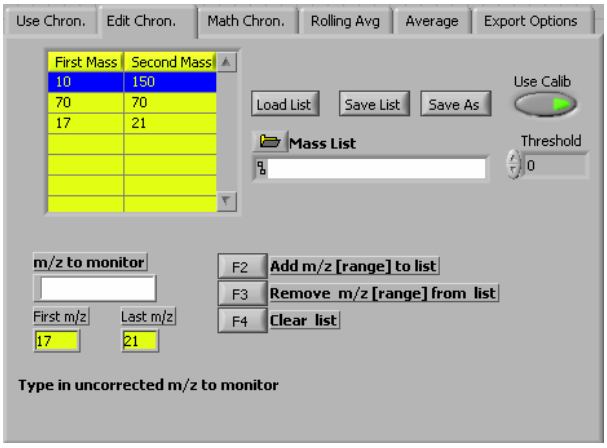

b)

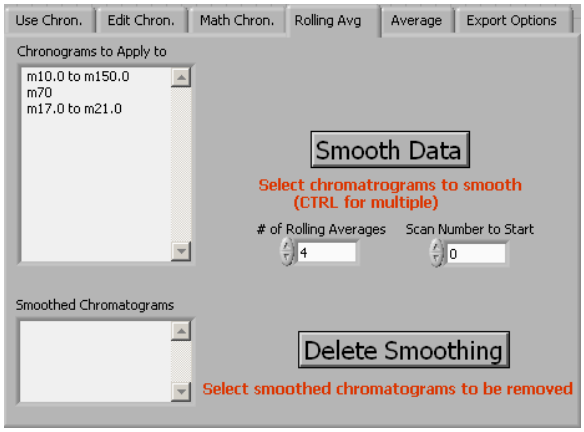

c)

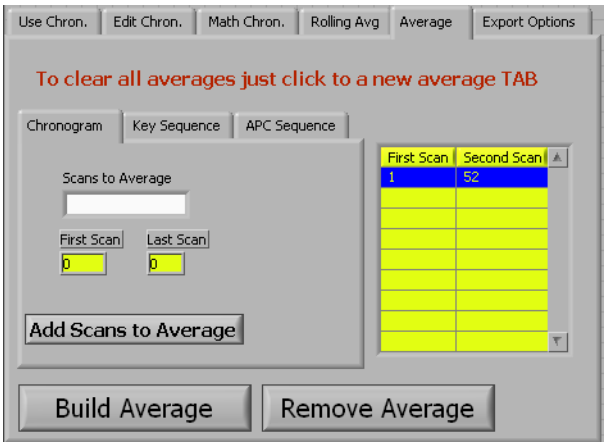

d)

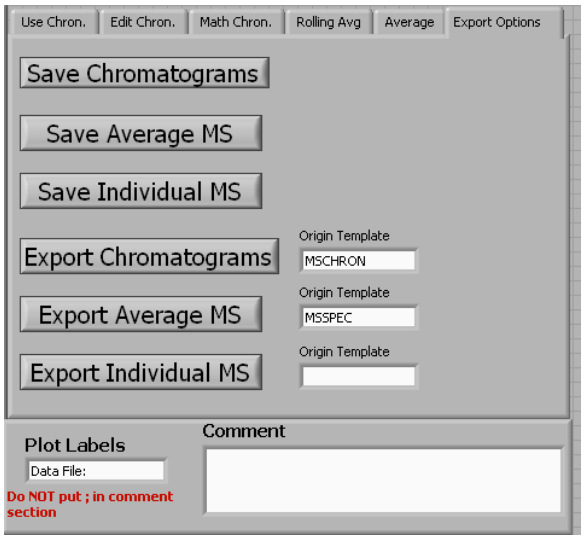

Figure A.11 – GUI for Data Analysis Chronogram.llb illustrating a) “Edit chron.” tab b) “Rolling avg.” tab, c) “Average” tab, and d) “Export options” tab.

and export the data to Origin™ graphing software (Origin Labs). Some additional features, only available to the CCIT, are printing a report which includes the saved scan function and viewing the scan function using the Build Scan Function.vi described in **Section AI1.1**.

Before running the software the user selects the instrument that was used to acquire the data. After running the software the user selects which data files are to be analyzed by pushing the "Load Spectra" button. The program then opens the data file and displays the first mass spectrum. The data is stored in a n × 2 array, where n is the number of points in the mass spectrum and the two columns are the mass scale and the ion abundances. The program operates in a while loop waiting for the user to push a button. Once a button is pushed, the programming operation associated with that button is performed and the program returns to the while loop. The hierarchy of the subprograms used by the Data Analysis.llb is shown in **Figure AI.12**. **Table AI.4** contains the list and descriptions of the main subprograms used in Data Analysis.llb.

AI4.1.1 Export to Origin

Data can be exported to Origin graphing software and plotted with in this software. This is done by creating a client server protocol with Origin, called a data dynamic exchange (DDE). Origin is opened and a spread sheet is created. A 2-D array, which contains all of the necessary information to create a mass spectrum, is transfer to the spread sheet. Origin has a programming language, referred to as LABTALK ©, that allows the user to programmatically plot data. These programs are written in text form in Lab VIEW and then executed through the DDE connection. Once the plot is made, the DDE client server connection is broken and all temporary files are deleted. The program "export to origin.vi" written in Lab VIEW, which calls and executes the scripts, allows the user to input a file path

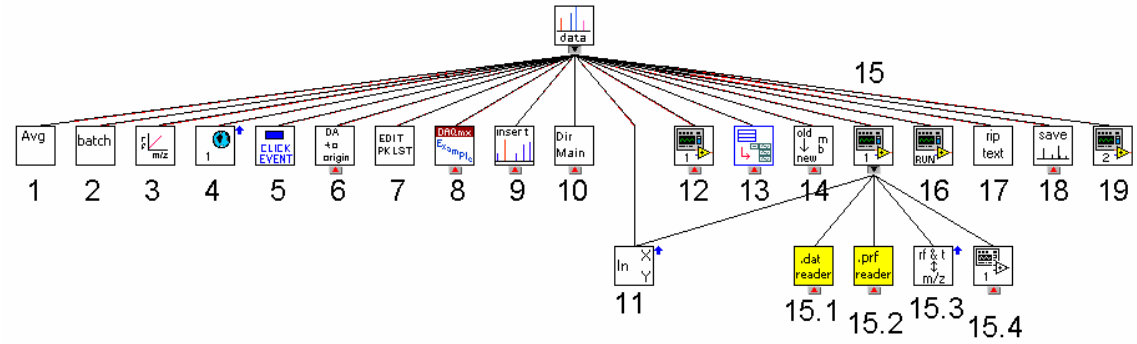

Figure AI.12 – Hierarchy for data analysis software.

#	Program name	Description
1	Average Scans_DA.vi	(Pop up) Allows user to select which files to average together. The data is then averaged and a new spectrum is created and exported to origin in the main program
2	batch.vi	(Pop up) Allows user to select which files to batch process. The mass spectra for all files selected are exported to origin
3	calibrate.vi	(Pop up) Allows user to recalibrate mass spectrum using selected peaks in peak list. Assign expected values with observed then uses vi # 14 to recalibrate.
4	CCITGLOB.glb	CCIT global variables
5	Click_Event_DA.vi	Determined what action was performed by the user
6	csv to Origin.vi	Exports data to origin graphing software using data dynamic exchange scripts
7	Edit Peak List.vi	Allows the user to remove peaks from the peak list
8	haas DA.vi	Reads and converts data acquired with runtime software described in **Section AI.3**
9	In_out.vi	Pulls out X and Y columns of 2-D array coming from a spreadsheet file
10	Insert peaks.vi	Adds peaks to array of peaks based on graph curser position
11	main.vi	For ITMS and Bruker popup asks user if files are coming from one directory or multiple. An array containing the path of files in the directory is returned. If multiple files is selected uses vi # 13.
12	Make Report.vi	Only works for CCIT. Creates printout report based on scan function
13	Multiple File Selector.vi	Allows user to select multiple files from multiple directories. An array of the paths for these files is returned.
14	oldmb_newmb.vi	Recalibrates mass scale based on old and new calibration
15	Open Files	Opens the data files from the different instruments
15.1	DAT data reader.vi	Reads EXP binary data from ITMS
15.2	PRF data reader.vi	Reads space delimited profile data from ITMS
15.3	rf and movers and conversions.vi	Gives the increment and start values so the x-axis can be created for the CCIT
15.4	Bruker TIC.vi	Opens data from the Bruker (must be MSP data)
16	Open fp and run.vi	Opens CCIT build scan function for viewing the scan function.
17	rip text.vi	Pulls out the comment from the data file for the CCIT
18	Save Spectrum.vi	Saves the mass spectrum to a file or updates the saved spectrum comment and calibration
19	type ripper.vi	Removes the .Dat and .Prf extensions from the file names

Table AI.4 – List and description of subprograms for **Figure A1.12**.

for a text file which is the script. This external introduction of a script prevents the user from having to modify the export to origin.vi each time they wish to update their script.

AI4.2 Data Analysis Chronogram

Data Analysis Chronogram analyzes mass spectra that were taken continuously over a period of time. The over all mass spectra are essentially a 3-D mass spectrum of abundance versus *m/z* versus time, with each time segment being one mass spectrum. As shown in **Figure AI.10 t**he program GUI has three plots in it. The upper left plot is for ion chronograms, which are the abundance of an ion(s) as a function of time. The ion chronograms are selected using the on/off buttons and the drop down list boxes in the "Use Chron." tab. This tab also shows the average, standard deviation, and relative standard deviation for the selected ion chronogram. The ion chronograms are created by entering in the mass range and clicking add on the "Edit Chron." tab (**Figure AI.11a)**. A rolling average of the ion chronograms can be created using the option on the rolling average tab (**Figure AI.11b)**. The lower left plot displays the mass spectrum at each time segment. The user can change the displayed mass spectrum by dragging the slider bar or moving the cursor in the ion chronogram plot window. The lower right plot displays the average mass spectrum. The averages are creating by specifying the number of scans (or time) to average on the Average tab (**Figure AI.11c)**. Note the math tab is currently not in use. This tab was intended to allow the user to perform simple mathematical operations to selected ion chronograms. The individual mass spectrum, average mass spectrum, and all of the ion chronograms can be exported to origin or saved to comma delimited files (**Figure AI.11d**).

The hierarchy of the subprograms used by the data analysis chronogram.llb is shown in **Figure AI.13**.

Table AI.5 contains a list and description of the subprograms used in the Data Analysis Chronogram program.

The program operation of the Data Analysis Chronogram was updated from the Data Analysis.llb software. This program uses the “click event” structure that is described in **Section A1.2** instead of the simple while loop based user interface that the Data Analysis.llb uses. The other differences are that once the data file is opened, the data is stored as a y × n × 2 array, where y is the number of mass spectra acquired and n are the number of points in a mass spectrum. A selected ion chronogram is extracted from the 3-D array by summing the ion abundances over the selected range for each of the y mass spectra. All of the ion chronograms are stored in memory as an array with dimensions y × z, where z is the number of selected ion chronograms. When average mass spectra are created they are stored as a m × n × 2 array, where m is the number of average mass spectra created. When a file is loaded an average of all the mass spectra is created, this average mass spectra initialized the 3-D array so that it is a 1 × n × 2 array. Rolling averages are stored as new ion chronograms with the prefix “sm_” added to the averaged ion chronogram’s name.

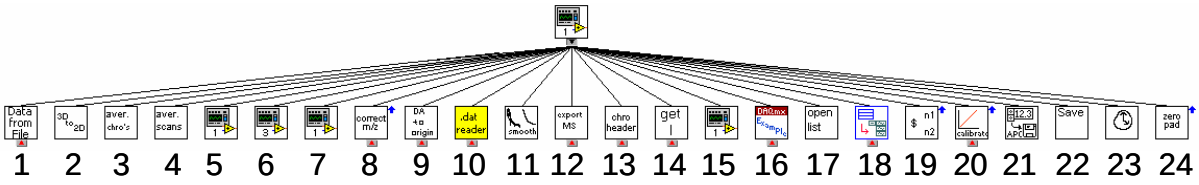

Figure AI.13 – Hierarchy for data analysis chronogram software.

#	Program name	Description
1	11_data_continousdata_open.vi	Opens the continuous data acquired on the CCIT
2	3Dto2D.vi	Turns the 3-D MS array into a 2-D ms array where column 1 is the mass scale and all subsequent columns are the ion abundances of the mass spectra
3	Average Chronograms.vi	Averages portions of an ion chronogram based on a key sequence of APC sequence.
4	Average Scans.vi	Created the average mass spectrum from a selected number of scans
5	Bruker Chrnogram reader.vi	Reads in continuous data from the Bruker
6	Chronoonoff.vi	Builds the ion chronogram plot seen in **Figure A.10**. When ion chronograms are not selected they are not put into cluster array that is sent to the plot
7	Column_header_for_origin.vi	Builds a script that creates the column header in origin. The header represent the masses that were selected for the ion chronogram
8	Correct mass.vi	Recalibrates the mass scale for the ITMS data
9	csv to origin.vi	Exports the chronogram data, mass spectra, or average mass spectra to origin. Different data dynamic exchange script for each mode.
10	DAT data reader.vi	Reads in continuous EXP binary data from ITMS
11	Data_smooth.vi	Performs rolling average on selected on chronograms
12	Export_Items.vi	Allows the user to export multiple mass spectra from the full set of scans
13	Get Average Output Header.vi	Creates the string header representing the scans that were average together
14	Get Intensities.vi	Generates the selected ion chronograms for the selected mass ranges
15	Get_File_String_name.vi	Removes the full path from the files and just returns an array of the file names
16	hass Da_chron1.vi	Opens the continuous or APC data saved with the runtime software described in **Section AI.3**
17	Loadmass.vi	Loads the list of masses used to make the ion chronograms. The ion chronograms are then created in the main program

18	Multiple file sleector	Allows user to select multiple files from multiple directories. An array of the paths for these files is returned.
19	Parse Simple String 2.0.vi	Takes a string "123 - 125" and separates it into two numbers, 123 and 125
20	recalibrate.vi	Calibrated the mass scale based on the user changing the slope and the intercepts
21	Save_APC.vi	Saves ion chronograms or average mass spectra to a comma delimited file
22	Saving.vi	Saves the list of masses used to make the ion chronograms
23	Time_Scan_conversion.vi	Converts the x-axis of the chronograms to time based on the input time of the scan function
24	Zero Pad.vi	Adds zeros around the data points for the ITMS to make displaying the data easier

Table AI.5 – List and description of subprograms for **Figure A1.13**.

Appendix II

Mechanical Drawings and Circuit Diagram

This appendix contains various mechanical drawings that were used in the construction of necessary equipment for the experiments described in chapters 2, 3, and 6. Unless otherwise noted on the drawing, the materials for a given device are listed in the figure caption for that device. Each figure caption refers back to the section in which the device was described or first mentioned. For the circuit diagram provided for a power amplifier a description will be provided, which is more detailed than when the circuit was described in the **Chapter 2**.

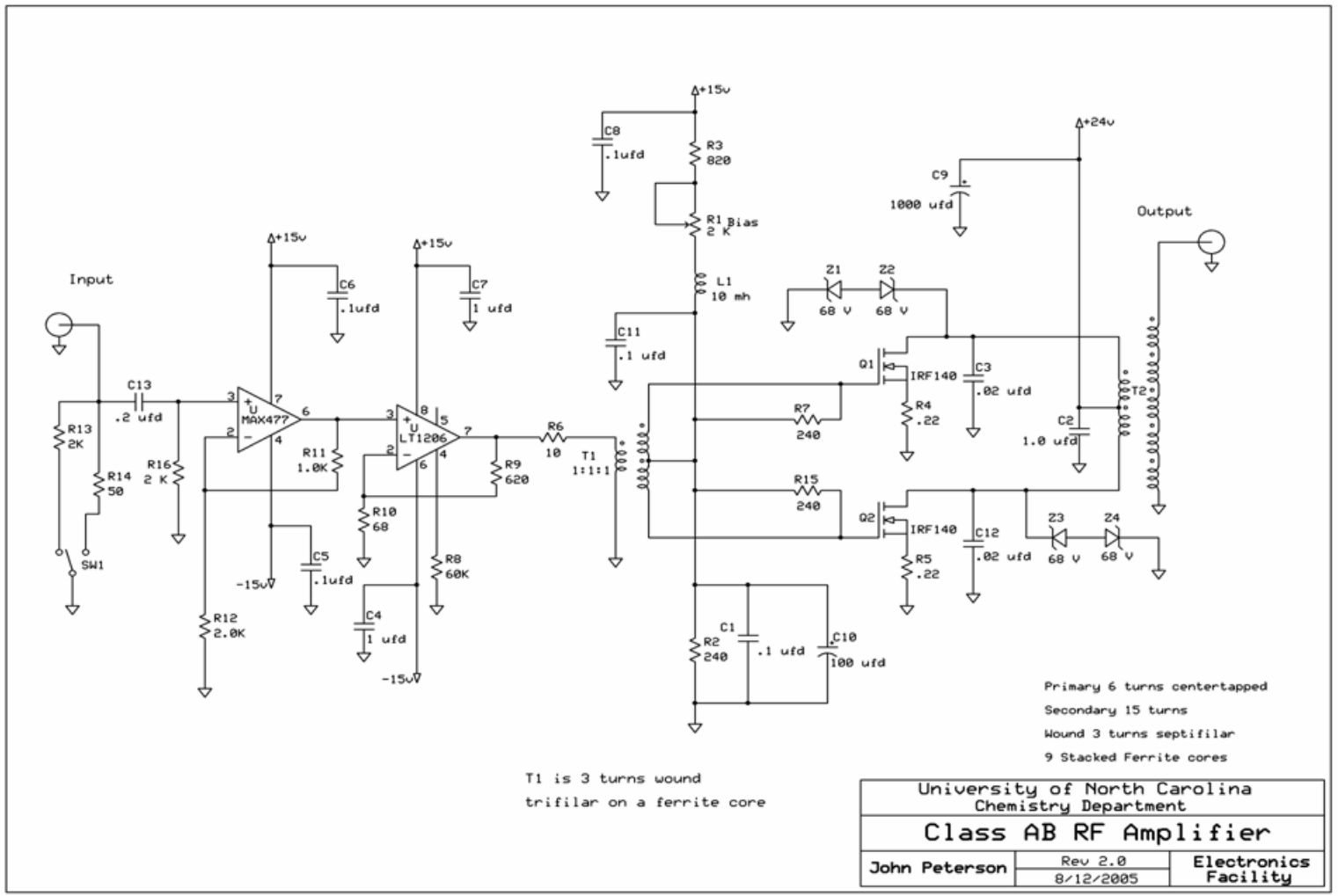

Figure AII.1 – Circuit Diagram of Electronics Design Facility Class AB rf Amplifier described. in **Section 2.3.3**

AII.1. Description of rf amplifier

The Electronics Design Facility built rf amplifier generates rf power using the latest integrated circuit technology and power MOSFET output devices. The driver stage consists of a Linear Technology LT 1206 current feedback operational amplifier operated at high quiescent current and components selected to give a voltage gain of 10 and a 0.1dB bandwidth of 35 MHz. The energy is coupled to the final output stage using a transformer wound upon a ferrite core, using a turns ratio optimized to transfer power from the driver stage to the output stage.

The final output stage consists of two MOSFET transistors driven in a push-pull arrangement with the output power being coupled to a transformer wound upon a ferrite core. Bias voltage for the gate of each MOSFET is adjusted individually by adjustable potentiometers to compensate for the fact that the threshold of each transistor may vary due to manufacturing tolerances. The bias voltage that supplies the bias potentiometers is provided by a regulator that has four silicon diodes in thermal contact with the heatsink. The diodes provide a reduction of the bias voltage with temperature rise in the heatsink, the variation being around 8 mV less per degree Centigrade rise in the heatsink temperature. Radio frequency power is developed across the primary winding of the output transformer, which consist of a single turn and four turns for the secondary. Ferrite cores are used in the output transformer and the winding ratio gives an output impedance of 50 ohms. Power outputs of more than 100 watts are easily achieved, with low distortion, over a bandwidth form 500 KHz to 10 MHz. The design is robust and free from spurious artifacts.

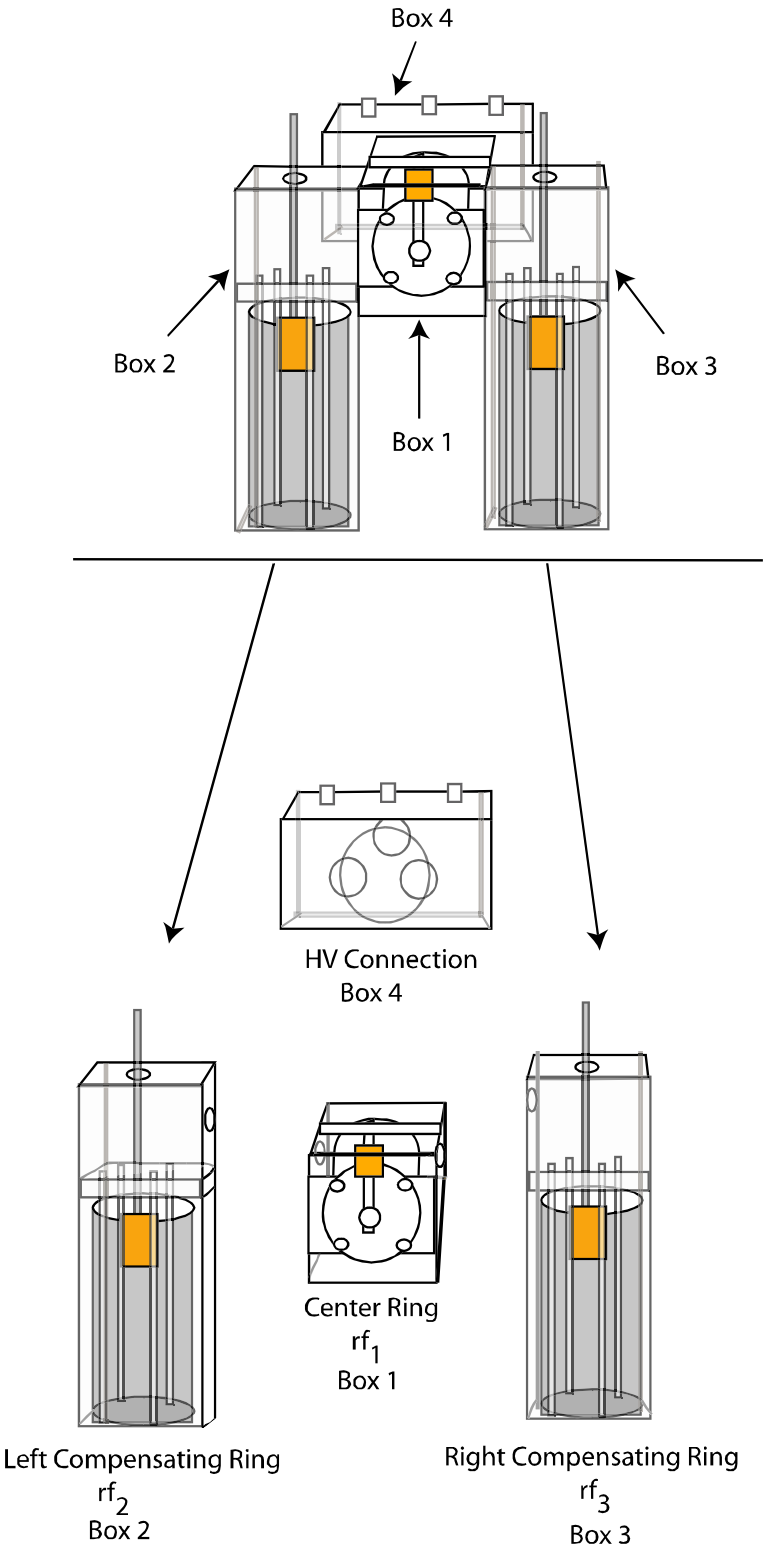

Figure AII.2 – Exploded view of enclosures for second generation rf circuitry used to operated a compensated cylindrical ion trap mass spectrometer described in **Section 2.4**.

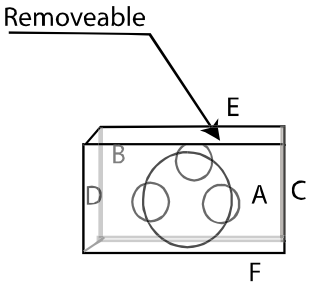

Face Legend for Box 4

Face A is the front face connects to Box 1
Face E is the top face and is removeable
Face F is the bottom face
Face C and D are sepearate faces
Face B is open to high voltage ceramic feed throughs

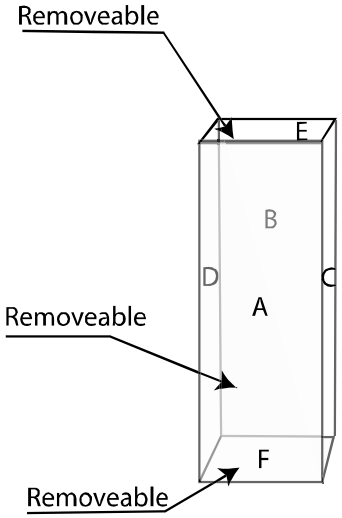

Face Legend for Box 1-3

Face A is the front face and is removable
Face E is the top face
Face F is the bottom face
Face B, C, and D are bent from one piece of sheet metal
Box 2: Face C connects to Face D of Box 1
Box 3: Face D connects to Face C of Box 1
Box 1: Face F connects to Face A of Box 4

Figure AII.3 – Legend describing faces of rf enclosure described in **Section 2.4**.

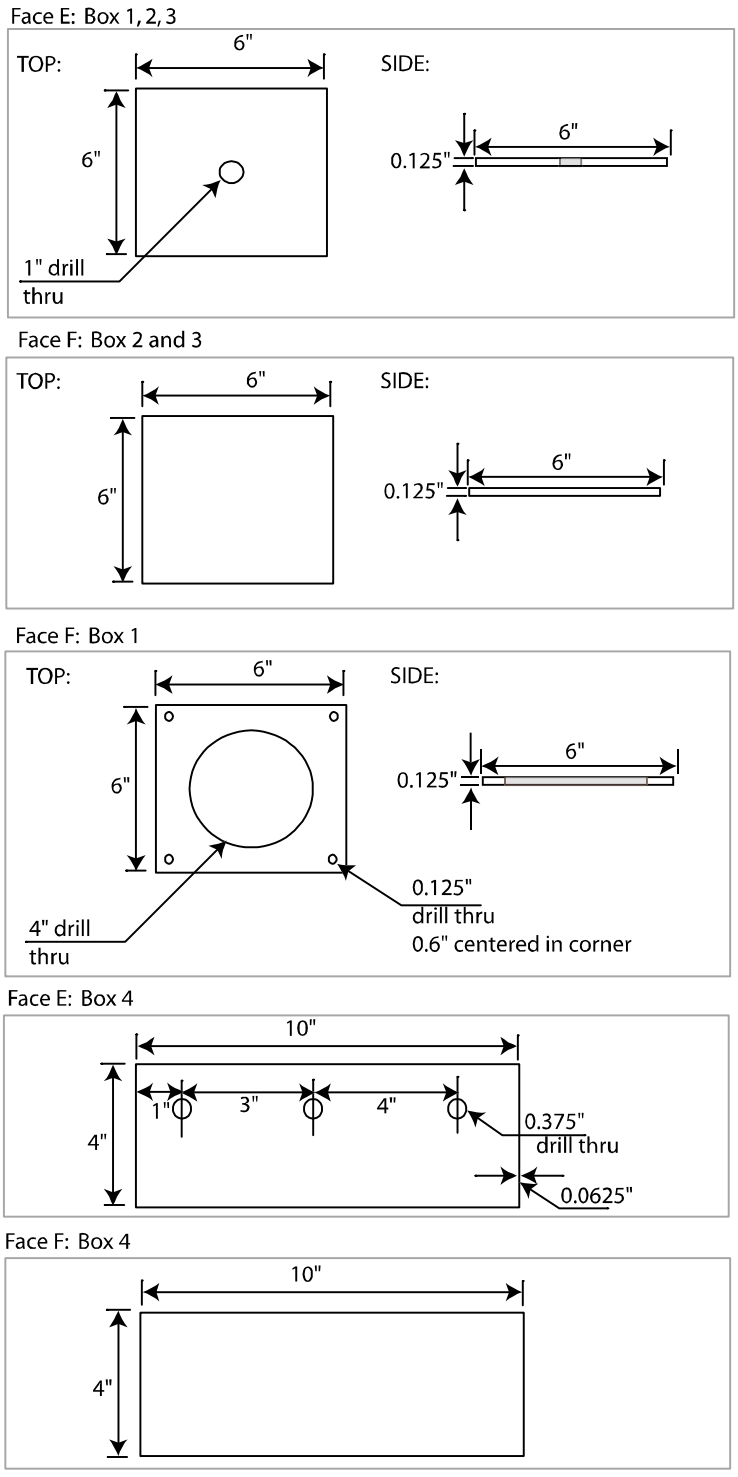

Figure AII.4 – Mechanical drawings of rf enclosures described in **Section 2.4**.

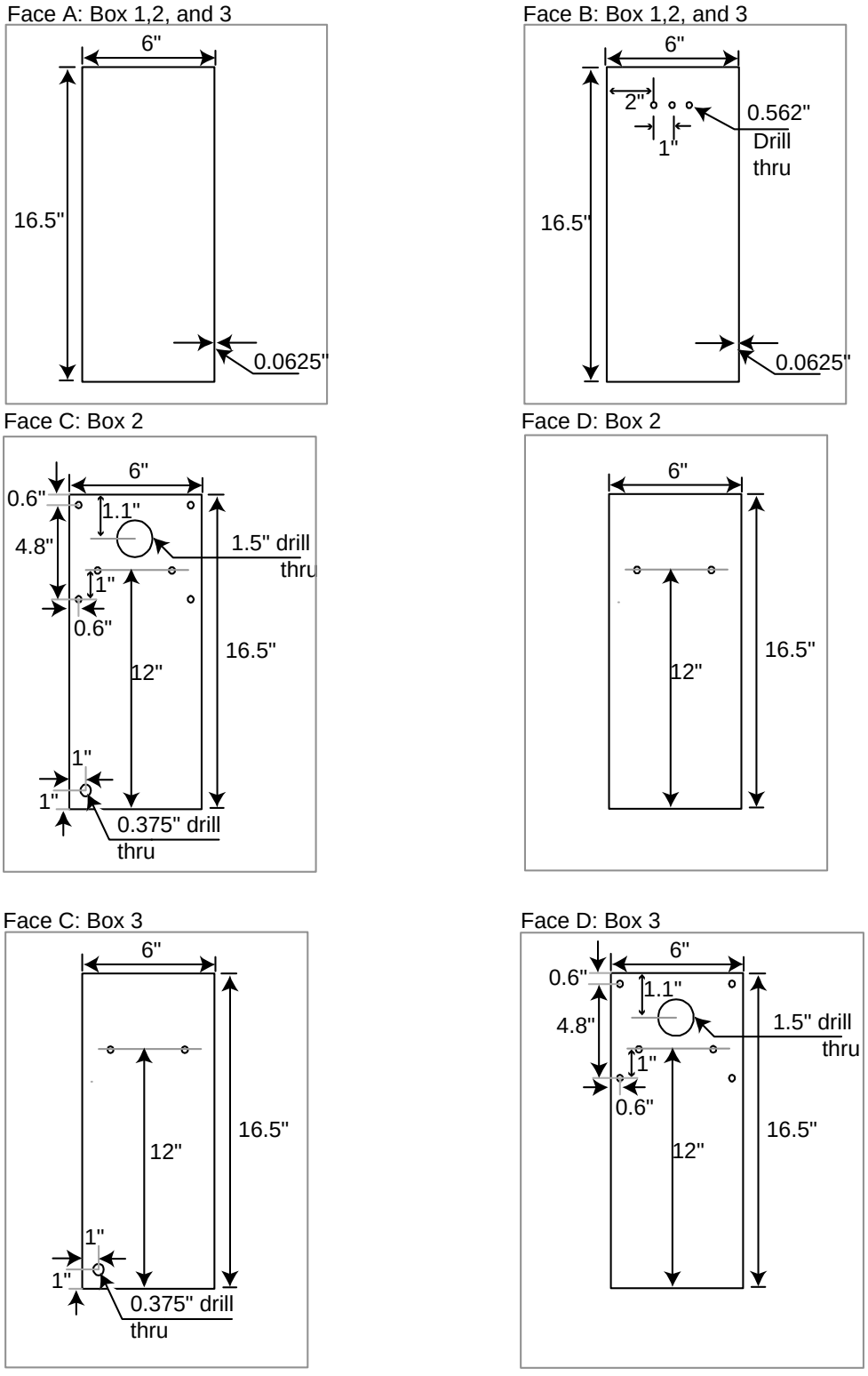

Figure AII.5 – Mechanical drawings of rf enclosures (continued) described in **Section 2.4**.

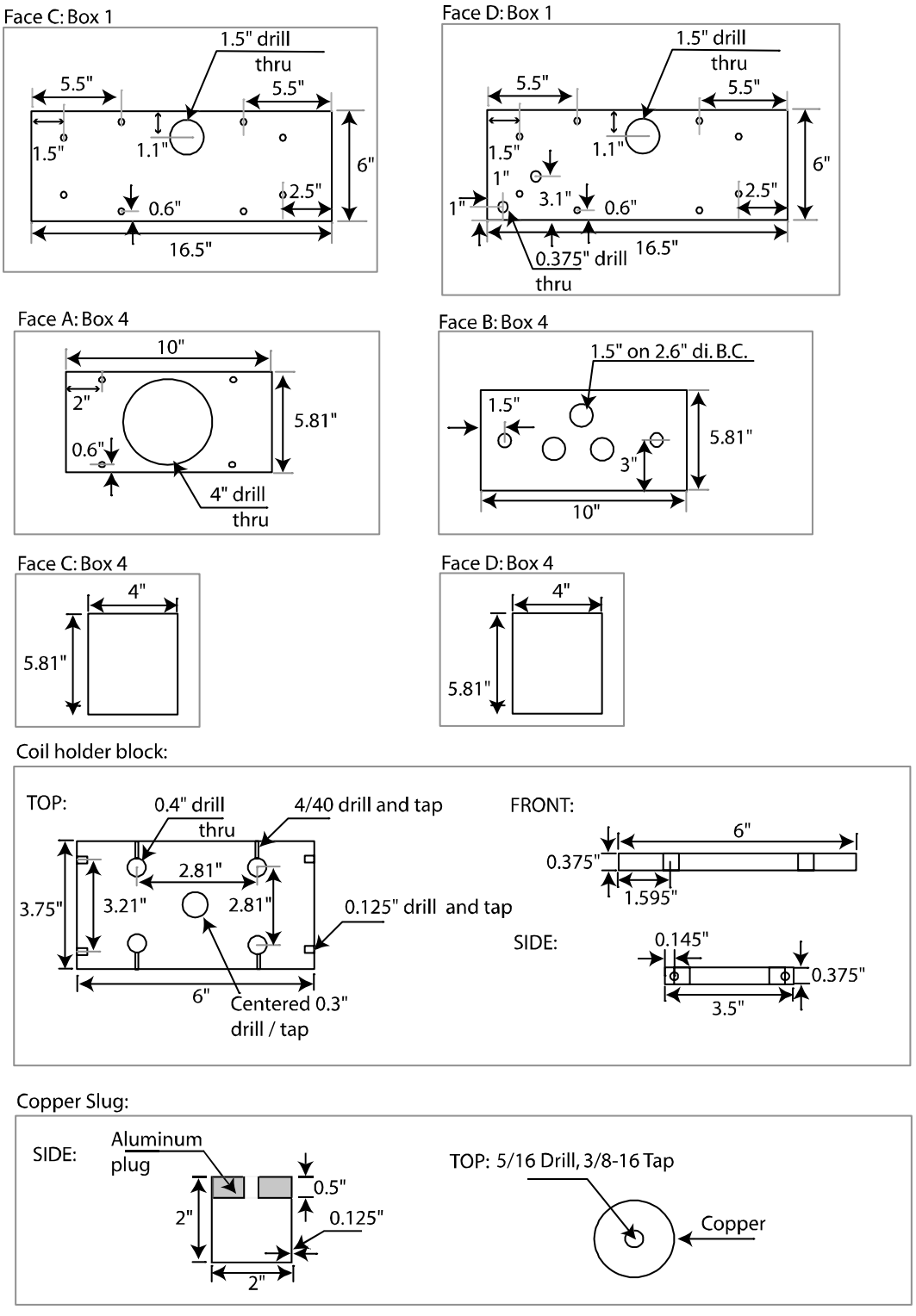

Figure AII.6 – Mechanical drawings of rf enclosures (continued), Coil holder block, and Copper slug described in **Section 2.4**.

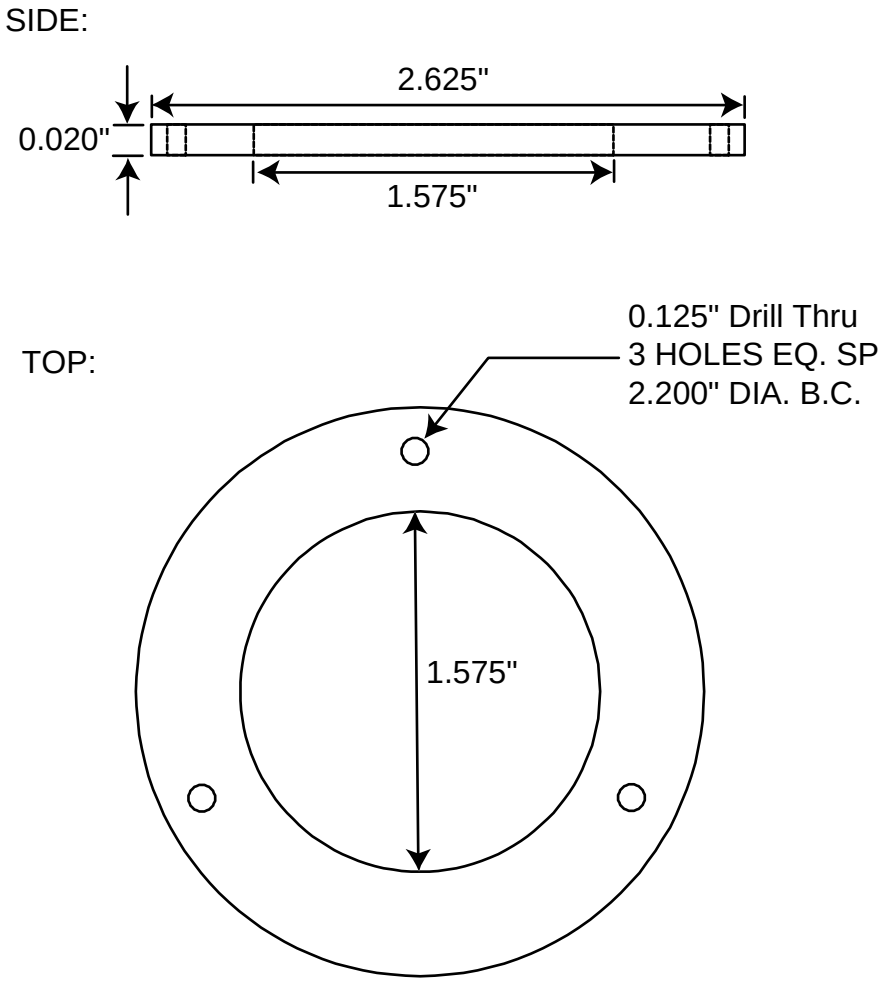

Figure AII.7 – Shielding electrodes for compensated cylindrical ion trap mass spectrometer, described in **Section 2.8.3**.

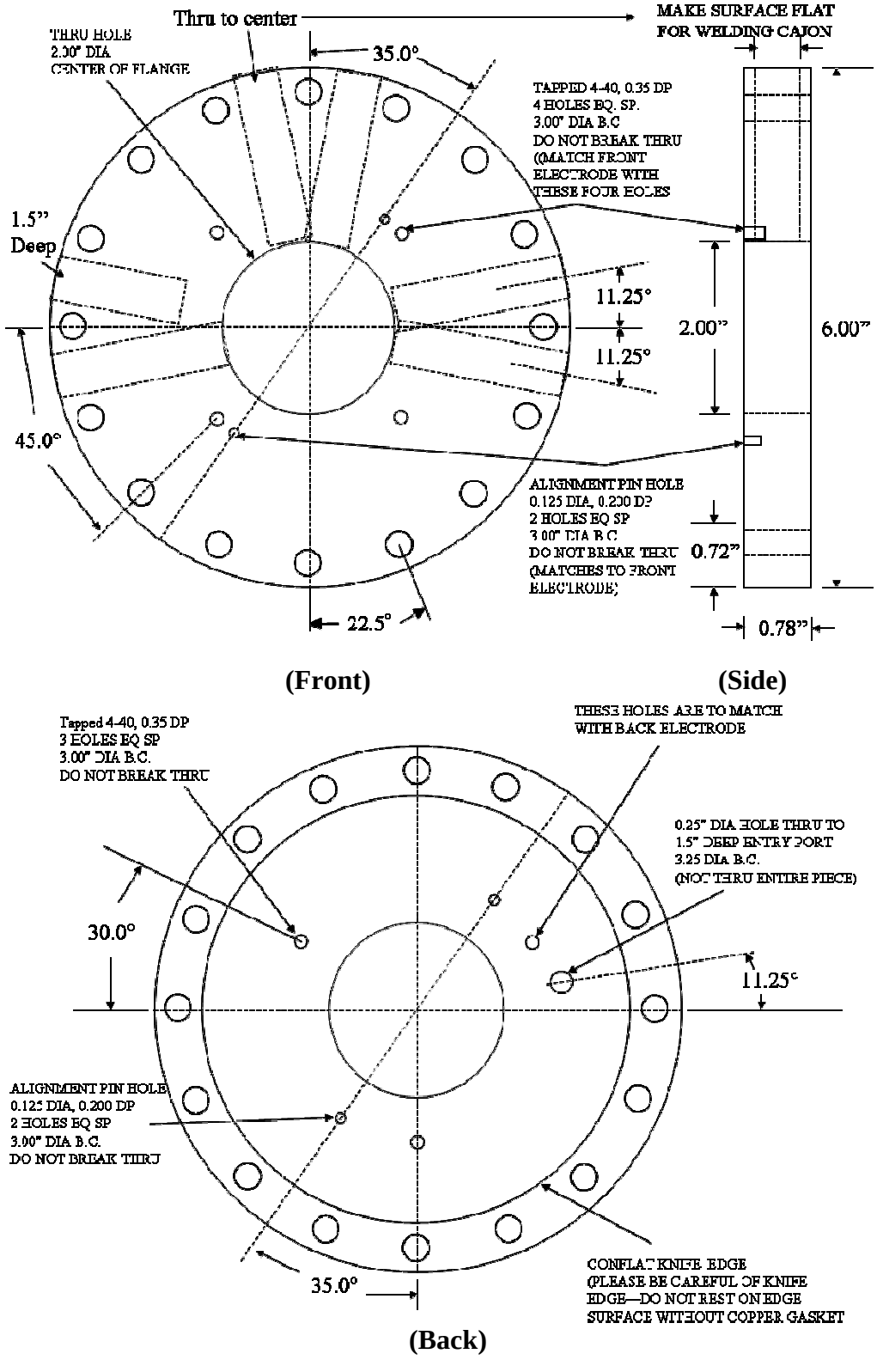

Figure AII.8 – Mechanical drawings of modifications for 6 inch conflat flange used for GDI source described in **Section 3.6.3**.

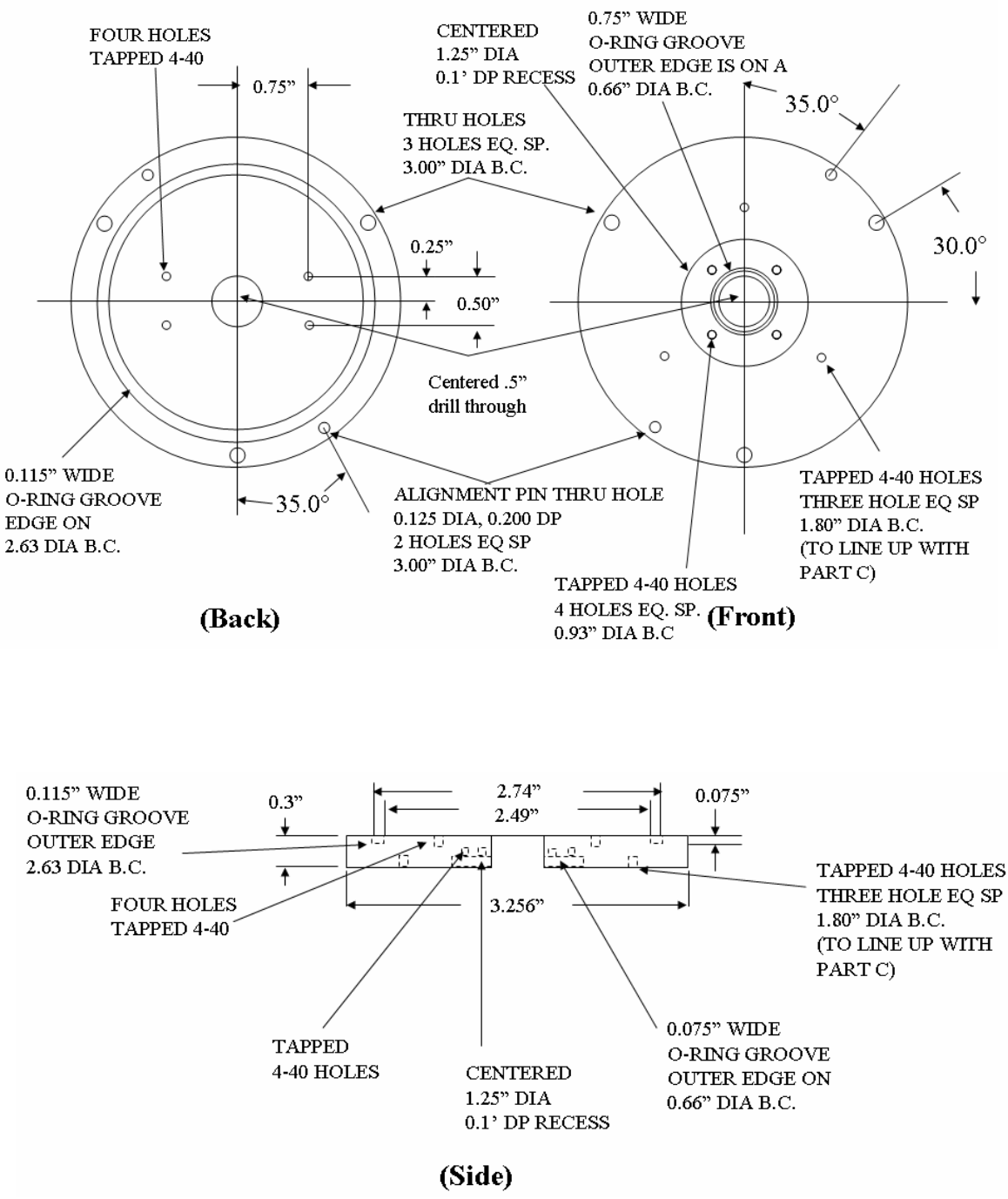

Figure AII.9 – Back Electrode for GDI source described in **Section 3.6.3**.

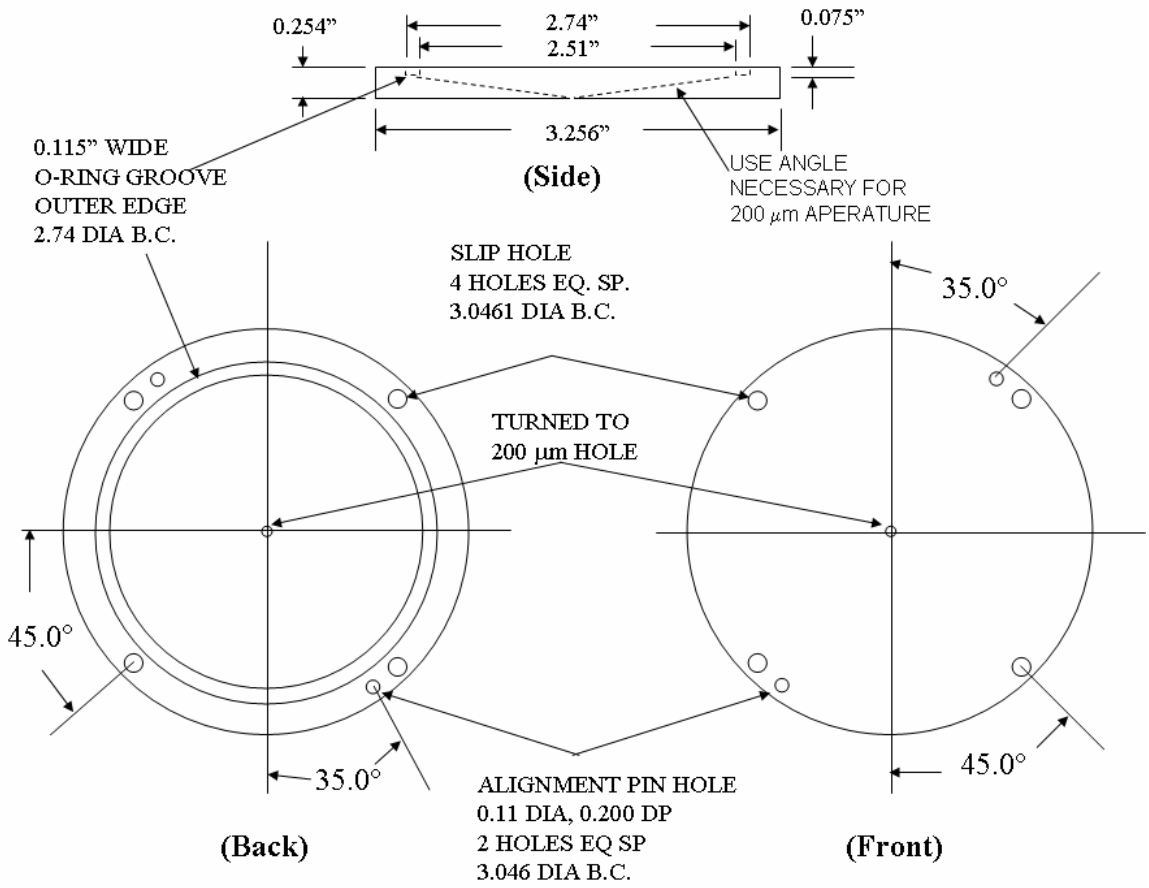

Figure AII.10 – Front Electrode for GDI source described in **Section 3.6.3**.

Endcap Electrode (2):

top:

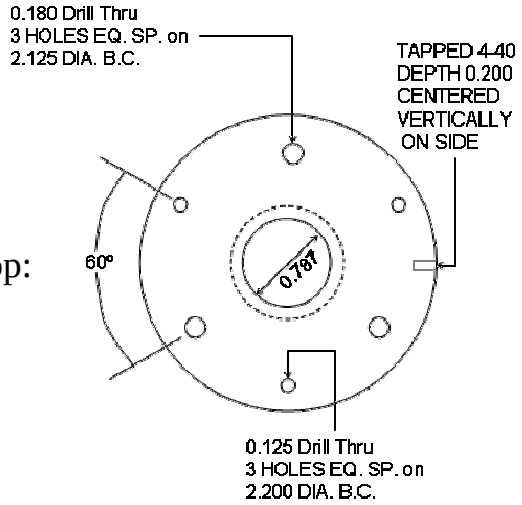

side:

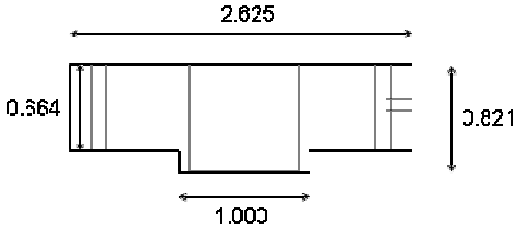

Intermediate Ring Electrode (2):

top:

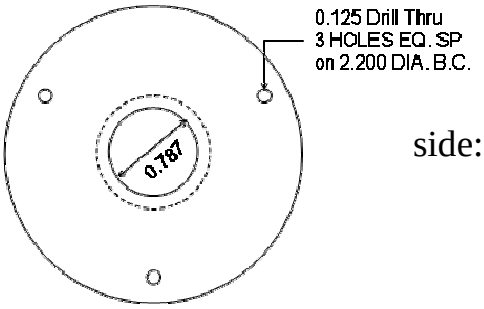

side:

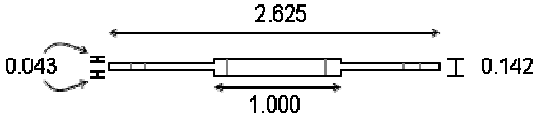

Central Ring Electrode:

top:

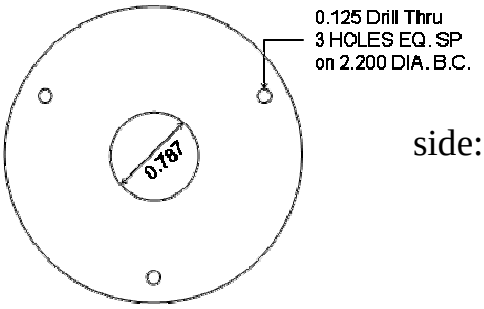

side:

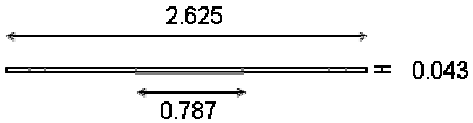

Figure AII.11 – Open endcap octapole ion trap electrodes discussed in **Chapter 6**. All dimensions are in inches and electrodes made from 316 stainless.